WorldAutoSteel

# COMBINED REPORTS – AHSS IMPLEMENTATION SOLUTIONS:

# LIQUID METAL EMBRITTLEMENT STUDY

June 2020

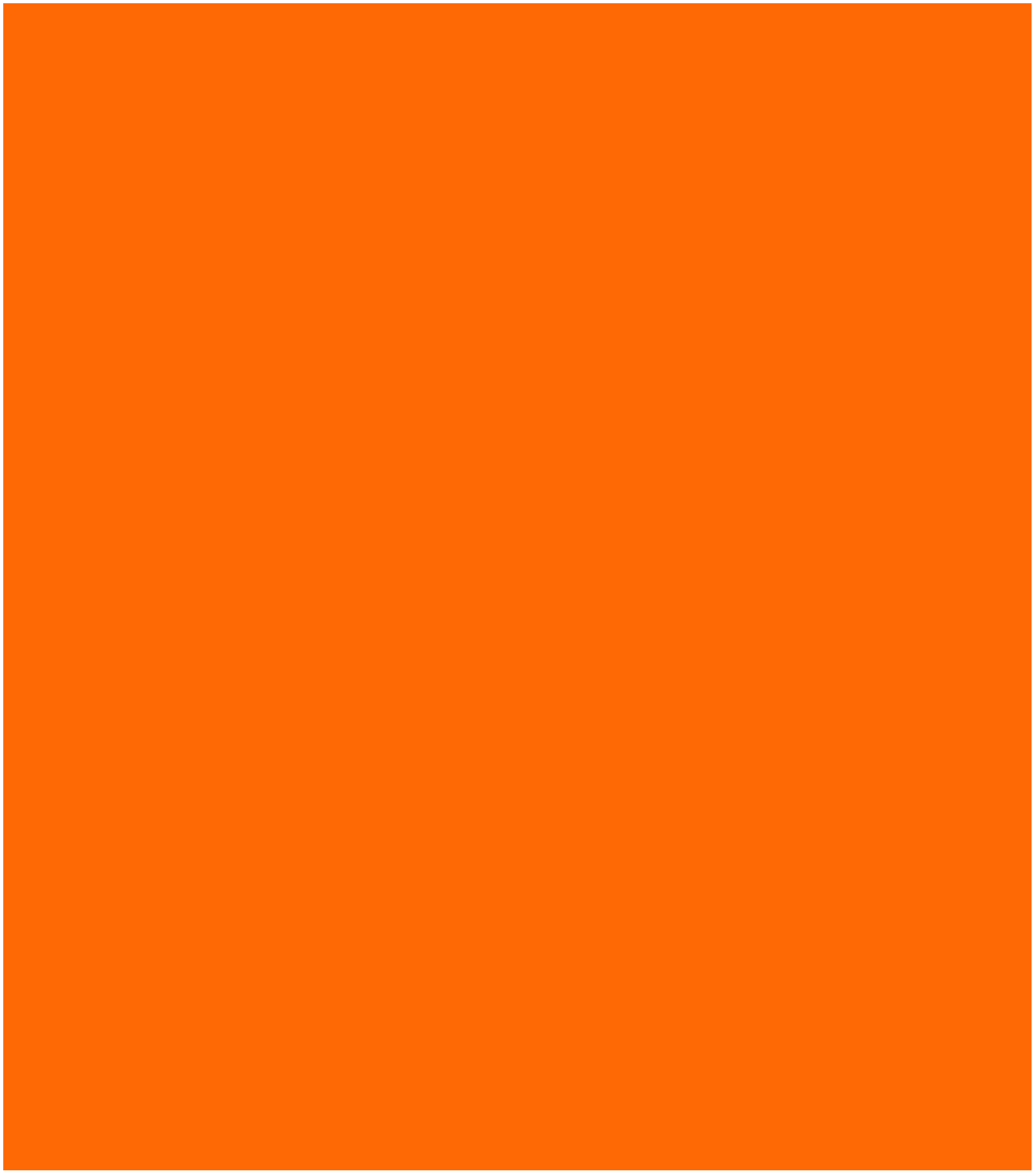

This three-year study of Liquid Metal Embrittlement was commissioned by WorldAutoSteel, the automotive group of the World Steel Association, with its 22 member companies providing the required materials to conduct the study, and a Core Team of member subject matter experts to provide feedback to the research. The reports represent the cumulative research of independent Institutes who conducted the study, as follows:

LME study commissioned by:


and conducted by:


Experimental Research


Simulation


Non-Destructive Testing

## AHSS Implementation Solutions – LME Program

# Final Report

**3 JUNE 2020**


Prof. Dr.-Ing. Gerson Meschut

Christoph Böhne, M.Sc.
Laboratory for material and joining technology
University of Paderborn
Germany

Prof. Dr.-Ing. Michael Rethmeier

Max Biegler, M.Sc.
Julian Frei, M.Sc.
Fraunhofer IPK
Germany

# Contents

Click to Navigate the TOC

# 1 Executive summary

During the resistance spot welding (RSW) of zinc coated Advanced High-Strength Steels (AHSS) liquid metal embrittlement (LME) related cracking may be observed. Since LME is often associated with a reduction of the mechanical properties, it is desired to gain a broader understanding of the phenomenon and its possible impacts. The Goal is to understand the influence of process- and welding set-up related parameters behind LME, acquire the knowledge to prevent and be able to judge possible consequences of residual LME.

A portfolio containing 13 anonymized AHSS with an ultimate tensile strength (UTS) of 800 MPa and higher was used to set up a testing matrix, which enabled the replication of the most relevant and LME-susceptible material thickness combinations (MTC). All considered MTCs show a sufficient weldability under use of standard parameters according to SEP1220-2. At the same time the weld nuggets, as visible in cross-sections, are well distributed over the sheet thickness even for thin materials in LME-susceptible MTCs. No significant cracking was detected during determination of weldability. In parallel, a 3d-electro-thermomechanical simulation model was set up to study LME. The model is based on temperature-dependent material data for dual phase AHSS as well as electrical and thermal contact resistance measurements and calculates local heating due to current flow as well as mechanical stresses and strains. After the model setup, the result accuracy was compared to experimental measurements for the temperature development and cross-section. Good results could be achieved both for the joining of two dual phase steels as well as for one dual phase and one mild steel sheet. After the successful validation, the model was deemed to be useable for LME research.

Subsequently several influences resembling deviations which might occur during car-body production were experimentally investigated. The influences were: excessively elongated weld times, worn out electrodes, switched off electrode cooling, sharp electrode tip geometries, increased electrode forces, angular and lateral electrode positioning deviations, gaps between the sheets and welding during application of

external loads. The impact of the influences was judged based on the degree of cracking observed for each factor. Generally, the most frequent cracking was observed for sharp electrode geometries, increased weld times and application of external loads. All three factors were closely analyzed by combining the experimental and numerical approach utilizing the simulation model.

For the welding under external load experiments the locations of the experimental crack occurrence were correlated with the strains and remaining plastic deformations computed by the simulation model. It was seen that the cracks form at the location of the highest plastic strains and material-specific threshold values for critical strains were derived. The threshold values were used to judge the crack formation during the trials at elongated weld times. Intense and high-depth penetration cracking was experimentally observed, even though the simulation model revealed strains below the critical threshold values. At the same time, the simulation model points out a significant difference in the stress-assisted liquid zinc diffusion time for elongated weld times. Therefore, the additional factor of liquid zinc exposure time influencing the formation of LME was considered as a second highly relevant factor for the formation of LME.

The results for the remaining influence factors were highly dependent on the investigated MTCs. While there were several influences (i.e. change in materials and thicknesses) interfering which each other, it can be concluded that the MTCs needing higher maximum weld current are to be considered more susceptible. For the non-susceptible MTCs even extreme situations and weld setups (like the described elongated weld times) did not result in significant LME cracks within the investigated AHSS grades. For the susceptible MTCs, no significant cracking was observed when these combinations were welded with an idealized laboratory setup at the maximum weld current. Light cracking was observed for most of the investigated influences like low electrode cooling rate, worn electrode caps, electrode positioning deviations or for gap afflicted spot welds. More intense cracking (higher penetration depth cracking) was only observed when welding under extremely high external loads (0.8 Re) or, even more, as a consequence of highly increased weld times.

Subsequently, methods for the avoidance of LME were investigated. Methods which performed well on flat specimen were re-tested in a more complex welding scenario

when joining misaligned hat profiles with gaps in the joining zone. During these trials, the effect of pre-pulses to push zinc out of the joining zone or of post-pulses to relieve local stresses could not be confirmed via experiment and simulation. A positive effect was observed for a change in the electrode tip geometry to larger working plane diameters and for an elongation of the hold time.

When changing the electrode tip geometry, cracking was widely prevented. A change from 5.5 mm working plane to 8.0 mm allowed the creation of LME free welds even at doubled weld times above 600 ms. With a flat-headed cap even the most extreme welding schedules with weld times greater than 1000 ms did not result in cracked spot welds. The in-depth analysis revealed a clear reduction in the local plastic deformation around the indentation for larger electrode tip geometries. Especially at longer weld times this plastic strain reduction is important, as longer weld times contribute to a higher liquid zinc exposure interval, creating a higher potential for LME cracks.

It was also seen that as more energy flows into a spot weld, it gets more important to parameterize an appropriate hold time—depending on the scenario, the selection of the correct hold time alone can make the difference between cracked and crack-free welds. A risk of scenarios without sufficient hold time is the temporal coincidence of liquid zinc on the steel surface with the typical stresses which form after the lift-off of the electrode caps. A sufficient hold time avoids this encountering of liquid zinc on the spot-weld surface and stresses, minimizing the potential for the formation of LME cracks.

However, suitable measures should always be adapted to the specific use case. Generally, the most effective measures for avoidance of LME are:

- Avoidance of excessive heat input (e.g. excess welding time, current)
- Avoidance of sharp edges on spot welding electrodes, instead use electrodes with larger working plane diameter, while not increasing nugget-size
- Usage of suitable hold times (allowing for sufficient heat dissipation)
- Avoidance of improper welding equipment (e.g. misalignments of the welding gun, highly worn electrodes, insufficient electrode cooling)

A destructive testing program for an evaluation of the impact of LME on the mechanical joint strength was conducted. The destructive testing program was based on two MTCs consisting of a susceptible AHSS grade combined with a higher strength martensitic steel or combined with a thick mild steel. Three categories of crack intensity were distinguished for each MTC. Surface cracks as well as interface cracks were tested, each in a shear-tensile and a cross-tensile load case. The results of the crack afflicted specimen were compared to crack free reference specimen, created by zinc removal prior to welding. The parameters for welding of all categories were matched to ensure similar nugget diameters as basis for the comparison of the results. In parallel, the simulation model was used to study the effects of a variation of the crack location by implementing a failure criterion. Cracks could be introduced without scatter and it could be shown that the location of the crack in regard to the RSW notch (i.e. the edge of the nugget) is critical for the joint strength. Even with severe simulated cracks, the sample fails at the notch like an undamaged specimen and reduction in load bearing could only be observed when the crack interacted with the notch.

Under cyclic load no significant influence of the fatigue life was observed. For quasi-static and crash load cases the strength reduction is dependent on the intensity of the cracks. For artificially enforced highly intense cracks, a significant reduction in maximum load and energy consumption is observed, when compared to the reference specimen. The specimens show a failure along the enforced cracks, confirming their impact on failure behavior. A mild reduction of maximum load and energy consumption is observed for the cracks with a medium intensity, which were created using a less extreme welding setup. An influence on failure behavior is still noticeable for this crack intensity in some cases. The tested light cracks were set up to meet the cracking intensity caused by typical process deviations (e.g. bad part fit up, worn electrodes). They reassemble an uncritical scenario in terms of weld strength, since they have no influence in any of the load cases.

Additional specimens were tested in combination with a prior corrosive load of six weeks (VDA 233-102). Four categories of specimen were compared. Zinc coated specimen with intense LME cracks were compared to crack free zinc coated references, which were created by an optimization of the electrode geometry. Additional cracked and crack free specimens were welded and applied with a cathodic

dip coating (CDC) prior to application of the corrosive load and contrasted to the zinc coated specimen. Results showed no significant pitting inside LME-cracks, while typical pitting was observable on the surface of the zinc coated specimen. The CDC-specimen were not influenced by the corrosive load. No impact of the corrosion process on the load bearing capacity of the LME cracked spot welds was observed.

Lastly dedicated specimens consisting of a combination of hat- and L-profiles were used to investigate a possible impact of LME in a more complex structure under a quasi-static load case. The specimens were tested in a three-point-bending load case. For both, the reference and the LME specimen a failure within the base material was observed, resulting in similar energy absorption rates as well as maximum load. No effect of the LME-cracks therefore was observed during these investigations. The results and observations made during the destructive testing program, can be summarized as follows:

- Notch effect of nugget is large in all spot welds
- Crack size needs to be excessive to show any influence on tensile strength and load-bearing capacity of a spot weld
- No significant impact on dynamic load was observed for intense cracks
- Significant weakening is only observed under quasi-static and crash load, if the crack is large and located close to the notch
- No Interactions with an additional corrosive load were observed

In summary of all project results it can be concluded that LME-cracks, which might be caused by typical process deviations (e.g. bad part fit up, worn electrodes) have a low intensity. These cracks do not affect the mechanical strength of the afflicted spot weld. A complete avoidance of LME during resistance spot welding was shown to be possible by the application of measures for reducing the critical conditions from local strains and exposure to liquid zinc.

# 2 LME findings – summary

The following findings are summarized according to the results generated within this study. All statements are given based on the investigated boundary conditions, which include the use of extreme welding parameters (e.g. use of excessive weld times), being necessary in order to enforce significant amounts of LME. No case of random appearance of LME was noted throughout the entire study.

## 2.1 Understand LME

**Impact of material-thickness-combinations (MTCs)**

- LME susceptibility is dependent on the type of MTC
  - MTCs consisting of AHSS-grades (similar) were less prone to cracking compared to MTCs including mild steel (dissimilar)
- LME susceptibility is dependent on the thickness of the joining partner
  - MTCs including thinner (1.00 mm) mild steel were less prone to cracking compared to MTCs including thicker mild steel (2.00 mm) as the joining partner

➔ MTCs requiring more energy have an increased LME-susceptibility

➔ Thicker MTCs require longer time for heat dissipation, thus, cracking potential increases

**Observed crack intensities**

Non-susceptible MTCs:

- Even extreme situations and weld setups (e.g. 4x weld time) did not result in significant LME cracks in investigated AHSS grades

Susceptible MTCs:

- With use of weld parameters from standardized guidelines (SEP1220-2 or ISO18278-2)
  - No cracking was observed on a typical laboratory welding setup at Imax
  - Light cracking (< 20 % sheet thickness) was observed due to application of investigated influences (e.g. low electrode cooling rate, worn electrode caps, electrode positioning deviations, gaps)
  - Medium – Intense cracking (> 20 % sheet thickness) was only observed as a consequence of increased (multiplied) weld times

**Location of observed LME cracks**

- Electrode indentation cracks were observed for most investigated materials (during enforcement phase)
- HAZ crack were only observed for some of the investigated materials
- Interface cracks were only observed for the most LME-susceptible MTCs under extreme weld times or specific 3-layer stack-ups

**LME's time-interval of origin**

- LME cracks can be initiated any time from the heating phase (weld time) to the cooling phase (hold time) or after the electrode lift-off based on the individual boundary conditions

## 2.2 Control LME

**Measures for controlling and investigating LME (laboratory)**

- Local removal of zinc from the joining area before welding allows for complete LME avoidance
  - Including alloying at the contact area of the electrode caps
  - Technique suitable for creation of crack free reference specimen under use of extreme parameters
- Dye-penetrant testing may lead to incorrect results (false crack detections)
- Local removal of zinc from the joining area after welding enables the uncovering of hidden cracks
  - Full visual inspection of surface crack area as basis for quantification of cracks

**Reference test methods for the enforcement of LME**

- Reproducible enforcement of significant amounts of LME by…
  - Welding with extremely elongated weld times in combination with LME-susceptible MTCs
  - Welding under externally applied high tensile loads (and weld time according to SEP1220-2)
- Quantification of LME cracking intensity by determination of surface crack area

➔ Testing of entire AHSS-portfolio for determination of individual LME susceptibility

**Welding process adaptions for controlling LME**

- Electrode force profiles (high force in hold time) can reduce the crack penetration depth
- Pre-Pulses are not capable of evacuating zinc from the joining area before the main welding process
  - ➔ Increase LME cracking by redistribution of zinc accumulations to critical areas
- No significant effect on crack formation was determined for…
  - ➔ …use of post-pulse welding schemes
  - ➔ …the order of the weld sequence

➔ LME can be controlled (and prevented) by adaption of the electrode geometry and hold time

**Mechanical strength impacts of LME**

- CT-Scan supported testing of 3 crack intensities…
  - Light cracks (< 20 % sheet thickness) were not found to have an impact on mechanical joint strength
  - Medium cracks (20 – 50 % sheet thickness) may have an impact (depending on load type and MTC)
  - Intense cracks (> 50 % sheet thickness) have a significant impact
    - Cyclic load is not affected for most investigated cases
- No impact of / interaction with additional corrosive load was observed

## 2.3 Prevent LME

**Achieving an LME free welding process**

- LME free welds could be achieved on all investigated MTCs by optimization of the welding process
  - Including a combination of LME-susceptible MTCs, elongated (2x) weld times and increased stresses (e.g. presence of gaps, complex geometry)
  - Even extreme welding setups (4x) were found to generate LME free weld results based on use of suitable electrodes
- ➔ Immense impact of electrode cap configuration on welding process
  - Larger working plane (contact area) for increased supporting effect around weld nugget (reduced formation of gaps), quicker heat dissipation
  - More complex weld schedules (e.g. measures for welding of asymmetrical 3-sheet-combinations) still applicable

**General supportive measures for LME reduction**

- Avoid any excess welding time
- Avoid sharp edges on spot welding electrodes
- Avoid improper welding equipment (e.g. misalignments of the welding gun, highly worn electrodes, insufficient electrode cooling)
- Use suitable hold times (allowing for sufficient heat dissipation)

# 3 Introduction

The automotive industry faces the key tasks of reducing the fuel consumption and the pollutant emissions of their vehicles. At the same time there is the continuous strive for an increase in passive occupant protection. To achieve these distinct goals a possible solution is the implementation of modern AHSS-grades into the car body. These innovative steel grades stand out to alternative material solutions due to their superior combination of tensile strength and ductility.

To protect these steels from corrosion it is a standard to provide them with a zinc coating. The most used joining technique for steels in car body manufacturing is resistance spot welding (RSW), since this joining process has major benefits in terms of profitability and can deliver a high process stability. During the RSW of AHSS grades cracks on the sheet surface have been observed inside the joining area. It is assumed that the cracks are initiated by liquefied low-melting zinc phases, which infiltrate the grain boundaries of the steel base material, potentially leading to a brittle fracture. This phenomenon is usually referred to as Liquid Metal Embrittlement (LME).

It is the main task of this program to investigate the LME of AHSS and provide solutions for their unrestricted implementation in the future automotive body structure. This program features a three-step approach, illustrated by Figure 3-1, which is incorporating experts from multiple fields of expertise. In a first step the aim is to get a better understanding of the influence of process- and welding set-up related parameters behind LME. This process is based on literature research as well as multiple experimental investigations supported by process simulations in order to decode the relevant cause-effect-relations. Afterwards, a transfer to industrial production conditions is to be made by an identification of the relevant main influences responsible for LME based cracks during production. Second step is to control the LME cracks. A controlled enforcement of the cracks then serves as a basis for various types of destructive testing planned throughout this program and lays the foundations for a future avoidance of LME cracks. For all these investigations, a crucial point is to be able to detect the cracks in a detailed manner by a suitable non-destructive testing method. Different techniques are to be developed satisfying the demands both for a

laboratory and a production environment. The third step is to identify and quantify the possible consequences of LME cracks, e.g. in terms of joint strength. In a final effort all the knowledge gained during this project will be merged to deliver solutions for the future reduction or even avoidance of LME.

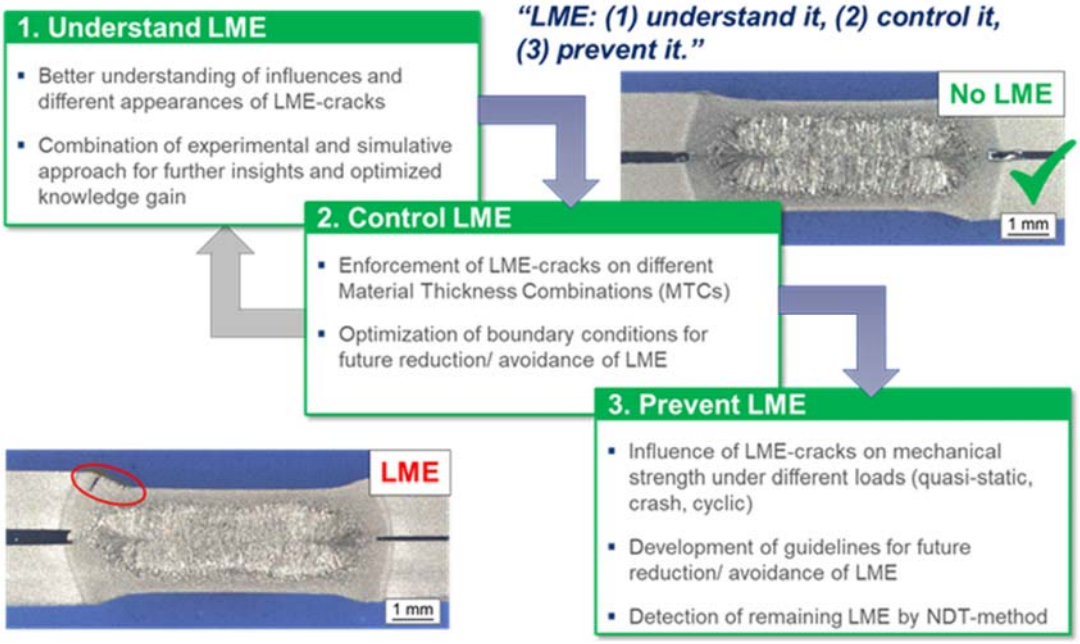


*Figure 3-1: Overview of the applied materials and their properties as characterized by WorldAutoSteel.*

# 4 Experimental setup and boundary conditions

## 4.1 Testing materials, material properties and stack-ups

Within the framework of the investigations, a total of 18 different steel grades were investigated. The steels were anonymously secured and characterized by WorldAutoSteel (WAS). Representative steel grades identified as possibly LME susceptible were chosen and as a result not all available grades or coatings are included in this program. Thirteen of the steels were AHSS grades and five conventional steels supplied for generation of differing stack-ups. Table 4-1 provides an overview of the applied AHSS materials and their properties.

*Table 4-1: Overview of the AHSS and their properties as characterized by WorldAutoSteel. (As currently there is no standard for the naming of 3rd generation AHSS, the Terms DP, DH, TRIP and RA might refer to identical material concepts.)*

| Type | Strength (MPa) | | | | | Elongation (%) | | | Size (mm) | | | Coating |
|---|---|---|---|---|---|---|---|---|---|---|---|---|
| | TS | UTS | YS | $RE_L$ | PS | %A5 | %A80 | %EL | WIDTH | LENGTH | GAUGE | |
| DP1000 | 1030 | | | 748 | 748 | 21.0 | 11.0 | | 1000 | 1250 | 0.8 | EG 75/75 g/m2 |
| DP1000 | 1022 | | 850 | | | | 10.5 | | 1400 | 1000 | 1.48 | EG 53/53 g/m2 |
| DP1000 | | 1001 | 780 | | | | 9.5 | | 1350 | 500 | 1.00 | HDGI 50/50 g/m2 |
| DP1000 | | 999 | 779 | | | | 9.0 | | 1400 | 500 | 1.50 | HDGI 50/50 g/m2 |
| DP1000 | 1033 | | 629 | | | 19.0 | 13.0 | | 1000 | 1084 | 1.20 | HDGI 100/100 g/m2 |
| DP1000 | 1014 | | 593 | | | | 13.0 | | 1250 | 625 | | HDGI 50/50 g/m2 |
| DH1000 | | 1011 | 712 | | | | 14.0 | | 1200 | 500 | 1.50 | HDGI 50/50 g/m2 |
| DP1200 | 1220 | | 1050 | | | | 7.5 | | 1000 | 630 | 1.34 | EG 53/53 g/m2 |
| | | | | | | | | | | | 1.58 | |
| TRIP800 | | 826 | 492 | | | | | 28.8 | 1230 | 510 | 1.40 | EG 60/60 g/m2 |
| RA1000 | 1007 | | 567 | | | | | 24.0 | 1200 | 500 | 1.20 | EG 60/60 g/m2 |
| TRIP1200 | | 1216 | 896 | | | | 13.4 | | 1200 | 500 | 1.40 | EG 50/50 g/m2 |
| TRIP1200 | | 1236 | | | 1054 (0.2 PS) | | 15.0 | | 500 | 500 | 1.00 | EG 48/51 g/m2 |
| MS1400 | 1395 | | | 1140 | 1140 | 6.0 | 4.0 | | 1000 | 1000 | 1.50 | EG 75/75 g/m2 |
| | 1382 | | | | | | 4.8 | | 1000 | 1000 | 1.20 | EG 75/75 g/m2 |

Table 4-2 provides an overview of the applied conventional steels and their properties.

*Table 4-2: Overview of the applied conventional steels and their properties as characterized by WAS.*

| Type | Strength (MPa) | | | | | Elongation (%) | | | Size (mm) | | | Coating |
|---|---|---|---|---|---|---|---|---|---|---|---|---|
| | TS | UTS | YS | $RE_L$ | PS | %A5 | %A80 | %EL | WIDTH | LENGTH | GAUGE | |
| Mild Steel | 280 | | 149 | | | | 25.0 | | 1010 | 650 | 0.72 | HDGI 53/53 g/m2 |
| Mild Steel | 309 | | 171 | | | | 47.0 | | 500 | 500 | 2.00 | HDGI 53/50 g/m2 |
| | | | | | | | | | 1200 | 800 | | |
| Mild Steel | | 295 | 154 | | | | | 53.0 | 1600 | 500 | 1.00 | Uncoated |
| HSLA | | 420 | 340 | | | | | | 1300 | 1000 | 1.00 | HDGI 50/50 g/m2 |
| | | 490 | 400 | | | | | | | | | |
| HSLA | 507 | | 395 | | | | | 25.0 | 1300 | 500 | 1.25 | EG 43/39 g/m2 |

During the investigations, a variety of different stack-ups were investigated. Starting with a wider portfolio during the initial screening phase and ending on specifically selected combinations for the last investigational setups, a systematic approach on selection of stack-ups was pursued throughout the program. Figure 4-1 aims to clarify this process of stack-up formation.

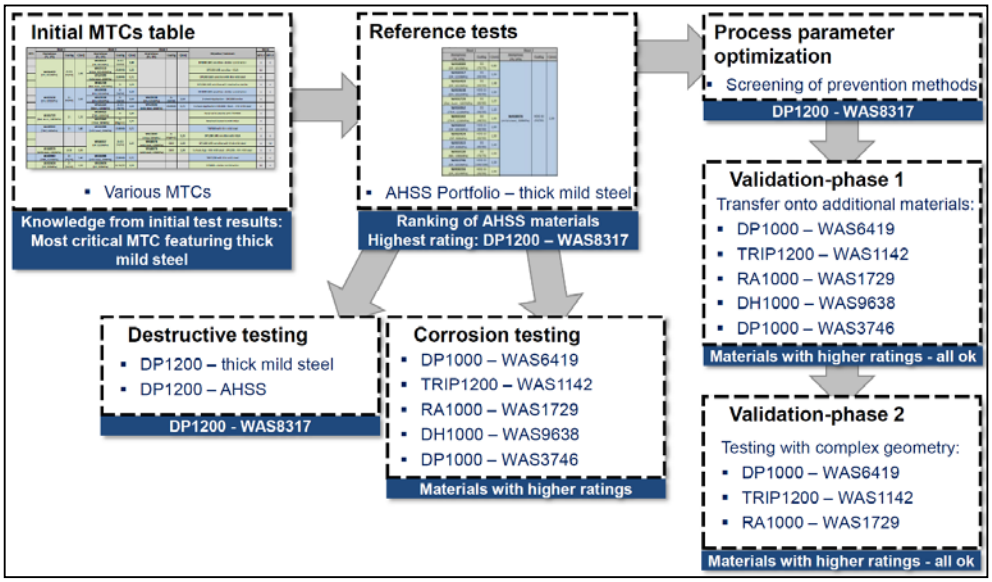


*Figure 4-1: Overview of the applied materials and their properties as characterized by WorldAutoSteel.*

The initial MTC-table was the basis for the investigation during the determination of the weldability. During these initial investigations it was observed that an LME-susceptible AHSS in combination with a 2.00 mm thick mild steel was the most critical, i.e. LME-susceptible combination. In a next step, each of the available AHSS materials was

tested for its LME susceptibility by two reference test methods based on the selected laboratory boundary conditions (see 6.2.9 and 0 ). Based on the reference test results, a single LME susceptible material (DP1200) was selected to be used as the test candidate throughout the destructive testing process, to allow for an enforcement of various crack intensities. It was combined in two stack-ups to map two distinct situations: a rather uncritical scenario, in which the LME afflicted AHSS grade is the material with the higher strength (DP1200 – Mild steel, hereinafter referred to as thick mild steel) and another scenario, in which it is the lower strength material (DP1200 – MS1400). Because of the high material consumption during the destructive testing phase and limited material availability the DP1200 was partially substituted by an identical grade with a slight variation in thickness. A selection of five (later three) LME susceptible AHSS grades was used throughout the remaining program to ensure the validity of the investigated prevention methods.

## 4.2 Specimen geometries

Within the framework of this research project, different single-spot and multi-spot specimen geometries are used. During the LME enforcement trials dog bone specimens allow for an application of external loads, while more complex hat profile specimens were used for the validation phase of the process parameter optimization. Destructive testing is relying on LWF-KSII specimen and double hat profile specimen with attached L-profiles.

### 4.2.1 Laboratory flat and strip specimen

For the determination of weldability 45 x 45 mm² specimen were welded as specified in SEP1220-2 (see 6.1).

During the LME enforcement trials (see 0) strip specimen were used. The distance between the spot welds on these specimens was above a minimum of 25 mm to avoid an influence on the results by shunt effects. Additionally, each first spot on a strip was used as a shunt spot weld and not evaluated. Strip specimen were as well utilized during the corrosion testing process (see 6.7.5) and during the process parameter optimization (see 6.4). Figure 4-2 provides a schematic view of the laboratory flat specimen.

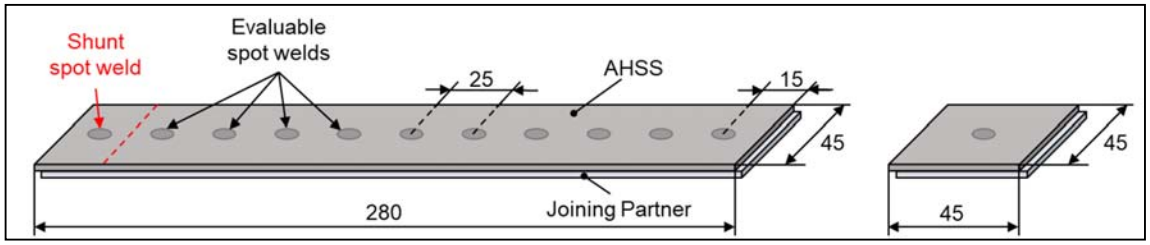


*Figure 4-2: Overview of the laboratory flat and strip specimen used within this research program.*

### 4.2.2 Dog bone specimen (welding under external load)

During the LME enforcement trials dog bone specimens allowed for an application of external loads onto the AHSS testing candidate. The geometry of this specimen type is depicted in Figure 4-3. It was welded to a joining partner of the size 60 x 15 mm, while being externally loaded by the shown device. The specimens were manufactured using water jet cutting.

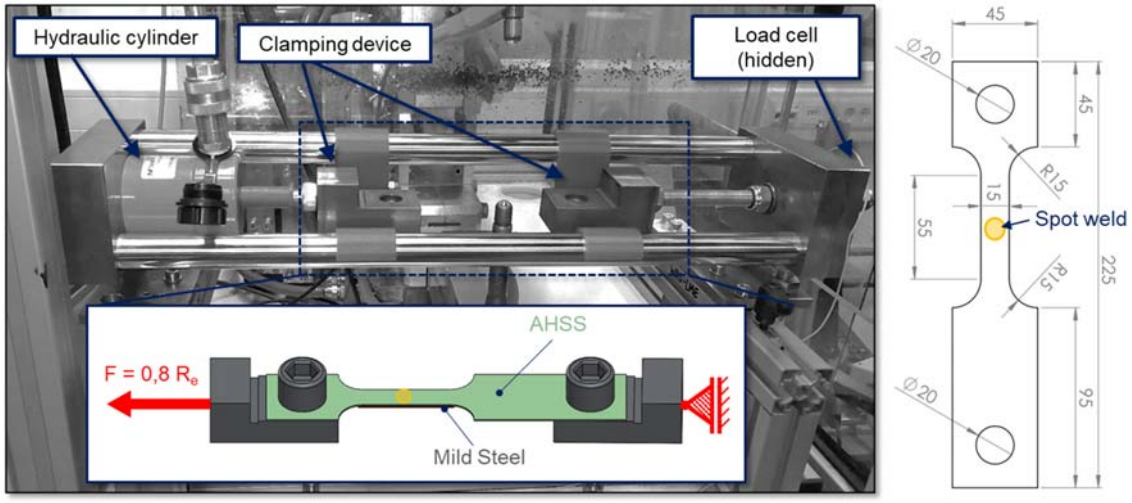


*Figure 4-3: Overview of the laboratory flat and strip specimen used within this research program.*

### 4.2.3 LWF-KSII specimen

For all destructive testing LWF-KSII specimen with an inner width (IW) of 34 mm were used. The LWF-KSII specimen consists of two symmetrical u-profiles, which are joined on the profile bottom. This specimen geometry, which is shown in Figure 4-4, provides the advantage of an increase stiffness and therefore allows to put a higher load concentration on the actual joint rather than on the surrounding sheet metal.

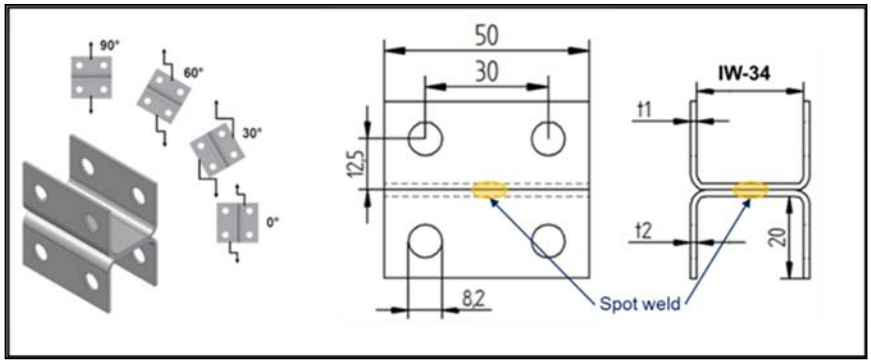


*Figure 4-4: Load bearings and geometry of the used LWF-KSII specimen.*

This is especially relevant during the investigation of cross tensile load cases, which typically leads to a higher material deformation than for flat iso-specimen. Another major benefit of LWF-KSII specimen, also illustrated in this figure is the possibility to use the identical specimen geometry for a variation of load angles between shear-tensile testing (0° load angle) and cross-tension (90° load angle). This specimen type was used in combination with an optical displacement measurement system.

### 4.2.4 Hat profile specimen

This specimen type was used during the optimization of process parameters, to allow for a transfer to a more complex welding scenario, caused by its increased stiffness compared to flat specimen based on its three-dimensional geometry. It was combined with spacers to adjust a gap between the inner spots of 1 mm height. The hat profile specimen and the set-up gaps are pictured in Figure 4-5.

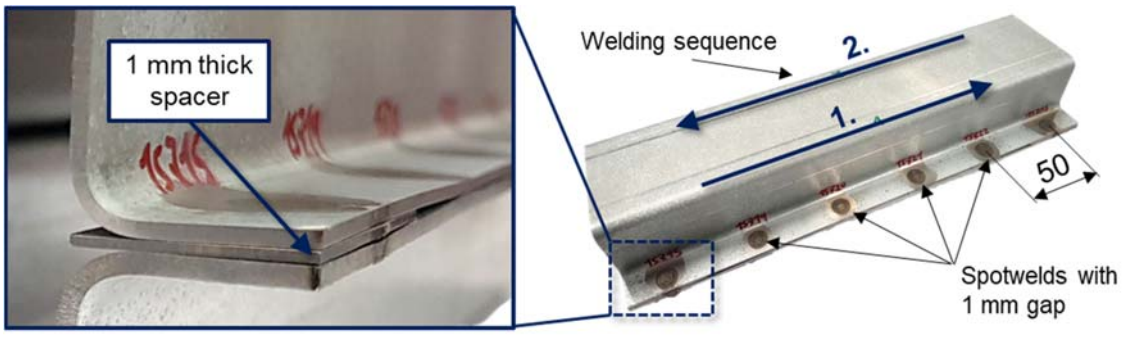


*Figure 4-5: Schematic of Hat profile specimen used during optimization of welding parameters.*

### 4.2.5 Double hat profile specimen with attached L-profiles

The specimen geometry shown in Figure 4-6 was selected to be tested via a 3-point-bending test. Highlighted are two of the four spots (symmetrical specimen) which experience the highest load during the testing process. Each specimen is joined by 32 spot welds. It consists of two 145 mm long hat profiles with two accompanying striking plates. The two hat profiles are joined by two 145 mm L-profiles.

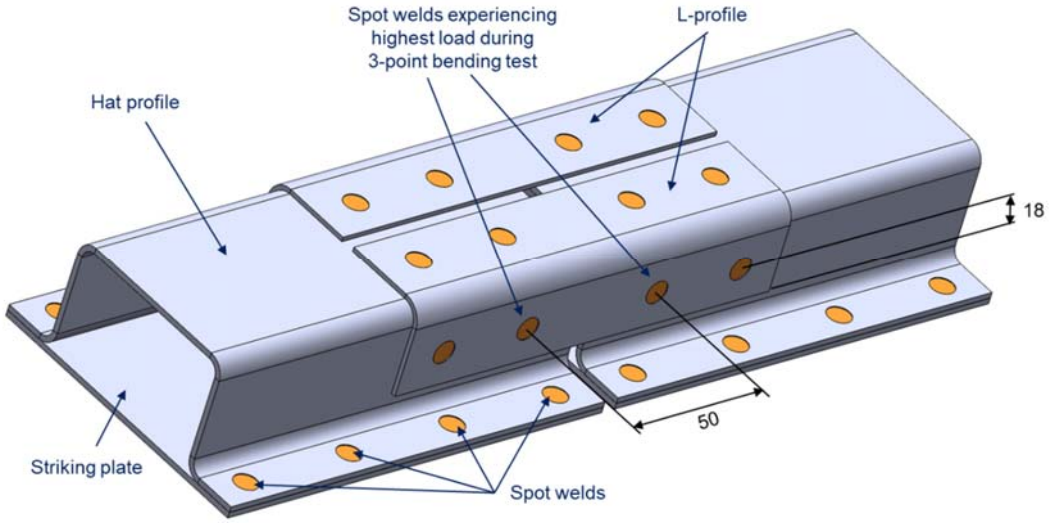


*Figure 4-6: Schematic of Double hat profile specimen with attached L profile specimen.*

## 4.3 Resistance spot welding equipment

Resistance spot welding machine

A resistance spot welding machine from Bosch Rexroth AG is used to produce the welded joints. It is equipped with an electromotively guided X welding gun with a maximum electrode force of 8 kN. The current source provides a constant current controlled medium frequency direct current with 1000 Hz and a maximum current strength of 50 kA. The measured variables force, current and voltage can be documented both internally via the system and externally. Figure 4-7 shows the welding system with the most important technical data. A SK71LA/4 tip dressing machine from SVS Schweißtechnik GmbH is used to tip-dress the electrode caps.

| | | |
|---|---|---|
| Welding gun type | | Düring Euro-X, Servo-motor driven, $F_{max}$ = 8 kN |
| Welding current control | Inverter | PSI64C0.759W1 |
| | Interface | SPS Control 2. Gen. (CML25, Firmware XLC V13), ProfiNet / Ethernet, SercosIII-Master, EAs expandable |
| | Transformer | PSG 6180.00 RSTK, $I_{max}$ = 50 kA |
| | Controls | Constant current control, U-I, ALR |
| Operating- and Diagnosis software | | BOS6000, 1.44.0 |
| Measuring technology | | internal + external (F, I, U) |

*Figure 4-7: Resistance spot welding equipment and its most important technical features.*

Spot welding electrode geometries

Different electrode cap types were used during the investigations. Figure 4-8 shows schematics of the relevant electrode geometries. As a general basis for all of the investigations the electrode caps F1-16-20-50-5.5 (F1-5.5) were used. During the research on process optimization for the avoidance of LME, the additional electrode geometries F1-16-20-50-8.0 (F1-8.0) and A0-16-20-100 (A0-100) were investigated on their impact on the welding process and on crack formation. These electrode geometries were chosen, because their outer dimensions are identical to the F1-5.5 electrode geometry. As a consequence they do not influence the accessibility when welding typical automotive flanges and can directly replace the F1-5.5 electrode geometry. By using appropriate tip dressing equipment F1-5.5 electrode caps were also successfully tip dressed to F1-8.0 tip shape, during the experiments of this project.

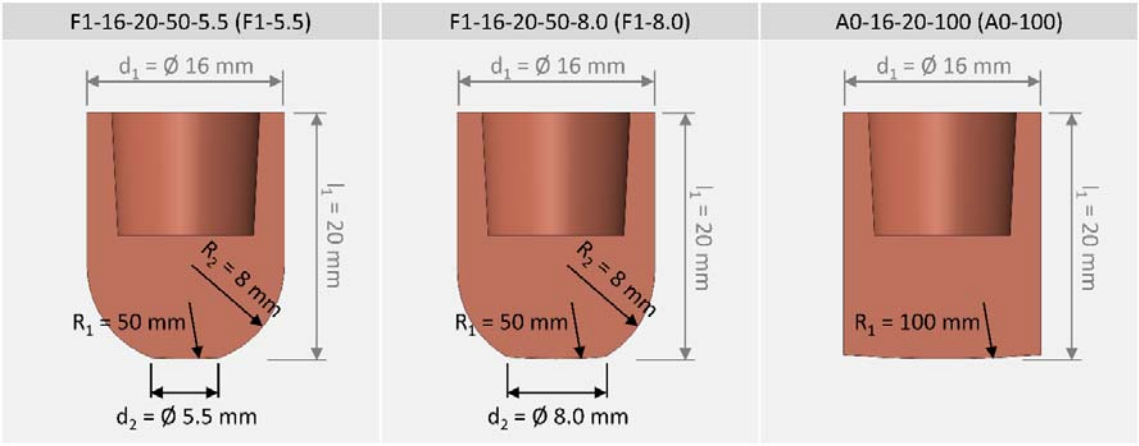


*Figure 4-8: Dimensions of investigated resistance spot welding electrodes. [1]*

## 4.4 Testing and evaluation methods

### 4.4.1 Chisel testing

The chisel test is a destructive test method standardized according to DIN EN ISO 10447. A fork chisel is inserted between the welded sheets above the spot weld until it fails. During testing the joint is mainly strained by cross-tensile load, i.e. stresses in the normal direction to the surface of the joint. Based on the type of fracture that results, an initial judgement about the quality of the joint can be made. A distinction was made between plug fracture (pf), partial interfacial fracture (pif) and interfacial fracture (if), see Figure 4-9.

The evaluation of the type of fracture is first carried out by means of an optical check. In case of a plug fracture, the welded joint remains intact. A failure inside the base material or in the heat-affected zone occurs. If the so-called interfacial fracture occurs, the welded joint fails, and the sheets are separated along the joining plane. A mixed fracture is a combination of plug fracture and interfacial fracture. After the chisel test has been performed, the weld nugget diameter can be determined which, together with the type of weld spot joint, serves as the initial basis for assessing the welding quality.

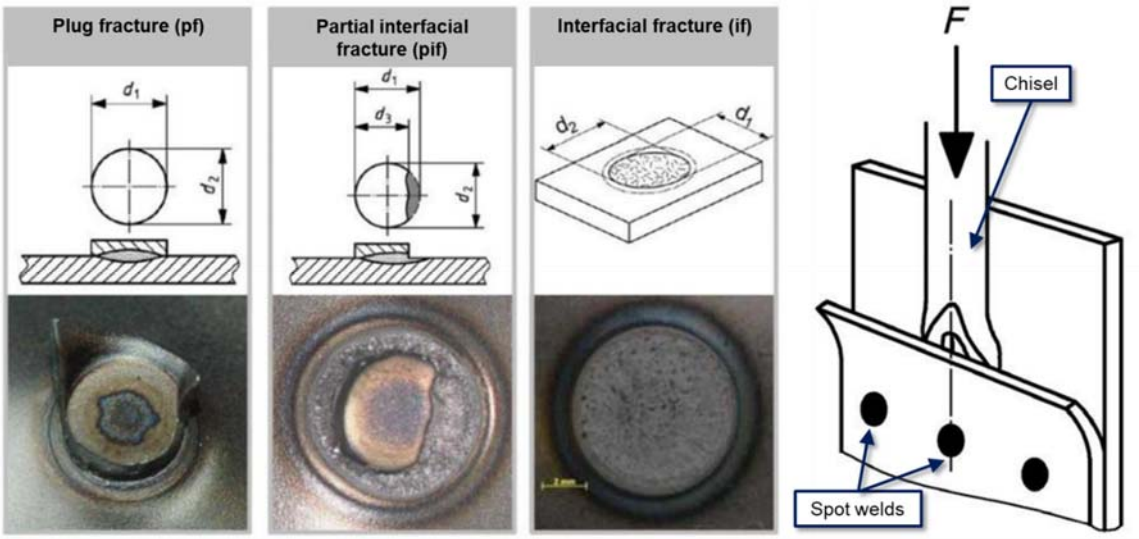


*Figure 4-9: Chisel test based on DIN EN ISO 10447 (right) and possible fracture pattern (left). [2]*

### 4.4.2 Visual inspection and metallographic cross-sections

To enable a precise crack characterization different approaches for crack detection were tested. Figure 4-10 shows exemplary results achieved by these techniques.

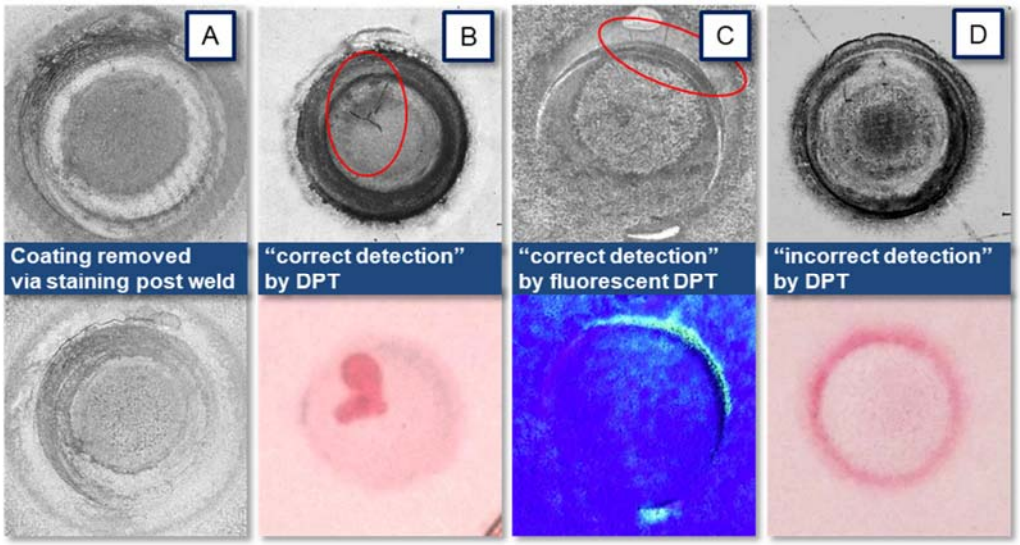


*Figure 4-10: Overview of visual inspection techniques via macroscopic images: A – Effect of coating removal on crack visibility; B and C – correct crack detection via dye-penetrant-testing; D – incorrect crack detection via dye-penetrant-testing.*

Dye penetrant testing was initially tested in a standard (B) and fluorescent (C) variant during this project, but then discarded as several incorrect detections were observed.

Additionally, a removal of the coating (A) by staining of specimen in 20% hydrochloric acid was tested. This technique was found to allow for a detailed analysis of the spot weld surface, and the detection of very fine irregularities and cracks. To allow for a determination of local crack depth additional metallographic examinations were carried out. Figure 4-11 shows an exemplary macroscopic image of a crack afflicted spot weld next to the correlating cross-section.

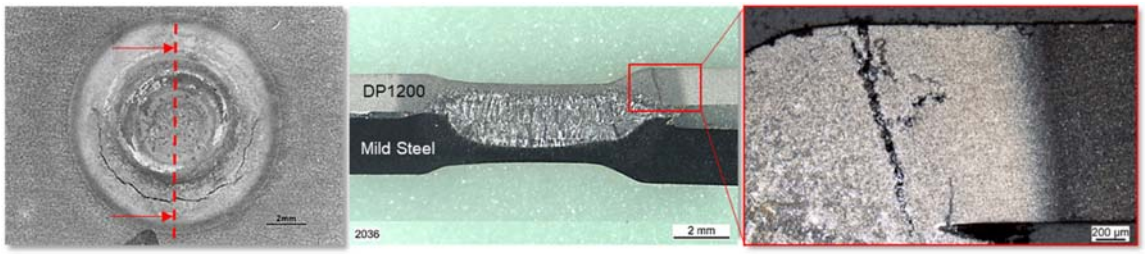


*Figure 4-11: Exemplary results of visual inspection and metallographic cross-sections: Left: Macroscopic surface view of cracked spot weld; Middle: Metallographic cross-section of same spot weld in lower magnification; right: Detail from same metallographic cross-section in higher resolution and magnification.*

### 4.4.3 Quantification and characterization of LME cracks

The created macroscopic images of the spot weld surface could be used ideally to allow for a thorough quantification of crack intensity, via an evaluation of the surface crack area. This technique is believed to result in a better representation of the observed crack intensity in comparison to the measurement of crack length, because of the additional inclusion of the crack width. Once the crack area is determined, it can easily be highlighted for an easy visualization, as shown in Figure 4-12.

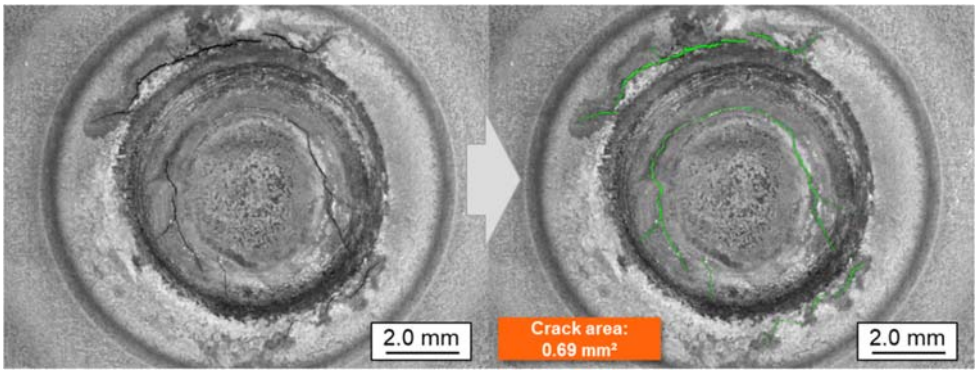


*Figure 4-12: Macroscopic image of spot weld surface before and after quantitative evaluation via determination of surface crack area.*

The evaluation was performed with an open-source image editing software and is based on the counting of the crack's pixels. Based on the quality (i.e. contrast ratio) of the image, the evaluation process can be assisted by use of a threshold tool. This technique was widely applied, when reference testing the entire AHSS portfolio (6.4).

At later stages of the project, computer tomography (CT) scans of specimen before destructive testing were performed to assess more complete information on the volumetric three-dimensional appearance of LME cracks. The result of the CT scans in form of a grayscale images was manually evaluated. Only heat affected zone (HAZ) cracks were considered. Each spot welds circular area was divided into 32 sectors. Each sector was further dissected into discrete layers each 0.05 mm in direction of sheet thickness. The resulting crack-matrix can be illustrated as shown in Figure 4-13, to provide an impression of the three-dimensional crack geometry in a two-dimensional graphic. Cracks progressing from the sheet surface are advancing from outer to inner circle of the symbol and cracks progressing from the sheet interface from inner to outer circle.

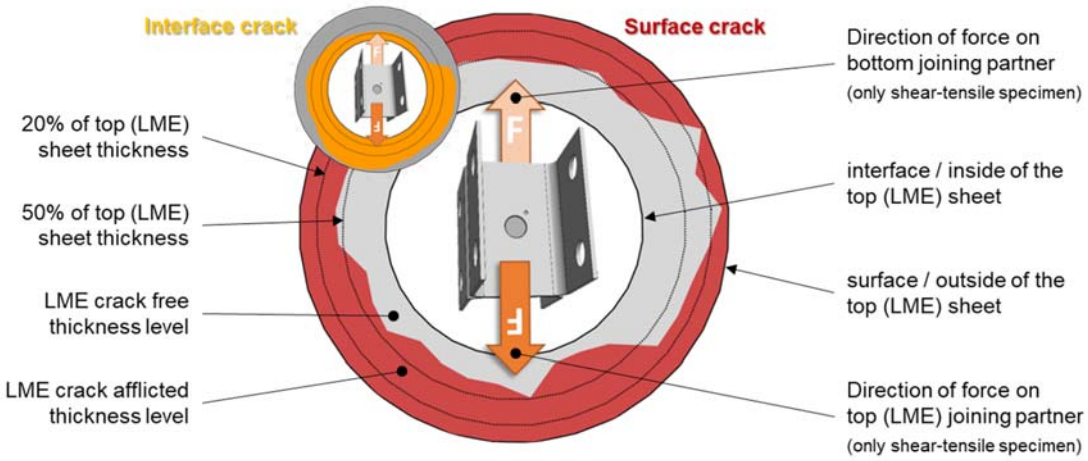


*Figure 4-13: Exemplary result of a CT scan evaluation*

Three categories of crack intensities were defined as a basis for the destructive testing: light cracks are meant to represent a maximum crack depth of 20% of the sheet thickness. Medium cracks refer to a crack depth of 20% to 50% of the sheet thickness. Intense cracks exceed 50% of sheet thickness.

# 5 Simulation model setup

## 5.1 Requirements on the simulation model

The following requirements were imposed on a resistance spot welding simulation model for liquid metal embrittlement investigations:

- Fully coupled calculation of electrical current flow, heat generation, temperature flow, mechanical forces and stress development
- Adjustable boundaries for electrical contact and thermal cooling
- Modelling of phase transformations, considerations of associated material properties and volume changes
- 3-dimensionality to model crack influence on mechanical performance

The commercial finite element tool ‘Simufact Welding’ was chosen and all calculations were conducted in this software. The cross-section of a simple model for welding of a single spot on a 50 x 50 mm² sheet is shown in Figure 5-1.

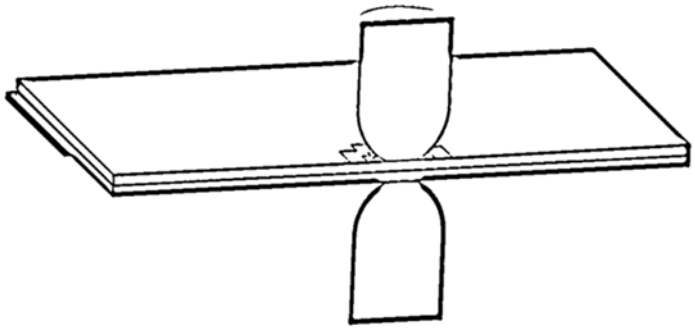

*Figure 5-1: Cross-section of the 3-dimensional model comprising two sheets, two electrodes and the clamping at the rear.*

## 5.2 Material modelling

Especially for AHSS that have been introduced recently, temperature dependent material data for welding simulation are not widely available and their experimental acquisition is costly and time-consuming. Past studies have shown that the temperature dependent properties of these materials vary little within a single class (e.g. Dual Phase steels), thus we were comfortable accepting the 600 MPa strength

material data to be representative of the higher strength DP steels evaluated in the study. For the project, the parameters are acquired from a mixture of literature sources and targeted experiments. The thermophysical properties of a 600 MPa strength class dual phase steel are determined experimentally by Schwenk et al. [3], shown in Figure 5-2.

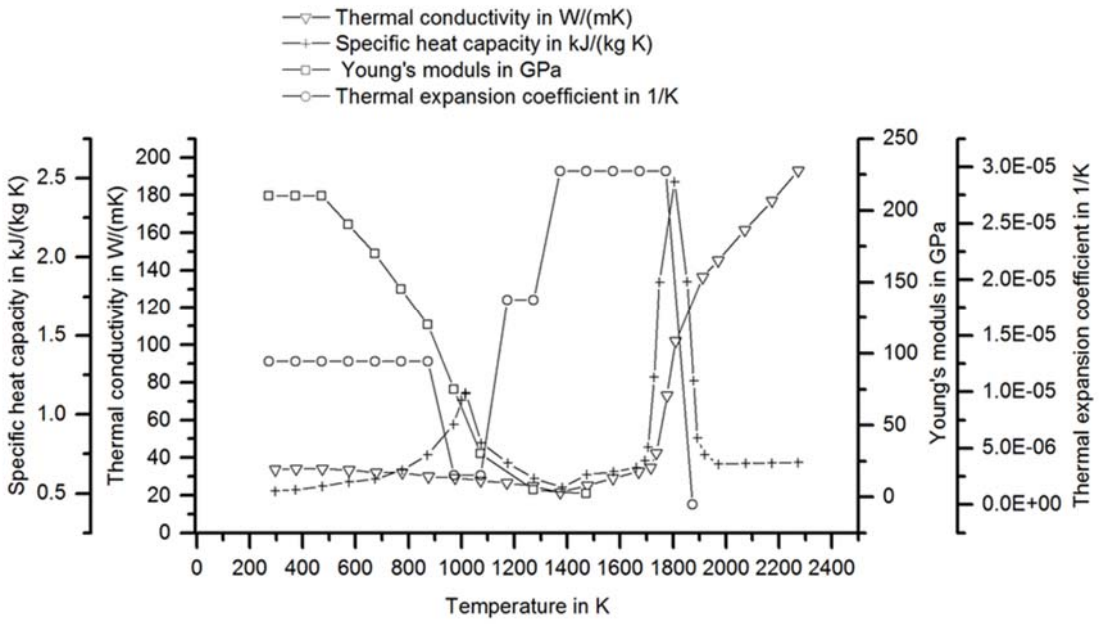


*Figure 5-2: Thermo-physical and Thermo-mechanical material parameters according to Schwenk [1]*

The assumption is made, that the data remains the same for different strength classes of dual phase steels. The same assumption is made for the thermomechanical material data, i.e. that the young's modulus remains at ~210 GPa at room temperature, and the softening with heat remains equal. The temperature dependent thermal expansion coefficient remains unchanged. The simplification is made, that only the yield strength and ultimate tensile strength must be scaled for different grades of the same material class. The flow behavior is also determined by Schwenk for DP600 [1] from room temperature up to 800 °C and can be scaled to the yield strength of 750 MPa and an ultimate tensile strength of 1010 MPa to mimic the DP1000 steel. This approach is already demonstrated in [4] and shown graphically in Figure 5-3. To correctly account for compression occurring during spot welding, the data is extended manually by flow curves with progressively lower flow stresses until solidus temperature. In addition, phase dependent data for plastic flow is necessary for the austenitic phase in the high

temperature range as well as for the martensitic phase forming during cooling. Both data sets are not readily available for DP1000 steels in the literature. Therefore, data determined by Wink et al. [5] for austenitic and martensitic phases of a press-hardening 22MnB5 steel are taken. The electrical bulk resistivity is determined in relation to temperature in the same publication by Wink et al. [5].

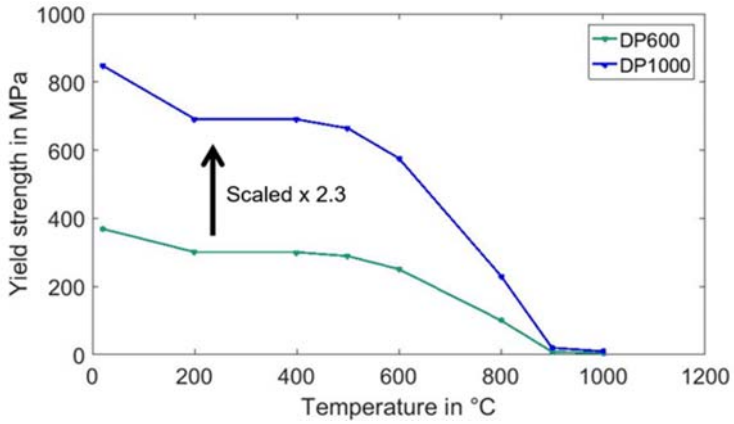


*Figure 5-3: Temperature dependent yield strength scaling from DP600 to DP1000*

The electrical contact resistivity is strongly dependent on steel grades, coatings and electrode forces [6]. Figure 5-4 shows the determined values for electrode/sheet and sheet/sheet resistances for clamping forces between 1 kN and 5 kN.

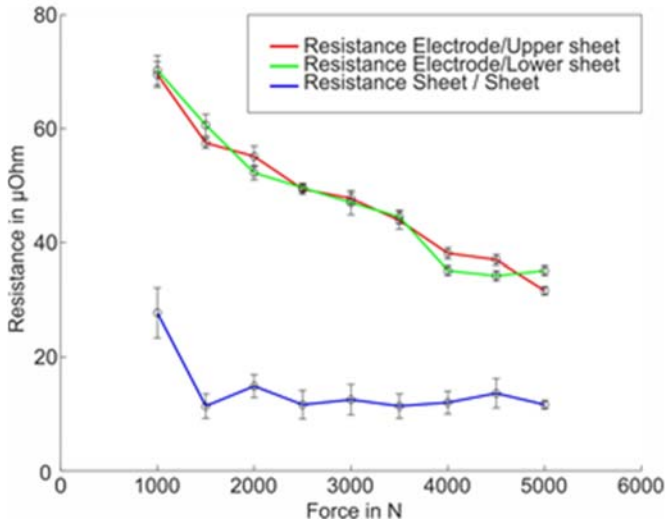


*Figure 5-4: Contact resistance measured according to DVS 18594*

While the contact resistances change strongly for low force levels, they remain almost constant at the high forces relevant for RSW and are in a similar range as the values

determined in [7], if the contact area of the electrodes is taken into account. In accordance with the publication by Rogeon et al. [8], the contact resistance is kept constant over the temperature.

## 5.3 Simulation model validation

With the simplifications regarding material parameters, a thorough calibration of the model has to be conducted. The calibration is done in three stages: First temperatures are measured during welding using thermocouples and compared to experiments for deviations in peaks and cooling behavior.

Validation experiments are conducted using a servo-mechanical C-type welding gun and a medium frequency inverter power source, used in constant current regulation. F1-16-20-5.5 flat type electrode caps according to ISO 5821 are used. A welding current range (WCR) is determined for the testing material. Two different welding currents, and two electrode forces are chosen for validation. The welding time is kept constant at 380 ms, hold and squeeze times at 200 ms each. To measure the thermal history, a line of three type K thermocouples is micro-welded to the top sheet (see Figure 5-5 left). The thermocouples are located at a distance of approximately 4 mm, 5 mm and 6 mm to the weld center. Based on an assumed electrode indentation diameter of 7.5 mm, these are the closest possible positions without coming into direct contact with the electrode. After welding, a macroscopic top view image of the sample is used to determine the exact distances of the thermocouples to the actual weld center. Metallographic cross sections are used for comparing the indentation depth and weld nugget size/shape. In Figure 5-5, the simulated and experimental temperature development is compared at the location of the three thermocouples.

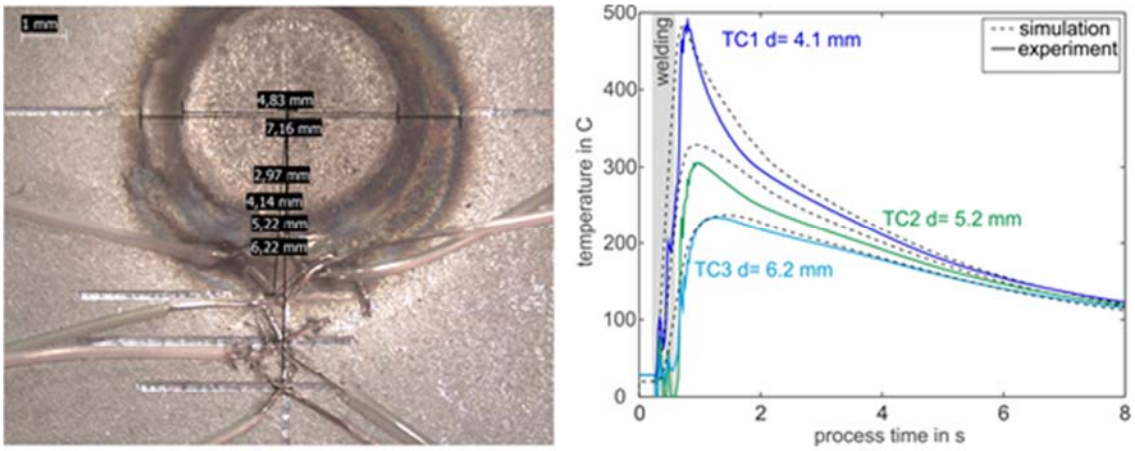


*Figure 5-5: Temperature history of welding process, comparison of experiment and simulation (d = distance to weld center)*

It is well-visible that the simulated temperature curves match the experiments in the peak temperature and, with small deviations, in the cooling speed. Subsequently, metallographic cross sections are prepared and the weld nugget size and shape are compared, shown in Figure 5-6 with very good agreement between the actual and modelled nugget shape and size.

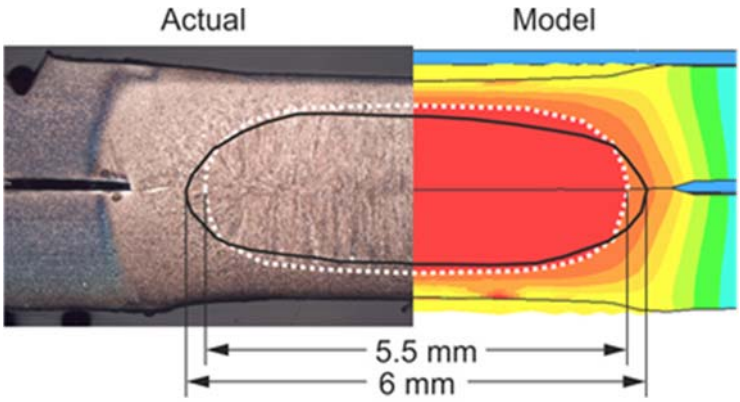


*Figure 5-6: Actual and simulated weld nugget size for validation*

## 5.4 Stop weld trials

As an additional validation step, so-called stop-welds were conducted. The RSW welding process was deliberately stopped early and cross sections were taken to observe the nugget growth. In Figure 5-7, the growth of the brighter austenitized zone

is visible in three cross-sections. It is clearly visible that the growth starts at the bottom sheet and only reaches the top sheet 20 ms later.

*Figure 5-7: Stop weld cross-sections after 25, 35 and 45 ms welding time*

This effect was studied with the simulation that usually shows fully symmetrical nugget growth. In the analysis, it could be shown that the weld gun stiffness and associated sheet bending cause asymmetrical contact conditions. In Figure 5-8, a sketch shows that bent sheets follow the electrode curvature at the top, leading to larger contact areas and at the same time cause a smaller contact area at the bottom electrode. As the amount of heat generated from electrical current is dependent on the cross-section area the current flows through, a higher amount of heat is generated at the bottom electrode with the small contact area.

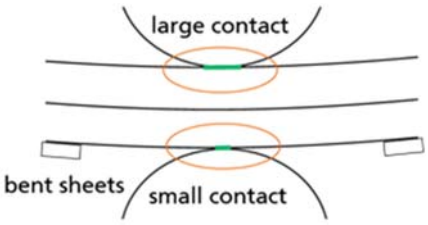


*Figure 5-8: Sheet bending due to weld gun stiffness causes asymmetry*

When accounting for the electrode stiffness in the simulation, the same asymmetry can be observed. In Figure 5-9, the simulation results are compared to the experimental stop-welds with the austenitized areas colored in yellow. The same general behavior could be reproduced in the simulation and the asymmetric nugget growth can be attributed to sheet bending from the weld gun stiffness.

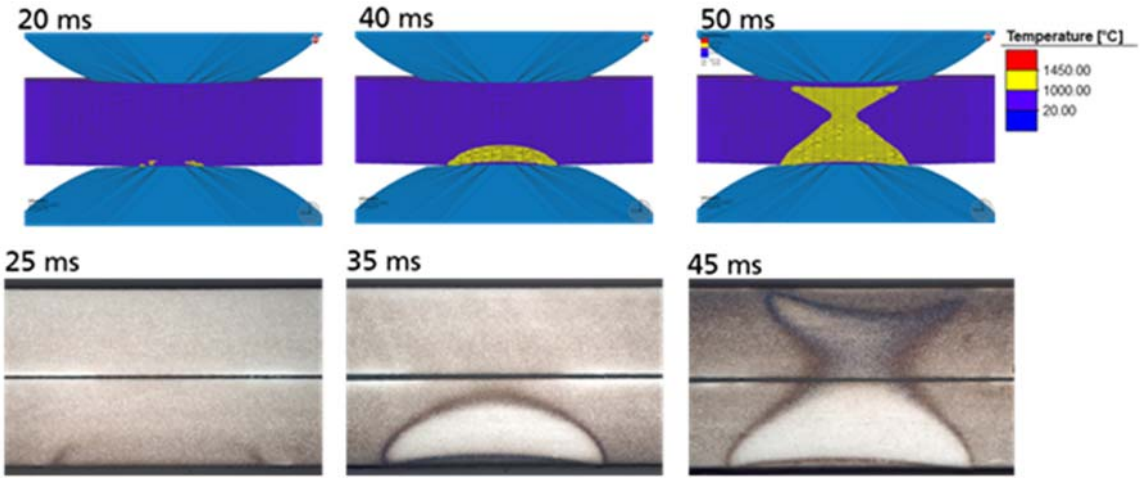


*Figure 5-9: Simulation of the asymmetric stop welds and comparison to the experimental cross-sections.*

With the successful comparison of process temperatures, post-process cross section size and shape as well as nugget formation in stop-welds, the model is considered to be validated. The thorough validation process ensures that all results generated during the process have significance and the values from the simulation can be trusted.

## 5.5 Model for investigation of external load

The model used during the simulation of the external load trials is shown in Figure 5-10. It consists of 14,556 linear hexahedral elements with a selective 2-fold refinement in the weld zone leading to an edge length of 0.3 mm and a refined element count of 23,684. A mesh convergence study for 3-fold refinement resulted in 3.1 % change in the peak process temperatures and was discarded due to long calculation times. For reduction of calculation time, only the middle part of the tensile sample is modelled. On a workstation equipped with two 8-core Intel Xeon E5-2667 CPUs, solving the model with 2-fold refinement took 1.8 h.

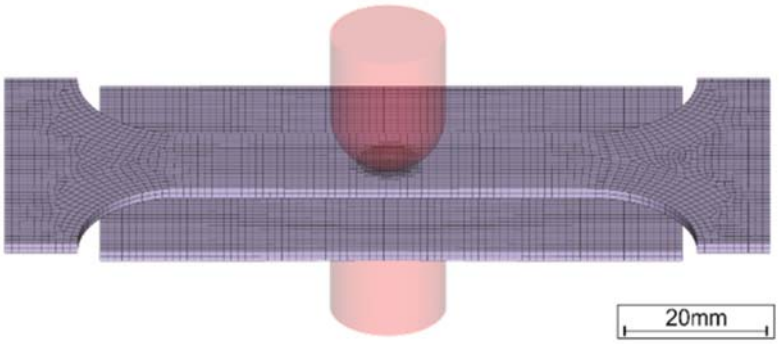


*Figure 5-10: Simulation model of welding under external load procedure.*

Initially, the mechanical model is solved to reproduce the closing of the electrodes and clamping forces. With the electrode/sheet and sheet/sheet contact areas established, the first electrical increment is calculated. The analysis comprising of electrical, thermal and mechanical steps in each increment is weakly coupled, i.e. the thermal increment has no feedback to the electrical increment and the mechanical increment has no feedback to the thermal increment within a single time step. A welding parameter set is chosen according to [9]: electrode force is 4.5 kN, weld time 380 ms. While the right side of the sample is fixed, a tensile force is applied to the left side, which results in the uni-axial stress field shown in Figure 6-15, corresponding to 60% of the material's yield strength. This value is determined experimentally to be required to reproducibly enforce LME. The simulative replication of the experimentally determined load case is an easy and effective way to determine and visualize local stress and strain values during the RSW process responsible for LME formation.

# 6 Results

## 6.1 Determination of weldability

In a first step a sufficient weldability needed to be verified for the initial MTCs. The spot-welding simulation SORPAS was used to support these investigations. All considered MTCs show a sufficient weldability under use of standard parameters according to SEP1220-2 by use of a F1-5.5 electrode cap. At the same time the weld nuggets as visible in the prepared cross-sections are well distributed over the sheet thickness even for thin materials in LME-susceptible MTCs. The observed electrode indentations were within an acceptable range. No signs of cracking were detected during determination of weldability for these MTCs. Figure 6-1 illustrates the results for the determination of the weldability for a combination of DP1200 and HSLA grade (3849).

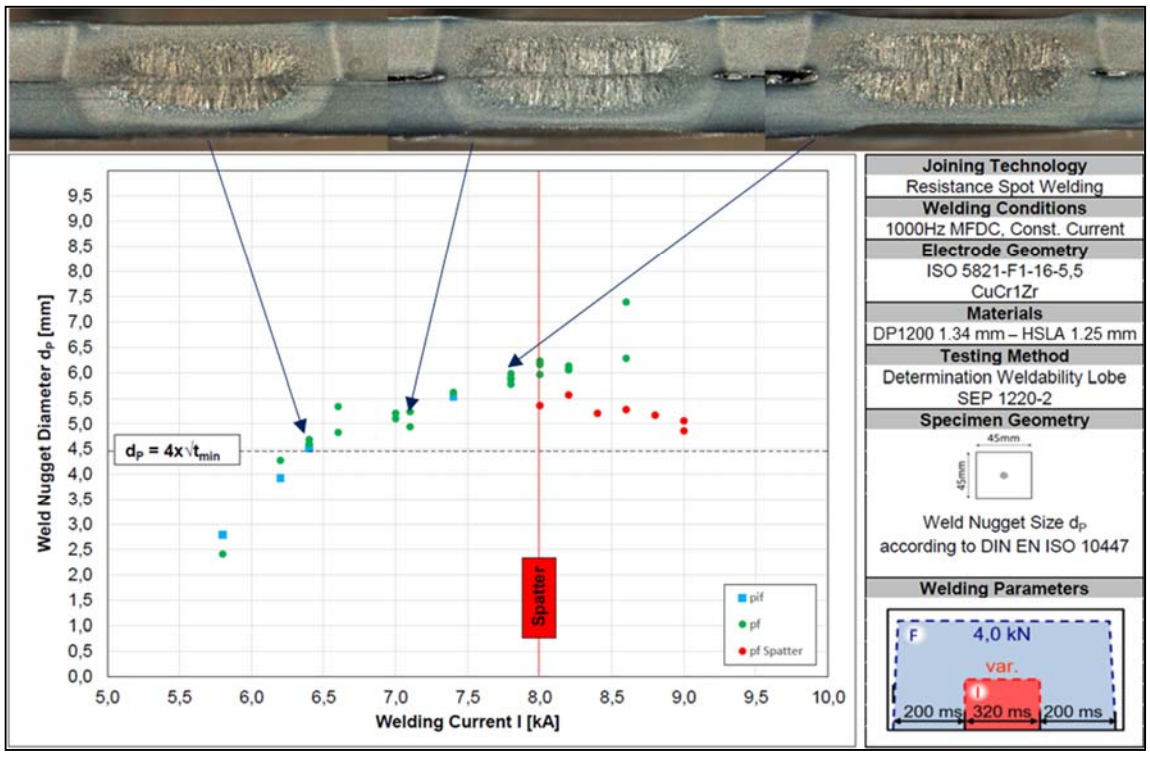


*Figure 6-1: Determined weldability lobe and correlating cross-sections for the MTC DP1200 (upper)-HSLA (1.25 mm).*

For an increase in the welding current an increase in the nugget diameter is observable in the provided cross-sections. In parallel, a light increase in electrode indentation depth and sheet separation at the sheet interface can be seen here. Providing a welding current range of 1.4 kA this MTC provides a good weldability with respect to the good nugget penetration into the HSLA steel beginning at a minimum welding current. To be able to identify suitable (i.e. LME susceptible) MTCs for the further testing process, additional MTCs were created and their weldability determined, based on literature research and in consultation with the project committee. In one of these MTCs (DP1200 - thick mild steel) light cracking was to be seen, when welding at the maximum spatter free weld current. The MTC was selected as an LME-susceptible combination and used throughout many of the research programs trials. The following Figure 6-2 shows its weldability lobe and correlating cross-sections.

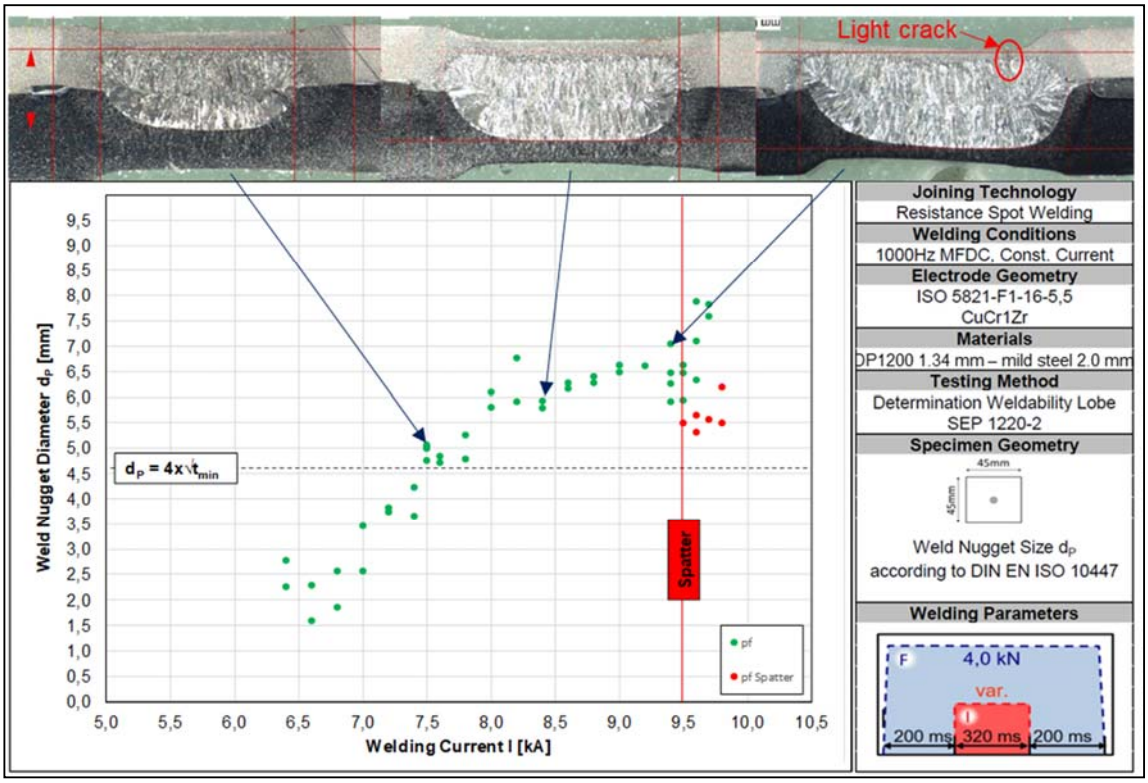


*Figure 6-2: Determined weldability lobe and correlating cross-sections for the MTC DP1200 (upper) thick mild steel (2.00 mm).*

The cross-sections reveal deeper and more asymmetric electrode indentations and a significant sheet separation at the interface for the maximum weld current, compared to other MTCs. This is assumed to be a result of the high heat input caused by the high

maximum weld current of this MTC. In comparison to additional MTCs formed with this AHSS grade provided by (Table 6-1) it can be seen, that this MTC even has the highest spatter free welding current of all investigated MTCs.

*Table 6-1: Overview of the weld current ranges for MTC based around DP1200.*

| Sheet 1 | | | Sheet 2 | | | Sheet 3 | | | Welding Current (kA | |
|---|---|---|---|---|---|---|---|---|---|---|
| Material (TS, UTS) MPa | Coating | t(mm) | Material (TS, UTS) MPa | Coating | t(mm) | Material (TS, UTS) MPa | Coating | t(mm) | Imin | Imax |
| DP1200 | EG (53/53) | 1.34 | HSLA 500 | EG (43/39) | 1.25 | | | | 6.4 | 7.8 |
| DP1200 | EG (53/53) | 1.34 | Mild Steel 300 | HDGI (53/50) | 2.00 | | | | 7.5 | 9.4 |
| DP1200 | EG (53/53) | 1.34 | Mild Steel 295 | Uncoated | 1.00 | | | | 6.2 | 8.4 |
| DP1200 | EG (53/53) | 1.34 | Mild Steel 295 | Uncoated | 1.00 | Mild Steel 295 | Uncoated | 1.00 | 5.8 | 8.8 |

The listed MTC were further investigated during the LME enforcement experiments (see 0). As a preparation for the application of the reference test methods the determined values for the maximum spatter free welding current were adjusted and reconfirmed several times during the further testing process. For the experiments under application of an elongated weld time, a spatter free welding process was assured by performing additional welds around the maximum weld current at elongated weld times prior to the main trials. Here a light lowering of the weld current around 200 A was found to be a suitable measure. To enable a spatter free welding under external loads, the welding current was even further reduced. This was due to the changed specimen geometry, which only has a width of 15 mm at the joining zone.

Summary:

Determination of weldability was performed successfully for all investigated MTCs. All MTCs provide sufficient welding current ranges. A special focus was set on the adaptation of the maximum weld current in order to allow for widely spatter free welding during the following investigations. Using extended weld times (4x), the MTC combining DP1200 with a 2.00 mm mild steel would develop cracks and was therefore identified as an LME-sensitive combination. This MTC was used throughout many of the research program trials.

## 6.2 Enforcement of LME

The following chapter focusses on the results obtained during the investigation of the MTCs listed in Figure 6-3. All listed MTCs were tested across all influence factors – excluding the welding under external loads (see 6.2.9), which has only been investigated during reference testing in (6.4). All welding was performed at a weld current close to the highest possible spatter free weld current ($I_{max}$) (see 6.2.1). During preliminary investigations performed on less susceptible MTCs and with currents below $I_{max}$, no cracks were observed for any of the investigated factors. One of the following chapters is dedicated to each of the influences studied.

### 6.2.1 Reference weld setup

All of the following results can be referenced to crack free spot welds achieved by applying a welding schedule according to SEP1220-2. The following Figure 6-3 gives an impression of the condition of these welds. Listed aside is the reference welding schedule for the investigated MTCs. The used weld current is reduced by 400 A compared to the values for $I_{max}$ listed in Table 6-1. All deviations from the listed welding schedule are described in the respective chapter.

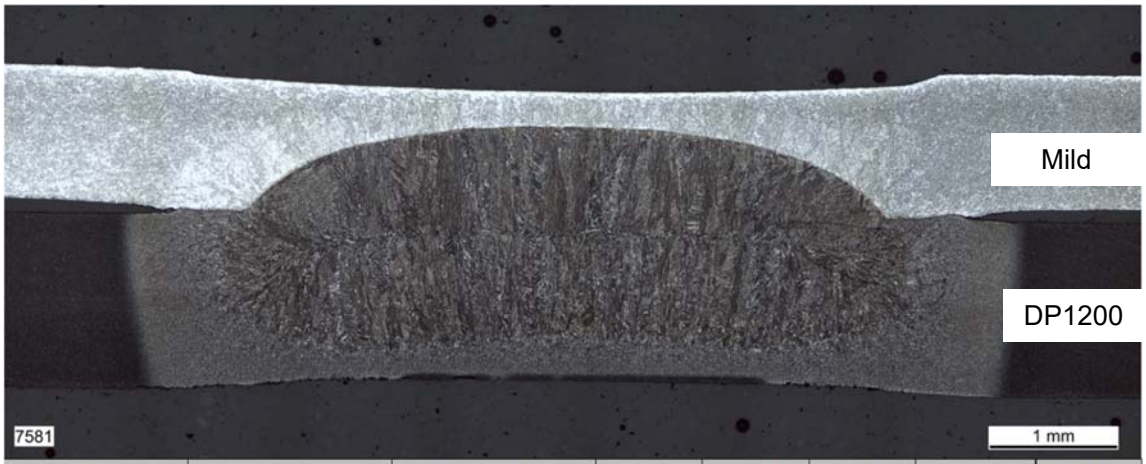


| Material top layer | Material middle layer | Material bottom layer | Squeeze time (ms) | weld time (ms) | Hold time (ms) | weld current (A) | electrode force (N) |
|---|---|---|---|---|---|---|---|
| DP1200 1.34 mm | mild steel 2.00 mm | | 200 | 320 | 200 | 9000 | 4000 |
| DP1200 1.34 mm | mild steel 1.00 mm | | 200 | 240 | 200 | 8000 | 3500 |
| DP1200 1.34 mm | mild steel 1.00 mm | mild steel 1.00 mm | 200 | 260 | 200 | 8400 | 3500 |

*Figure 6-3: Basic parameters used during Investigations on enforcement of LME and exemplary cross-section of resulting crack free reference spot weld for MTC DP1200 (1.34 mm) (lower) – Mild steel (1.00 mm).*

### 6.2.2 Worn electrodes

Electrode caps were conditioned with 100 welds of extremely elongated weld times higher than 1200 ms at $I_{max}$ to achieve a defined worn out condition of the electrode tip. During the evaluation of the tests only light cracking was observed. Figure 6-4 is giving an overview of this influence by providing a photo of the electrode caps after the conditioning, along with a surface view and cross section through one of the most LME afflicted spot welds created during the investigations on this influence factor.

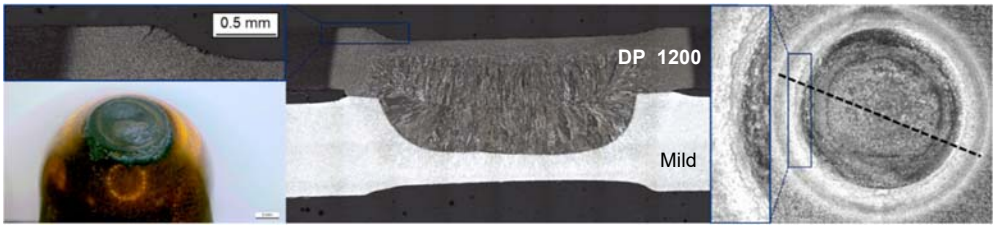


*Figure 6-4: Exemplary result of the trials performed with worn out electrodes. Conditioned electrode cap (left) and crack afflicted spot weld in top view and cross-section.*

### 6.2.3 Reduced cooling rate

To be able to estimate the effect of a poor electrode cooling, the reference setup was used, and the cooling of the electrode caps was completely disabled. Figure 6-5 shows the experimental setup and exemplary results from one of the most susceptible MTCs.

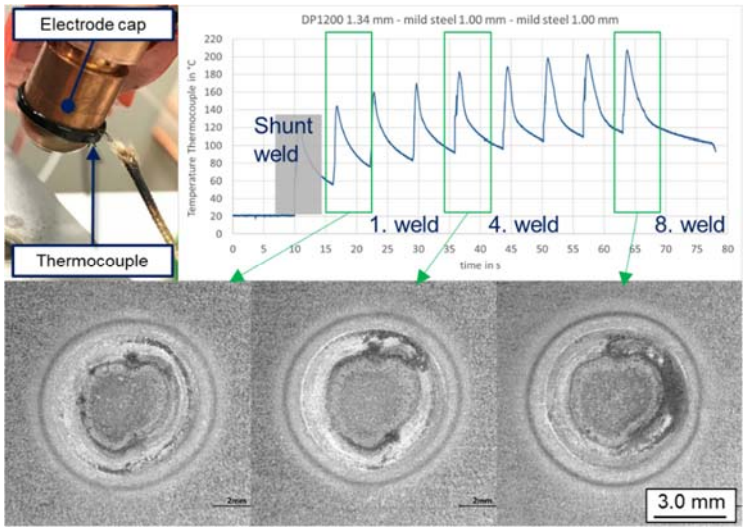


*Figure 6-5: Experimental setup and exemplary results of the trials performed with switched-off electrode cooling. Electrode cap with thermocouple (top left) and resulting spot welds in top view (below).*

Beginning with the shunt weld, spots were welded every six seconds and the temperature of the electrode cap near the tip was measured. The exact position of the thermocouple at the side of the electrode cap is shown on top left. The temperature curve shows a fast and intense increase and decrease in electrode cap temperature for each weld cycle. After each weld cycle a slightly higher residual temperature of the electrode can be observed. Resulting in a delta of peak temperature of 80 °C between the shunt weld and the last weld. A smaller delta of 60°C was observed six seconds after the shunt weld and the last weld. During the experiments no significant cracking was observed for none of the spot welds regardless of their position in weld cycles, i.e. electrode heat level.

### 6.2.4 Variation of electrode tip geometry

In these experiments the electrode geometry was varied in an extreme manner. Three different electrode tip geometries were created, by milling sharp edges to the electrode tip of a F1-5.5 electrode geometry, as shown in Figure 6-6 top.

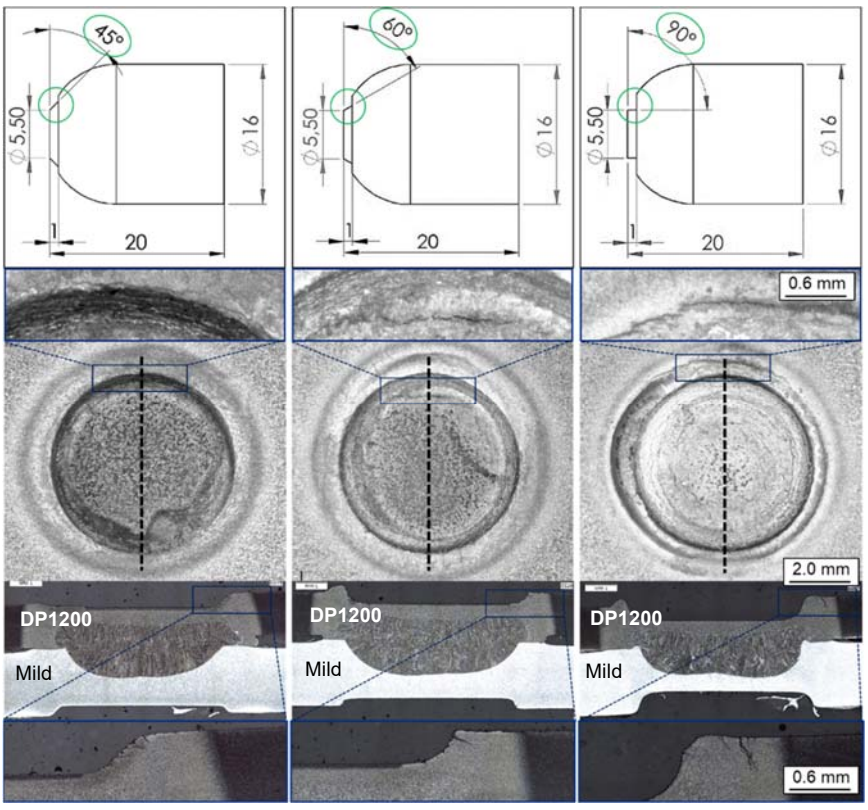


*Figure 6-6: Experimental setup and exemplary results of the trials performed with modified electrode tip geometry.*

The current was initially adjusted to 9.0 kA but kept constant for each of the tip geometries. As a consequence, the formation of spatter could not be avoided for the 90° geometry. For the 45° electrode geometry only very light cracking along the electrode indentation edge was observed. In the welds created with the 60° angle the observed intensity of the cracks remained very light but additional light cracks were now frequently found within the electrode indentation, the position of these cracks typically oriented around the sharp edge created by the milling process. When welding with the 90° geometry typically more intense cracks inside the HAZ with a wider opening to the sheet surface and a higher penetration depth were observed. For this electrode geometry also the most frequent cracking within the electrode indentation was observed. In summary, it can be said that for this influence the most frequent cracking was observed but simultaneously all of the observed cracks had a limited crack depth, not exceeding 30% of the sheet thickness.

### 6.2.5 Lateral offset of electrodes

The welding gun was reconfigured to implement a misalignment of 2 mm between the two welding electrodes. Figure 6-7 provides the experimental setup and an exemplary cross-section of a resulting spot weld.

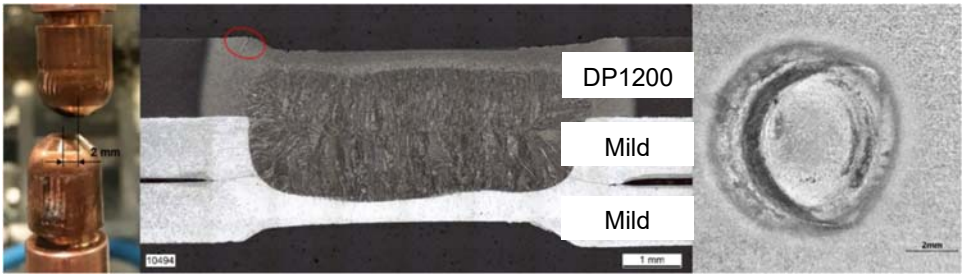


*Figure 6-7: Experimental setup and exemplary result of the trials performed with lateral electrode offset.*

The misaligned electrodes cause a clearly asymmetrical electrode indentation with one side of the indentation experiencing a light deformation and the opposite side with an intense deformation. On this intensely deformed side of the indentation frequent cracking was observed inside the HAZ. Crack depth typically was below 30% of the sheet thickness. Also, rather big scatter of results was observed, reaching from unremarkable spot welds with little to no sign of cracks, to spots experiencing intense spatter on the sheet surface and a high surface crack intensity.

### 6.2.6 Angular offset of electrodes

The welding gun was reconfigured to implement a misalignment of 3° between the two welding electrodes. Figure 6-8 provides the experimental setup and an exemplary cross-section of a resulting spot weld.

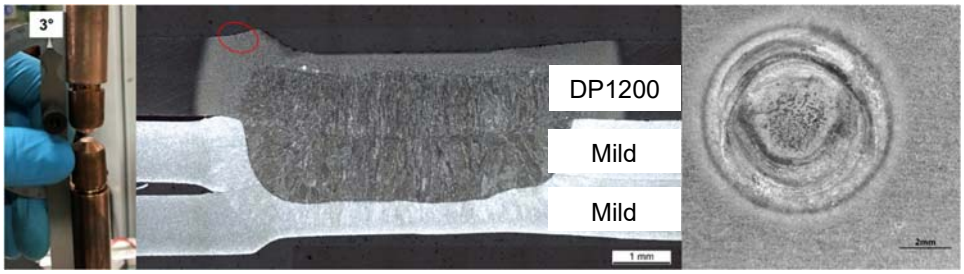


*Figure 6-8: Experimental setup and exemplary result of the trials performed with angular electrode offset.*

The angular misalignment of the electrodes caused asymmetrical electrode indentations on one side of the spot. No significant impact on crack formation was observed.

### 6.2.7 Gaps between welded parts

The experimental setup is shown in Figure 6-9. The gaps were created via an insulated gap template with a width of 20 mm and a height of 0.5 mm.

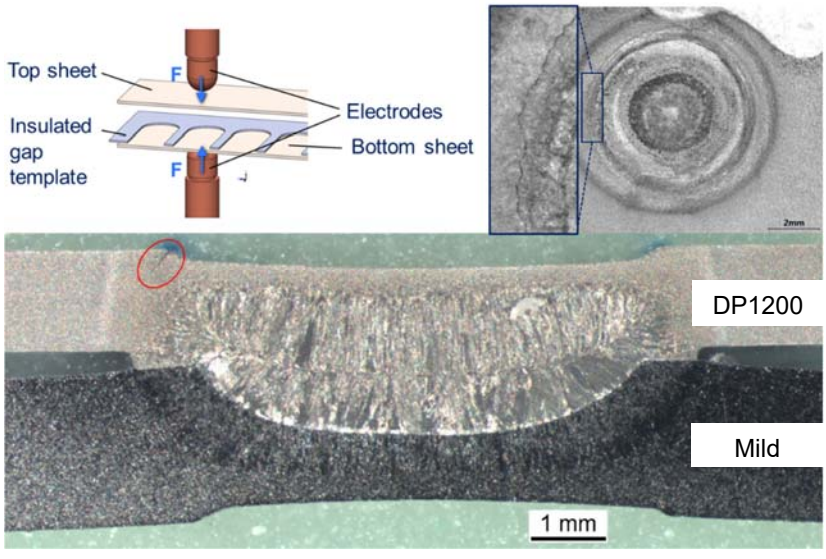


*Figure 6-9: Experimental setup and exemplary result of the trials performed with angular electrode offset.*

During these experiments significant cracking was observed from the sheet surface but in cross-sections no cracking with a high penetration depth was observed.

### 6.2.8 Increased electrode force

The electrode force applied throughout the welding process was increased to 125% and 150% of the reference value. Weld current remained the same for all force levels. Typical results are shown in Figure 6-10.

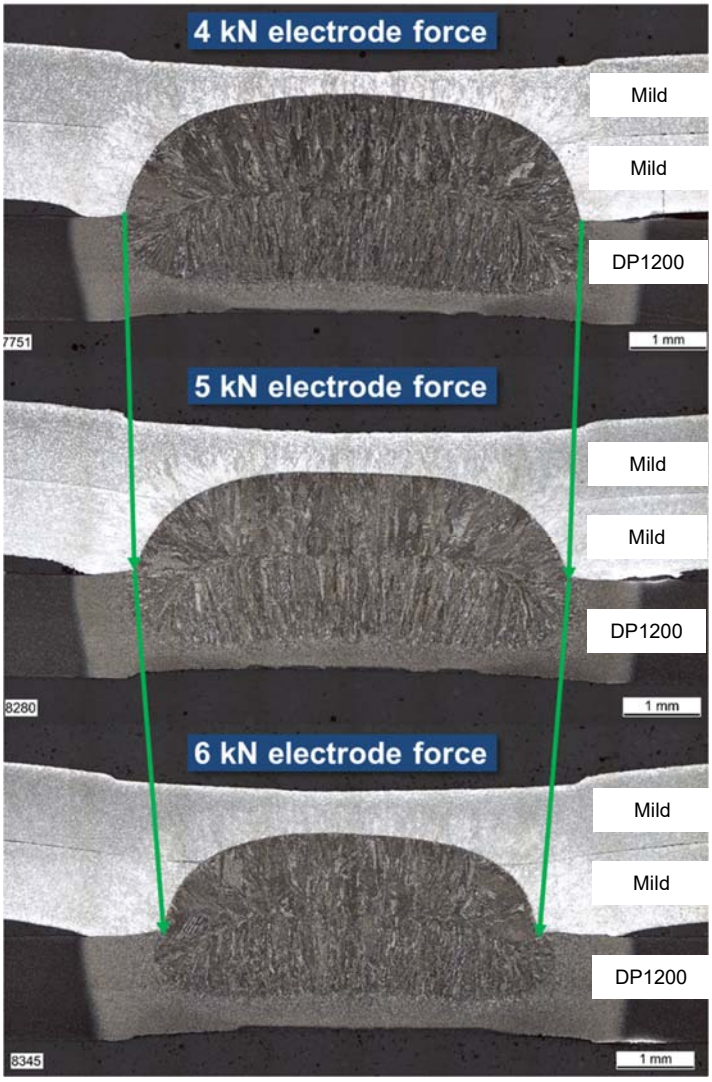


*Figure 6-10: Experimental setup and exemplary result of the trials performed with increased electrode force.*

For an increase in force a reduction of the weld nugget diameter was observed. This can be regarded as a consequence of the reduced contact resistances due to the

increase in force. Also, a reduction of the nugget height is visible within the cross-sections, which is a result of intensified cooling by the better contact situation of electrodes and sheets. No cracking was observed as a consequence of increased electrode force.

### 6.2.9 Welding under external loads

The welding under external load procedure enforces LME cracking of zinc coated AHSS materials by applying a tensile stress field to a sample during spot welding [10], thereby creating extreme welding conditions. The stress field is induced hydraulically by a simple experimental setup as shown left in Figure 6-11 and can be adjusted to different load levels according to the materials' mechanical properties. The initially applied stress is not adjusted during welding, but a preloading only. As a result value, the total crack length on the sample surface is measured optically (by aid of image editing software) after chemical removal of the zinc layer. The level of tensile stress necessary to reproducibly provoke LME cracking can be determined by incremental increase of the applied stress for a testing material, e.g. in 10 % steps of the material's Rp0.2 (yield strength).

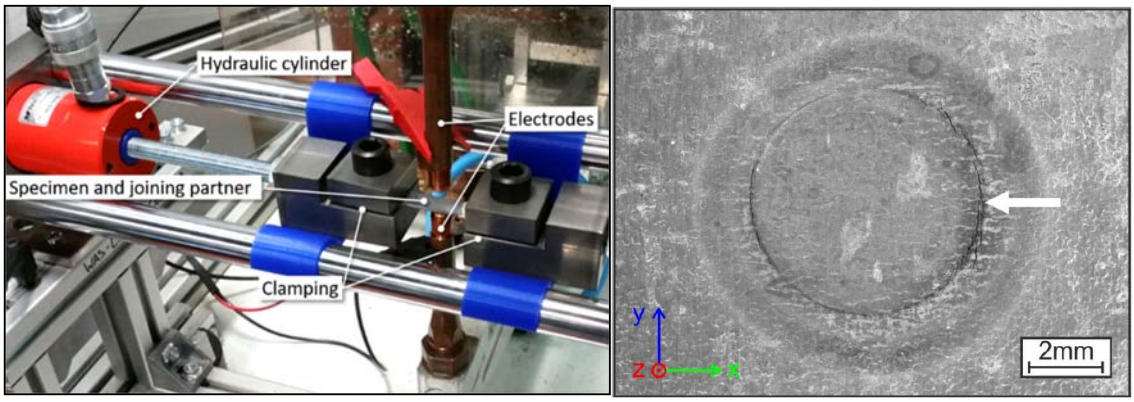


*Figure 6-11: Experimental setup of welding under external load and typical LME cracking site.*

The external tensile stress level necessary to reproducibly enforce LME cracking of the testing material was determined experimentally to be 60 % of the material's Rp0.2 (yield strength). The right side of Figure 6-11 shows the typical LME initiation site of a welding under external load sample in top view. Without externally applied tensile

stresses, i.e. under standard welding conditions, the material does not exhibit LME. With lower external stress levels, only occasional LME is observed.

Simulation of welding under external loads

The calibrated and validated simulation model is being used to reproduce the experimental welding under external load trials. Thereby, the temperature, stress and strain fields are made accessible. The evaluation of these results helps define the boundary conditions which lead to LME cracks. After calibration to a dual phase steel of the 1000 MPa tensile strength class, it is used to analyze the thermo-mechanical system of an experimental procedure to enforce liquid metal embrittlement during resistance spot welding. In this procedure, a tensile stress level is applied to zinc coated Advanced High-Strength Steel samples during welding. Thereby, liquid metal embrittlement formation is enforced, depending on the applied stress level and the selected material. The model is suitable to determine and visualize the corresponding underlying stresses and strains responsible for the occurrence of liquid metal embrittlement. Simulated local stresses and strains show good conformity with experimentally observed surface crack locations.

The simulation provides in-situ temperature, stress and strain values during welding. These are, amongst other internal/external factors like coating thickness / type [11], grain boundary diffusivity / solubility, or grain boundary energy – interfacial energy relation, responsible for LME cracking formation. The same welding parameters were used for all simulation investigations:

*Table 6-2: Weld parameters for the welding under external load simulation*

| | |
|---|---|
| **Tensile load specimen** | DP1000 x 1.5 mm |
| **Bottom sheet** | DP1000 x 1.5 mm |
| **Weld current** | 9.4 kA |
| **Weld time** | 380 ms |
| **Electrode force** | 4.5 kN |
| **Squeeze/Hold times** | 200 ms |

The following result figures focus on the weld zone. They either show it in top view or in cross section view, corresponding to Figure 6-12.

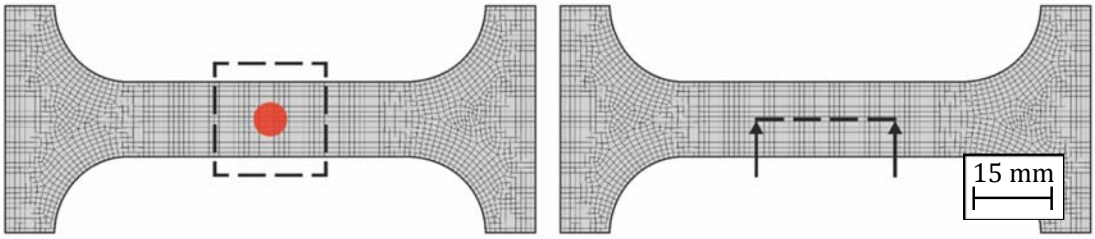


*Figure 6-12: Schematic views of results graphs in top view (left) and cross-sectional (right)*

Temperature field

The temperature field simulation visualizes the weld nugget growth as expected. The typical nugget shape and size are met as can be seen in Figure 6-14. It is not homogeneous but exhibits gradients and changes in each time increment. In top view, a local ring-shaped temperature maximum at the momentary edge of the electrode contact area is observed. This is caused by the reduced contact pressure and subsequently higher contact resistance during the process of electrode indentation here. Temperatures of approximately 900°C are reached. Meanwhile, heat is dissipated through the water-cooled electrode. The cross-sectional view visualizes the effect, which prevents heat accumulation and liquefaction of the sample surface underneath the electrode. Towards the adjacent surface area, a temperature gradient is observed, with a local maximum of the surface temperature.

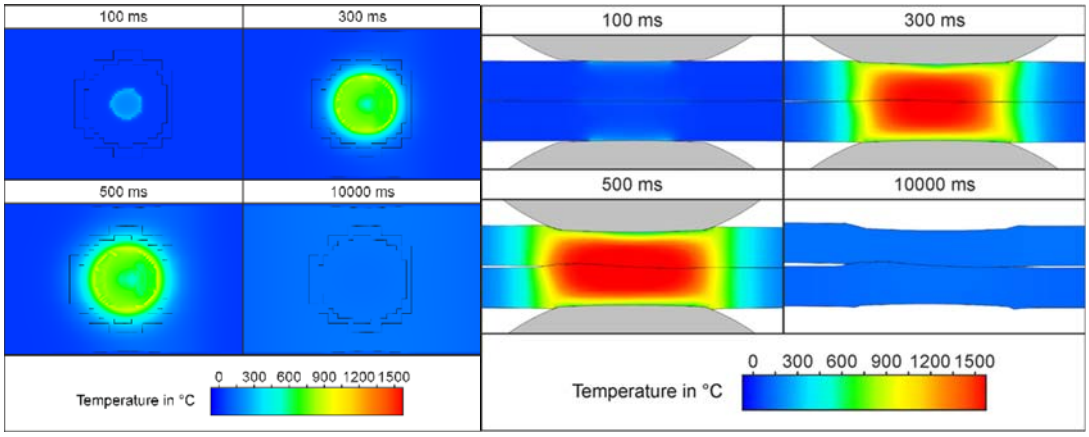


*Figure 6-13: Temperature field during welding under external load in top view (left) and cross sectional view (right)*

At the LME sensitive location at the edge of the electrode indentation, the temperature over time curve is extracted, see Figure 6-14. The horizontal dashed line represents the melting point of zinc, which determines the potential time window, in which LME theoretically can occur. This evaluation of the thermal history may be specified based on the results of Béal [12]. The simulated transient temperature field is considered during the following evaluations of stress/strain fields.

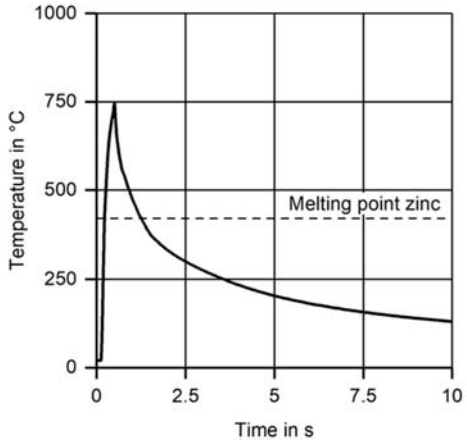


*Figure 6-14: Time range relevant for LME occurrence*

Stress field

Figure 6-15 shows the initial state of the simulated welding under external load trial before the start of the welding process. The sample is pre-stressed to approximately 60 % of its Rp0.2 (yield strength). On the right side, the sample is fixed, while on the left side a boundary condition is used to create the force necessary to reproduce the laboratory test conditions.

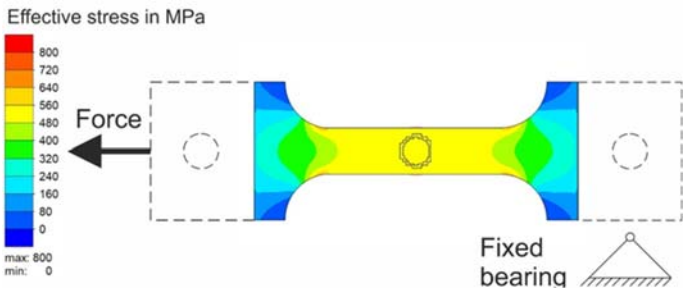


*Figure 6-15: Simulation model of sample, uniaxial pre-stress*

Figure 6-16 shows the effective stress distribution at various time steps of the welding process in top view. Areas adjacent to the electrode indentation have been identified experimentally to be the main sites of LME formation, and are therefore in focus for evaluation of the simulation [13]. Thermally induced tensile stresses mainly form during cooling due to shrinking of material. After cooling down close to room temperature, local stress maxima up to approximately 800 MPa are observed. During heating, in the highly heated/molten area, little to no stresses can be transferred, which leads to a redistribution of the initial tensile stress field towards the outer areas of the sample (top left). Excessive tensile stresses are transformed into plastic strain. Subsequently, necking of the sample is visible at the sample's outer edges. The significant stress pattern shown in the last frame (bottom right) forms during the cooling process, after 10 seconds. Values of approximately 800 MPa are reached in areas which have cooled down near room temperature.

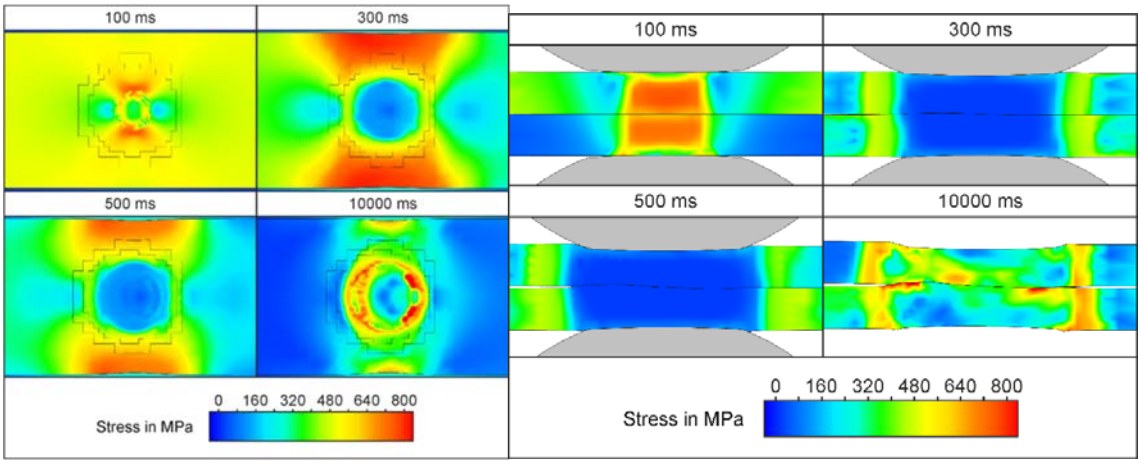


*Figure 6-16: Effective stress field during welding under external load in top view (left) and cross sectional view (right)*

The cross-sectional view shows the corresponding effective stress fields. The loss of the capability to transfer stresses of the material at high temperatures is clearly visible. Furthermore, the stress maxima after cooling are not only present on the surface but reach down circumferentially around the weld nugget (bottom right), covering the heat affected zone of the weld. Evaluation of the resulting stress field shows that the absolute maximum values on the surface form after significant cooling time. Essential for LME formation however is the presence of zinc in liquid state – which occurs roughly between 420°C and 900°C [14]. As shown in Figure 6-14 this leads to a critical time

range in the simulation between 250 ms and 1300 ms in which the zinc is liquefied on the sample surface. The maximum stress values on the surface of about 800 MPa can therefore be disregarded, as they form after this period.

Strain field

Figure 6-20 shows the effective plastic strain which forms during the heating phase of the welding process in top view.

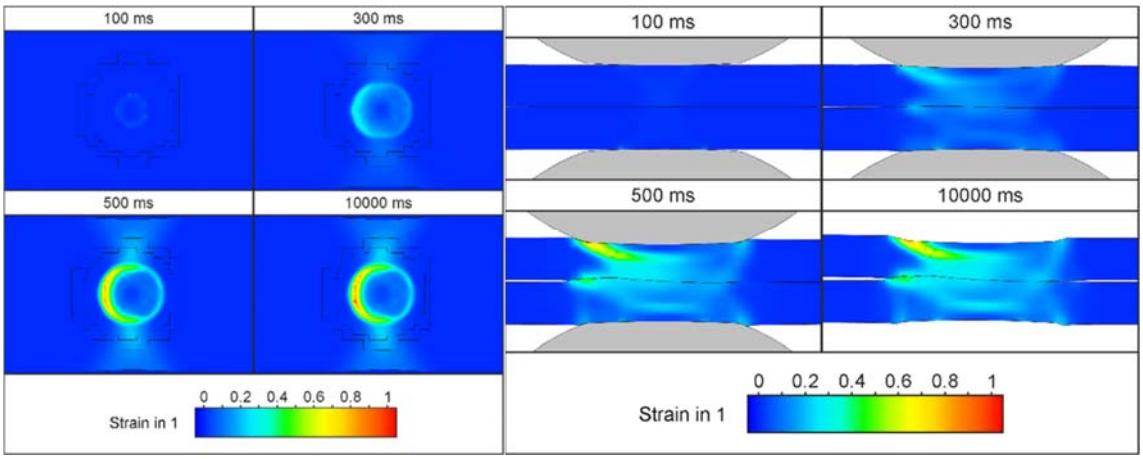


*Figure 6-17: Effective plastic strain field during welding under external load in top view (left) and cross sectional view (right)*

It is calculated by integrating incrementally the plastic strain over time. Although the externally applied force lies in the elastic region initially, the material's mechanical properties deteriorate with increasing temperature. This leads to plastic deformation and displacement towards the side of the movable clamping. The electrode holds the material underneath it back, while the external load pulls on the adjacent, weakened material. Therefore, the main plastic strain is observed left of the electrode. Surface strains mainly form on the side of applied load, and reach down towards the center of the weld nugget as can be seen in the cross-section view in Figure 6-20. Locally, values of 1 are reached, which are considered to be critical for LME. Correlation between the plastic strain maximum and experimentally observed LME locations is found. Figure 6-18 shows the simulated areas of high plastic strain, and an image extracted from computed tomography of an LME afflicted sample.

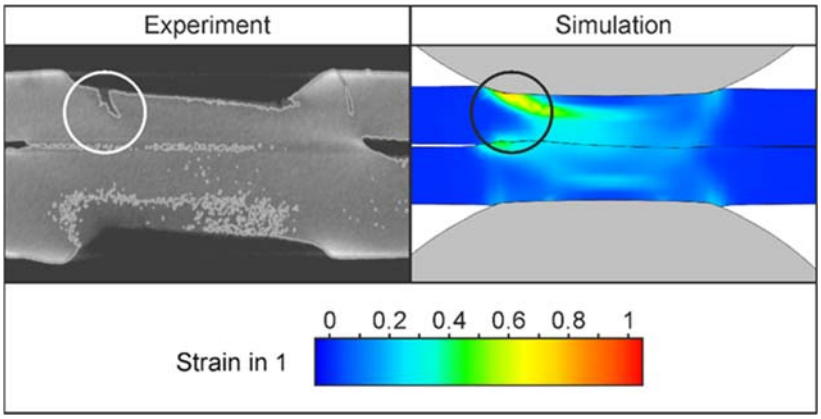


*Figure 6-18: Correlation of simulated effective plastic strain maximum with experimental LME cracking sites*

The main plastic strains occur within the critical time range, and in an area where LME formation is frequently observed experimentally. It can therefore be assumed, that plastic strain in combination with the presence of liquid zinc increases the LME susceptibility.

### 6.2.10 Definition of an LME criterion for the simulation model

The software Simufact welding allows the definition of user-defined specified result values. Thereby, the calculated results known to influence the LME sensitivity may be combined by mathematical operators. Thereby, an LME criterion can be formed, which helps identifying and visualizing LME sensitive regions. Figure 6-19 schematically shows the values chosen for an exemplary LME criterion.

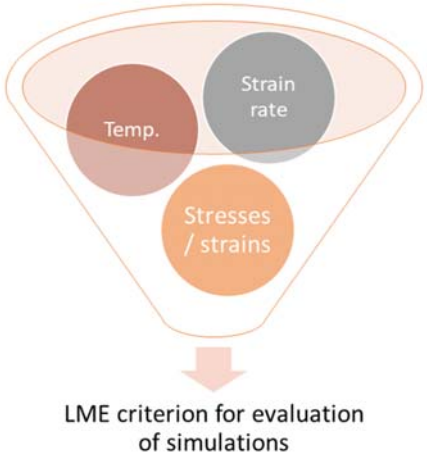


*Figure 6-19: Input values of LME criterion.*

This approach was tested with the following formula, consisting of the arithmetic mean of a strain, strain rate and stress parameter:

$$LME\ criterion\ (\varepsilon, u, \sigma) = \sqrt[3]{P_{strain}(\varepsilon) \times P_{strainrate}(\varepsilon) \times (\sigma / R_{p0.2})} \qquad 6\text{-}1$$

*ε:* *effective plastic strain*
*ε̇:* *strain rate*
*σ:* *effective stress*

The critical values for effective plastic strain, strain rate and effective stress were determined by simulation of two load cases of the welding under external load procedure, a subcritical one [sample stressed to 45% of the material's Rp0.2 (yield strength)] and a critical one [sample stressed to 60% of the material's Rp0.2 (yield strength)]. Figure 6-20 shows the corresponding comparison of the maximum local effective plastic strain between the two load cases. A value of approximately 0.7 was identified to be critical for LME accordingly. Subsequently, a logistic function is used to normalize these values to a factor between 0 and 1.

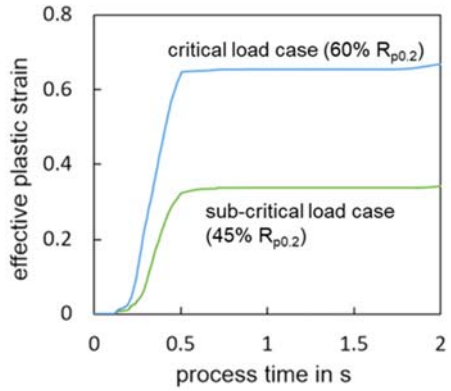


*Figure 6-20: Local plastic strain maxima of critical and subcritical load case*

The same procedure is applied for the effective stresses and the strain rate. The temperature range is set by means of if conditions. Thereby, only temperatures between the melting and evaporation point of Zinc are considered. Figure 6-21 shows the applied LME criterion result view of the 60% load case in top view. The indicated area coincides with the experimentally observed LME crack initiation sites as shown before. Still, the mere effective plastic strain shows a comparably good correlation with experimentally observed LME crack sites (see Figure 6-11), and is therefore recommended to efficiently check simulations for LME sensitive regions.

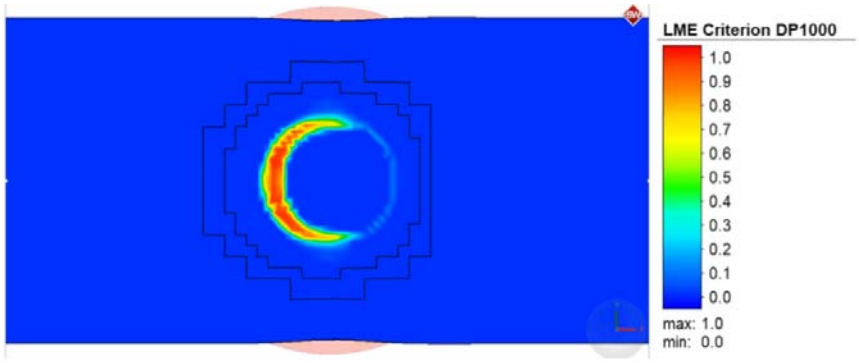


*Figure 6-21: User-defined results value: LME criterion*

As the simulation cannot provide all factors which play a role in LME formation, the criterion remains incomplete, despite the effort for calibration. Therefore, it is recommended for matters of efficiency to evaluate the mere plastic strain field, directly provided by the simulation software.

### 6.2.11 Extended weld times

Another LME enforcement setup frequently used in the project is the extended weld time. By extending the weld time, LME cracks can be forced with a very high repeatability in the experiment. The intensity of the enforced cracks varies based on the investigated MTC and used weld time elongation factor. Figure 6-22 provides an overview of representative results.

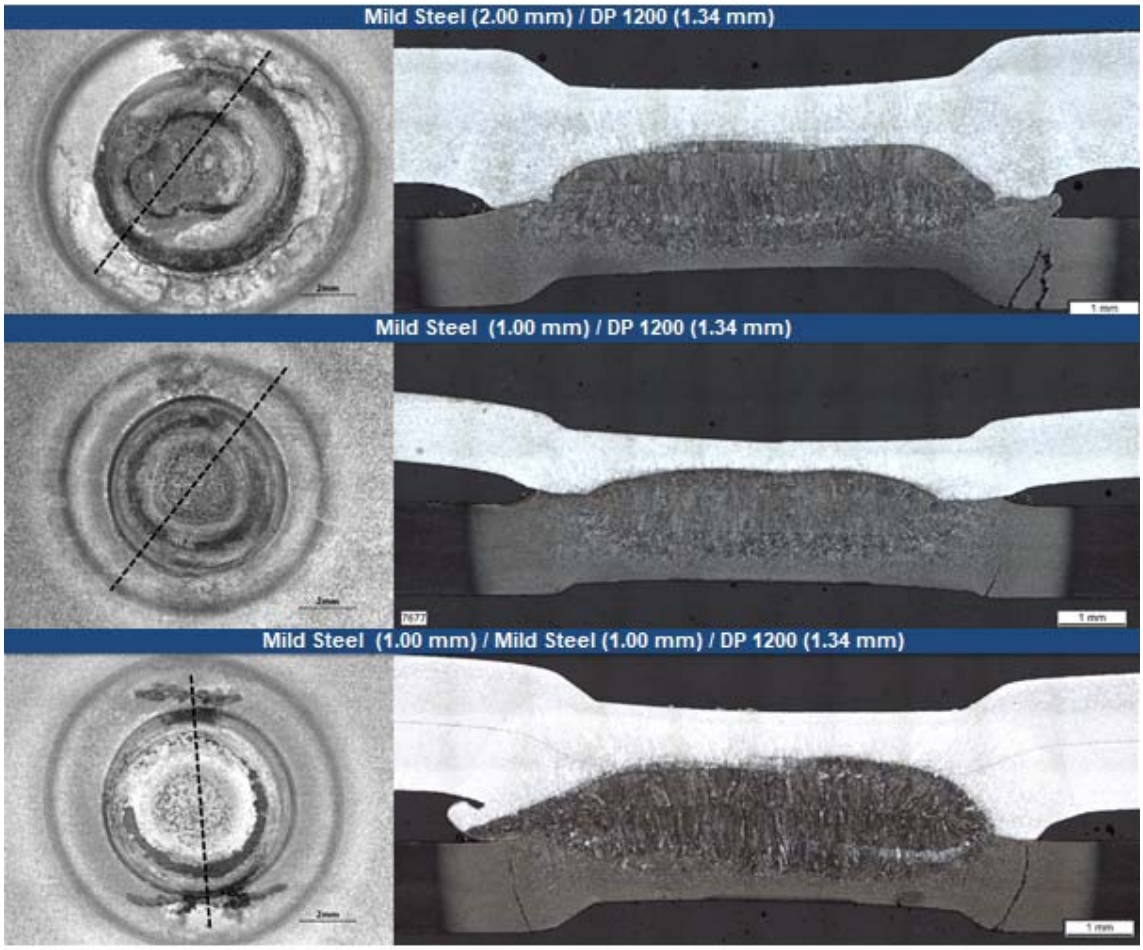


*Figure 6-22: Exemplary result of the trials performed with 4x elongated weld times.*

For extremely elongated weld times crack penetration depth of the entire sheet thickness were observed. Also, cracks enforced with this technique have the highest circumferential extent. The weld parameters used are as follows:

*Table 6-3: Weld parameters for the 4x elongated weld times case*

| | |
|---|---|
| **Tensile load specimen** | DP1000 x 1.5 mm |
| **Bottom sheet** | DP1000 x 1.5 mm |
| **Weld current** | 9.4 kA |
| **Weld time** | 1520 ms |
| **Electrode force** | 4.5 kN |
| **Squeeze/Hold times** | 200 ms |

The simulated strains for a 4-fold increase of the weld time is shown in Figure 6-23 on the right. It is clearly visible that the plastic strains do not reach the same high values observed in the welding under external load enforcement setup. As cracks form experimentally, it is suspected that a second effect of LME generation is in effect here: Due to the longer weld-times the duration of liquid zinc on the surface is increased by a factor of 2.5 from 1.6 s to 3.9 s. Hence, a far greater time window for the stress-assisted zinc diffusion is available, facilitating LME cracking.

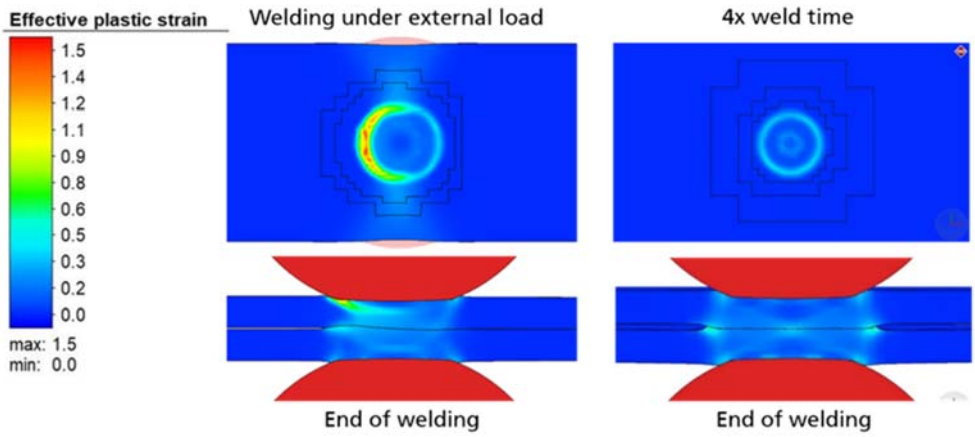


*Figure 6-23: In the prolonged weld time trial (right) the local strains do not exceed threshold values from the welding under external load setup but the time for stress-assisted zinc diffusion is increased greatly.*

## 6.3 Influence of Material-thickness-combinations (MTCs)

In an additional work-package, the applicability of the LME-detection methods to different steel grades was investigated. During the project, it was decided that this investigation should be aimed at joining an AHSS to a thin or thick mild steel (see Table 6-1), because experimental cracks could be observed when the AHSS was joined to the thick mild steel and none occurred when joining it with the thin mild steel. Figure 6-25 shows the cross sections for both investigated cases with the following parameters:

- Welding parameters 1.5 mm DP1000 to 1 mm HSLA: 7.6 kA, 3.5 kN, 240 ms
- Welding parameters 1.5 mm DP1000 to 2 mm HSLA: 9.1 kA, 4 kN, 320 ms

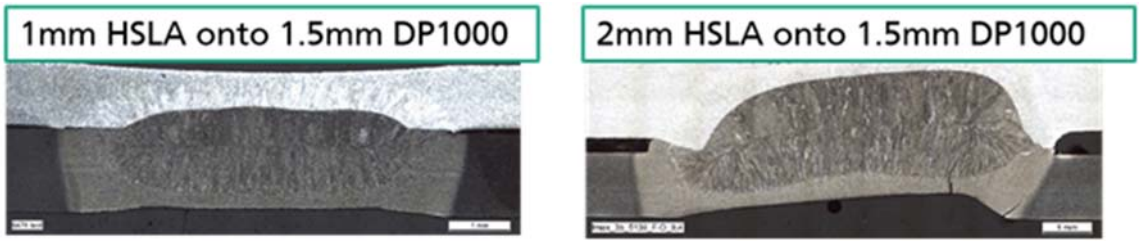


*Figure 6-24: Cross section of the spot weld for DP1000 to a 1 mm and 2 mm HSLA with LME cracks for the 2 mm HSLA case.*

It can be clearly observed that the nugget penetrates less into the mild steel (on the top in both cross sections). Because of the increased thermal conductivity of the HSLA grades, the heat is dissipated more quickly and a smaller, rounder nugget forms. Due to the different steel grade used in the experiment, another validation loop was conducted to ensure the applicability of the models. The results are shown in Figure 6-26: On the left, simulated and measured temperatures are compared for the 2 mm mild steel case with good agreement. The right side shows measured and simulated cross sections. Both the size and shape of the nugget could be reproduced.

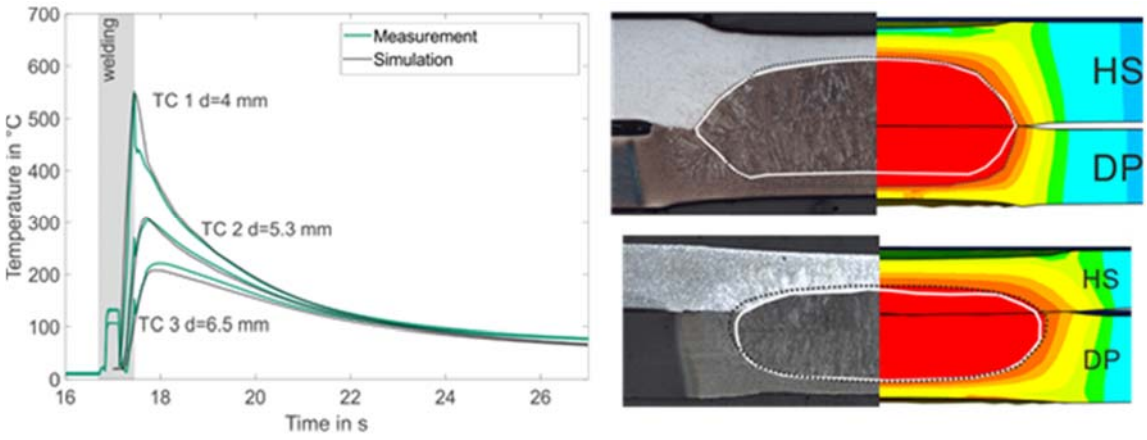


*Figure 6-25: Validation for the AHSS to mild steel simulation study. With temperature cycles on the left and comparisons of the virtual and actual cross sections on the right.*

To evaluate the reason for the greater LME susceptibility of the thick-sheet weld, the in-situ temperatures were extracted at an ‘inner’ point, 0.5 mm from the inner edge of the indentation and at an ‘outer’ point 0.5 mm outside of the indentation. The results are compared in Figure 6-26 for the thin and thick sheet at the same locations. It is clearly visible that the temperatures in the thick sheet case are far higher and exceed the melting point of zinc for a significantly longer time. For the ‘inner’ location, the thin sheet case exceeds the melting point of zinc for 0.31 s and the thick sheet for 1.46 s, marking an increase by a factor of 4.7. For the ‘outer’ location, the increase is by a factor of 4.2 from 0.29 s to 1.23 s.

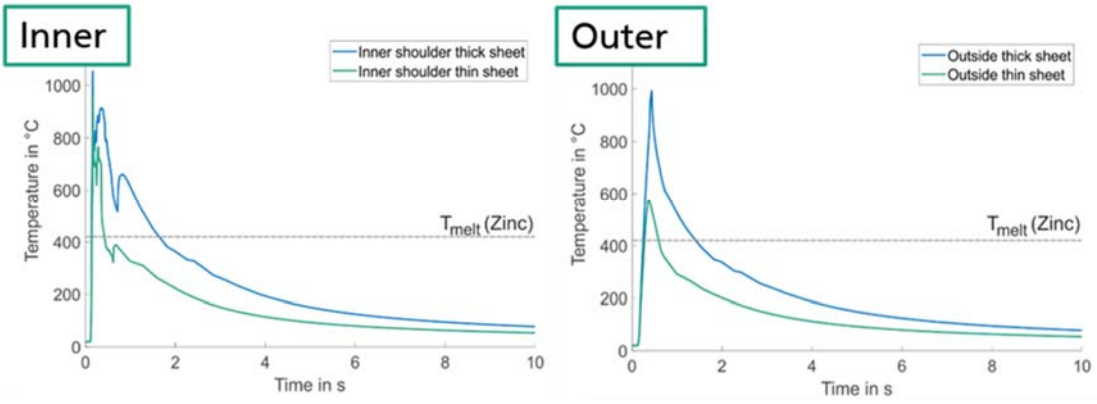


*Figure 6-26: Comparison of the temperature development at the inner edge of the indentation (left) and just outside of the indentation (right) for welding an AHSS to a thin or thick mild steel.*

The model was extended to simulate the joining of DP steels to mild HSLA grades with good agreement. To investigate increased LME susceptibility when welding thick mild

steels to DP steels, a 1 mm and 2 mm HSLA was welded to a 1.5 mm DP1000. In the results, it could be seen that the thick mild steel experiences far longer times where molten zinc is present on the surface. It can be concluded that welding a thick mild steel to an AHSS is more likely to cause LME because of the greater energy introduced into the weld. The nugget area is far larger and because of the 80 ms longer welding time and the 1.5 kA increased current, the electrical energy input is 60% larger.

Summary:

During the enforcement of LME trials, the impact of several process related influences on the formation of LME was investigated. While using the maximum spatter free weld current most factors were found to cause only light cracking in case of LME-susceptible MTCs and no cracking in case of non-susceptible MTCs. Only by the use of highly elongated weld times significant cracks were enforced on susceptible MTCs. The factors that cause a combination to be considered susceptible have been analyzed.

## 6.4 Process Parameter optimization

### 6.4.1 Pre-Pulse welding schedule

The idea of the pre-pulse welding schedule is to remove the zinc from the exposed surface areas by application of a high current pre-pulse, similar as described in [13]. The shown investigations were performed on the MTC DP1200 - thick mild steel (2.00 mm). The initial experimental investigations combined a variable pre-pulse current with a constant main weld pulse, to determine a suitable spatter free pre-pulse current. Figure 6-27 provides an overview of the surface sheet condition after pre-pulse and after weld pulse.

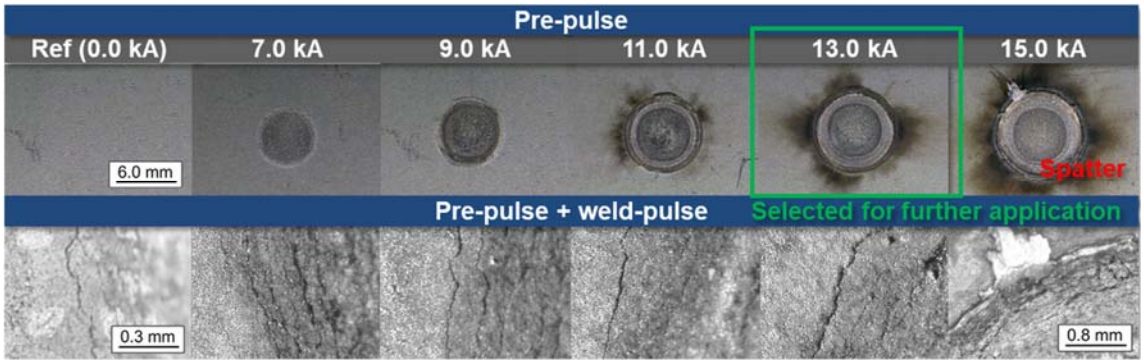


*Figure 6-27: Experimental results of pre-trials for pre-pulse welding schedule for MTC DP1200 - thick mild steel (2.00 mm)*

For further trials a pre-pulse current of 13 kA was selected as highest spatter free pre-pulse current. During the trials no improvement in cracking behavior compared to the reference (single pulse weld) was seen. It could be rather observed that with an increase in pre-pulse current, more intense crack formation took place inside the HAZ. No cracks inside the indentation were observed. For the main trials the experimental setup was set up to be more critical with a main welding current of 11 kA, to allow for a better distinction of results between reference and optimization procedure. The results of these trials are shown in Figure 6-31. The green lines highlight the cracked parts of the spot welds circumference.

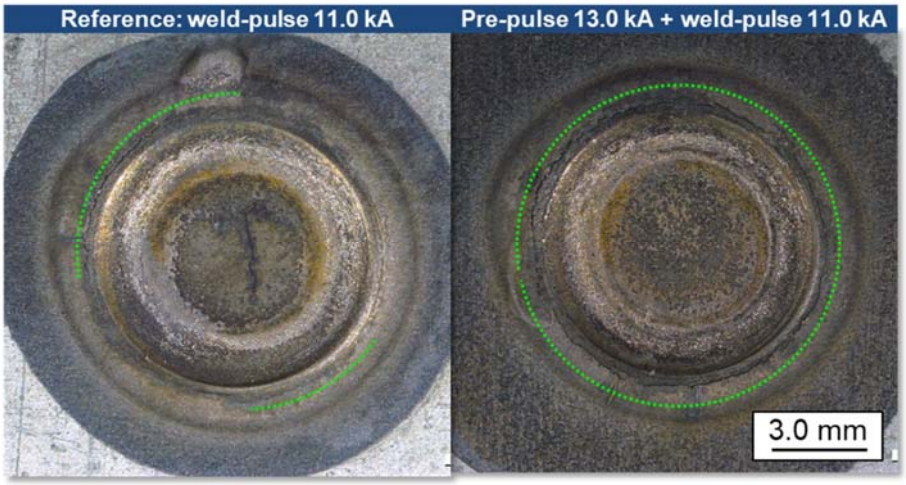


*Figure 6-28: Experimental results of main-trials for pre-pulse welding schedule for MTC DP1200 - thick mild steel (2.00 mm)*

The results show that no improvement of the cracking behavior could be achieved. Instead it was seen that the pre-pulse supplies zinc to the critically stressed areas

beside the electrode cap, allowing for an enhanced zinc availability, results in almost 360° cracking. Additional experiments were performed with bigger working plane diameter electrode caps successively, but even A0-100 caps used in pre-pulse did not allow for a sufficient experimental zinc removal.

In order to investigate this approach numerically, a corresponding welding simulation was set up. The welding schedule used for simulation purposes is shown in Figure 6-29.

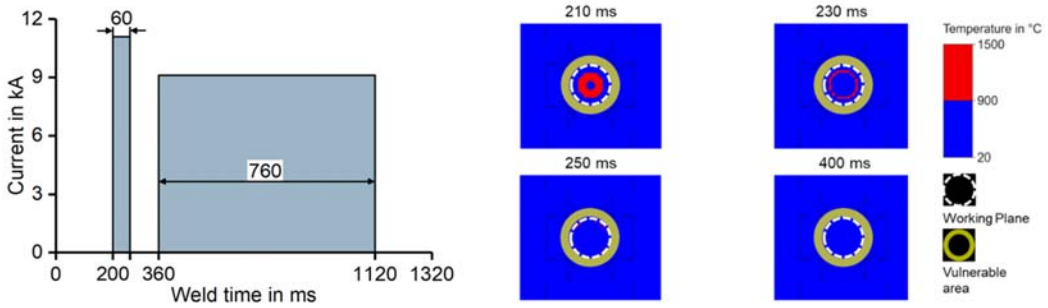


*Figure 6-29: Pre-Pulse welding schedule (left) and Temperature field in top view with customized scaling (right).*

The evaluation of the surface with regards to the evaporation temperature of zinc shows that 900 °C are only reached beneath the electrode working plane (see Figure 6-31). However, according to the simulation, zinc appears to be present in vulnerable areas. The temperature field simulation does not confirm any advantages of welding with pre-pulse.

### 6.4.2 Post-Pulse welding schedule

The idea of the post-pulse welding schedule is a reduction of nugget growth rate and thermally induced stresses by low-current 1st pulse, followed by high-current 2nd pulse [15]. The experimental setup for the correlation trials is shown in Figure 6-30. The shown investigations were performed on the MTC DP1200 - thick mild steel (2.00 mm). The first (longer) pulse is used for creation of a minimum size weld nugget. A short pause allows for the formation of a corona bond around the nugget for stabilization and postponing of spatter within the second pulse. The second (shorter) pulse then is used to generate additional nugget growth. Both used welding schedules were matched to allow for a similar resulting nugget diameter of 6 mm. 100 spots were welded for each

category, of which 20 spots showed very light signs of cracking, regardless of the used welding schedule.

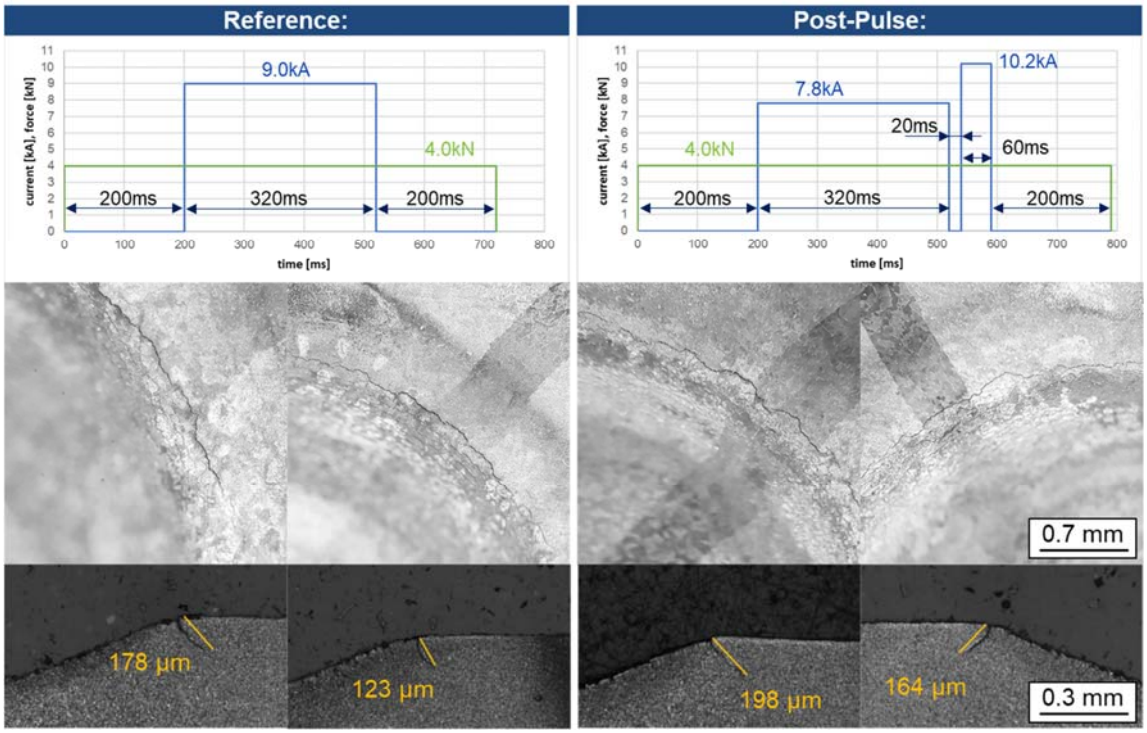


*Figure 6-30: Experimental reference weld schedule (left), post-pulse welding schedule (right) and results for both schedules (below) for the MTC DP1200 - thick mild steel (2.00 mm)*

In order to verify whether or not the method bears a potential for LME avoidance, temperature and strain field simulations are performed. Subsequently, a comparison between a reference case and a post-pulse welding schedule is made. Figure 6-31 shows the welding schedule and the parameters of the post-pulse case.

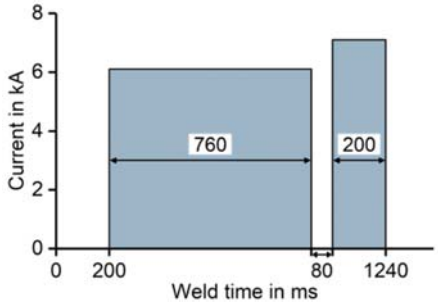


| Parameter \| weld schedule | Post-pulse | Reference |
|---|---|---|
| Hold/squeeze times | 200 ms | 200 ms |
| Weld time 1st pulse | 760 ms | 760 ms |
| Welding current 1st pulse | 6.1 kA | 6.5 kA |
| Weld time 2nd pulse | 200 ms | - |
| Welding current 2nd pulse | 7.1 kA | - |

*Figure 6-31: Numerical post-pulse welding schedule (left) and welding parameters (right).*

The heat input is not kept constant, for the multi-pulse welding schedule includes some additional cooling time, so the resulting nugget diameters differ. Instead, the reference welding current is chosen in a way that the resulting nugget diameters are equal, see Figure 6-32.

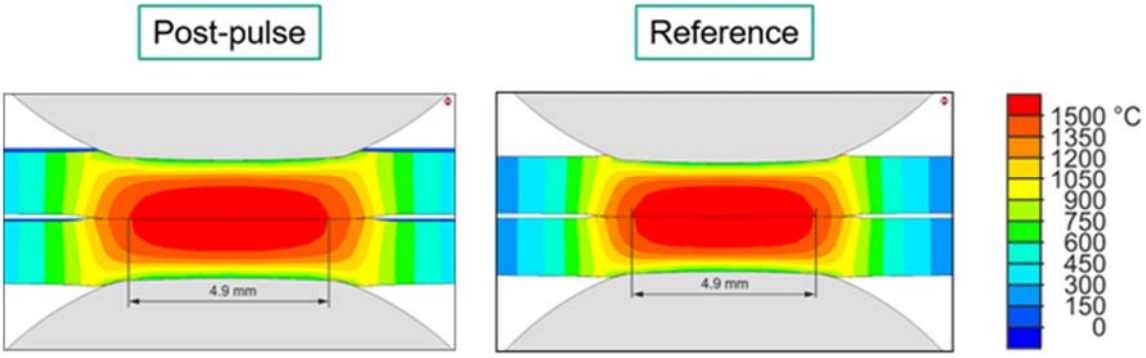


*Figure 6-32: Compared simulations of post-pulse and reference.*

Figure 6-33 shows the plastic strain and the temperature over time of the two simulated cases on the sample surface. The post-pulse is clearly divided into the two phases, which the strain over time curve reflects. In total, a higher plastic strain is reached locally for the post-pulse welding schedule in comparison with the single pulse reference case: ∆=0.02, +12%. Due to the reheating of the weld for the post-pulse welding schedule, the Znliq time range appears elongated: ∆=0.6 s, +35%.

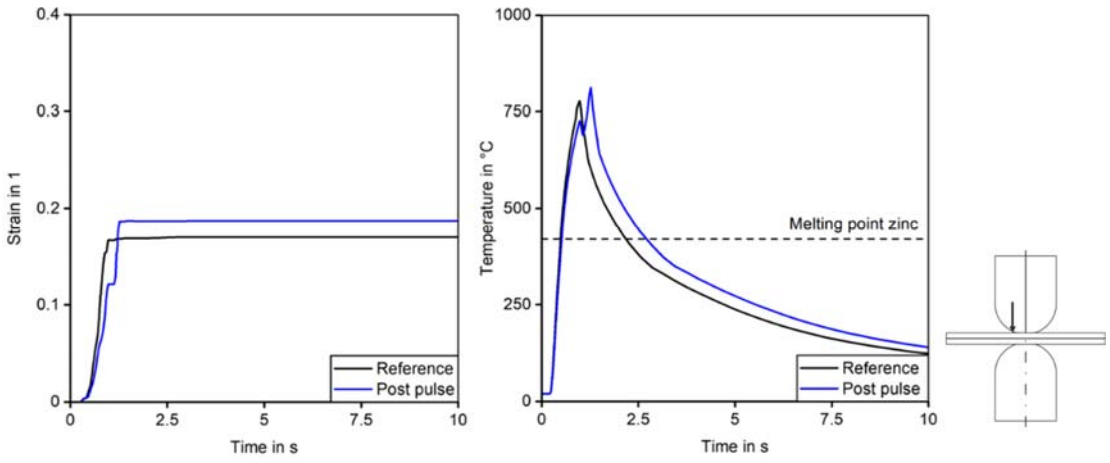


*Figure 6-33: Strain (left) and Temperature (right) over time comparison of post-pulse and reference.*

### 6.4.3 Electrode force profiles

The trials on electrode force profiles were used to investigate the potential benefits of increased electrode cooling within the hold time without sacrificing a sufficient nugget diameter by modifying the force during flow of the weld current. The electrode force was varied in three steps during the hold time and compared to a constant reference force level. Figure 6-35 gives an overview of the used weld schedules and recorded welding processes achieved.

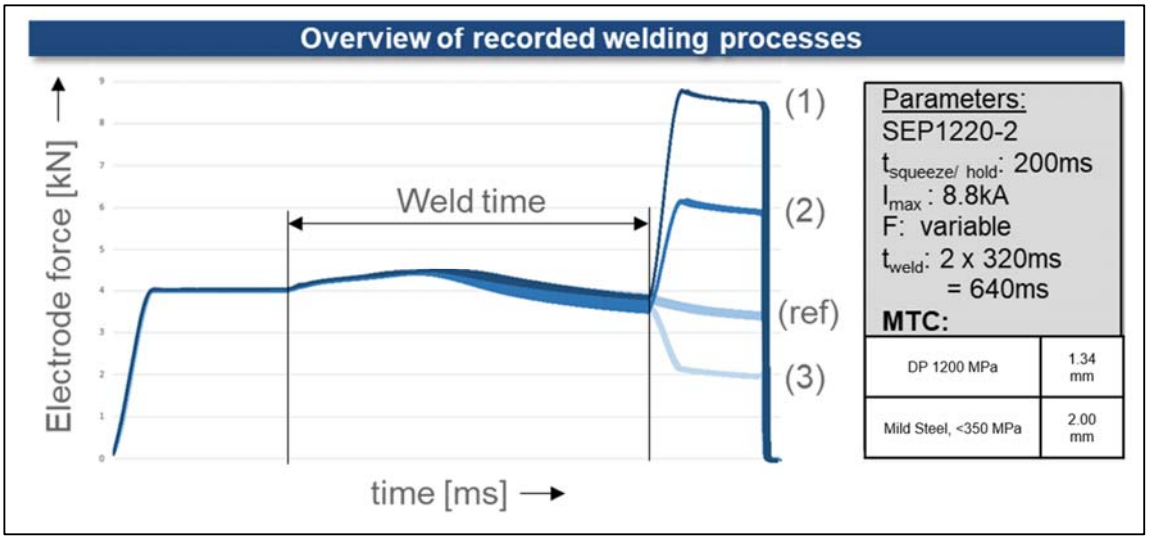


*Figure 6-34: Overview of the recorded welding processes implementing electrode force profiles.*

As a result of these trials only a slight reduction in of the observed crack area can be reported. This is due to a variation in crack appearance. For lower electrode force profiles wider cracks with a smaller circumferential extent were observed, while for higher electrode force profiles finer cracks at higher circumference were found. A much more significant impact could be determined on the crack depth. As can be seen in Figure 6-35 the higher electrode force profiles allowed for a clear reduction in penetration depth, although no complete crack avoidance was achieved.

The pictures also show the slightly more intense electrode indentations and a reduced nugget height due to a high electrode force profile.

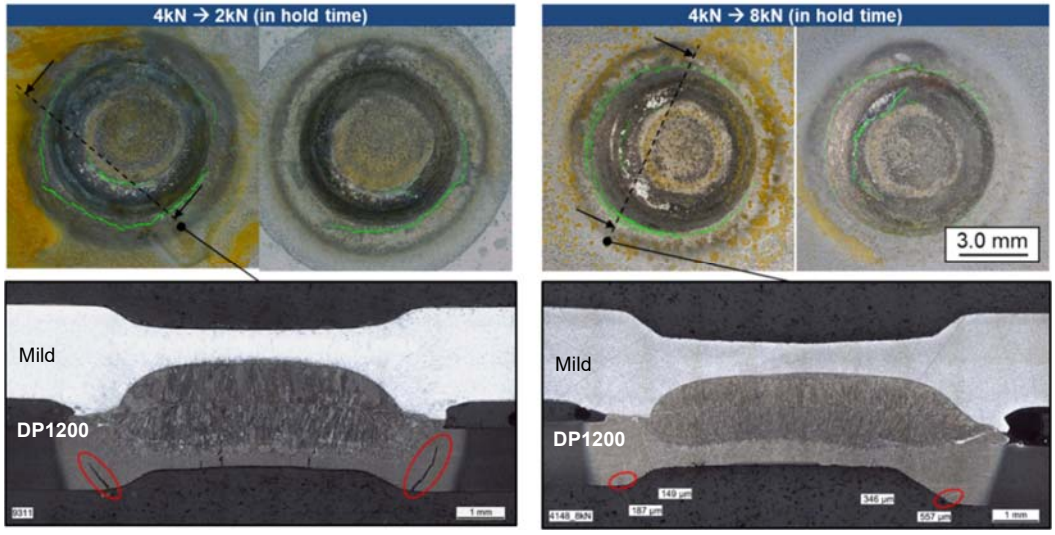


*Figure 6-35: Comparison of results for different investigated electrode force profiles.*

### 6.4.4 Extended hold times

The extended hold time trials are based on the hypothesis that the electrode lift-off causes an erratic increase in tensile stresses, while zinc is still liquefied on the sample surface. The use of extended hold times shall therefore delay the electrode lift-off until the temperature dropped below T < 420°C. The experimental setup and received results are summarized in Figure 6-36.

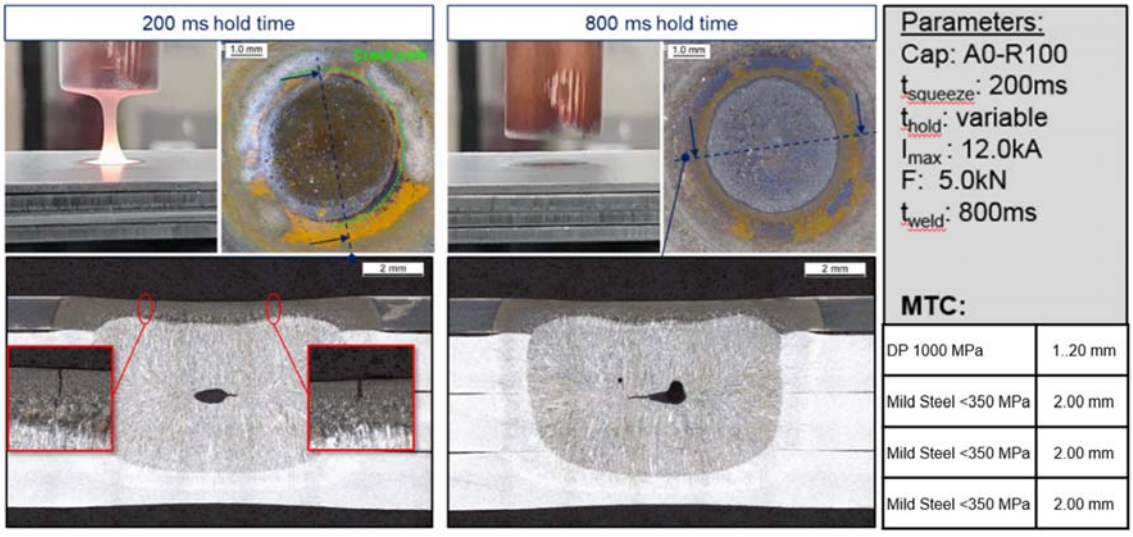


*Figure 6-36: Experimental setup and results of experimental trials with extended hold times.*

During this study a high energy welding scenario is investigated. A combination of elongated weld time, a high weld current and a thick MTC cause a high accumulation of thermal energy within the joining zone, stressing the importance of the cooling capacity for a sufficient energy dissipation. As shown in Figure 6-36 for a hold time of 200 ms a release of illuminated fume is observed at the moment the electrodes lift of the spot weld surface. An intense whitish glowing of the joining area clearly indicates a very high surface temperature and caused by the insufficient degree of energy dissipation during the short hold time of 200 ms. As a result, all welds show clear signs of surface cracks, but no interface cracks were observed. The specimen welded with a hold time of 800 ms do not show cracks. After 800 ms of hold time no fume is observed and little to no dark red glowing of the spot weld surface is noticeable at electrode lift off, indicating a significantly lower surface temperature.

For numerical verification, a thermal field simulation is performed. A comparison between a reference case with normal hold time and a second case with extended hold time (3x) is evaluated. Figure 6-37 shows the welding schedules of the corresponding cases.

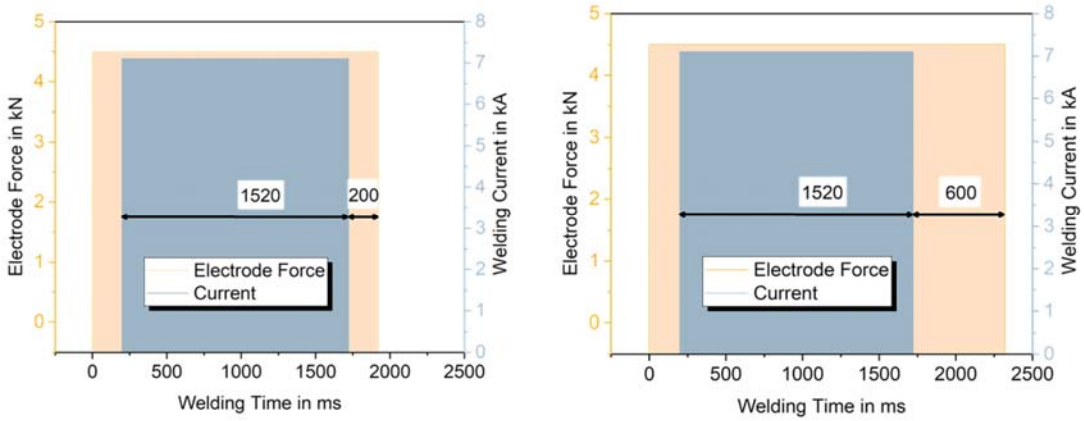


*Figure 6-37: Welding schedule of reference case and extended hold time.*

Figure 6-38 shows the deducted temperature over time curves of the two simulated cases on the sample surface. The time range of Znliq appears shortened by approximately 1.1 sec (-30%). The time for stress-assisted zinc diffusion is shortened accordingly, while the temperature at electrode lift-off is reduced from approx. 700 °C to approx. 530°C. Therefore, the potential benefit of increased hold time is confirmed.

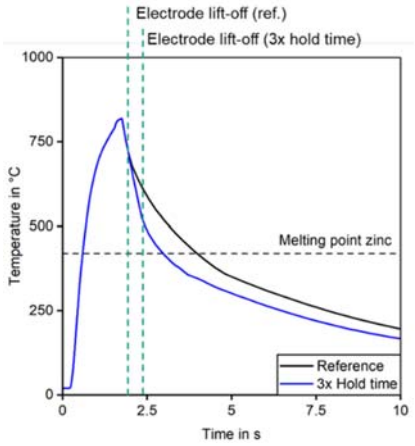


*Figure 6-38: Temperature over time comparison of 3x hold time and reference*

### 6.4.5 Variation of electrode tip geometry

The three different electrode tip geometries (see Figure 4-8) were compared for their potential in LME prevention at four different weld times. The weld current for each of the different electrode caps was adjusted to receive an identical nugget diameter. All used parameters are listed in Table 6-4.

*Table 6-4: Overview of the applied process parameters during the variation of electrode tip geometry trials.*

| Electrode geometry | F1-5.5 | F1-8.0 | A0-100 |
|---|---|---|---|
| Electrode force | 4.0 kN | | |
| Weld current | 8.7 kA | 9.1 kA | 9.7 kA |
| Weld time | 320 ms, 640 ms, 960 ms, 1280 ms | | |
| Hold time, squeeze time | 200 ms | | |

Figure 6-39 provides a summary of the key results. For the electrode geometry with the smallest working plane diameter significant cracking was already observed for lightly elongated weld times. At 4x weld time this electrode geometry produced welds with a very high penetration depth, which can be equal to the sheet thickness. At the same time the surface view shows the very high circumferential extent of these cracks. For the F1-8.0 geometry the formation of cracks was observed for 3x weld time. While also a high penetration depth could be noticed for this electrode geometry at 4x weld time, the surface views indicate a much lower circumferential extent compared to the welds created by use of the F1-5.5 electrode geometry. For the A0-100 electrode geometry no cracking was observed for any of the used weld times.

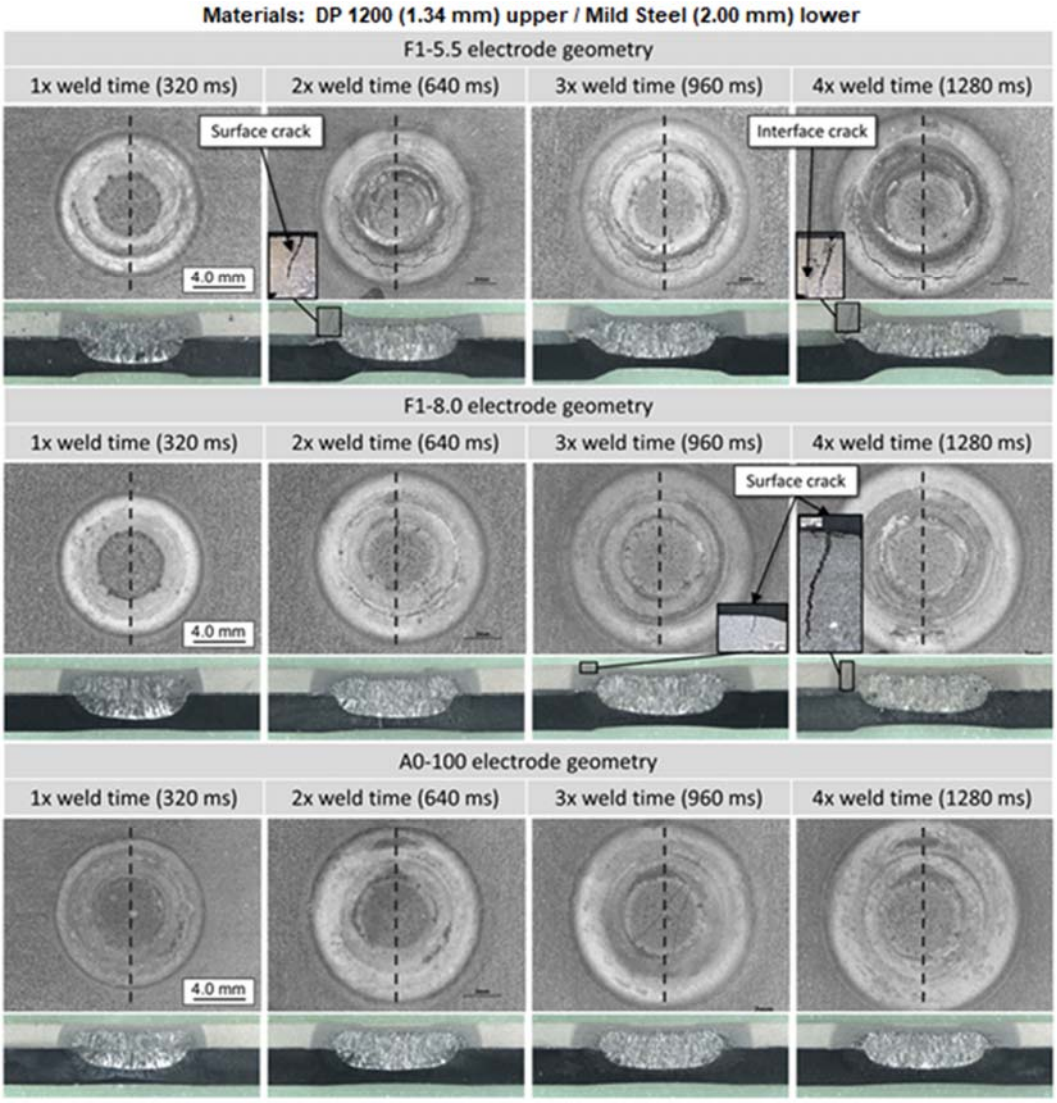


*Figure 6-39: Resulting surface views and cross-sections of spot welds created with the three different electrode geometries at four different weld times. [1]*

The three different electrode geometries and four different weld times investigated in the experiments were also reproduced in electro-thermomechanical finite element simulations. The experimental parameters from Table 6-4 were used as input for hold times, weld times and geometry-dependent weld currents. The results for the calculated nugget size and -shape are shown in Figure 6-40. The nugget diameters are comparable for the different electrode geometries and the nugget does not grow significantly with increased weld time.

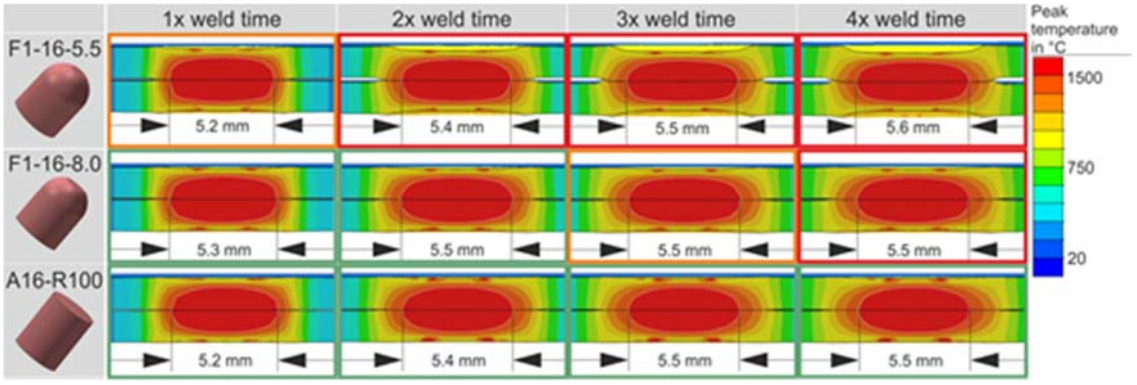


*Figure 6-40: Simulated nugget dimensions for the three different electrode geometries and four weld times. [1]*

In the previous work packages, it was shown that local strains and plastic deformations facilitate LME cracking. Figure 6-41 shows the residual plastic deformation after cool-down for the different electrode geometries and weld times. The F1-16-5.5 electrode geometry causes the largest local deformation (i.e. indentation) and the deformation grows in size with the weld time. Maximum local strains of 0.3 are reached at the shoulder of the indentation area for the 4x weld-time case. For the F1-16-8.0 and the A0-16-R100 electrode geometries, the plastic deformations are significantly lower and do only lightly increase with longer weld times. These observations can explain the larger susceptibility to LME cracking for the 5.5 mm working-plane electrode: The localized plastic strain increases due to the small electrode working plane, making LME cracks more likely.

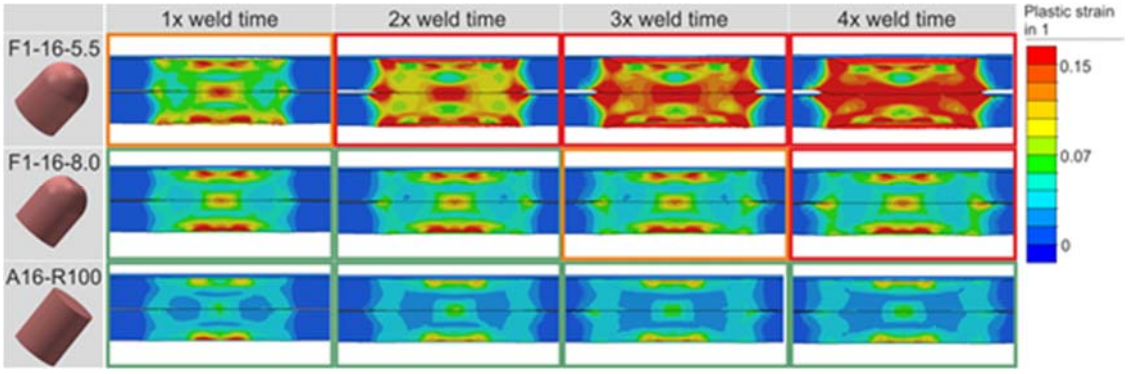


*Figure 6-41: Residual plastic strain after welding and cooling for the three different electrode geometries and four welding times. [1]*

Also the effect of the prolonged weld time on the occurrence of LME for the F1-16-8.0 electrode cap can be explained with the plastic deformation. The quadrupled weld time

leads to a significant LME occurrence and additional plastic strain is observed for the F1-8.0 geometry.

Another possible explanation for the increased LME susceptibility for longer weld times is the amount of introduced energy and, hence, the longer presence of liquid zinc on the surface. As zinc diffusion into the grain boundaries is largely governed by the temperatures and higher temperatures cause higher diffusion rates [12], the surface temperatures can be analyzed as a measure for LME susceptibility. Figure 6-44 shows the time that the surface at the shoulder of the spot weld, 2 mm from the edge of the indentation, is above 420 °C and the zinc coating is liquefied. The three electrode geometries show similar behavior for all four weld times. For the single weld time, the time that the surface is heated above zinc melting temperature is 1.2 s and a linear increase is observed for increasing weld time. Although the plastic strain on the surface does not increase for the F1-16-8.0 electrode, the time at which zinc can diffuse into the grain boundaries increases by a factor of 3.2 for the quadrupled weld time. The same occurs also for the A0-16-R100 electrode geometry but experimentally, no cracks are observed. This is likely due to the very low local plastic deformation caused by the large working plane and strong support of the growing nugget. Hence, little stress-assisted zinc diffusion takes place for the flat electrode cap even at the longest weld times.

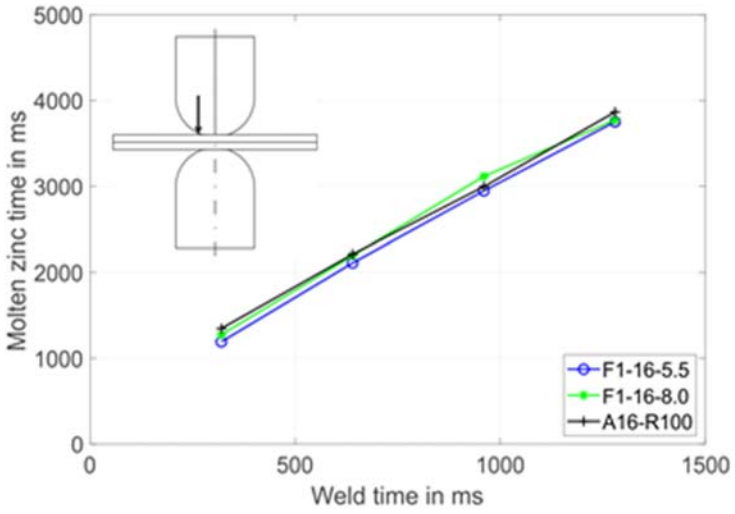


*Figure 6-42: Comparison of the molten zinc time for the three electrode geometries and four weld times. [1]*

Summary:

Different measures were tested for their potential to reduce or completely avoid the formation of LME cracks in spot weld. No positive effect was seen for the investigated pre- and post-pulse welding schedules. An increased force during the hold times was seen to allow for a reduction in crack penetration depth. Most effective measures were the adaption of the electrode tip geometry to larger working plane diameters and an extension of the hold time. Both measures in combination allowed for crack free welds, even under extreme conditions (weld times >1000 ms and MTCs consisting of four-layers).

## 6.5 Application of optimized process parameters

The found measures on LME crack prevention were used to generate LME free spot welds for various LME susceptible materials of the available AHSS portfolio, identified during reference testing. The goal was to achieve an LME and spatter free welding process, while generating a nugget diameter above $5\sqrt{t}$ by application of up to 2x weld times. This goal was to be achieved while welding gap afflicted double hat profiles to resemble a more production-like use case. Figure 6-43 shows a schematic model and the typical resulting effect when welding without a proper weld process setup.

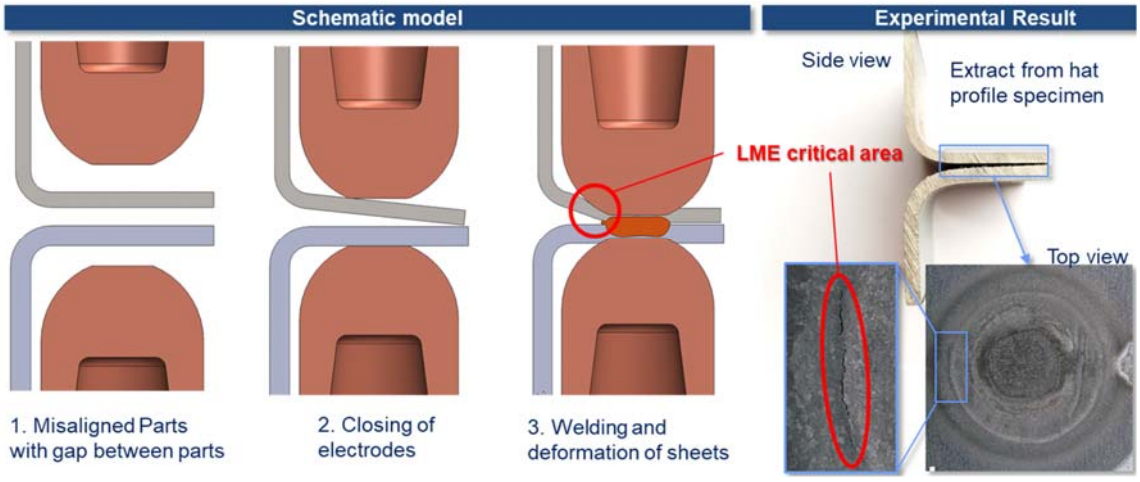


*Figure 6-43: Schematic model and typical experimental result when welding gap afflicted flanges.*

For all tested material the desired LME free welding process could be established by tip dressing the electrode caps to an 8.0 mm working plane diameter and dialing in

suitable hold. This worked despite of the increased stresses by the gaps and the necessary elongation in weld time for generation of a sufficient nugget diameter. Figure 6-44 shows resulting spot welds for three of the AHSS grades.

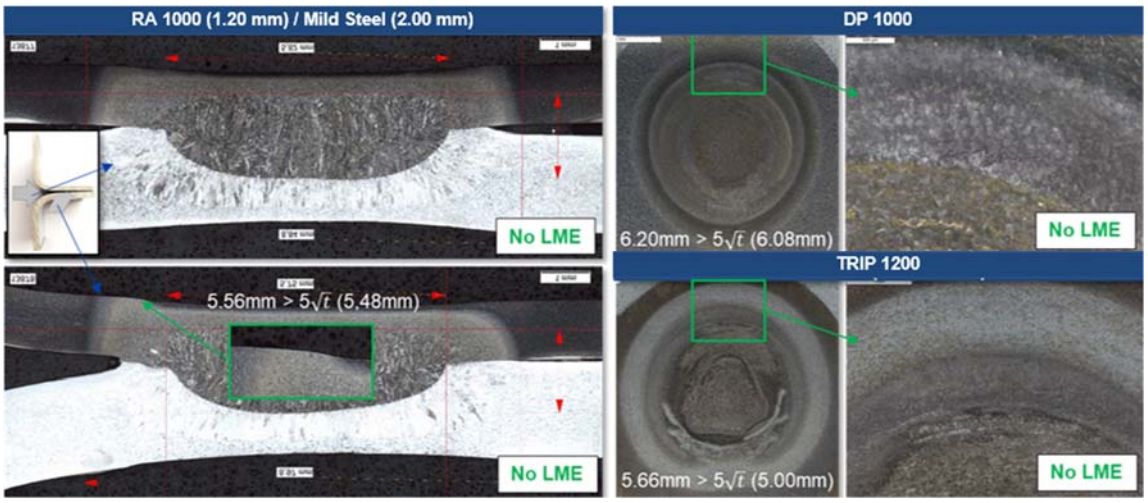


*Figure 6-44: Resulting LME free welds on gap afflicted hat profiles for three AHSS grades.*

## 6.6 Time of LME occurrence

The acoustic emission data of 4x weld time trials is provided by the Institut de Soudure, see Figure 6-45 (left and middle). Changes are only visible in the form of a more discrete signal of the LME afflicted sample. The assumption is therefore, that LME occurs at approximately 1000 ms, which equals the end of heating phase. Thermal field simulations, however, provide surface thermal histories in critical areas, as shown in Figure 6-45 (right).

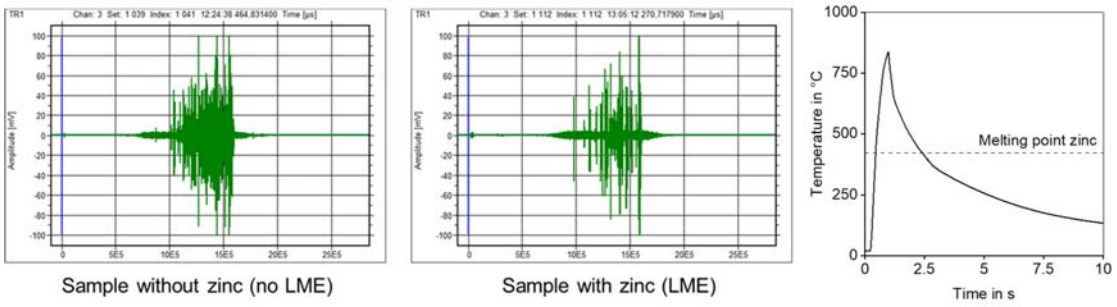


*Figure 6-45: Acoustic emission measurements (left and middle) and simulated thermal history on sample surface close to electrode indentation area (4x weld time).*

So, the preliminary assumption of LME occurrence during the heating phase may not be exclusive. The longer exposure to liquid zinc during the cooling phase is considered to increase the LME risk, and may lead to LME during this phase. Although acoustic emission measurements indicate that LME might occur during the heating phase, it must not be ruled out that LME cracking can occur at later occasions, i.e. during the cooling phase. The determination of the potentially critical time window is based on the physical properties of zinc only. It can easily be specified according to more precise temperature values, e.g. from literature.

## 6.7 Experimental destructive testing

### 6.7.1 Enforcement of varying crack types and intensities

As basis for all destructive testing performed throughout this program the reproducibility of all destructive specimen had to be assured. By usage of dedicated welding tool for a proper alignment of the LWF-KSII specimen halves a limiting of uneven sheet separation and the uncontrolled formation of spatter by the extreme welding parameters used (e.g. excessive weld times) could be widely avoided. Reference specimens were created by a removal of the zinc-coating on the sheets surface and interface before welding. Additionally, only electrode caps which have had no contact with zinc before were used during welding of the reference specimen. This way a guaranteed crack-free spot weld could be generated. Electrode caps of the type F1-5.5 were used for all reference welding except for the specimen allocated to corrosion testing. Here A0-100 caps were used.

LME afflicted specimens were also created by usage of F1-5.5 type electrode caps. Table 6-5 provides an overview of the applied weld schedules. The basic method for the enforcement of different crack categories was the elongation of the weld time. This technique was combined with the application of a short pre-pulse for an increase in crack intensity and homogenization of the crack around the weld’s circumference (moving of zinc into the critical areas). 4x weld times were used for the generation of intense LME cracks. 2x weld times were used for the enforcement of medium LME cracks. 1x weld times were used for the creation of light LME cracks. A dezincing of

the sheets either on the surface or on the interface allowed for the controlled creation of just one crack type at a time.

*Table 6-5: Overview of the weld schedules used for joining of LWF-KSII-specimen.*

| Crack category | Squeeze time (ms) | Electrode force (N) | Pre-pulse current (A) | Pre-pulse time (ms) | Cool time (ms) | Weld time (ms) | Hold time (ms) | Weld current (A) |
|---|---|---|---|---|---|---|---|---|
| light | 200 | 4000 | no pre-pulse applied | | | 320 | 200 | 9400 |
| medium | 200 | | 13 | 50 | 100 | 640 | 200 | 9000 |
| intense | 200 | | 13 | 50 | 100 | 1280 | 200 | 9000 |

## 6.7.2 Quasi-static load

Two MTCs were tested in two load cases and the behavior of cracked spot welds was compared to the behavior of crack free reference spot welds. Figure 6-46 shows one of the most critical cases investigated. The intense surface cracks lead to a reduction of the maximum Force of 21%. The energy consumption is reduced by 40%.

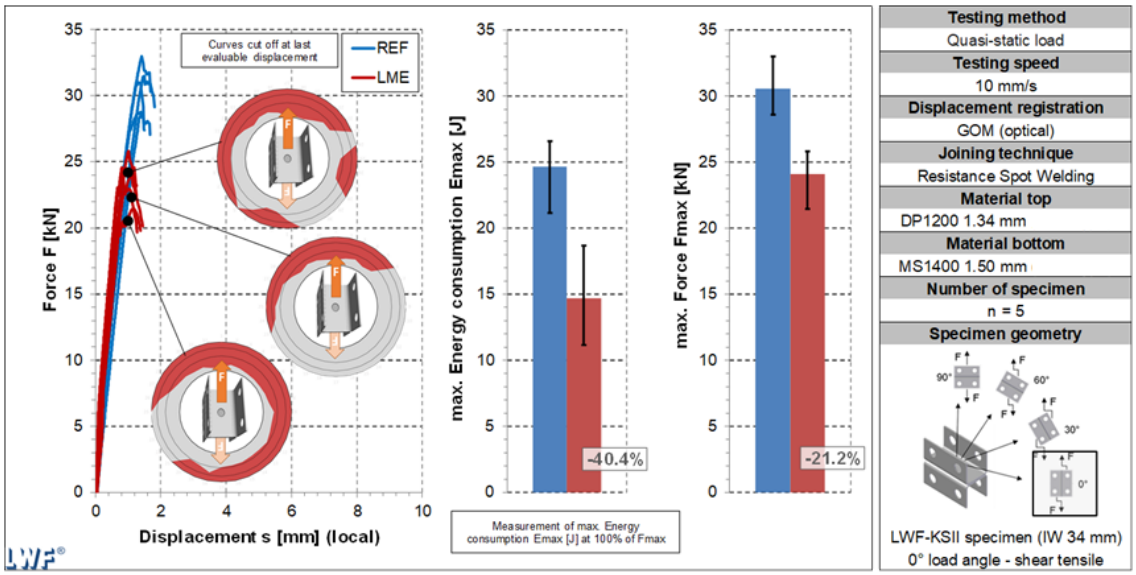


*Figure 6-46: Destructive testing results for quasi-static load 0°: DP1200 (intense surface cracks) – MS1400.*

The typical failure behavior for this and similar cases, where LME cracks have an influence is shown in Figure 6-47. It can be seen how the spot welds fail along the weakened areas afflicted with the LME cracks.

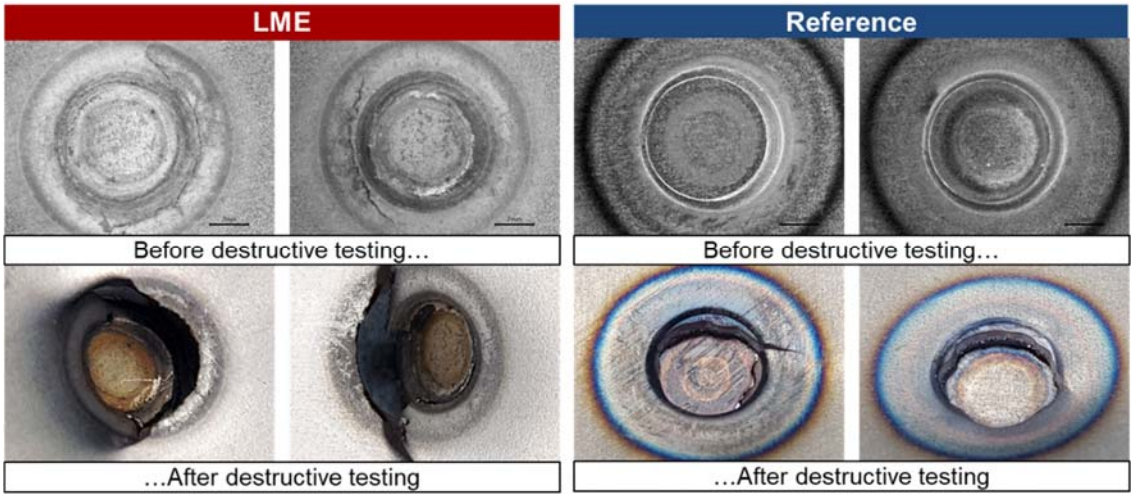


*Figure 6-47: Comparison of failure behavior between reference and intensely LME afflicted spot welds.*

Medium sized cracks did not show any influence on the joint strength or load bearing capacity of the tested spot welds during quasi-static testing: In the below shown Figure 6-48 medium sized interface cracks had no influence on the failure behavior or load bearing capacity of spot welds tested in a 0° load case. For the combination of DP1200 to MS1400 no negative influence on load bearing capacity or failure behavior of medium sized cracks was seen as well. Testing of light cracks revealed no impact of this crack category on the failure behavior or load bearing capacity of the tested spot welds.

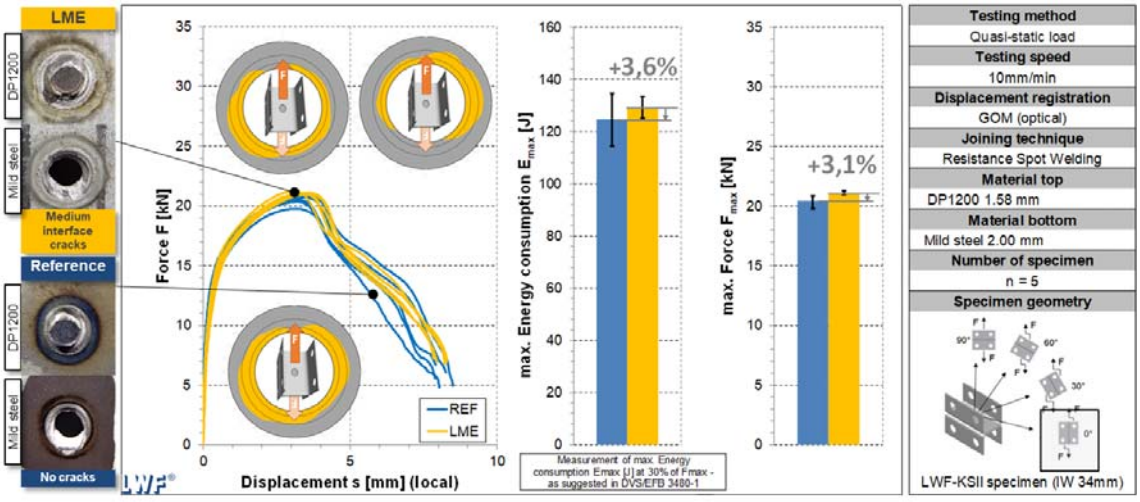


*Figure 6-48: Destructive testing results for quasi-static load 0°: DP1200 (medium interface cracks) – Mild steel.*

## 6.7.3 Crash load

The identical MTCs and same load cases were also tested under crash load. Figure 6-49 provides an overview of the tested surface crack categories in a 0° load case via the shown exemplary specimen. For intense cracks a clear negative impact of the cracks on mechanical joint properties can be seen. Cracks with a medium size typically showed a minor but still significant reduction of the tested spot welds load bearing capacity, when loaded in 0° direction. Light cracks did not result in any reduction in spot weld performance.

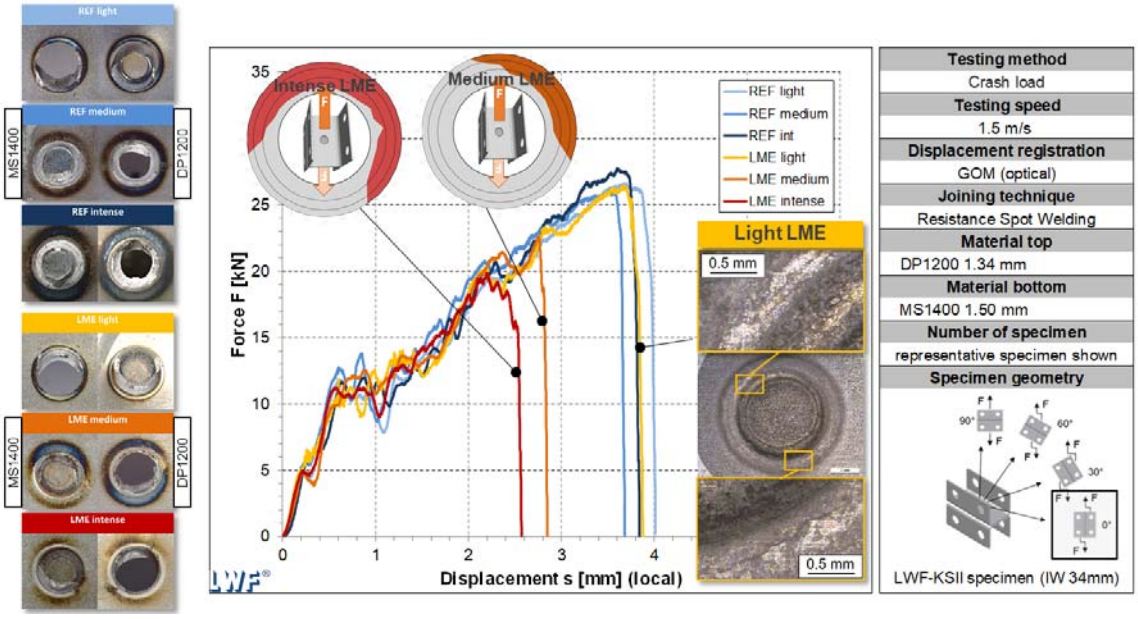


*Figure 6-49: Destructive testing results for Crash load 0°: DP1200 (variable surface crack intensity) – MS1400.*

When testing the 90° load case, no reduction of the joints properties was seen for specimen afflicted with medium or light cracks. Figure 6-50 provide exemplary results of lightly cracked specimen. No difference in the failure behavior or the force displacement curves can be seen between crack afflicted and reference specimen.

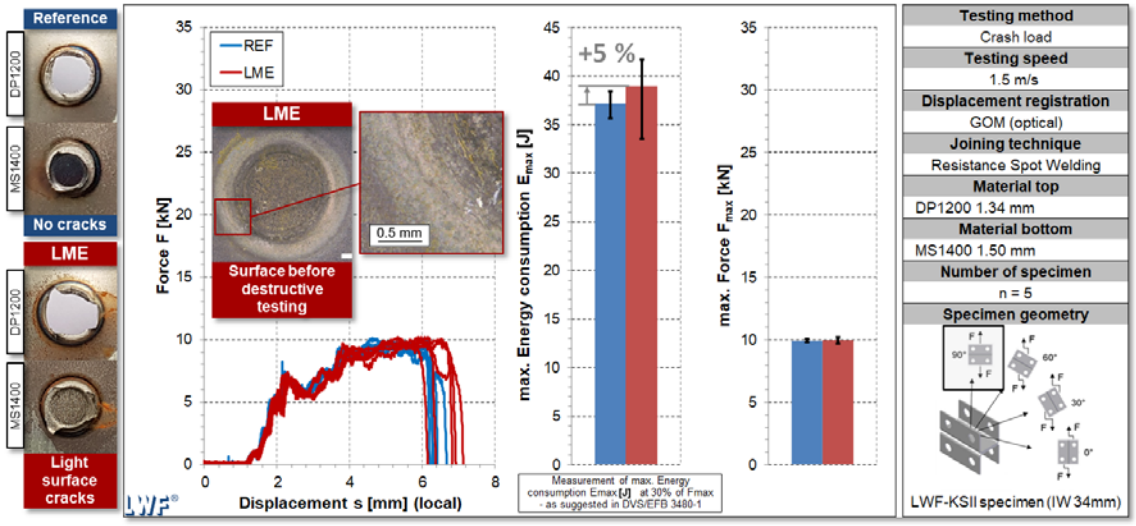


*Figure 6-50: Destructive testing results for Crash load 90°: DP1200 (light surface cracks) – Mild steel.*

## 6.7.4 Cyclic load

Under cyclic load typically no impact of intense LME crack on the fatigue life was observed. The deviation of the results from reference and LME specimen were within the scatter as can be seen in Figure 6-51.

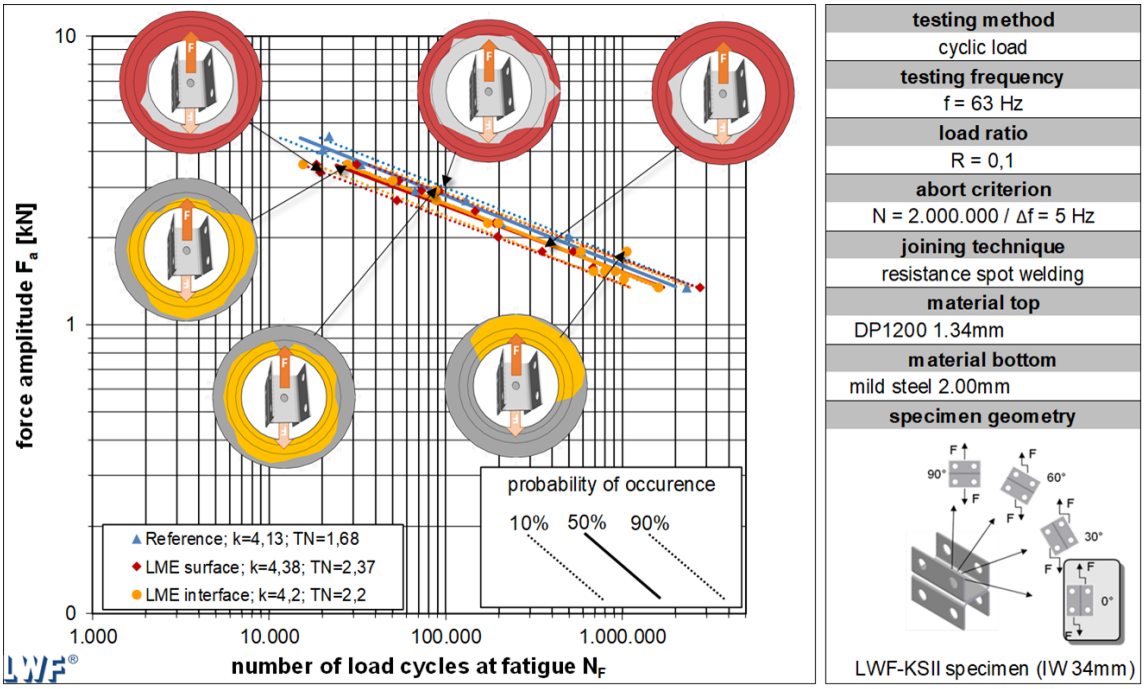


*Figure 6-51: Destructive testing results for cyclic load 0°: MTC DP1200 (intense surface and interface cracks) – Mild steel.*

The observed failure behavior during cyclic testing is illustrated in Figure 6-52. The reference spot weld shows a typical surface view after fatigue failure of a healthy spot weld. The typical initialization of the fatigue cracks is at the interface between the sheets in the joint notch. In case an LME crack is directly within the typical crack path, the fatigue cracks coalesce with the LME-crack and a light redirection of the fatigue crack can be observed. In some cases, the fatigue cracks were observed to cross the crack path of LME cracks. If an LME crack not directly within the typical crack path no interaction takes place at all. Typically, this scenario can be seen when cracks in the HAZ are on the opposite spot side or are inside the indentation.

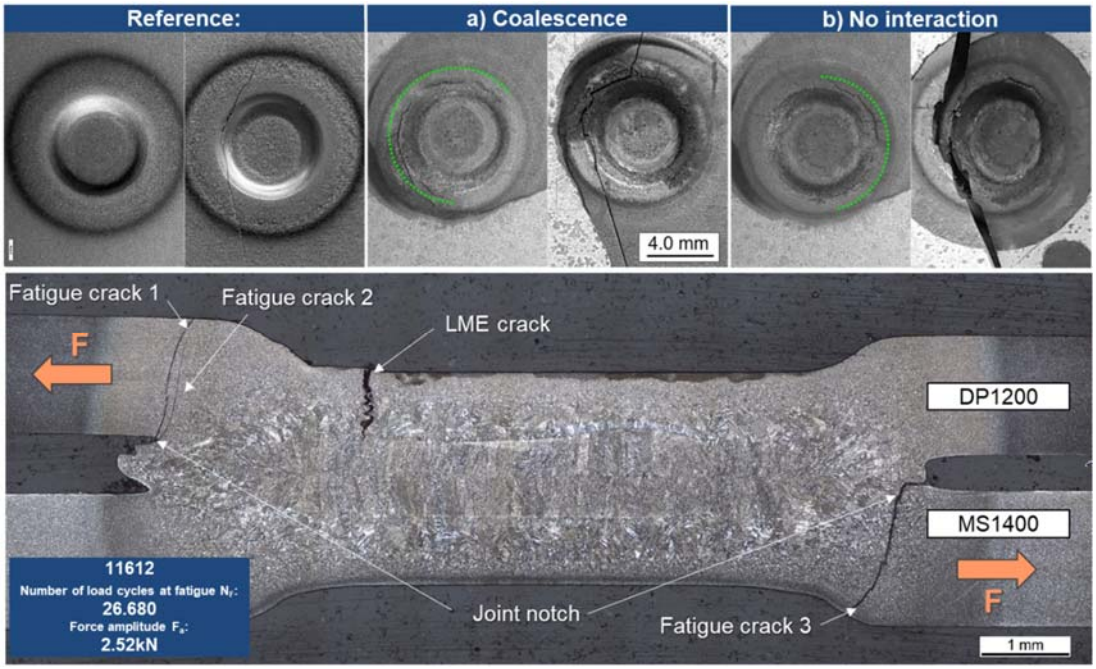


*Figure 6-52: Fatigue crack paths observed during cyclic testing in 0° load case.*

The results for the MTC DP1200 – MS1400 are shown in Figure 6-53. No difference in fatigue life can be observed for the specimen afflicted with surface cracks compared to the tested reference category. However, a light deviation for the results of the interface crack specimen can be observed, leading to a separation from the reference specimen. When referring to the CT scanned interface crack specimen it can be seen that the cracks progress through the entire sheet thickness for wide areas of the loaded zone. The additional specimens show a similarly high local penetration depth. For most of these specimens the enforced LME interface cracks are visible from the surface.

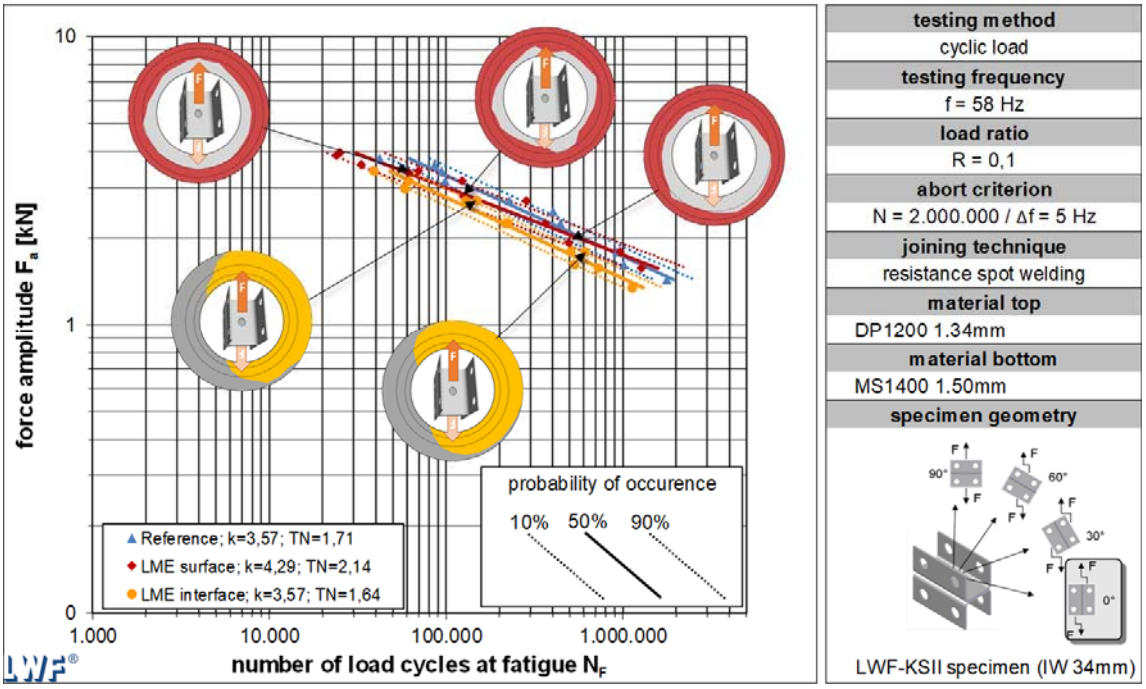


*Figure 6-53: Destructive testing results for cyclic load 0°: MTC DP1200 (intense surface and interface cracks) – MS1400.*

The following Figure 6-54 and Figure 6-55 show the destructive testing results for the 90° load case. The applied load is very low compared to the 0° load case.

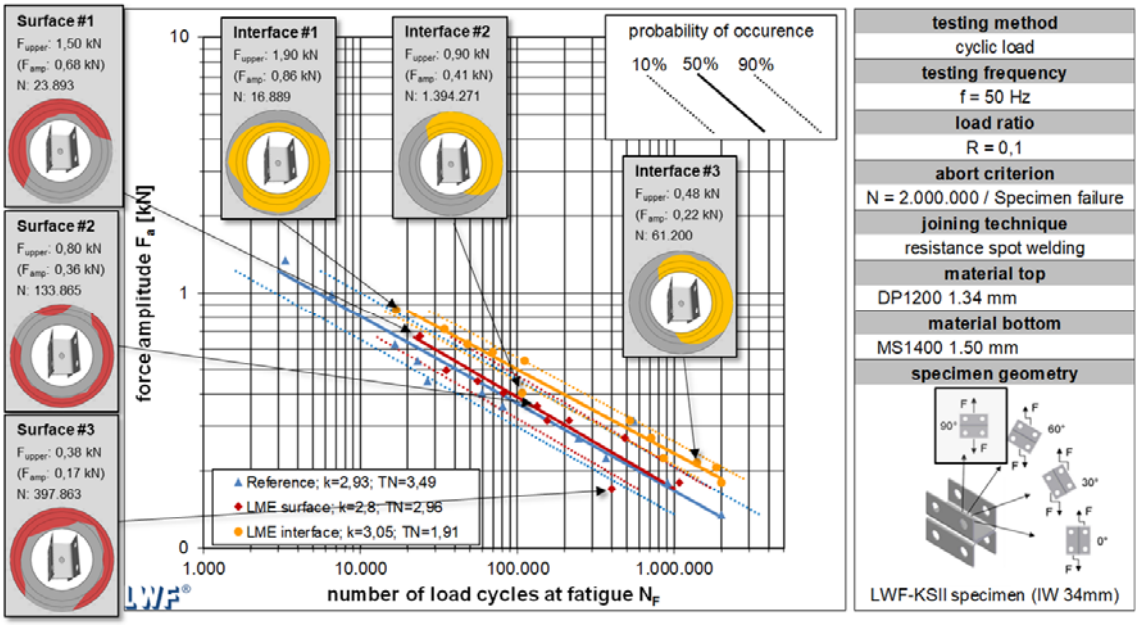


*Figure 6-54: Destructive testing results for cyclic load 90°: MTC DP1200 (intense surface and interface cracks) – MS1400.*

The reference fatigue curve shows a slightly increased spatter, almost completely including all surface crack specimen. For both MTC no reduction of fatigue life can be detected in the 90° load case

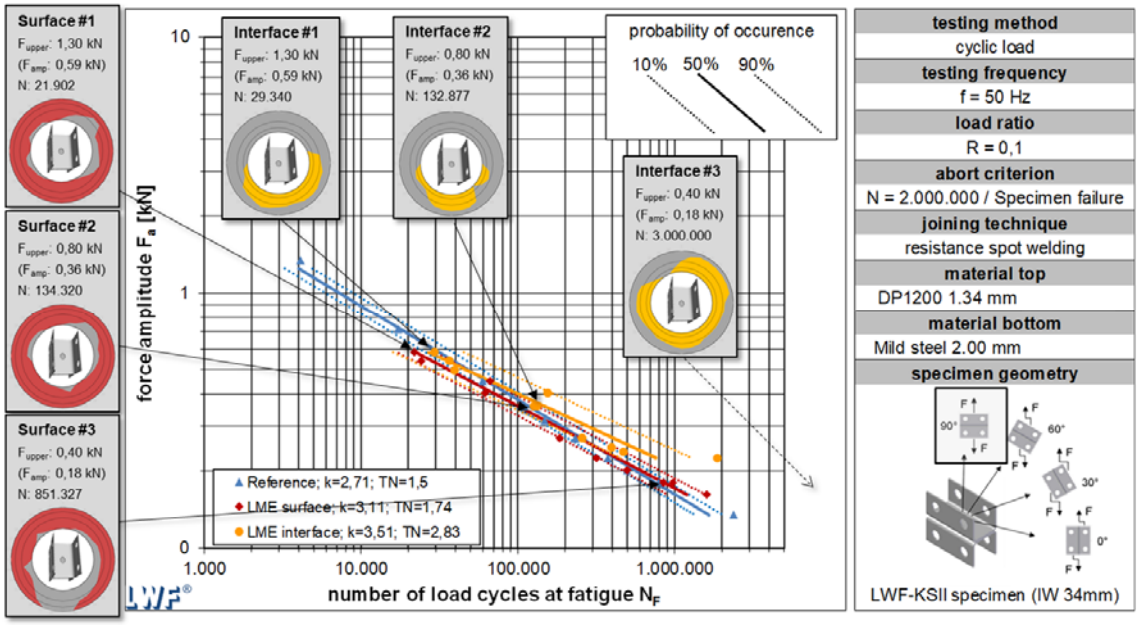


*Figure 6-55: Destructive testing results for cyclic load 90°: MTC DP1200 (intense surface and interface cracks) – Mild steel.*

## 6.7.5 Corrosion testing

Corrosion test cycles

Five materials from the AHSS portfolio were chosen to be tested in a climate cycling test according to VDA 233-102. The goal was to detect possible interactions between the applied corrosive load and intense LME cracks. Two different intensely crack afflicted categories were tested for each of the five materials: specimen in a zinced state and specimen which had been through a cathodic dip coating process prior to the corrosion cycles. Strip specimen as describes in 4.2.1 were welded and analyzed during and after the corrosion cycles. Five cross-sections were created for each the zinced specimen and the cathodic dip coated specimen. Figure 6-56 shows exemplary results after the corrosion cycles for both categories.

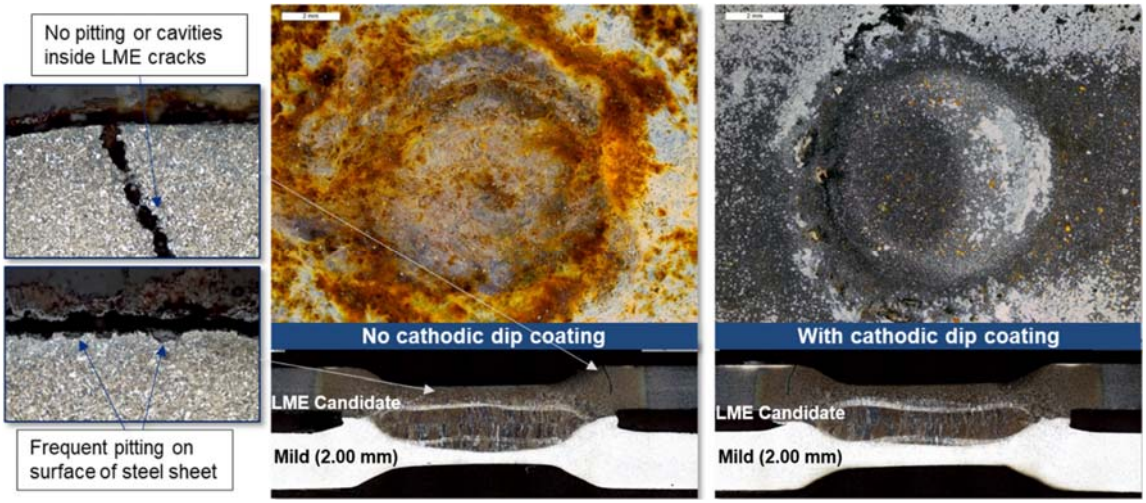


*Figure 6-56: Exemplary results of climate cycling test with intensely crack afflicted strip specimen, LME-candidate / Mild Steel (2.00)*

For the zinced specimen a brittle oxide layer had formed at the surface, while for the cathodic dip coated specimen no effect on the coating was detected. The cross-sections of the dip coated specimen revealed no indications of a corrosive influence. The zinced specimen showed frequent cases of pitting on the surface, but no pitting (e.g. cavities) or other effect of the corrosion cycles could be detected inside the LME cracks.

Quasi-static load testing

Additionally, to the strip specimen LWF-KSII specimen were welded and underwent the same climate cycling test. Multiple Categories were welded, and their load bearing capacity compared. Few of the specimen were CT-scanned for crack characterization. Figure 6-63 provides an overview of the testing matrix and an exemplary result in form of a gray scale image received by CT-scanning.

For creation of reference specimens, it was not possible to make use of the typical procedure by removing the zinc from the specimen before welding, because of a possible impact on the corrosion behavior. Reference specimens were instead created by use of A0-100 electrode caps, which allowed for LME free welding at the extreme welding parameters used. Similarly, a change had to be implemented in the welding process for the LME specimen category: The zinc coating was left intact on the surface and interface. As a follow-up typically surface and interface cracks were detected in parallel, often coexisting or merging into each other. The following Figures show a comparison of results for the two tested load angles. The results for the 0° load case (shear-tensile load) is shown in Figure 6-58 via representative specimen.

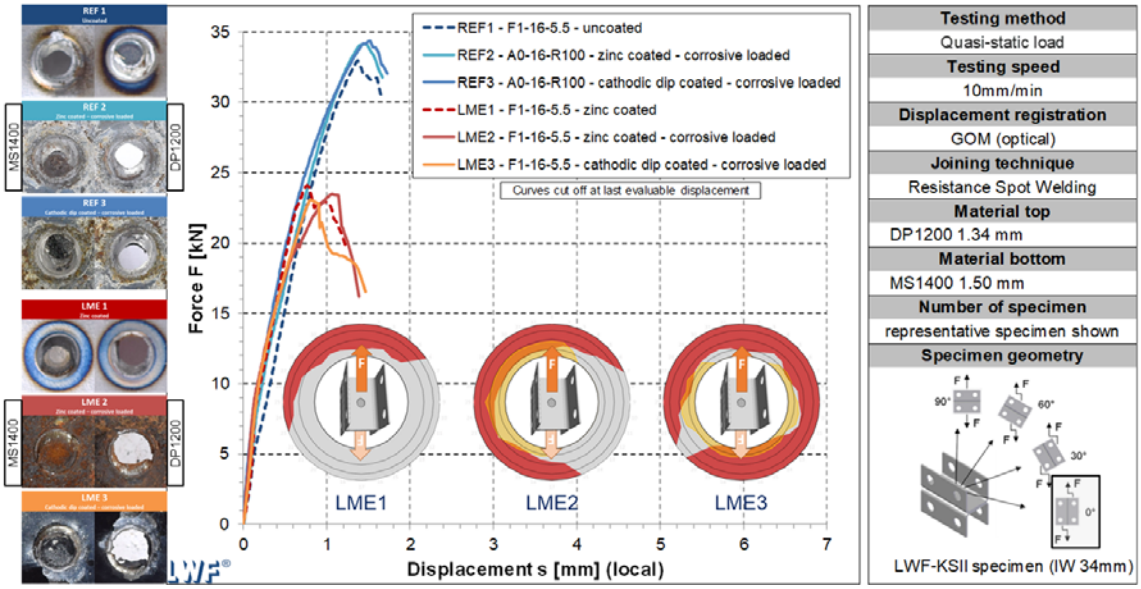


*Figure 6-58: Results for destructive testing of corroded specimen in 0° load case (cross-tensile load).*

Within the diagram an exemplary CT Scans of each of the tested crack categories gives an impression of the extreme enforced crack intensity. As a consequence of this a clear reduction of maximum force values can be seen between reference specimen and crack afflicted specimen. At the same time, however, no clear difference between the LME specimens shown can be detected, although the corroded specimens appear at first glance to be more severely damaged by LME due to the additional interface cracks. The similar force displacement curves are due to the fact that the critical areas under shear stress are weakened to a similar extent in all shown LME specimens. When further comparing the non-corroded to the corroded zinc coated and corroded

CDC specimen no additional difference in the force displacement curves can be observed, indicating no significant influence of the corrosion test cycles on the weld strength of crack afflicted spot welds. The 90° load case (cross-tensile load) is shown in Figure 6-59. Since this load case is a more critical one for spot welds only a slight difference can be seen in maximum force or energy consumption. In contrast to the 0° degree specimens, however, the load carrying capacity here varies between the different LME categories due to the different crack intensity over the areas of the welded joint that are highly stressed under cross-tensile loading. For the reference specimen again no distinction between the tested categories can be made based on their corrosive status. Hence, no impact of the corrosive load on the (crack afflicted) spot welds was observed.

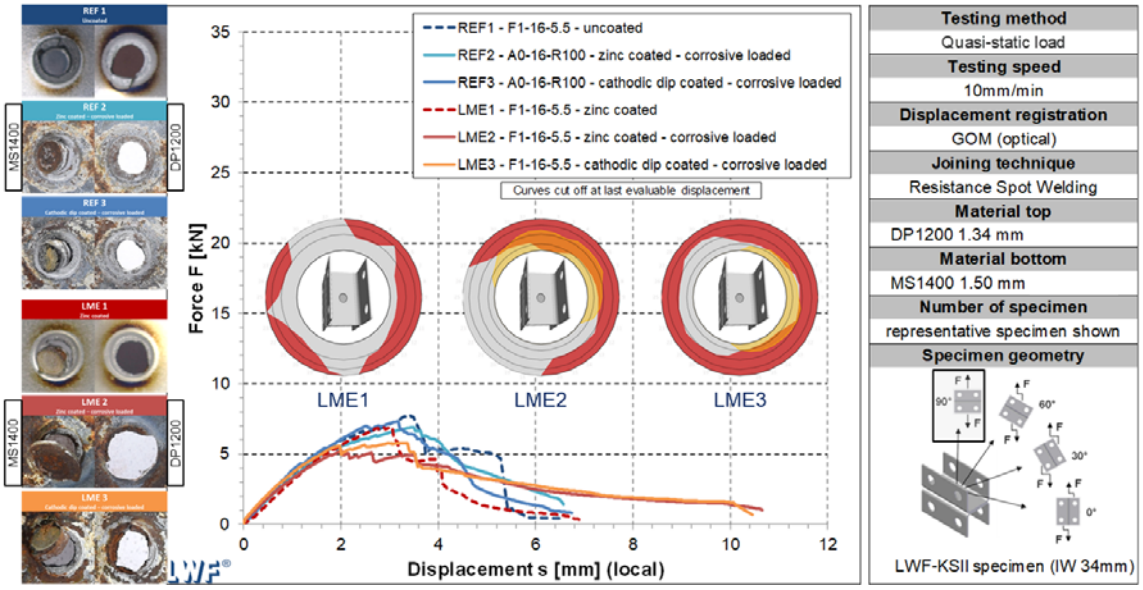


*Figure 6-59: Results for destructive testing of corroded specimen in 90° load case (shear-tensile load).*

## 6.7.6 Hat-profile testing (Quasi-static load)

Hat-profile testing of intensely crack afflicted spot welds was performed. The specimen geometry is described in 4.2.5. The experimental setup is shown in Figure 6-60. A comparison between crack free reference welds and LME afflicted weld was made.

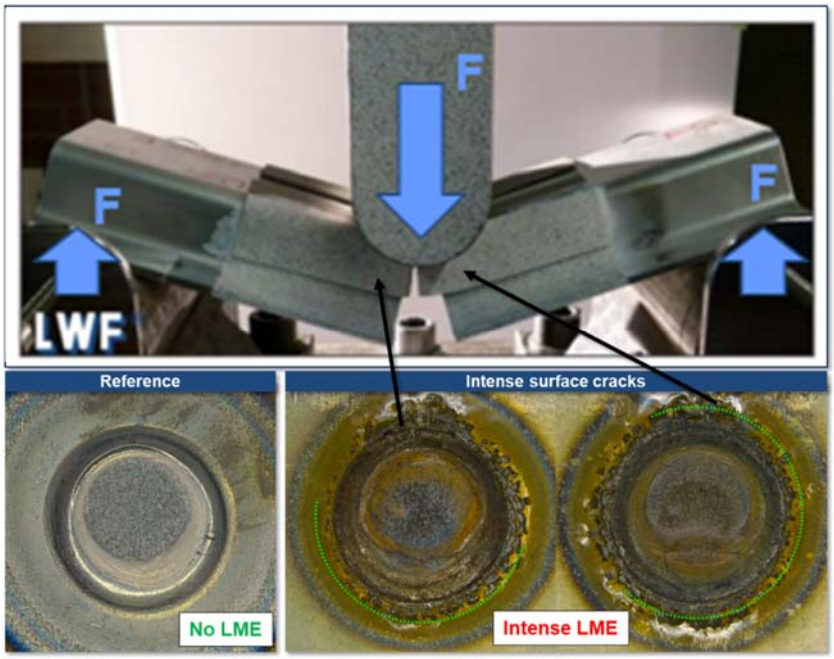


*Figure 6-60: Experimental setup for destructive testing of hat-profiles.*

Exemplary results are provided in Figure 6-61. The bottom two images show the testing process shortly before both specimens fail in the base material between the sheets. The spot welds of the reference specimen are invisibly covered behind the crayon texture applied for the optical measurement system. For the LME specimen the loading of the crack afflicted spots is visible due to the significant deformation at this area. The first drop in the force displacement curve after 20 mm is related to the failure of the first L-profile. The second drop is related to the failure of the second L-profile at 23 – 24 mm. The difference between the exemplary LME und reference curves shown is well within the typical scatter observed during the experiments. While the slightly later failure of the reference specimen leads to a slightly higher energy consumption, the maximum force of the LME specimen surpasses the one of the reference specimens by a few hundred N. Synoptically it can be stated that no influence of the intense LME cracks on the failure behavior or load bearing capacity was observed.

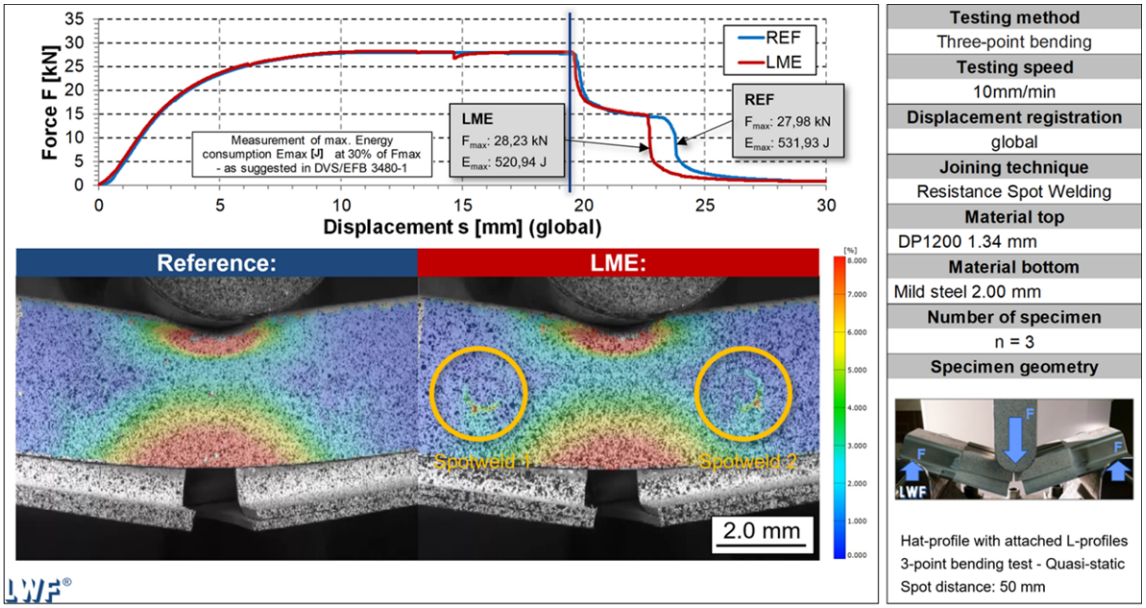


*Figure 6-61: Exemplary results for destructive testing of hat-profiles.*

Summary:

A CT-Scan supported testing of LWF-KSII-specimens afflicted with three crack intensities (light, medium, intense) was performed for two load cases (0° and 90°). Intense cracks (> 50 % sheet thickness) were found to have a significant impact on spot welds performance for quasi-static and crash load, while cyclic load is not significantly affected. During hat-profile tests under quasi-static load no impact of intense cracks was seen. Medium cracks (20 – 50 % sheet thickness) had no impact on spot welds loaded quasi-statically. An impact was seen for crash load in 0° load direction. Light cracks (< 20 % sheet thickness) were not found to have any impact on mechanical joint strength. No impact of / interaction of LME cracks with additional corrosive load was observed.

## 6.8 Virtual tensile testing

The virtual tensile tests were conducted with the aim to show the effect of LME cracks in a reproducible, scatter-free way. At first, a failure criterion was introduced and calibrated against shear-tensile tests. Subsequently, experimental tensile tests were reproduced for the shear-tensile test on LWF-KSII specimen. At first, the resistance spot welding was simulated for the specimen, subsequently, the shear, tensile load

was applied, and failure was predicted via the criterion. The welding is shown in Figure 6-62.

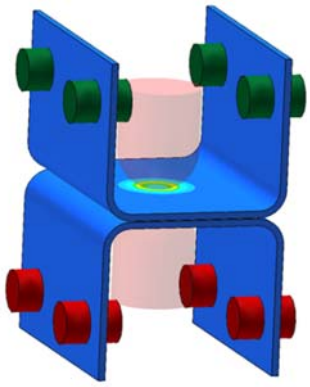

*Figure 6-62: Welding of the KSII specimen for virtual tensile testing.*

Failure criterion

The introduction of a failure criterion is necessary to determine the failure load and –elongation in the simulation model. Without an additional criterion, the model is deformed elasto-plastically until the finite elements are too deformed and the simulation aborts. The failure criterions commonly applied to steel materials rely on the observation that triaxial stresses cause shape change and eventually lead to failure. During the project, the 'Oyane damage criterion' [16] was used in the virtual tensile tests. After welding, all stresses, strains and phases were used as a basis for the tensile tests.

$$\int \left( \frac{\sigma_H}{\sigma_{eq}} + \alpha \right) d\varepsilon = C_{Oyane} \qquad 6\text{-}2$$

$\frac{\sigma_H}{\sigma_{eq}}$: *Triaxiality*
$\alpha$: *Material constant*
$\varepsilon$: *Equivalent strain*
$C_{Oyane}$: *Critical damage value*

The critical damage value needs to be calibrated against experimental tests for each material combination. The calibration was done for a flat spot-welded shear-tensile test at 10 mm/min. The sample is shown in Figure 6-63.

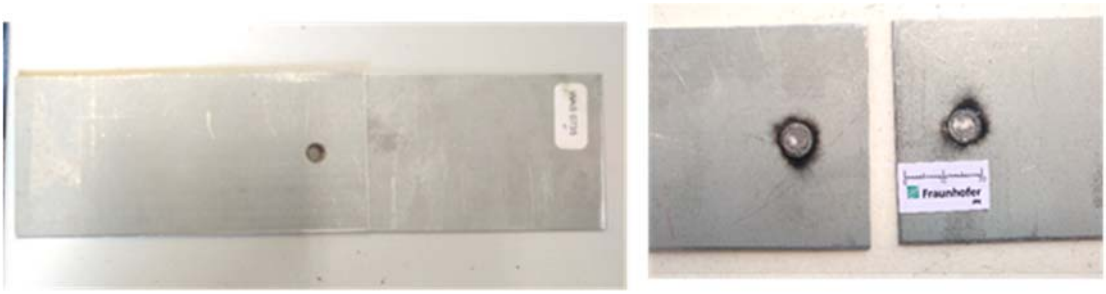

*Figure 6-63: Calibration shear tensile specimen.*

The tensile test was simulated, and the experimental tensile test results are plotted together with the simulated force/displacement curve in Figure 6-64. The simulation is able to reproduce the experimental stiffness well. At the point of failure, the maximum local damage parameter Cmax is determined to be equal to 1.5. In all future investigations, failure will be assumed, whenever the damage parameter C reaches the value of 1.5 at a single location in the model. As per the theory behind the damage criterion, the value of 1.5 leads to local crack formation and subsequent propagation of the crack through the sample.

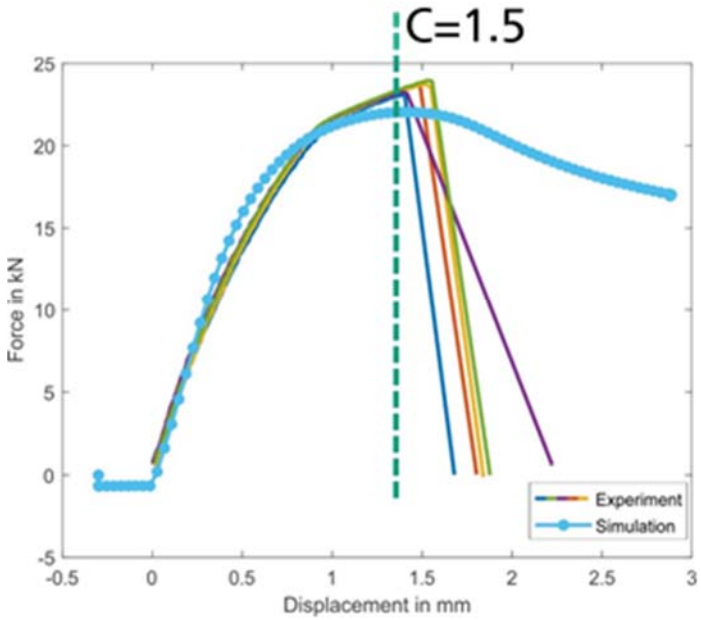


*Figure 6-64: Simulated and experimental force/displacement behavior for a spot welded shear tensile test to determine the critical damage parameter C.*

Virtual tensile test validation

As a validation case, the KSII specimen was welded (as shown in Figure 6-62) and subsequently subjected to a shear-tensile load. As a reference, two crack-free KSII specimen were produced at LWF and subjected to the same load. The resulting force/displacement curves are shown in Figure 6-65. The experimental trials show great scatter, but it is clearly visible that the predicted behavior from the simulation approximates both the sample stiffness and the failure load as well as failure displacement. Hence, the virtual tensile testing method, comprising welding and tensile testing with a failure criterion, is considered to be validated and can be used to study the weakening due to cracks.

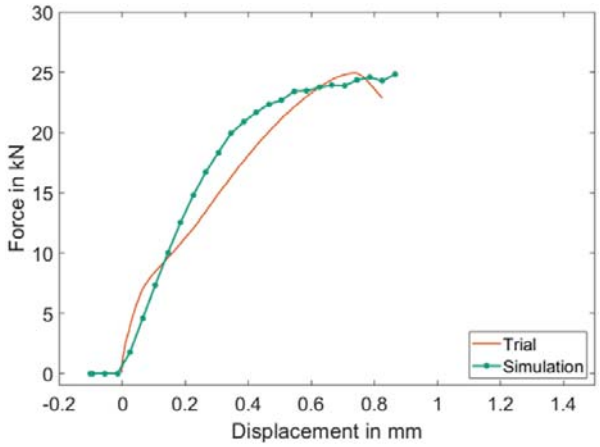


*Figure 6-65: Validation test for the failure criterion on a crack-free KSII specimen under shear-tensile load.*

Virtual tensile test simulations

In order to generate results that are easy to understand and discuss, an artificial crack geometry was established. The exact crack geometry and location can be seen in Figure 6-68: In the right-hand image, the ‘inner’ and ‘shoulder’ crack locations as well as the crack-shapes are shown from a top down perspective in relation to the indentation. Both cracks are located in the direction of the shear-tensile force. All cracks are scaled in three steps in the depth from ‘medium’ (0.54 mm) to ‘large’ (0.8 mm) and ‘severe’ (1.06 mm). The total thickness of the sheet is 1.34 mm. The weakening of the cross-section area is calculated by comparing the total load-bearing

area to what is lost due to the crack. It is supposed to be a simple measure to compare the extent of cracks between samples.

In the top left, the heavy ‘shoulder’ crack is shown in a cross section. It is still within the martensitic zone (red area).

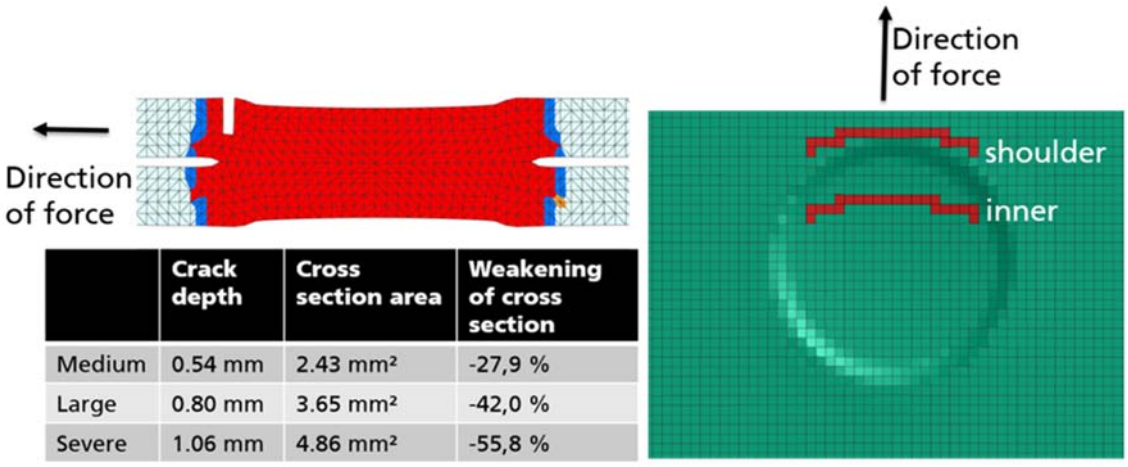


| | Crack depth | Cross section area | Weakening of cross section |
|---|---|---|---|
| Medium | 0.54 mm | 2.43 mm² | -27,9 % |
| Large | 0.80 mm | 3.65 mm² | -42,0 % |
| Severe | 1.06 mm | 4.86 mm² | -55,8 % |

*Figure 6-66: Crack location and crack depths. Two different academic cracks were investigated at the shoulder and inside of the indentation (right). In the cross section (top left) the ‘large’ shoulder crack is visible inside of the martensitic zone (red). The table at the bottom left shows the three crack levels and their respective weakening of the load bearing cross section.*

For the shoulder area, ‘large’ and ‘severe’ cracks were investigated. In Figure 6-67, the point of time, where the failure criterion exceeds 1.5 (i.e. the moment of failure) is shown for the heavy crack. The maximum damage parameter appears at the RSW notch, where the uncracked sample would also fail. No influence of the crack on failure elongation is observed.

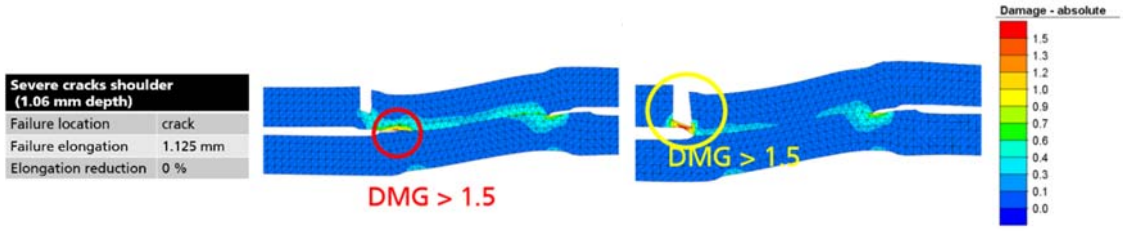


*Figure 6-67: The severe crack at the shoulder (left) leads to no earlier joint failure and The severe crack at the shoulder (right) causes the joint to fail at the crack but the same failure elongation is reached. This is the last ‘tolerable’ crack size.*

The severe crack causes failure at the crack rather than the notch. However, no elongation reduction is observed. As the sample fails at the crack but exhibits the same load-bearing capacity as an uncracked sample, this is still a ‘tolerable’ crack size. The force / displacement behavior of ‘medium’, ‘large’ and ‘severe’ cracks as well as the uncracked reference is depicted in Figure 6-68 for the ‘shoulder’ location. No influence of the cracks on the mechanical performance of the joint is visible and even the severe crack is still tolerable.

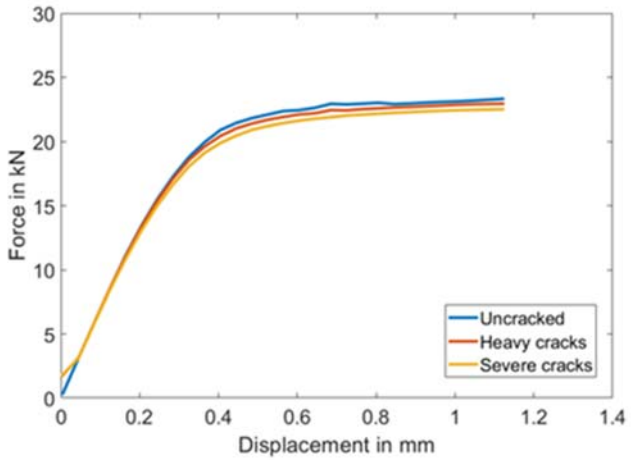


*Figure 6-68: Force displacement behavior of shoulder cracks. No weakening is observed for all investigated cracks.*

For the ‘inner’ crack location, an interaction between the notch and the crack is visible in the damage parameter in Figure 6-69. The failure occurs at the notch but a moderate reduction of the failure elongation of 14 % is observed.

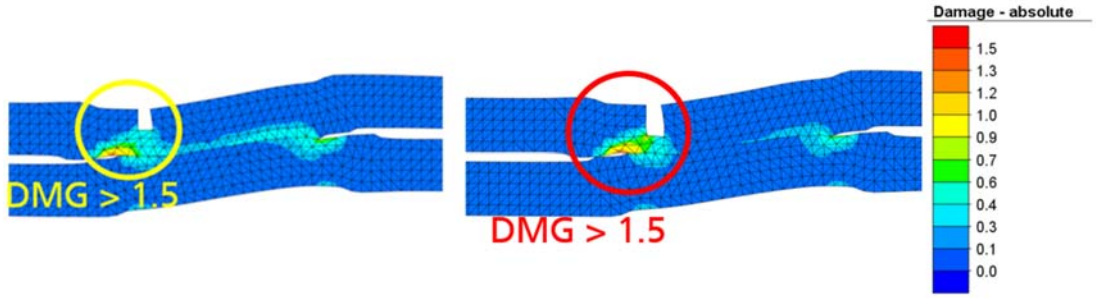


*Figure 6-69: The medium crack in the inner nugget area (left) interacts with the notch and causes slightly earlier failure. The heavy crack in the inner nugget (right) area interacts with the crack and causes earlier failure.*

Scaling up the crack by another 0.2 mm, the large crack reduces the failure elongation significantly by 24.5 %. In Figure 6-69 right, a clear interaction between the notch and the crack is observed, leading to the earlier failure. The force / displacement curve for the ‘inner’ crack location in Figure 6-70 shows the influence of the cracks on the joint performance. With growing crack depth, the failure occurs progressively earlier. In general, the failure load remains unchanged except for the ‘severe’ case, where a slight reduction is observed.

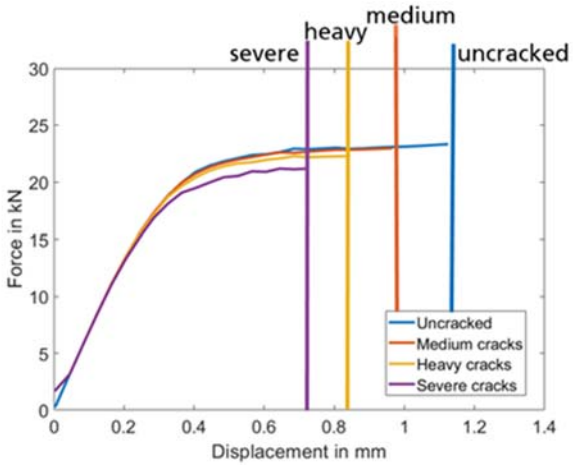


*Figure 6-70: Force/Displacement curve for shear tensile load in the inner nugget area. The introduction of cracks leads to earlier failure and slightly reduced load-bearing capacity.*

Summary

In the virtual tensile tests, a model was established that included spot welding the samples, introducing cracks and judging the sample failure according to the Oyane damage criterion. The model was calibrated against a flat shear tensile test and validated against experimental shear tensile tests on a KSII geometry.

The following conclusions were reached

- The crack location in regard to the RSW notch is very important for the influence of cracks on joint strength
- When the crack is far away from the notch, even ‘severe’ sizes do not lead to a reduction in mechanical performance
- When the crack is close to the notch, the notch-effects can overlap and a negative effect on the joint strength can be seen even for ‘medium’ crack sizes

# 7 References

[1] C. Böhne, G. Meschut, M. Biegler, J. Frei, and M. Rethmeier, “Prevention of liquid metal embrittlement cracks in resistance spot welds by adaption of electrode geometry,” *Science and Technology of Welding and Joining*, vol. 39, no. 4, pp. 1–8, 2019, doi: 10.1080/13621718.2019.1693731.

[2] *Resistance welding — Testing of welds — Peel and chisel testing of resistance spot and projection welds*, ISO 10447:2015, 2015.

[3] C. Schwenk, *FE-Simulation des Schweißverzugs laserstrahlgeschweißter dünner Bleche - Sensitivitätsanalyse durch Variation der Werkstoffkennwerte*. Berlin: BAM-Dissertationsreihe, 2007.

[4] J. Pakkanen, R. Vallant, and M. Kičin, “Experimental investigation and numerical simulation of resistance spot welding for residual stress evaluation of DP1000 steel,” *Weld World*, vol. 60, no. 3, pp. 393–402, 2016, doi: 10.1007/s40194-016-0301-4.

[5] H.-J. Wink and D. Krätschmer, “Charakterisierung und Modellierung des Bruchverhaltens von Punktschweißverbindungen in pressgehärteten Stählen, Teil II,” in *11. LS-DYNA Forum*, 2014.

[6] N. Harlin, T.B. Jones, and J.D. Parker, “Weld growth mechanism of resistance spot welds in zinc coated steel,” *Journal of Materials Processing Technology*, 143-144, pp. 448–453, 2003, doi: 10.1016/S0924-0136(03)00447-3.

[7] S. S. Babu, M. L. Santella, Z. Feng, B. W. Riemer, and J. W. Cohron, “Empirical model of effects of pressure and temperature on electrical contact resistance of metals,” *Science and Technology of Welding and Joining*, vol. 6, no. 3, pp. 126–132, 2013, doi: 10.1179/136217101101538631.

[8] P. Rogeon, P. Carre, J. Costa, G. Sibilia, and G. Saindrenan, “Characterization of electrical contact conditions in spot welding assemblies,” *Journal of Materials Processing Technology*, vol. 195, 1-3, pp. 117–124, 2008, doi: 10.1016/j.jmatprotec.2007.04.127.

[9] *Prüf- und Dokumentationsrichtlinie für die Fügeeignung von Feinblechen aus Stahl - Teil 2: Widerstandspunktschweißen*, SEP 1220-2:2011-08, 2011.

[10] J. Frei, H. Suwala, A. Gumenyuk, and M. Rethmeier, “Bestimmung der Rissanfälligkeit von hochfesten Stählen beim Widerstandspunktschweißen,” *MP*, vol. 58, 7-8, pp. 612–616, 2016, doi: 10.3139/120.110904.

[11] A. R. C. Westwood and M. H. Kamdar, “Concerning liquid metal embrittlement, particularly of zinc monocrystals by mercury,” *Philosophical Magazine*, vol. 8, no. 89, pp. 787–804, 1963, doi: 10.1080/14786436308213836.

[12] C. Béal, “Mechanical behaviour of a new automotive high manganese TWIP steel in the presence of liquid zinc,” Dissertation, INSA de Lyon, 2011.

[13] D. Bhattacharya, “Liquid metal embrittlement during resistance spot welding of Zn-coated high-strength steels,” *Materials Science and Technology*, vol. 34, no. 15, pp. 1809–1829, 2018, doi: 10.1080/02670836.2018.1461595.

[14] Y. G. Kim, I. J. Kim, J. S. Kim, Y. I. Chung, and D. Y. Choi, “Evaluation of Surface Crack in Resistance Spot Welds of Zn-Coated Steel,” *Materials Transactions*, vol. 55, no. 1, pp. 171–175, 2013.

[15] R. Ashiri *et al.,* “Liquid metal embrittlement-free welds of Zn-coated twinning induced plasticity steels,” *Scripta Materialia*, vol. 114, pp. 41–47, 2016, doi: 10.1016/j.scriptamat.2015.11.027.

[16] S. Burget and S. Sommer, “Characterization and modeling of fracture behavior of spot welded joints in hot-stamped ultra-high strength steels,” in *11. LS-DYNA Forum*, 2014.

**Business inspected by :**
INSTITUT DE SOUDURE - YUTZ
Site Assemblages et Matériaux
4 Boulevard Henri Becquerel
57970 YUTZ
FRANCE
03.82.59.13.80

**WORLDAUTOSTEEL**
Avenue de Tervueren, 270
B-1150 Brussels BELGIQUE

# TECHNICAL REPORT

## NDT detection and characterization of LME Cracks in RSW

| | Name | Position | Date | Visa |
|---|---|---|---|---|
| Written by | Fethi DAHMENE | Projects leader | 27/08/2019 | |
| Co-Authored by | Pascal NENNIG | NDT expert | 27/08/2019 | |
| Co-Authored by | Bruno GRZESKOWIAK | NDT expert | 27/08/2019 | |
| Co-Authored by | Eric RIFF | NDT expert | 27/08/2019 | |
| Co-Authored by | Pierre RABAEY | Developer Engineer | 27/08/2019 | |
| Co-Authored by | Mahjoub EL MOUNTASSIR | Developer Engineer | 27/08/2019 | |
| Revised by | Slah YAACOUBI | Operational manager | 06/11/2019 | |

## SUMMARY

This report concerns the detection and characterization of LME cracks in resistance spot welds, either in laboratory or in production conditions. Many non-destructive techniques and systems (10 in total) are investigated. These techniques are different and complementary, with various levels of costs. Some solutions are technically more mature than others, with regard to this specific item. The report provides detailed technical information concerning the experimental findings, the performances of each technique/system and their possible application cost.

**Notes:**

- Information about the material tested in the comprehensive "AHSS Implementation Solutions: Liquid Metal Embrittlement Study" can be found in detail in the LWF/IPK report and at the beginning of this report beginning on Page 11. However, the Specimen numbers referenced through this Institut de Soudure report have not been identified by material type since the main focus of this Non-Destructive Testing portion of the study was to investigate methodology that can identify and characterize LME cracks in the laboratory and in production. Therefore, the value in material is that it must be agnostic, that is, the methodology will potentially work regardless of material.

- This report is a part of the AHSS Implementation Solutions: Liquid Metal Embrittlement study conducted together with LWF and IPK and should be viewed within that study context.

## Acknowledgment

Many people from Institut de Soudure have been involved in this R&D project, in addition to those who appears as authors. Most of them are present in the photo below, which is not exhaustive. Are absent: Pascal Brustolin (mechanical design engineer), Alex Gutshmidt (welding engineer), François Nettange (Material technician), Alexis Chiocca (welding Dr. Eng., moved to ArcelorMittal), Aurélien Robineau (Material Engineer, Technical manager), Antoine Bastien (Manager)


Moreover, the authors are grateful for their partners: University of Paderborn, Fraunhofer IPK, ArcelorMittal, Baomarc, RayScan Technologies, and Tessonics. Several experimental works were carried out in their facilities.

The authors

## SUMMARY

Click to navigate TOC

## 1. Introduction

The members of WorldAutoSteel embarked on a program that specifically studies the conditions under which cracks caused by Liquid Metal Embrittlement (LME), can potentially appear in resistance spot welds (RSW) of zinc-coated advanced high strength steels. This study is a multi-year program 2017 – 2019.

The goals of this project include the following:

- The development of process and joining parameters that act to mitigate the occurrence of liquid metal cracks on high susceptibility materials;
- A confirmation that in-use properties are not affected by the presence of cracks;
- The development of laboratory and production-viable NDT methods that can detect and measure the presence of cracks with high reliability.

To accomplish these goals, WorldAutoSteel selected three contractors:

-**The University of Paderborn, Germany:** to perform the necessary tests of an array of steel grades provided by member companies. The aim is to focus on developing cracks and then optimizing parameters that can mitigate their origin and/or effects.

- **Fraunhofer IPK in Berlin, Germany:** for the simulation tasks.

- **The Institut de Soudure Association** in Yutz**, France:** A specific work package is devoted to Non-Destructive Testing (NDT) able to detect and measure such cracks.

## 2. Objectives

In the NDT work package, there are two main objectives:

- Find a suitable NDT technique (or a set of techniques) for laboratory conditions :
    - In a laboratory context, such techniques may be used for specific studies. For example, a set of spot welds may have to be tested non-destructively to assess the number, depth and extent of cracks created during the welding step, before these welds be tested destructively (strength of fatigue life measurements). In this context, the cycle time can be up to several hours, the sample size is limited to about 20 centimeters (not less if mechanical testing will be performed), and the samples can be tested individually
- Find a suitable NDT technique (or a set of techniques) for automotive serial production application :
    - In an industrial context (car-making), such techniques are to be used for production on-line control on thousands of spot welds. In this context, the cycle time must be strictly limited under a few seconds, the answer expected is probably binary (OK/ NOK) based on pre-defined criteria (like the maximum crack depth or the maximum crack depth at some position in the weld), and it must be carried out on large parts containing hundreds of spot welds
    - An optional consideration should the on-line solution be considered too complex or impractical, is an off-line solution where production panels are tested and then returned for further assembly operations. In this context, the NDT process must still compatible with an industrial environment and the studies performed in real-time, but the requirement for production speeds is removed.

This can imply the use of an existing NDT process, or the development / adaptation of a suitable process.
The following notes complement the above NDT criteria for automotive serial production application:

- The process must be capable of automation (little to no human interaction), and must be scalable, from the research center to an automotive production situation.
- The process must not damage the specimens/car body or components (no removal of zinc, spraying of black color etc.)
- For NDT to be integrated into serial car production, it must adhere to the cycle times (roughly 30s per station) – only for in-line, which surely would be preferred

- The process must be work-safe (e.g. if it uses x-rays, a housing must shield x-rays from human contact)
- Finally, the process must be low cost (affordable)

**Notes:** The word characterization in all ISA presentations and reports means that the NDT method is able to provide all LME crack features including **the depth** (length, opening, location). When the LME crack depth is not estimated by the NDT, the method was classified in the category of detection.

## 3. State-of-the-art

The topic of using NDT to assess the quality of RSW is not new; works were performed many decades ago (early the 60'). Various NDT techniques are used in literature, such as ultrasound, acoustic emission, IR thermography, shearography, acoustic scanning. All techniques are different and might be complementary. The limitations of each technique with regard to the current topic (i.e. cracks in RSW) were underlined in the bibliographic report n°4383-3DXYDF-V1. This was based on the bibliographic texts (articles, patents, standards …) as well as the experience feedback of Institut de Soudure NDT experts (one among them has worked on RSW NDT in the 90's). It is worth noting that the major studied topic is evaluating the **quality** of the weld through the size of the nugget, and minor efforts had been focused on detecting cracks (and more less) sizing it. For the knowledge of the authors, and until the date of writing this report, the literature is empty regarding crack detection in RSW and all NDT results found in this program are somewhat a significant advance to the state of the art.

## 4. NDT Solutions

In total, 6 NDT methods and 4 systems are investigated:

1. Acoustic Emission
2. Magnetic Particle Inspection
3. Eddy Current Pulsed Thermography
4. Eddy Current Array
5. Phased Array
6. Computed Tomography
7. Mini Scanner System (Amstech), which uses ultrasound
8. RoboTom System (Rayscan), which uses Xray
9. RSWA System (Tessonics), which uses ultrasound
10. RIWA System(Tessonics), which uses ultrasound

This deliverable summarizes the main findings.

### 4.1. Acoustic emission testing (AT)

#### 4.1.1. Background

The use of Acoustic Emission (AE) to monitor weld quality has been started long time ago in 1969 by W.D JOLLY [1]. He highlighted the wide-ranging applications of such as submerged-arc welding, gas tungsten-arc welding, brazing and in particular nugget diameter relation for spot welding. He underlined that the real-time nature of AE data sets this technique apart from other nondestructive methods used for inspection. The particularity of this technique is that it can only listen for the energy released by the object, thus only active features (*e.g.* crack initiation, propagation …) are highlighted.

Few years later, the application of AE to test the spot welding is patented [2]. The patented system allows "detecting the AE emanating from a spot weld in which the emission from spot weld nugget formation, weld

expulsion and **post-weld cracking** are separately detected…". No real application deployed since this patent. Few attempts are found in the literature [3] without significant success.

Let us look now at the physical principle of this method. AE, according to ASTM, refers to the generation of transient elastic waves during the rapid release of energy from localized sources within a material. The source of these emissions in metals can be linked to various phenomena such as melting, phase transformation, plastic deformation, cracks initiation and propagation... According to ASTM E751-96 [4], the AE produced during the production of a spot-weld can be related to weld quality parameters such as the strength and size of the nugget, the amount of expulsion, and the amount of cracking.

Acoustic emission covers a wide frequency range, but most often from 50 kHz to 1 MHz. The signal is non-stationary, detected by a piezoelectric transducer (sensor) and often comprises overlapping transients. The signal is represented by its amplitude versus time propagation. The unit of this amplitude is volt, but commonly converted to decibel, and noted dB.

In RSW, the release of energy during welding (online method) creates transient elastic waves that will propagate through the plate and the electrodes. AE is based on the detection and conversion of these elastic waves to electrical signals. This signal is synchronized to the welding time using an electronic device developed by ISA for RSW application (Figure 1). The system starts recording at the beginning of the current flow, which allow focusing on the time window of interest and avoiding extraneous noises. It is important to note that interpretation of data requires high background knowledge combined to strong test experience.

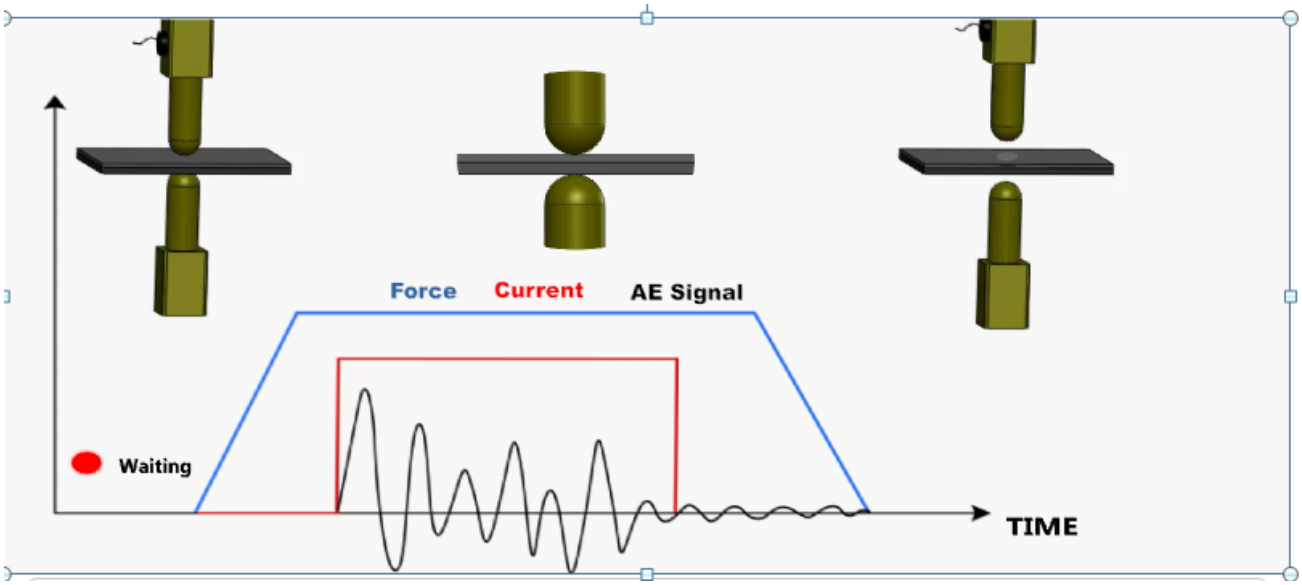


**Figure 1: Typical AE signal recorded during welding.**

### 4.1.2. Methodology & Experiments

A total of five campaign tests have been performed in this research program. Three campaign tests were carried out with the collaboration of LWF in Paderborn. Then, two campaign tests performed at ArcelorMittal Research. The welding process was always carried out by the host team (LWF and ArcelorMittal) and AE investigated by ISA team. The aim of trials with LWF was to explore the ability of AE technique on LME detection. Then, the validation step at industrial environment using new welding setup was investigated at ArcelorMittal. Detail of both setups is explained in paragraph 4.1.2.1.

In order to determine the AE signature of LME and avoid all factors that can modify the signal features, a novel protocol was defined which consists of two steps:

- Calibration step (called also learning step): Monitoring of RSW by AE for the case of healthy state. To be sure that no LME cracks generated in the spot weld, the Zn layer is removed before welding.
- Detection step: Monitoring of RSW by AE using the same welding parameters of the previous step. The presence of Zn layer combined to an extended weld time allows LME cracks generation.

The challenge was to define the damage index (the criterion) which is able to distinguish between the two states (or populations) as illustrated in Figure 2. Each dot of the graph represents the damage index of one spot weld. The greater the gap between the two spots populations, the better will be the detection.

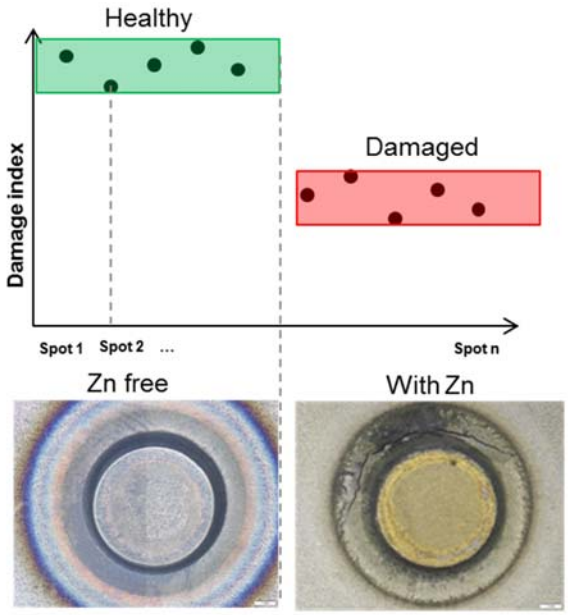


**Figure 2: Generation of LME crack using extended weld time. Healthy spot, Zn removed before welding (left). Damaged spot with LME cracks, Zn layer not removed.**

Different processing methods can be applied: time-analysis, frequency and statistical analysis. Some AE-features are described below:

**Signal Amplitude:** The signal amplitude is defined as the magnitude of the peak voltage of the largest excursion attained by the signal waveform from a single emission event (ASTM E 1316). It is taken as the absolute value of the peak value. Signal amplitude is usually measured in decibels (dBae), to which voltage is converted using the following equation:

$$A = 20\log(V/Vref) \qquad (1)$$

where

A = Amplitude in decibels (dBae),

V = Voltage of peak excursion, and

Vref = Reference voltage=1µV.

**Frequency:** The frequency is the number of cycles per second of the pressure variation in a wave, measured in hertz. An acoustic emission waveform usually consists of several frequency components.

**RMS:** The square root of the average of squared AE signal over a specified period of time), continuously sampled in a defined time interval.

**Shanon Entropy**: The spectral entropy (SE) of a signal is a measure of its spectral power distribution. The concept is based on the Shannon entropy, or information entropy, in information theory. It is widely used as a feature in speech recognition and biomedical signal processing.

**Gliding entropy:** GE is the RMS of Shanon Entropy. This feature was established by ISA (Work of Dr M. El Mountassir) which convert SE (scalar) to GE (vector). It provides precious information of the evolution of SE during the signal time. This parameter can be used to determine LME occurrence.

#### 4.1.2.1. Set-up

- **RSW Machines**

Experiments were conducted with a Bosch Rexroth RSW at LWF and Aro Controls at ArcelorMittal. These machines use electric generation of clamping force with continuous current with a frequency of 1000Hz.

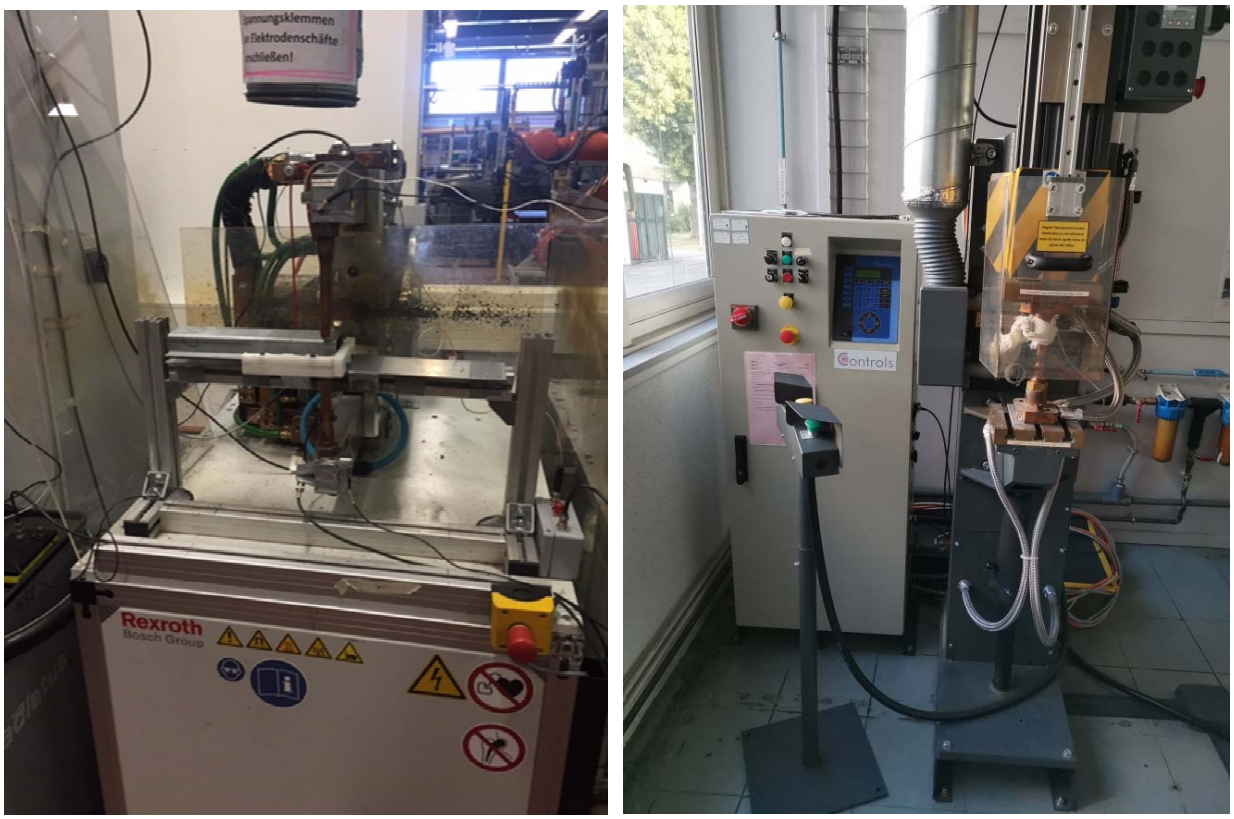


**Figure 3: LWF and ArcelorMittal welding machines. Left LWF, Right ArcelorMittal.**

- **RSW Specimens and welding parameters**

A large database was investigated in this program:

- Various Material combination (MTC) with different sensitivity to LME
- Specimen size and geometry
- Stuck-up : 2 sheets and 3 sheets
- One and multi-spots/specimen

- Welding cycles: one and three pulses during welding time

**Table 1: First AE trials in LWF Paderborn, 17/10/2017.**

| Number of samples | Samples dimensions (mm) | MTC (MPa) | Squeeze, weld, hold time(ms) | Current (kA) | Force (kN) | Zinc layer | Comments |
|---|---|---|---|---|---|---|---|
| **5** | 100*100 | DP1200/Mild300 | 200; 320; 200 | 8.4 | 4 | Yes | Reference 1 |
| **5** | 100*100 | DP1200/ Mild300 | 200; 640; 200 | 8.4 | 4 | Removed before welding | Reference 2 |
| **5** | 100*100 | DP1200/ Mild300 | 200; 640; 200 | 8.4 | 4 | yes | Small Crack |
| **5** | 100*100 | DP1200/ Mild300 | 200; 1280; 200 | 8.4 | 4 | Removed before welding | Reference 3 |
| **5** | 100*100 | DP1200/ Mild300 | 200; 1280; 200 | 8.4 | 4 | yes | Big Crack |

**Table 2: Second AE trials in LWF Paderborn 13-15/02/2018.**

| | Nb of Samples | Samples dimensions (mm) | MTC (MPa) | Squeeze, weld, hold time (ms) | Current (kA) & Force (kN) | Comments |
|---|---|---|---|---|---|---|
| Calibration stage | 5 | 45*45 | DP1200/DP1200 | 200; 1280; 200 | 7.1 & 4 | adjust sampling frequency and frequency bandwidth |
| | 3 | 45*45 | DP1200/DP1200 Zn removed | 200; 1280; 200 | 7.1 & 4 | adjust sampling frequency and frequency bandwidth |
| Refernce samples | 5 | 45*45 | DP1200/DP1200 Zn removed | 200; 1280; 200 | 7.1 & 4 | to be used to quantify the influence of Zn on energy |
| LME enforcement using the same welding parameters | 10 | 45*45 | DP1200/DP1200 | 200; 1280; 200 | 7.1 & 4 | Wearout of electrode |
| after wearout of electrode | 5 | 45*45 | DP1200/DP1200 | 200; 1280; 200 | 7.1 & 4 | Low LME obtained |
| After redressing of electrode | 5 | 45*45 | DP1200/DP1200 Zn removed | 200; 1280; 200 | 7.1 & 4 | reference samples |
| | 10 | 45*45 | DP1200/DP1200 | 200; 1280; 200 | 7.1 & 4 | Low LME obtained |
| Comparison between different MTCs with different sensitivity to LME | 5 | 45*45 | DP1200/ Mild300 Zn removed | 200; 1280; 200 | 7.1 & 4 | reference samples |
| | 5 | 45*45 | DP1200/ Mild300 | 200; 1280; 200 | 7.1 & 4 | High LME level |

| | | | | | | |
|---|---|---|---|---|---|---|
| Comparison between different MTCs with different sensitivity to LME | 5 | 45*45 | DP1000/ Mild300 Zn removed | 200; 1280; 200 | 7.1 & 4 | reference samples |
| | 5 | 45*45 | DP1000/ Mild300 | 200; 1280; 200 | 7.1 & 4 | intermediate LME level |
| Comparison between different MTCs with different sensitivity to LME | 5 | 45*45 | DP1000/ Mild300 Zn removed | 200; 1280; 200 | 7.1 & 4 | reference samples |
| | 5 | 45*45 | DP1000/ Mild300 | 200; 1280; 200 | 7.1 & 4 | Low LME level |

**Table 3: Third AE trials in LWF Paderborn 25/09/2018**

| | Samples dimensions (mm) | MTC | Squeeze, weld, hold time (ms) | Current (kA) & Force (kN) | Comments |
|---|---|---|---|---|---|
| Hat profile n°1 | | DP1200/ Mild300 | 200; 1280; 200 | 8.8 & 4 | 8 spots on the first flange with Zn layer. High level of LME crack expected. Spots 4-5: spatters |
| Change of electrode caps | | | | | |
| Hat profile n°2 | | DP1200/ Mild300 | 200; 1280; 200 | 8.8 & 4 | 7spots on the first flange without Zn layer. Spots 1-2: spatters |
| Decrease of the current | | | | | |
| Hat profile n°3 | | DP1200/ Mild300 | 200; 1280; 200 | 8.7 & 4 | 7spots on the first flange without Zn layer. Spots 1: spatter |
| Hat profile n°2 | | DP1200/ Mild300 | 200; 1280; 200 | 8.7 & 4 | 7spots on the second flange with Zn layer. Spots 1: spatter |
| Hat profile n°3 | | DP1200/ Mild300 | 200; 1280; 200 | 8.7 & 4 | 7spots on the second flange with Zn layer. |
| Worn electrode: 30 welds with weld time =1280ms | | | | | |
| Hat profile n°1 | | DP1200/ Mild300 | 200; 1280; 200 | 8.7 & 4 | 8 spots on the second flange with Zn layer. (spot1 not saved) |

**Table 4: Forth AE trials in ArcelorMittal 07/12/2018**

| | Samples dimensions (mm) | MTC | Squeeze, weld, hold time (ms) | Current (kA) | Comments |
|---|---|---|---|---|---|
| 11 specimens | 50*300 | A1 : AHSS1/MS/AHSS1 | 200; 3*200 (40ms hold time between pulses); 320 | 12.5 & 12 | 10 spots/specimen<br>12.5kA (spot 1-50)<br>12 kA (spot 51-110)<br>High sensitivity to LME |

**Table 5: Fifth AE trials in ArcelorMittal 13/05/2019**

| | Samples dimensions (mm) | MTC | Squeeze, weld, hold time (ms) | Current (kA) | Comments |
|---|---|---|---|---|---|
| 10 specimens | 50*300 | A2 : Same as A1 but Zn removed before welding | 200; 3*200 (40ms hold time between pulses); 320 | 11,1 | 10 spots/ specimen<br>No LME |
| 10 specimens | 50*300 | B : AHSS2/MS/AHSS2 | 200; 3*200 (40ms hold time between pulses); 320 | 12,1 | 10 spots/ specimen<br>Intermediate sensitivity to LME |
| 10 specimens | 50*300 | C : AHSS3/MS/AHSS3 | 200; 3*200 (40ms hold time between pulses); 320 | 12,4 | 10 spots/ specimen<br>Intermediate sensitivity to LME |

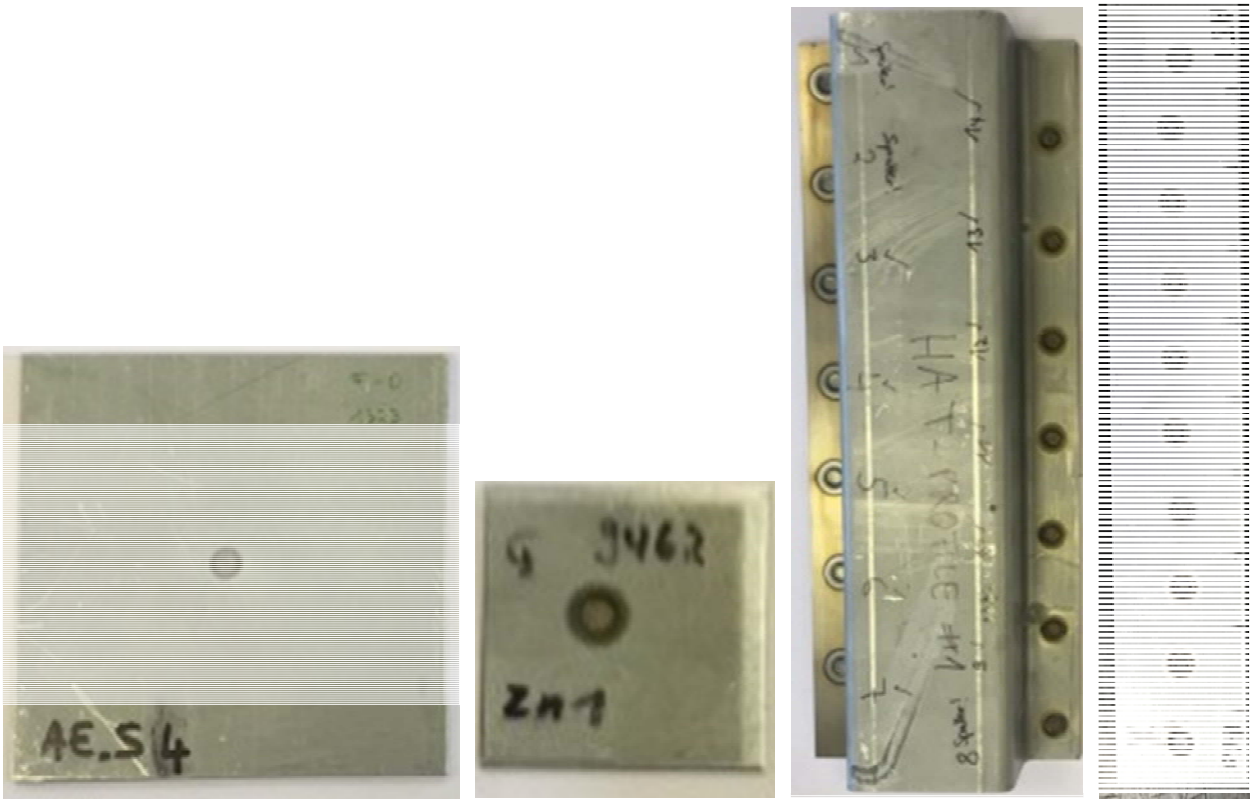


**Figure 4: All specimens used in this program (not scaled).**

- **AE Instrumentation**

The AE instrumentation is composed of four elements:

**1. Sensors:** Glued or fixed with grease couplant (Grease SKF, LGWA2/0.2) to the electrode holder; it converts mechanical vibrations into electrical signal. Sensors provide high impedance signal with low amplitude in a narrow frequency range. In this program, different sensors have been evaluated: R15α, WD, VS375RIC and B1025. The suitable sensor for RSW monitoring is R15α which is resonant at 150 kHz.

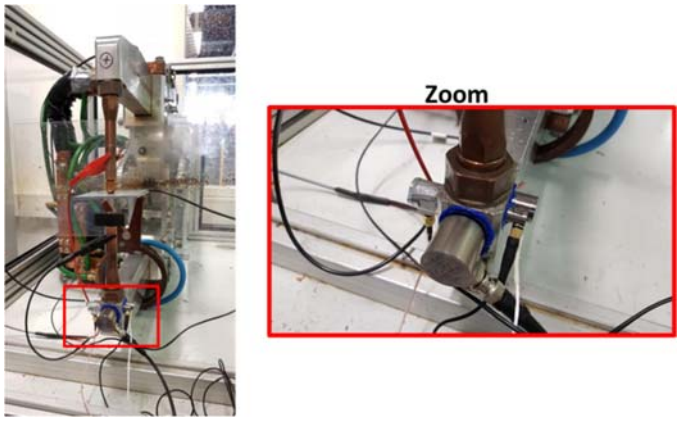


**Figure 5: Sensors position.**

**2. Preamplifier:** It adapts the signal in low impedance, provide a first amplification and filter unwanted frequencies. All measurements presented in this study were obtained with the preamplifier, VALLEN AEP3N with a 34 dB gain and frequency bandwidth 20 kHz-1MHz.


**Figure 6: AEP3N Preamplifier.**

**3. Trigger Device:** This trigger device was specially developed by ISA for this study. It uses Hall Effect sensor which will detect the current initiation and delivers 5V to the AE system providing the timing reference. The triggering of the acquisition is given by this device. Therefore, only the AE signal corresponding to the welding process is captured (Weld time + hold time + lift off).

**Figure 7: Trigger device.**

**4. Multi-channel System:** Vallen AMSY-5 is the digital multi-channel AE measurement system used in this study. It consists of parallel measurement channels and the system front-end software which runs on an external PC. A measurement channel consists of an AE sensor, preamplifier and one channel of an ASIP-2 (dual channel acoustic signal processor). Each channel combines an analogue measurement section and a digital signal processing unit. The complete waveform is recorded by a transient recorder module. For RSW monitoring, only one channel can be used, this will decrease the size of the system and the cost.

**Figure 8: Multi-channel system.**

The system front-end software runs on a PC and controls data acquisition, storage of data. This commercial software is not suitable for RSW data analysis. A new software was specially developed by ISA for this study.

It enables the offline analysis of waveforms by implementing novels signal processing methods. It is important to note that this module can be implemented to the commercial software for real-time analysis during RSW monitoring.

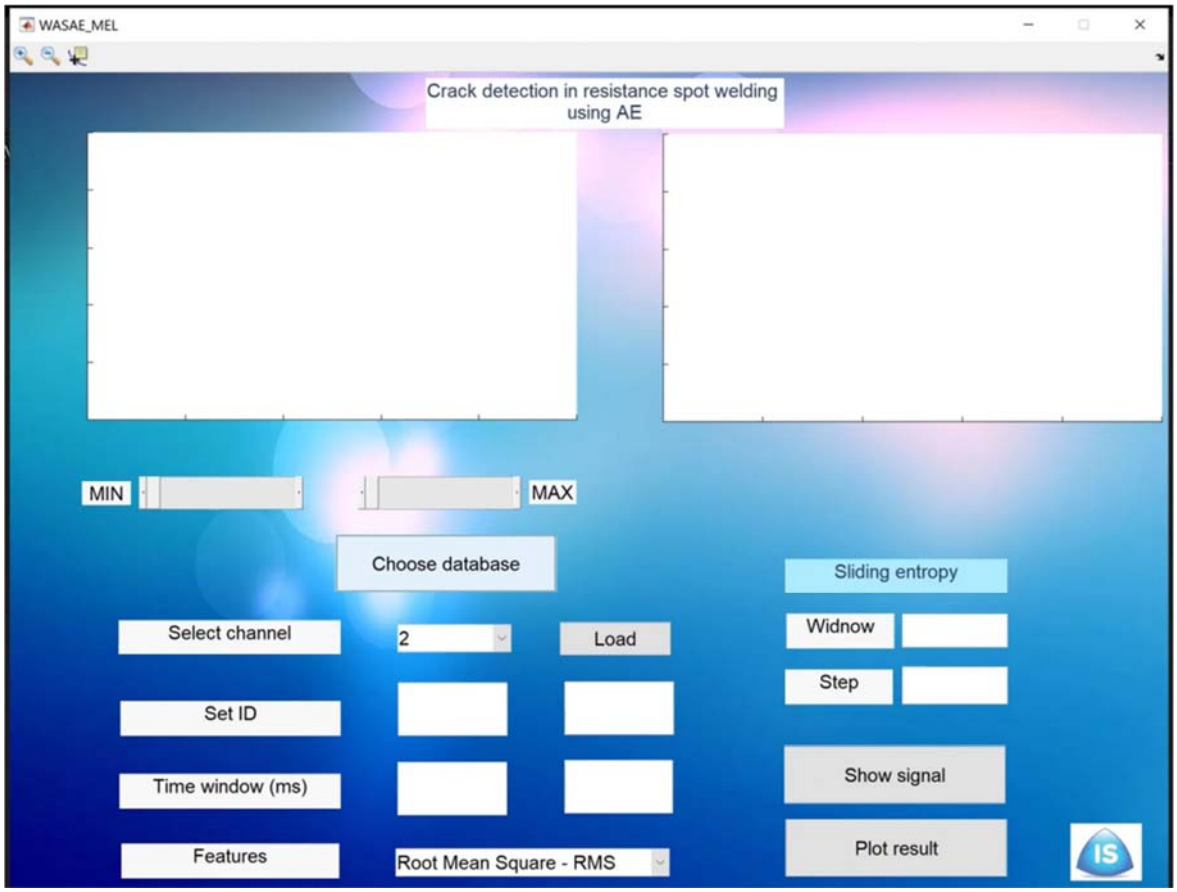


**Figure 9: AE Software developed by ISA for RSW monitoring.**

### 4.1.3. Results & discussions

The resistance spot welding process consists of different phases: the set-down of the electrodes, the squeeze, the current flow, the hold time or forging, and the lift off. The AE signal is triggered at the initiation of current flow. Therefore, phases covered by the AE signal are weld time, hold time and the lift off. These phases can be easily identified by observing the AE signal (Figure 10-a, b).

The particularity of the AE signal is the continuous character and also the absence of exploitable variation using standard signal processing methods, such as temporal (amplitude, duration, energy, Rise time…) and frequency analysis. The energy provided by the welding process is very high which complicates the research of LME crack features. Indeed, during weld time, a recurring signal with a period of 1000µs is observed in Figure 10-c which is linked to the frequency of the current (1000Hz). All these factors make the identification/detection of LME signature a very challenging task.

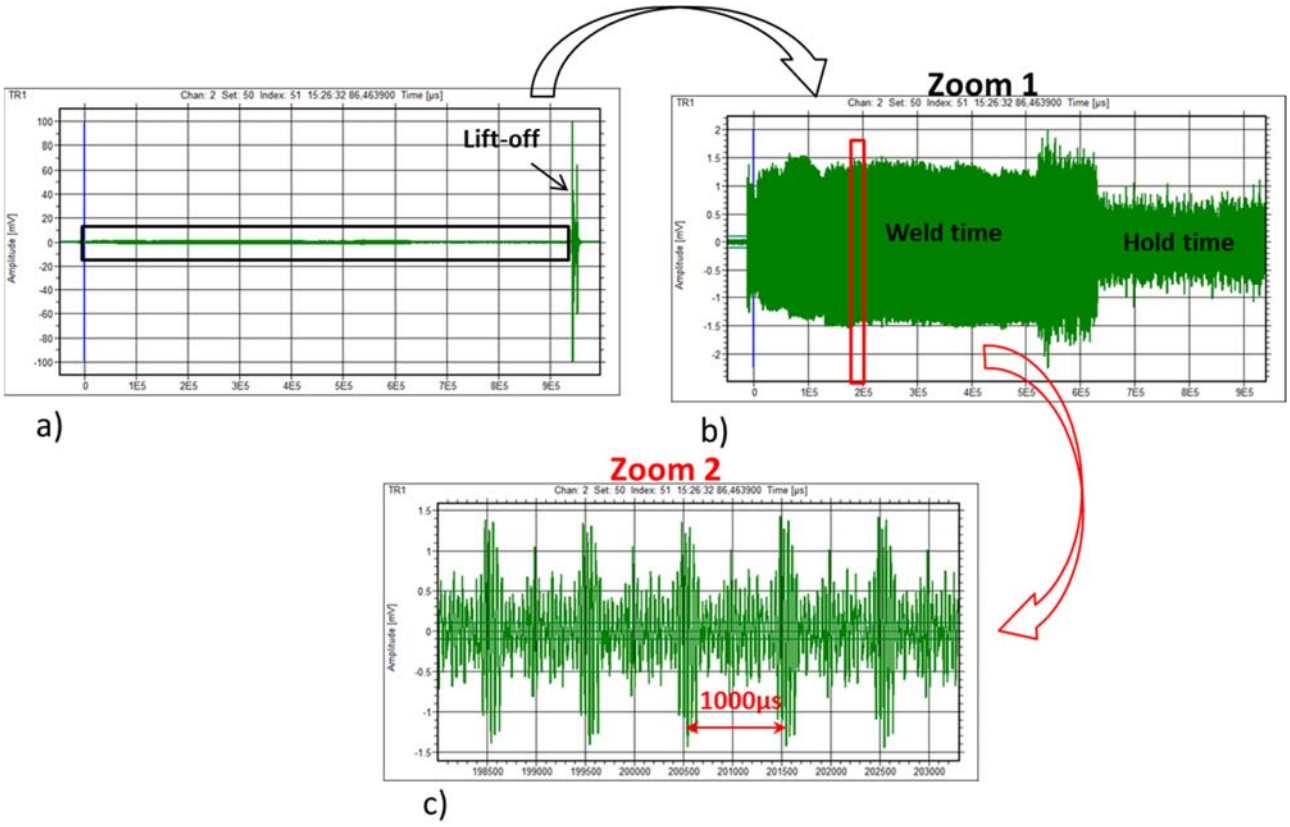


**Figure 10: Example of AE signal from the first campaign test: Weld time =640ms. a) Original signal detected with WD sensor. b) Zoom 1 of the weld time+ hold time signals. c) Zoom 2, which shows repetitive signals due to current flow.**

The first investigation was carried out by comparing AE waveforms for two cases (Table 1):

- Extended weld time= 1280ms, Zn removed before welding: Healthy state
- Extended weld time= 1280ms, with Zn: Damaged state with LME cracks

For each spot, the AE waveform (signal) is extracted and some features explored (RMS, standard deviation, Kurtosis, skewness, crest factor). Despite the fact that AE signals are noisy by the current flow, it has been found that the Root mean square (RMS) parameter which represents the mean energy of the signal is able to distinguish between healthy and damaged states. It is worth noting that AE waveform energy of the cracked RSW is lower compared to healthy RSW (Figure 11).

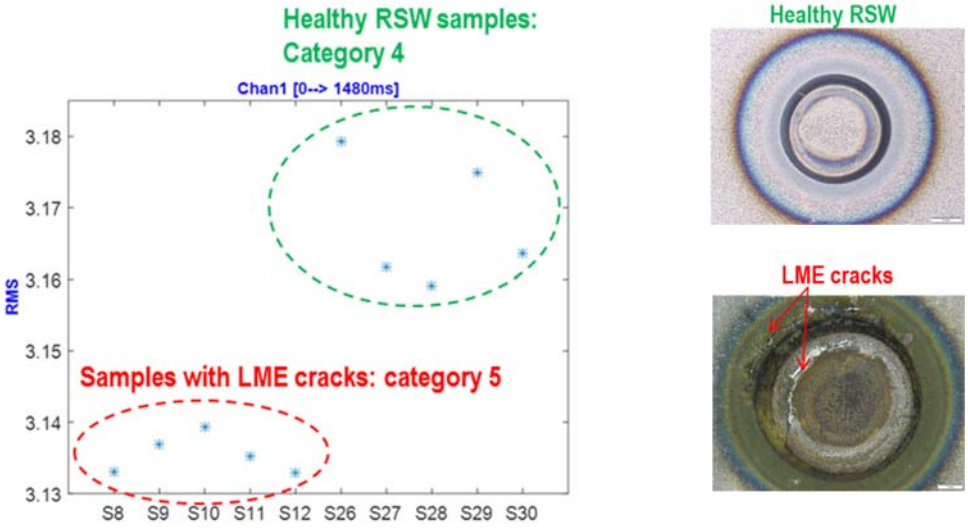


**Figure 11: RMS vs samples.**

This energy decrease is not linked to the presence of Zn coating but to the LME crack. According to the Joule rule, for the heat input occurring between electrodes at an electric resistance Q (calorie)=$I^2Rt$, the generated heat appears as a function of the current intensity (I), the resistance of the materials (R), and the time (t). For similar welding parameters (I, t), a higher heat input is generated for uncoated samples than for galvanized-coated samples, which results in a larger melting area and thus an extension in nugget diameter. More AE energy is then expected for the case of uncoated samples. This result has been verified by AE using uncoated and coated samples at a short weld time (320ms) to avoid LME crack generation. It has been found that energy of AE signals is slightly higher in the case of uncoated samples. The decrease of energy due to LME cracks could be explained by the energy dissipation during the crack creation or also the attenuation of waves induced by a discontinuous medium.

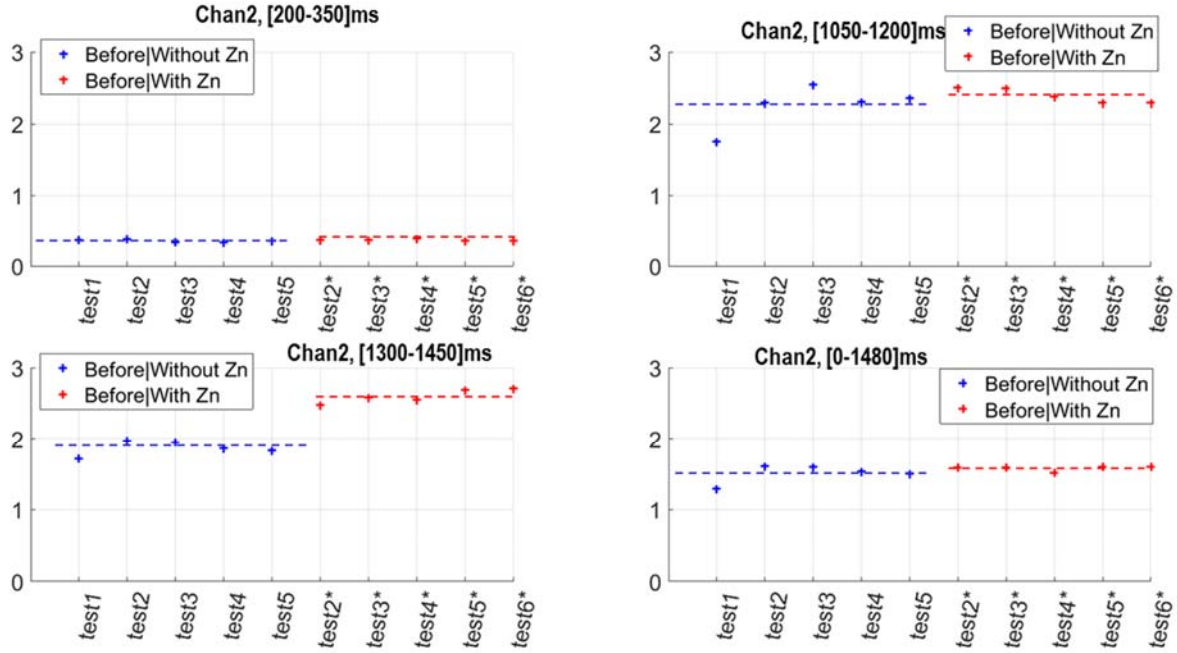


**Figure 12: Influence of Zn coating on AE energy.**

In some cases, it could be very difficult to detect LME cracks using simple feature extraction as proposed earlier. This is because; the LME signature in the AE signal is generally very small. Hence, if the reference signals amplitudes changed due to some variation in the welding parameters or in the environmental conditions, the feature extraction method would fail in detecting LME cracks and could generate false alarms. To deal with this issue, another method for detection of LME cracks is proposed. It consists in estimating the error between AE signals and a baseline signal (healthy state). It is based on the hypothesis that the reference signals contain sufficient information of the operational conditions (i.e. welding parameters). A comparison between the residual error of a healthy state signal and the current signal is necessary. A damaged state signal will be characterized by high residual error compared to that of a healthy state signal. The calculation of the residual error of a given signal is based on the Least Squares Method. Mathematically, it can be expressed as follows:

$$\widehat{\boldsymbol{\theta}} = \arg\min_{\boldsymbol{\theta}} \left(\mathrm{J}(\boldsymbol{\theta}) = \|C\boldsymbol{\theta} - \boldsymbol{x}\|_2^2\right) \qquad (2)$$

Where $C$ is the matrix of reference signals, $\boldsymbol{x}$ is the measured signal and $\boldsymbol{\theta}$ is the regression coefficients. $\mathrm{J}(\widehat{\boldsymbol{\theta}})$ is the residual error that will be used as damage indicator.
The solution of the minimization problem described in equation (1) is given by:

$$\widehat{\boldsymbol{\theta}} = \frac{C^T \boldsymbol{x}}{C^T C} \qquad (3)$$

The optimal regression coefficients $\widehat{\boldsymbol{\theta}}$ provide an estimation of the current signal using all the reference signals. In other words, if the current signal is from a healthy state, it will be well estimated by the reference signals. In this case, the residual error will be very low compared to the case where the signal contains LME cracks signatures.

The Least Squares Method was applied to the database of Table 1, which can be divided in five categories:

- Category 1: Healthy state, WT= 320ms; with Zn:
- Category 2: Healthy state, WT=640ms; Uncoated samples
- Category 3: Damaged state (with low LME cracks), WT=640ms; Coated samples with Zn
- Category 4: Healthy state, WT=1280ms; Uncoated samples
- Category 5: Damaged state (with high LME cracks), WT=1280ms; Coated samples with Zn

Baseline of healthy state is composed of spots from categories 1 and 4. A total of 10 spots are used to build the matrix of reference signals $C$. Then, other categories (2, 3, 5) were used for validation of the healthy state model explained previously.

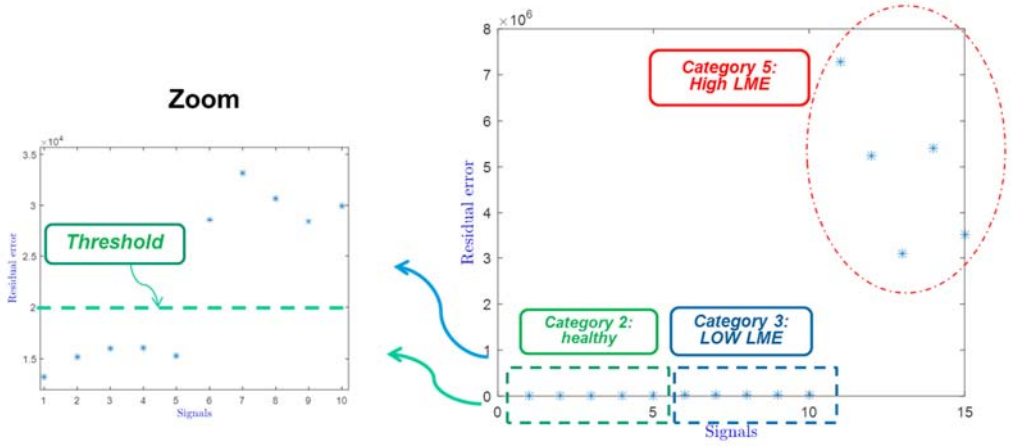


**Figure 13: Residual error $\mathrm{J}(\theta)$ calculated for three different categories.**

The result shows that the damaged state of category 5 can be clearly discriminated from healthy state of category 2. However, the category 3 state is not far from the healthy state. This is probably due to the nature of damage

with corresponds to a small crack. To ensure automatic damage detection, a threshold must be defined on the error of estimation for the healthy signals. This can be done firstly by considering a statistical distribution of the estimation errors that was found. After that, the threshold can be chosen by fixing a confidence limit of the statistical distribution.

It has to be noted that the healthy specimens illustrated in Table 1 contain different welding time. Thus, it is interesting to compare the signals from damaged specimen with same welding time as the healthy ones. For that purpose, the category 5 was compared with category 4 and category 3 with category 2. Indeed, the healthy state model has to be built over a representative database, but in this case the group of healthy specimen signals was divided into two sets: learning set and validation set. The results are presented in Figure 14. These results show that LME samples can be clearly identified from healthy ones with a significant gap.

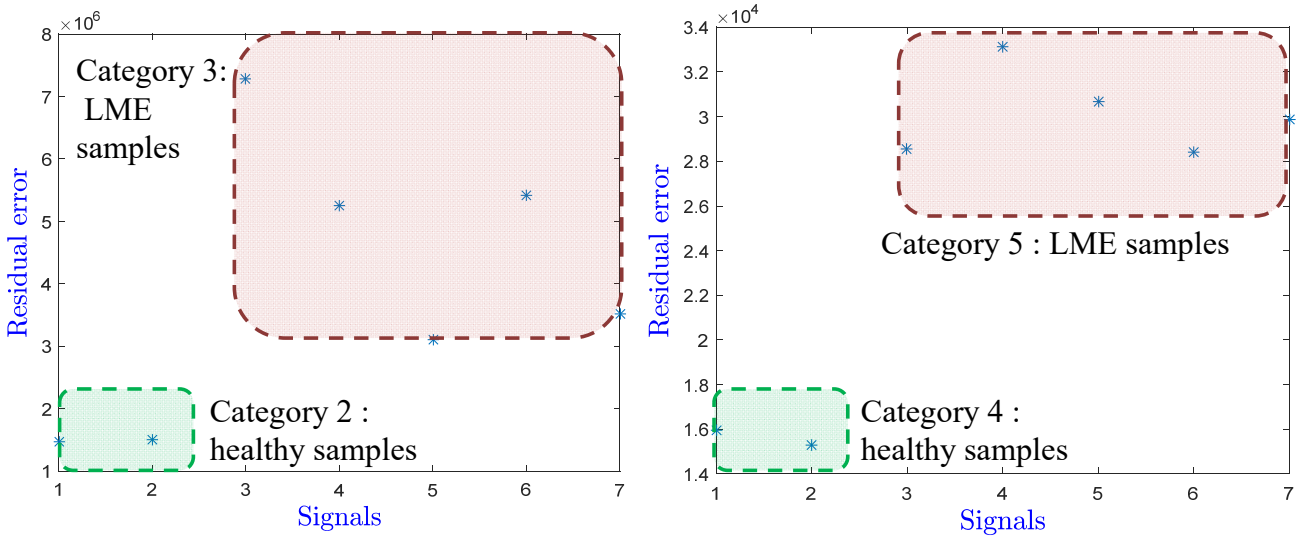


**Figure 14 : Detection of LME samples when using signals with the same welding time, (right: categories 5 and 4, left: categories 3 and 2).**

As discussed earlier, the quality of AE signals of the first campaign test (Table 1) can be improved. The high sampling frequency used (1MHz) combined to a large frequency range of the ASIP-2 filter (20-850 kHz) was not in our favor and highlighted unfortunately the current frequency (1000Hz).

The time-frequency behavior of the continuous signal calculated with wavelet transform (WT) is given in the Figure 15. Red color corresponds to the highest magnitude of the WT and pink to the smallest or zero-magnitude region. It is clearly shown that the maximum frequency of the AE waveform induced by the current flow is around 30 kHz. In order to improve the signal quality in particular during the weld time, continuous AE signals induced by current flow can be filtered using an analogic filter.

Since, various improvements have been applied to reduce this continuous character and enhance the signal quality. The solution was to reduce the sampling frequency to 700 kHz and the filtering frequency to 50-350 kHz.

Detection of LME crack has been also investigated in the case of smaller samples 45*45mm for different materials combinations. Four MTC's with different sensitivity to LME were tested (Table 2):

- DP1200 / Mild Steel
- DP1000 / Mild Steel
- DP1200 / DP1200
- DP1000 / Mild Steel

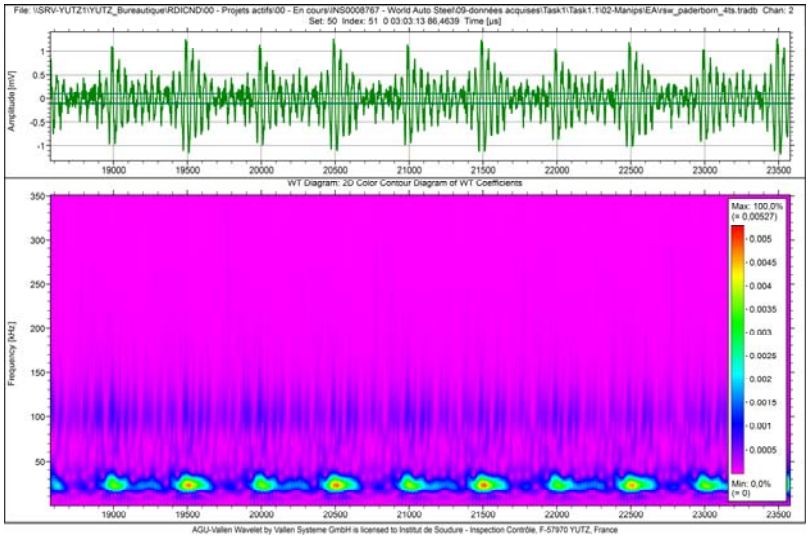

**Figure 15: Zoom of the AE waveform induced by current flow (upper graph) and its wavelet transform (lower graph)**

It is important to note that for each MTC, a calibration step is needed to determine the AE signature of a healthy state. The AE signature is mainly related to the steel microstructure and is different from one MTC to another. A good success rate of LME detection is obtained. For 80 spots controlled, only one misclassification is noted for MTC DP1200/DP1200. For this MTC, the LME crack level is low (barely visible with optical microscope). For the case of MTC DP1000/MILD300, sensors placed in the lower and upper electrode holder were not able to detect LME crack. However, the detection was ensured by the sensor placed directly on the sheet.

**Table 6: LME detection by AE of small samples (45mm*45mm)**

| LME detection using Acoustic Emission | Typical LME crack level |
|---|---|
| **MTC: DP1200/MILD300** | |
| 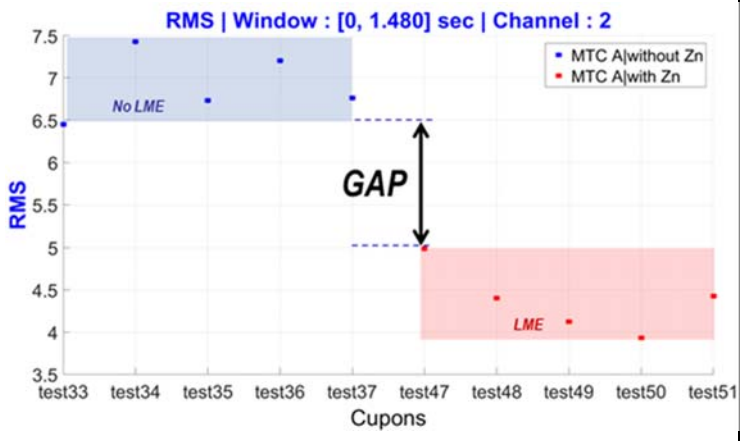 | 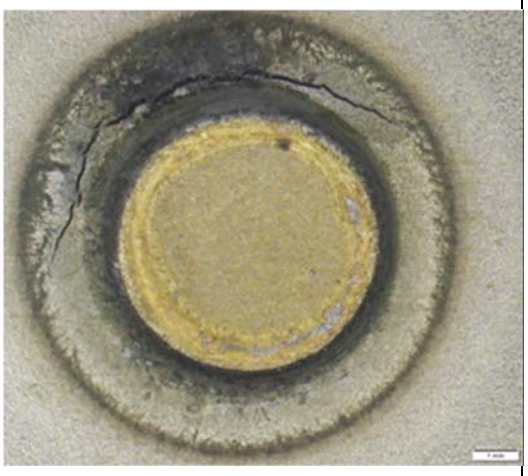 |
| **MTC: DP1000/MILD300** | |

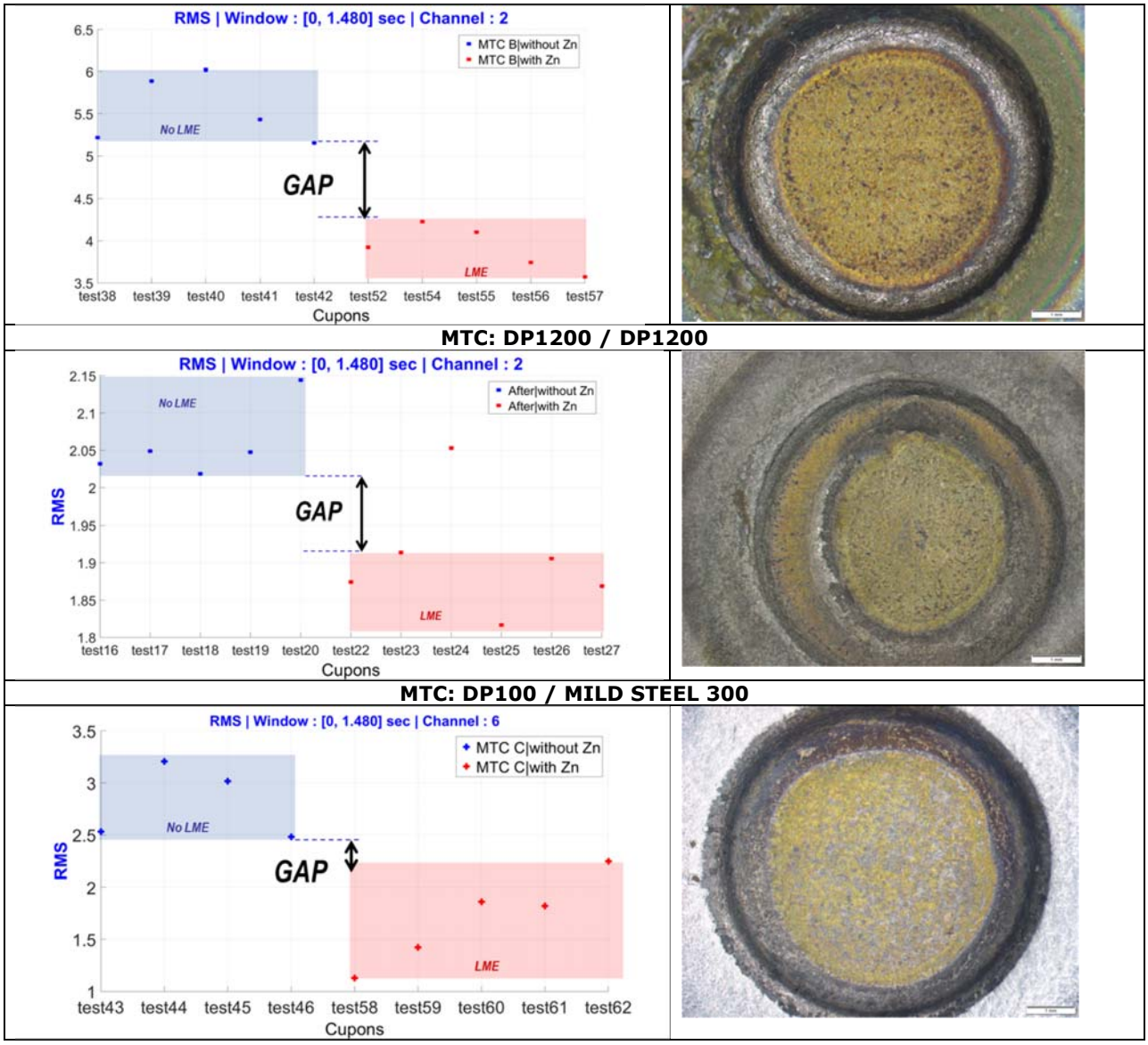


The case of multi-spots per sample is also investigated in this program. Closed hat profile geometry was proposed by the core team during April meeting 2018 in Amsterdam. This geometry was proposed to verify the LME crack detection in a large structure in presence of multiple spots. MTC is DP1200 for hat profile and Mild Steel as closer. The LME detection by AE is successful. For 23 spots controlled, only one is misclassified. Confidence index is high than 95% which is promising. This is true when a supervised classification is performed which mean that an *a priori* is known about the presence or not of LME crack. In our case, the use of extended weld time for galvanized samples promoted the LME crack generation. Their presence was also verified with optical microscope. In the other side, extend weld time for uncoated samples were not sufficient to generate LME crack. The comparison between the two states enabled as to determine the AE criteria suitable for LME crack detection (Figure 17). The time window used for criteria calculation is a determinant parameter and can vary with sample geometry and materials. The understanding of time occurrence and propagation of LME during welding will help to identify the time window of interest and therefore enhance LME detection. Unfortunately, currently, no method is able to provide this information. According to ISA experience, three-time windows can be relevant.

- All the AE signal explored i.e., Weld time and hold time.

- Only the last part of weld time i.e., the last 150ms
- Only the hold time

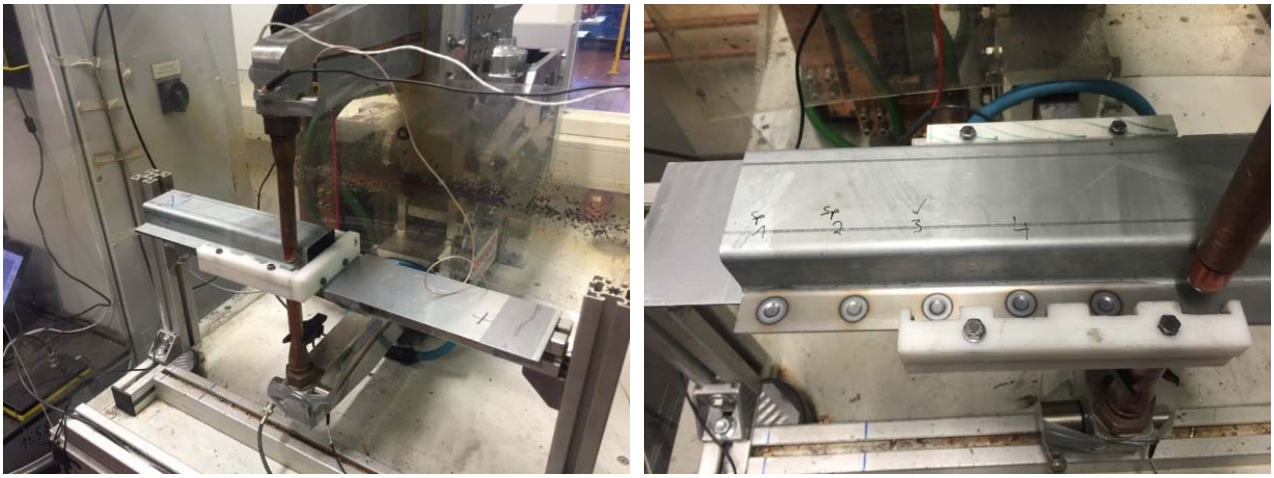

Figure 16: AE monitoring of closed hat profile.

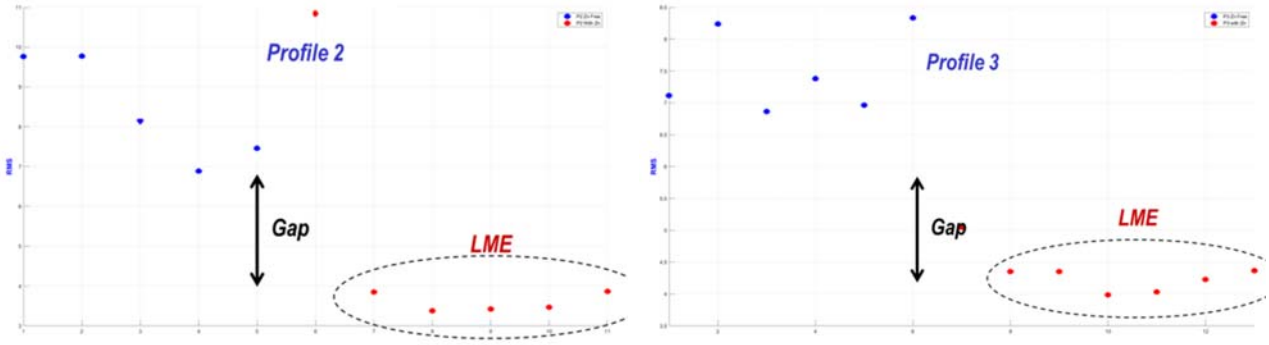


Figure 17: LME detection by AE for closed hat profile samples.

To get more information about LME occurrence, a new analysis approach was developed by ISA for RSW application. In this approach the RMS of the entropy is calculated over the time signal with a gliding step. For each spot, a vector of sliding entropy is calculated. This offers another presentation option, a two-dimensional presentation of data displayed as a top or planar view, where color represents the gated sliding entropy amplitude at each window. An image of cartography is then displayed with spots in X axis and magnitude of sliding entropy in Y axis. The analysis became very easy even visually. Spots from the same family will have similar color cartography. In the Figure 18, the left part of the image represents healthy spots from spot n°1 to spot n°6. One can note a similar color distribution of the healthy state. This can be considered as a signature of healthy state characteristic of weld time and hold time. The idea was to compare this signature to spots with LME cracks. Damaged spots with LME cracks are spots from n°7 to spot n°13. No need of an expert to detect the glaring difference between the two states. Furthermore, the time window at which a clear difference appears could be related to the LME occurrence time. For the example of Figure 18, it can be assumed that, for an extend weld time (1280 ms), the crack initiation begins at 1000 ms and continue propagating during the hold time.

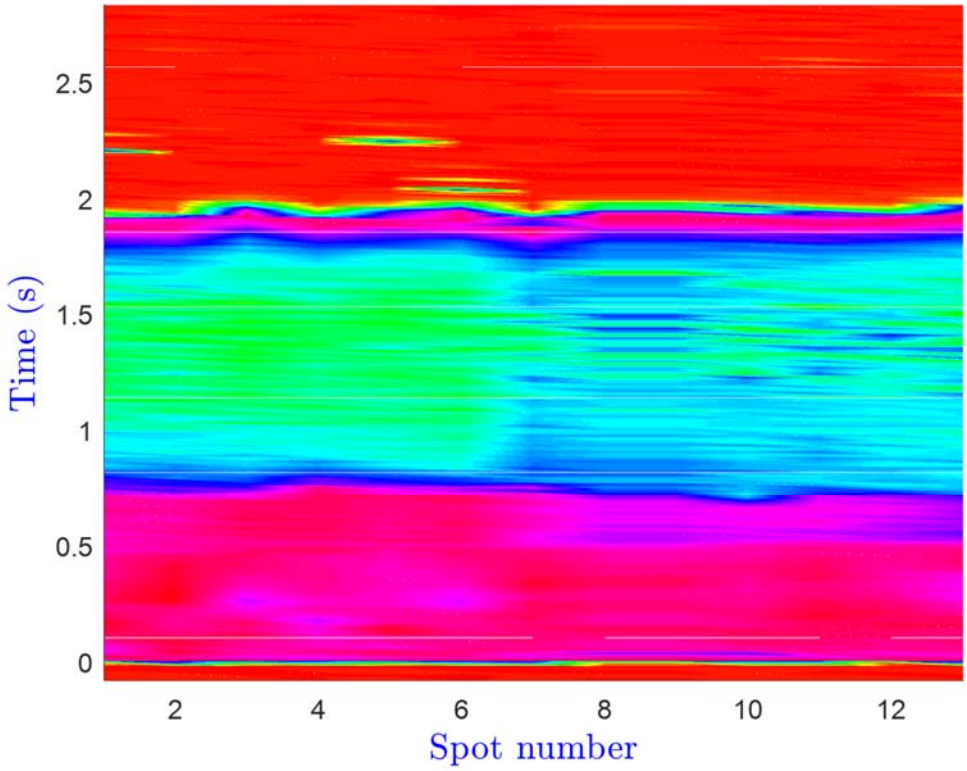


**Figure 18: Sliding entropy vs spot number (spot 1-6: healthy; spot 7-13: with LME)**

The conclusion that can be drawn at this stage is that AE is relevant for LME crack detection in laboratory condition using continuous electric spot welding machine of LWF. Results have been proven for the following conditions:

- Different specimen geometry and dimensions
  - Specimens (100*100mm): point spot /specimen
  - Specimens (45*45mm): point spot /specimen
  - Hat profile specimens (300*150mm): 16 spots /specimen
- Validation on more than 100 spots,
- Four MTC investigated

A calibration step is required for each MTC and welding parameters (F, I). Welding with worn electrode can also affect AE signals. It has been found that AE signal features changes after 44 spots performed at extreme welding conditions (Weld time=1280ms). This number can be significantly increased using « normal » welding conditions and should be taken into account for AE criteria development.

Furthermore, the main advantage of AE is that it is the unique method able to provide precious information on LME occurrence stage which can be very helpful for materials development

The question that will come to your mind now is “how about the detection in another environment closer to industrial conditions”.

To answer to this question, trials have been performed with the collaboration of ArcelorMittal. Various changes can be noticed compared to LWF, presented in the following table.

**Table 7: Difference between LWF and AM trials.**

| | Paderborn University, LWF | ArcelorMittal (ISO18278-3 ) |
|---|---|---|
| **Cadence** | Low | High |
| **Weld time** | 1280 ms | 200ms * 3 |
| **Number of pulses** | 1 | 3 |
| **Hold time** | 200ms | 3*40ms + 320ms |
| **Material** | DP1000, DP1200 / mild steel | AHSS/MS/AHSS (confidential) |
| **Number of layers (i.e. sheets)** | 2 | 3 |
| **Welding parameters (such as current magnitude, force, …)** | 8 kA | 12.5 and 12.0 kA |
| **Welding machine** | Bosch Rexroth | Aro Controls |
| **Electrode size and shape** | Electrode caps F1-16-5,5 | NA |
| **Specimen dimensions** | 100*100 ; 45*45; hate profile (300*150) | 50 * 300 |
| **Specimen thickness** | 1.4 ; 2 | NA |

Table 4 and Table 5, three type of MTC have been investigated. A total of 410 spots were monitored by AE.

- ✓ MTC A1: Galvanized specimens, 110 spots: High sensitivity to LME
- ✓ MTC A2: The same as MTC A but uncoated: reference state: 100 spots
- ✓ MTC B: Galvanized specimens, 100 spots: Intermediate sensitivity to LME
- ✓ MTC C: Galvanized specimens, 100 spots: Low sensitivity to LME expected

Despite a shake-up of welding conditions, The AE signal quality was satisfying with a high signal to noise ratio. The experience gained from previous trials allowed the definition of the acquisition setup. Perturbations linked to current flow and oversampling were solved. A typical AE signal of a spot weld is presented in Figure 19.

All welding phases can be clearly distinguished:

- The three pulses of weld time and three hold time in between
- The hold time
- The lift off of electrodes

The comparison between MTC A1 and MTC A2 using RMS criterion will depend on the time window of the AE signal. As explained before, the choice of time window for RMS calculation depends on MTC and is determinant for a good classification. To avoid this selection, the Entropy was used as a damage index. This parameter is more relevant for LME detection by considering the entire AE signal. The damage index in Figure 20 shows a clear difference between healthy and damaged states. A threshold can be then established for LME detection. All spots of MTC A2 were controlled with Dye penetrant method by ArcelorMittal and crack LME was found for all spots. It has been proven that AE is relevant for LME detection.

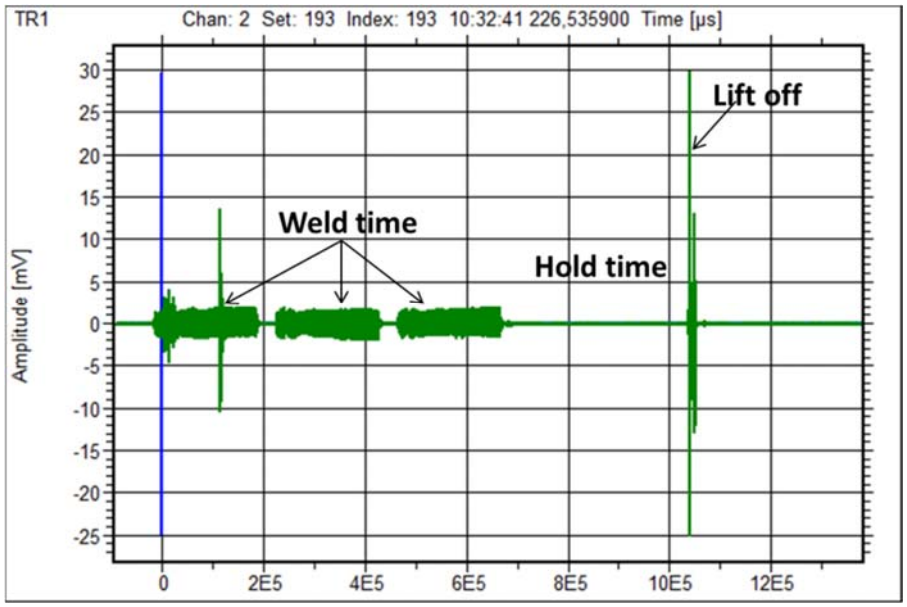


**Figure 19: Typical AE signal for spot weld (ArcelorMittal trials).**

For MTC B and MTC C, blind LME detection without a calibration step is not possible at this stage of the program. The ability of AE to predict LME depth and identify most critical cracks has been assessed. Two spots per specimen were selected by Dye penetrant method and then cross sectioned for depth measurement. Afterwards, Damage index was correlated to LME depth but unfortunately, no correlation found. Therefore, selection of the most critical LME with AE is not possible at this stage of the program.

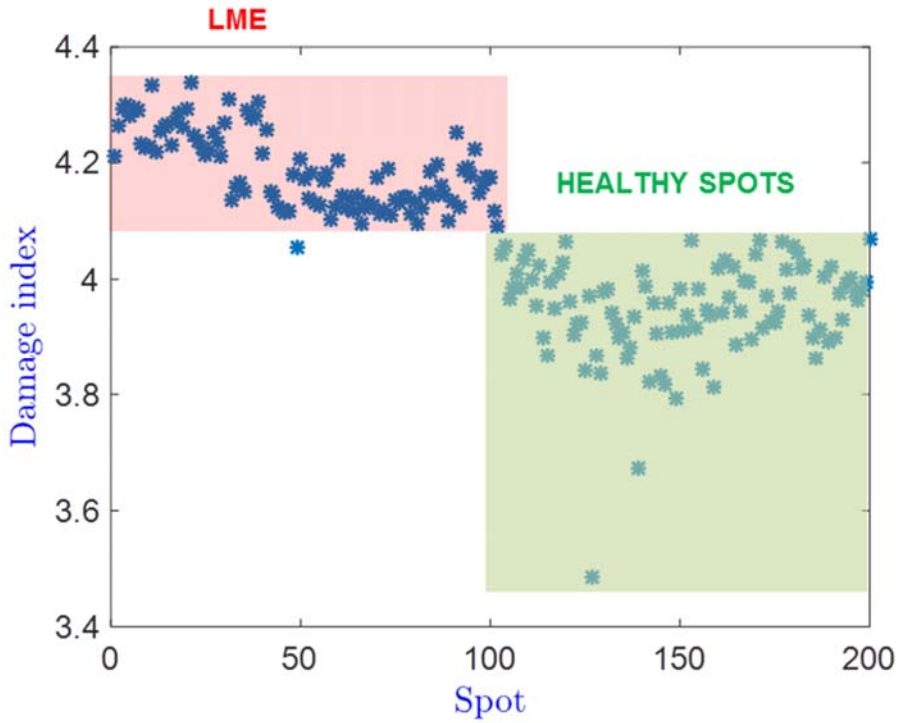


**Figure 20: Comparison between MTC A1 (Healthy) and MTC A2 (with LME).**

It is important to note that spattering during welding is well detected by AE. High amplitude appears often at the end of the weld time (end of the second and third pulse). Blind identification of spots with spatter can be helpful in some cases (high cadency, automatic process without operator) and classification can be automated. Below some examples of spots with spatters.

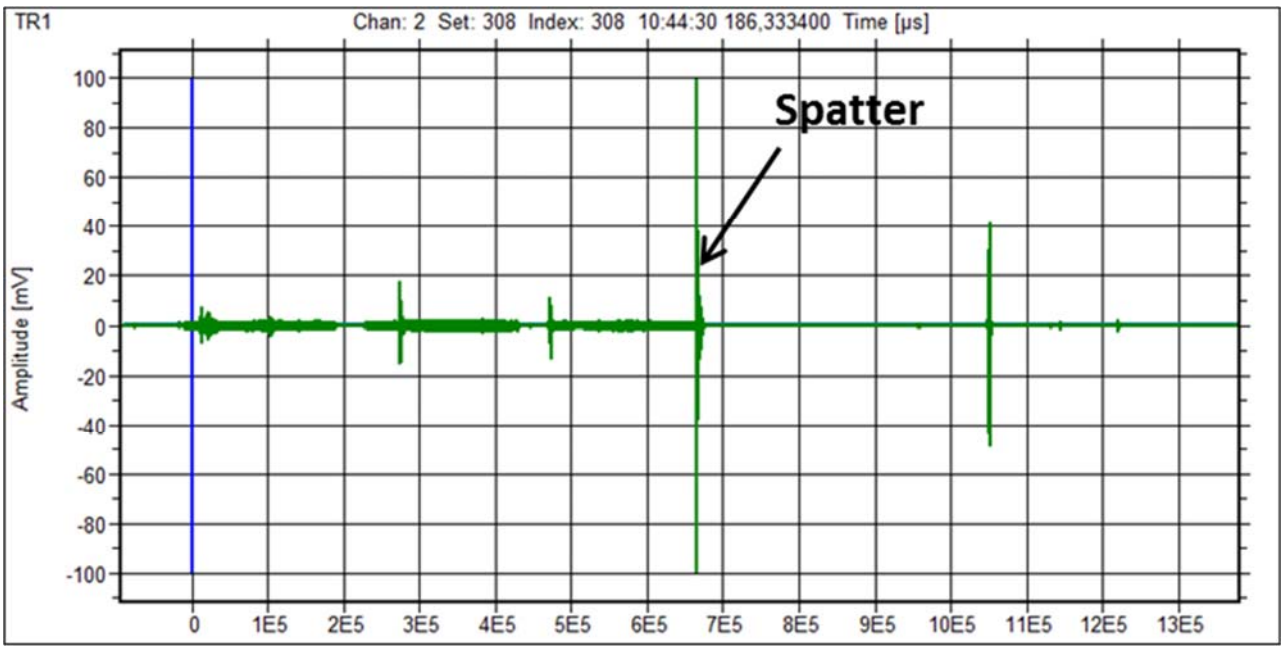

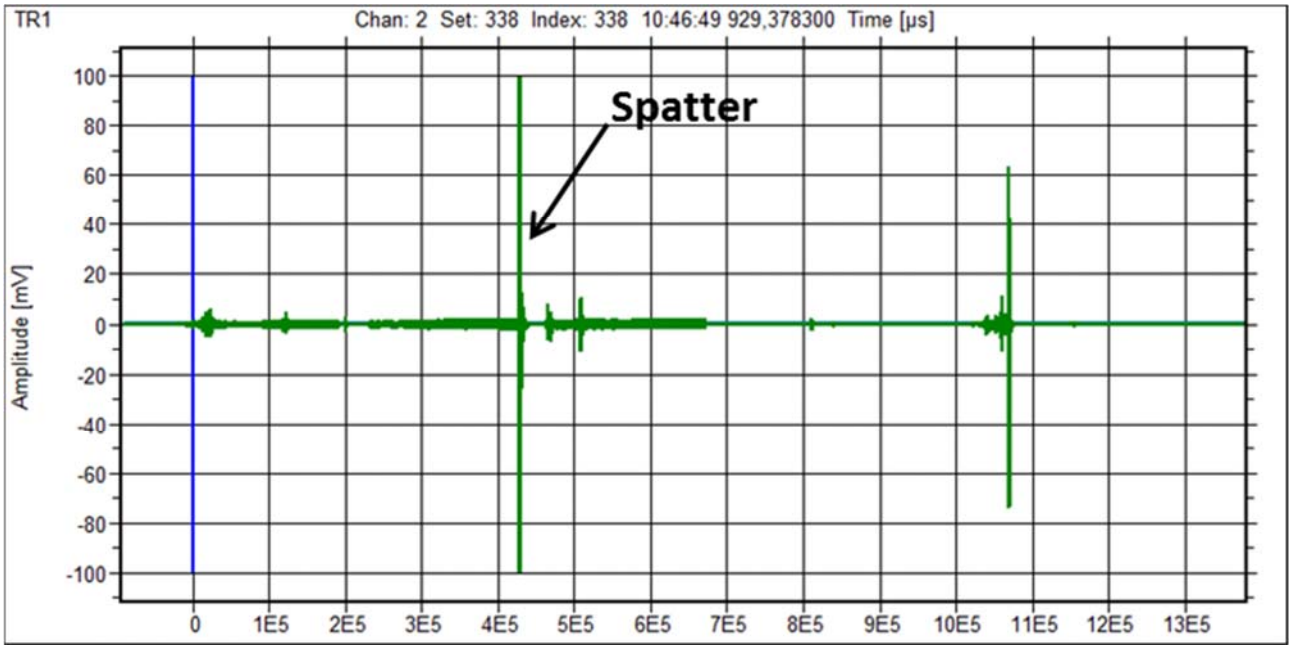


**Figure 21: Spatter detection by AE. Upper signal: spatter in the third pulse. Lower signal: spatter in the second pulse.**

### 4.1.4. Practice recommendations

#### 4.1.4.1. Applicability

The AE is the only method suitable for on-line LME detection in laboratory condition. Monitoring RSW by AE technique will offer precious information about the process stability and also will help the understanding of damage occurrence during the development of steel grade. It is important to note that AE provide binary answer on the presence of LME crack (Yes/No), and the only method able to monitor RSW in real time during welding.

In production environment, conditions are far from laboratory. First of all, guns are automatic, installed on robots. The kinetics of the electrodes can be pneumatic and electrics guns. Electrics guns are generally more powerful, more accurate but more expensive compared to pneumatic. Traditionally, alternating current (AC) power sources were used for resistance spot welding. However, recently, direct current (DC) power sources have become more common. Furthermore, the cadency is very high and various robots can operate simultaneously on the same piece. The audible noise in production environment is so high that operators have to wear hearing protection.

To evaluate the application of AE on production environment, trials have been carried out with the collaboration of the company BAOMARC which is a subsidiary of the BAOWU Group, member of WorldAutoSteel. BAOMARC is located in ARGANCY in FRANCE and is a producer of components parts for automotive industry and the leading supplier to the major car makers. The workshop is composed of roll forming process machines for steel and aluminum strips to obtain profiles. Various robots are operating simultaneously; more than 30 robots are available in the workshop. The number of robots by workstation can be one, two and more.

Tasks investigated during trials in production are:

- Implementation of AE instrumentation on RSW robots
- Evaluation of noise for electric gun and pneumatic
- RSW Monitoring for the case of one robot/piece electric and pneumatic gun
- RSW Monitoring for the case of two pneumatic robots working simultaneously.

For AE instrumentation of robot, it has been found that equipment is well adapted for production. Sensor, Hall Effect sensor, and preamplifier are easily positioned to the gun. The acquisition system is placed outside the workstation for security reasons and the two coaxial cables are inserted into a sheath to reduce installation time and also facilitate the passage of cables. Robot instrumentation takes approximately 30 min. No drift noticed after thousands of spot welds.

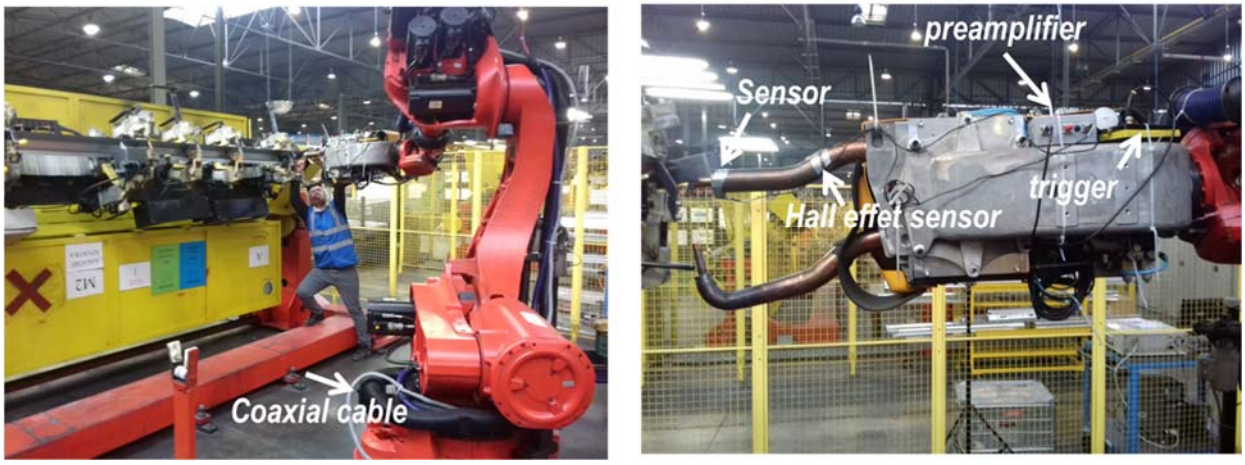


**Figure 22: Robot instrumentation.**

Despite a high audible noise in the workstation, the AE noise due to mechanical vibration in the gun is low for both guns type: pneumatic and electric. For electric gun robot, a low continuous noise is detected. The amplitude is 0.1mV which corresponds to 40 dB. This still acceptable and doesn't affect RSW monitoring. For pneumatic gun, the noise is lower than electric gun (0.01mV= 20 dB). The main noise seems to be due to electromagnetic interference (EMI) and not to mechanical vibration from the workshop.

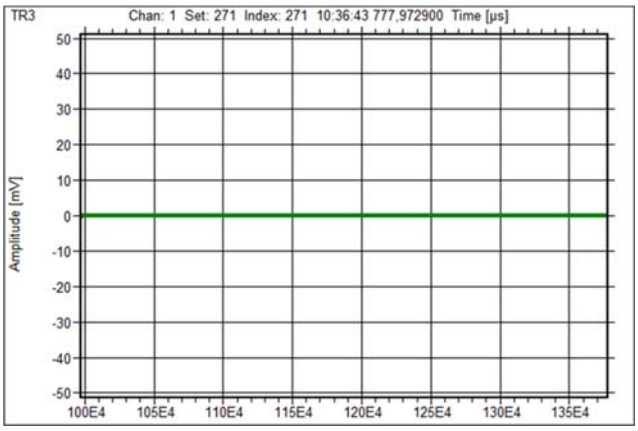


**Figure 23: Background noise recorded for electric gun of RSW robot.**

The signal to noise ratio was high for both cases: electric and pneumatic gun. The welding phases can be identified in the AE signal. For electric gun, the weld time is characterized by a continuous signal while for pneumatic gun the signal is totally different. One can note the presence of many short burst during the weld time and a low signal during hold time. Therefore, we realized that in this program, we succeed to prove the detection of LME in the worst case (electric gun). Considering the high quality of AE signal for pneumatic gun, LME detection will be easier.

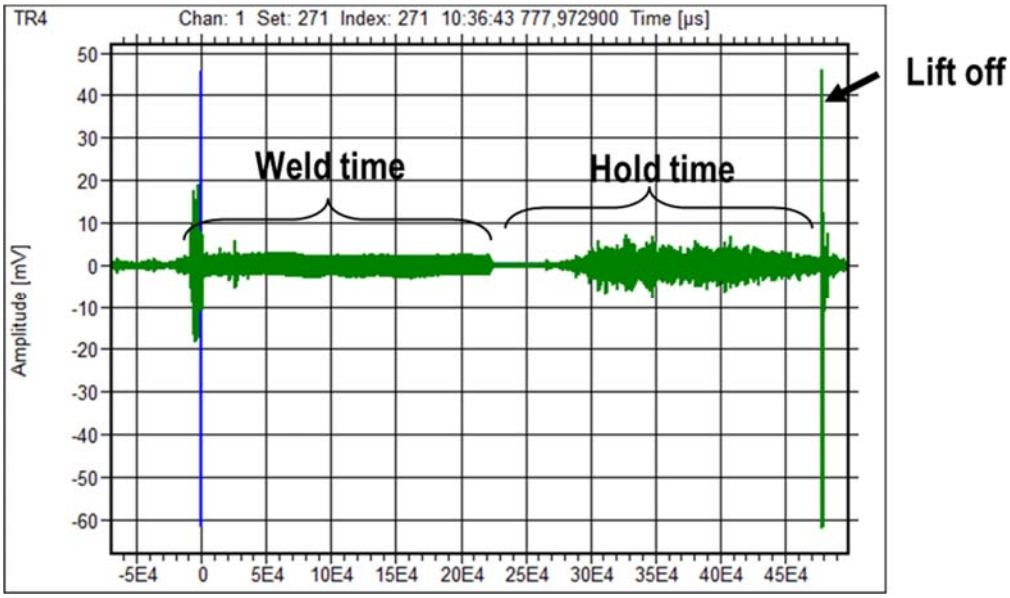


**Figure 24: Typical AE signal of electric gun in production environment.**

The main concern on production environment for the use of AE is the fact that for some piece, various robots can work (weld) simultaneously. In addition, at the beginning of the project we debated whether that it would be possible to use this technique in production environment. To answer to this question and evaluate the signal quality and determine if there is interference between robots, the case of two pneumatic robots welding simultaneously has been studied (Figure 26). Each robot is in charge of 10 spots for the same piece (6 spots/min). After the monitoring of thousands of spots (Figure 27), the result was promising. It has been proven that no interference generated between the two robots. Many reasons contribute to this result:

- Given the dimensions of robots, space displacement of each robot is well dimensioned/programmed to avoid any contact/incident between them. Generally the area covered by each robot is enough far (various cm). The propagation time of the wave from the spot generated by robot A to the sensor of robot B can be evaluated to few milliseconds.
- The wave is strongly attenuated from spot of Robot A to AE sensor of Robot B.
- There is a shift of welding time between spots of robot A and B. If an AE system should be used for monitoring, the time offset must be mastered.
- AE signal of each robot is trigged separately.

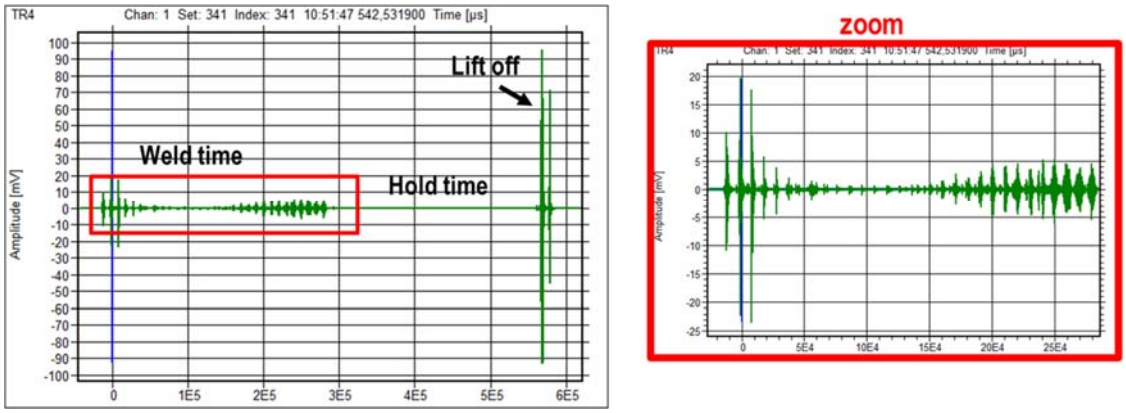


**Figure 25: Typical AE signal of pneumatic gun in production environment.**

**Figure 26: Two pneumatic robots working simultaneously on the same piece.**

For a perfect match between AE and robots, the deployment of a monitoring system in a workstation composed of more than one robot, a particular attention will be paid to robots synchronization.

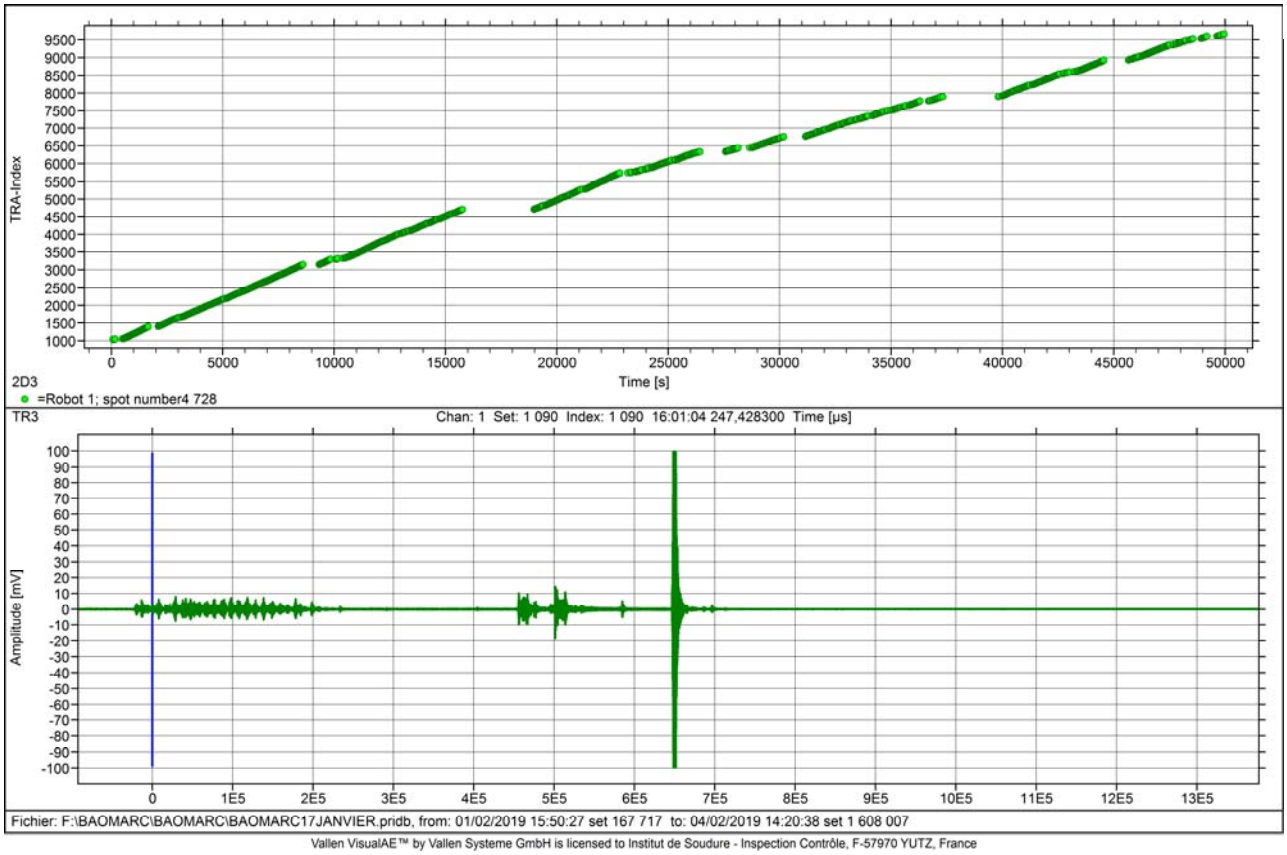


**Figure 27: AE Monitoring of robot n°1. Number of spot weld monitored in 13.8 Hours is 4728 spots.**

#### 4.1.4.2. Implementation

The implementation of AE monitoring system for resistance spot weld monitoring requires a learning step which is crucial for criteria definition. The training set must be representative of the actual welding parameters as well as the material combination and welding machine. A baseline is then formed, and its AE features determined. This would provide safeguards in order to detect any deviation and in particular LME crack. The better the training set, the better will be the reliability. Ideally, baseline should be free of LME cracks and obtained by representative welding conditions. If this is not possible, the alternative solution would be to remove the Zinc from pieces before welding to make sure that spots weld obtained are healthy and LME crack free.

AE implementation and data processing requires a qualified operator. A high background knowledge combined with strong field experience are major assets to achieve the calibration phase (learning step). It is important to note that various organizations around the world cover the training and certification of operators on NDT (COFREND, ASNT…) according to EN ISO 9712.

#### 4.1.4.3. Application Cost

The cost of AE monitoring is difficult to estimate since it depends on various factors (robots or manual machine, number of spots per day, cost of operators…)

*Production Environment*

To give estimation for production application different assumptions have been made:

- Cost of AE instrumentation = 50k€ (estimation of a complete system including the industrialization). AE systems available on the market contain only the option of one trigger for all channels (sensors). Therefore, AE system is required for each welding robot. below an example of prices of components:
  - Acquisition system: around 20k € (for one channel including Computer and monitor)
  - Sensor: 700 € (one sensor/gun)
  - Trigger: 500€
  - Preamplifier: 600€
  - Cable: 150 €
  - Software : 5000 € (but an RSW dedicated software must be developed for real time analysis)
- Depreciation period= 5 years
- Robot working time per year= 3760 hours (16hours per day, 5 days per week and 47 weeks per year; 5 weeks for maintenance)
- Time for operators per years = 3760 hours ( what was noticed during trials in BAOMARC, one operator is required for each workstation to put and remove pieces)
- Number of operators: one for each 8 hours per day
- Charged salary per operator per year= 40k€
- Overhead costs = 30%
- Number of spots per minute= 4 spots; Spot time= 0.25min
- Productivity= 80% => Spot time= 0.31 minute.
- Total number of spots weld per day= 3072 spots. (= 16*60/(0.31))

Considering this assumption, the depreciation per unit (one spot weld) is calculated as follow:

$$Depreciation\ per\ spot\ weld = \frac{Instrumentation\ cost\ \times Spot\ weld\ time}{Depreciation\ period \times Robot\ working\ time\ per\ year} = \frac{Instrumentation\ cost}{Number\ of\ RSW\ in\ 5\ years} \quad (4)$$

Depreciation per spot weld is estimated to 0.013 €.

The salary cost per spot weld unit is calculated as follows:

$$Salary\ cost\ per\ spot\ weld = \frac{1 + Overhead\ cost\ \times Total\ operators\ salary\ per\ year}{Number\ of\ RSW\ per\ year} \quad (5)$$

The salary cost per spot weld unit is estimated to 0.144 €. As indicated previously, one operator is required for each welding station to put and remove components. The operator presence is required independently of the AE system. The conclusion that can be drawn from this analysis is that the additional cost of RSW control by AE for production environment is ten times lower than the operator cost. This cost still marginal compared to the real cost of spot weld and the added value of such system.

### *Laboratory Environment*

Let's now focus on the case of laboratory application. The cadency can be low as well as the use of the welding machine.

For the following assumption:

- Instrumentation cost: 30k€ (basic equipment for each welding machine)
- Below an example of prices of components:
  - Acquisition system: 20k€ (for one channel including Computer and monitor)
  - Sensor: 700 € (one sensor/gun)

- Trigger: 500€
- Preamplifier: 600€
- Cable: 150 €
- Software : 5000 € (but an RSW dedicated software must be developed for real time analysis)

- 1 operator /machine
- Working time of the machine = 4Hours per day for 30 weeks per year.
- Number of spots per day=200 spots; Number of spots per year =200*5*30= 30000 spots; 150000 spots in 5 years

Depreciation per spot weld calculated according to the formula (4), is estimated to 0.2 €.

The additional cost per spot weld when a monitoring system is installed is estimated to 0.2 €. This cost will significantly decrease with the spots welds number.

#### 4.1.4.4. Automation

The actual software version of AE systems available on the market of the two main competing products MISTRAS and VALLEN are not suitable for RSW application. Indeed, the influence of the LME crack on the collected signals is too weak! Hence, we are in a problem of the so-called "weak signals". In other words, the difference cannot be distinguished by the naked eye. *Data fusion-based algorithms* are therefore required. Basing on this kind of algorithms, ISA has developed its own software. Currently, this software operates on off-line, but it is possible to be used for real-time, via some adaptations. Figure 28 shows an example of the Human-machine-interface of this software.

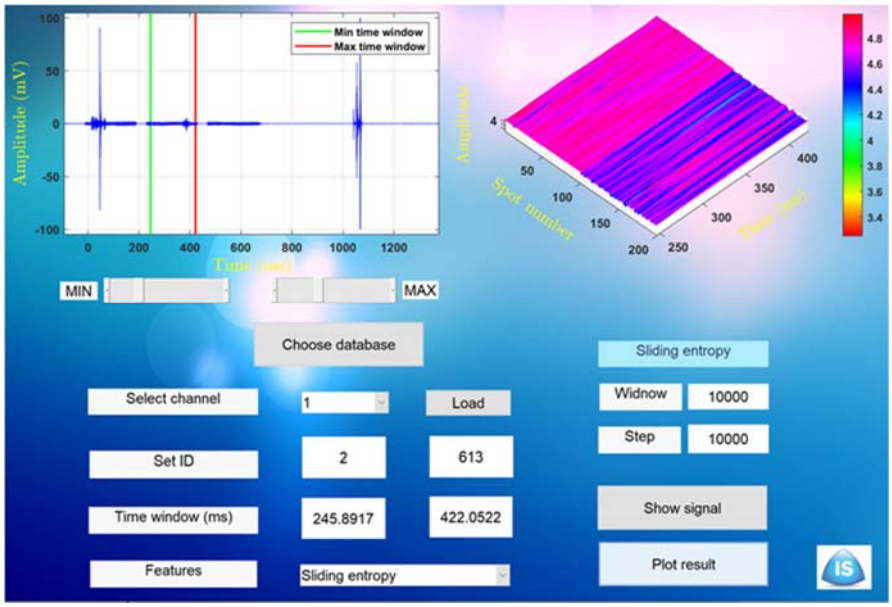


**Figure 28: Human-interface-machine example of the AE software developed to detect LME cracks in RSW.**

### 4.1.1. Conclusion

Acoustic emission is the only NDT technique that can be used during the spot welding (real-time) to detect cracks. It should be noted that detection is based on a learning step, and its reliability is closely linked to this step. However, this technique is not able to characterize cracks.

## 4.2. Magnetic Particle Inspection (MPI)

### 4.2.1. Background

Magnetic Particle Inspection (MPI)) also called Magnetic Testing (MT) is a nondestructive technique applied for surface and sub-surface defect in ferrous materials. The principle is to generate a magnetic flux in the piece by applying an electric current. The presence of defects will disturb the magnetic flux and create a leakage field. Iron particles, either in a dry or wet suspended form, are applied to the surface of piece. Particles will be attracted, and a cluster is formed above the defect which makes the indication visible by the controller.

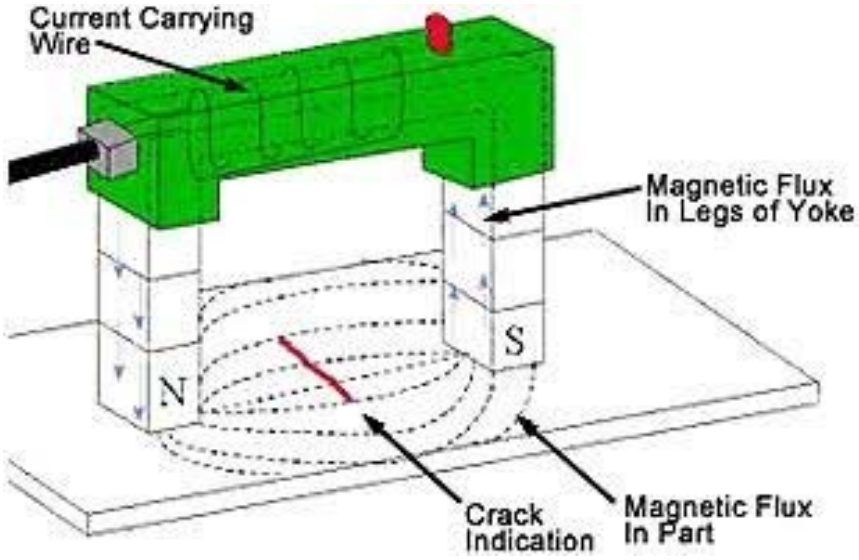


**Figure 29: Magnetic Particle Inspection principle.**

This method is used for a wide components/pieces obtained by welding, casting and forging. Many industries also use MPI such as automotive, petrochemical, power generation and aerospace industries [5].

Since the interpretation is visual and the principle of the method is relatively easy (application of the magnetic field and also liquid spraying can be performed in one shot), MTI has shown a high potential for automation in production conditions. In Automotive industry, MPI was used to detect cracks in drive shafts and crankshafts. A fully automated system based on MPI and machine vision was even been deployed in production condition [6].

### 4.2.2. Methodology & Experiments

At the beginning of this research program, conventional MPI method was applied to a large number of specimens with different LME crack levels. The aim was to evaluate LME crack detection capability in laboratory condition using conventional equipment:

- Dark chamber
- Hand-held, electromagnetic yoke "TIEDE TWM42N"
- UV Led lamp LABINO Big Beam
- Magnetic liquid "BABB CO B101C", grain size ranges from 1 to 10µm – Average size 4µm
- Visual inspection and camera for photo capturing


**Figure 30 : Electromagnetic yoke (left), Magnetic liquid (middle), UV lamp (right).**

The potential of this method for production conditions was also assessed by adapting the equipment to fit the serial production need. As the cadency is high, the need of automation is inescapable. To do that, below the equipment chosen:

- The same electromagnetic yoke and liquid
- A simple UV pocket torch (for cost optimization)
- Camera for photo capturing: the distance between camera and RSW is fixed to simulate automatic photo capturing by onboard camera in the robot.
- Automatic Analysis (using dedicated program developed by IS in this program)

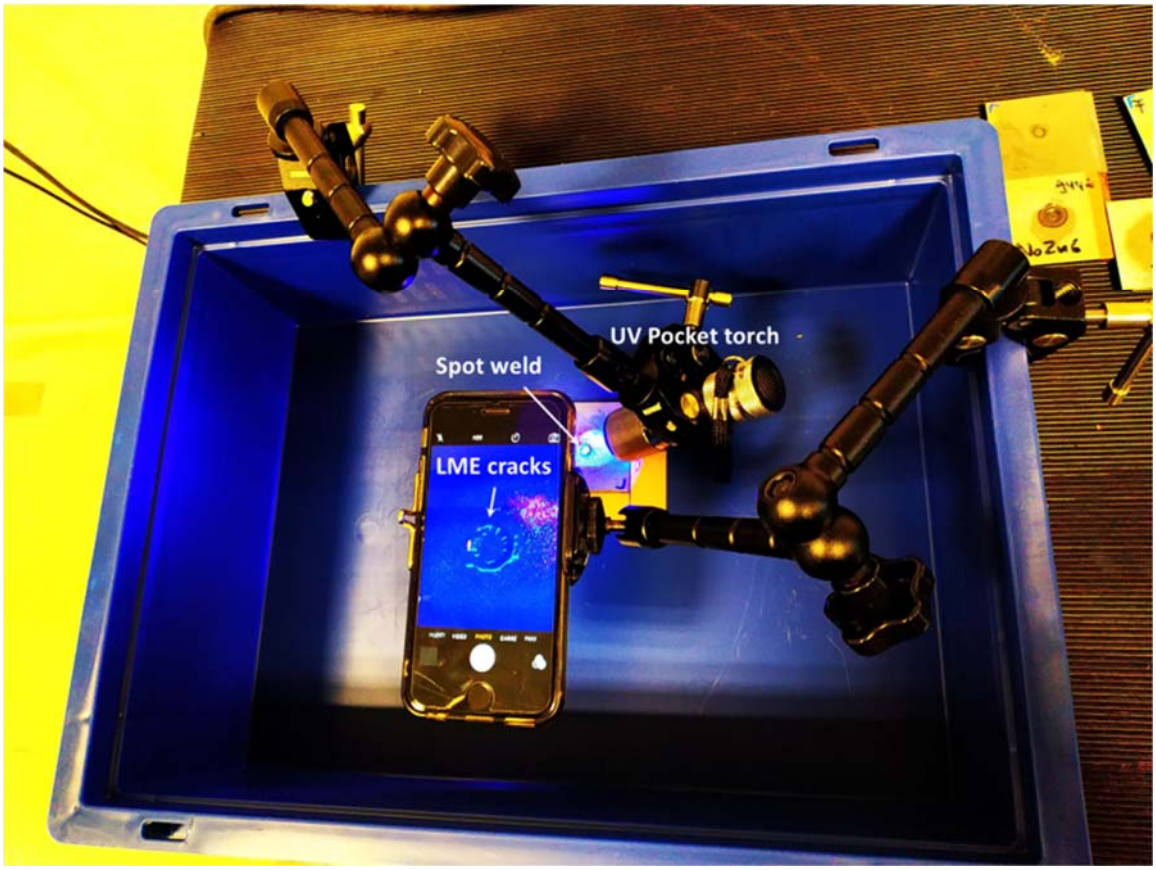


**Figure 31: Setup to simulate production implementation.**

### 4.2.3. Results & discussions

The application of MPI to a wide number of specimens has shown promising results regarding LME crack detection. The method is easy to apply, and the result is immediate. Once the operator applies the magnetic field and sprays the spot weld, the presence or no of crack is visually detected immediately by the operator. The control time is estimated to few seconds according to the dexterity of the operator (5-10s). To that is added few second for the image acquisition. The operator should find the best angle to avoid light reflection.

Above the crack a concentration of ferrous particles will reflect the UV light and lighten the exact form of the LME crack. Whatever the dimensions of LME, detection is proven to be relevant.

Some examples are given in the table below. Figure 32 is a Zoom of the specimen n°VN253. One can see clearly the crack features.

MPI can provide the following LME features:

- LME Crack presence or no (Detection)
- Location of the Crack, (Detection is ensured whatever the location, inside or outside the nugget)
- Length of the crack
- Orientation/ Form
- Opening (in some cases, according to the thickness of the form generated, we can distinguish visually between large or small opening)

| n°VN244 | n°VN247 | n°VN249 | n°VN252 | n°VN253 |
|---|---|---|---|---|
| 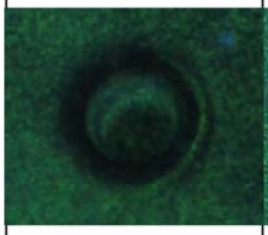 | 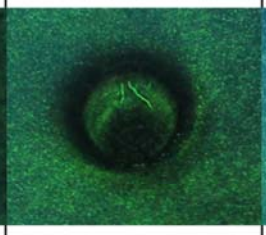 | 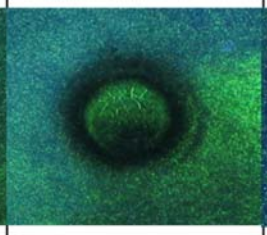 | 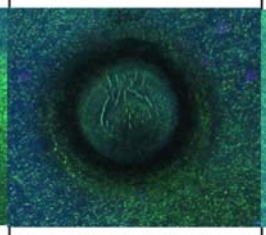 | 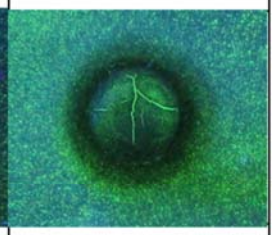 |
| WT= 640ms | WT= 960ms | WT= 1280ms | WT= 1600ms | WT= 1600ms |
| n°VN255 | n°VN258 | n°VN262 | n°VN264 | n°VN265 |
| 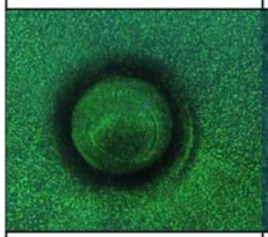 | 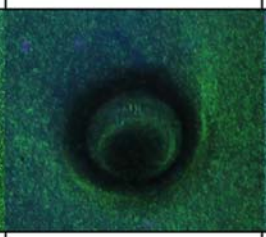 | 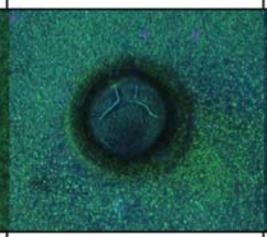 | 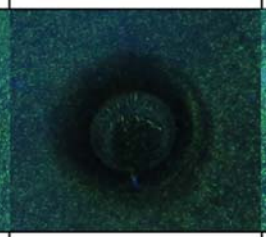 | 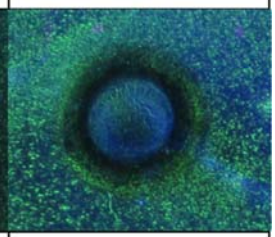 |
| WT= 640ms | WT= 960ms | WT= 1280ms | WT= 1600ms | WT= 1600ms |

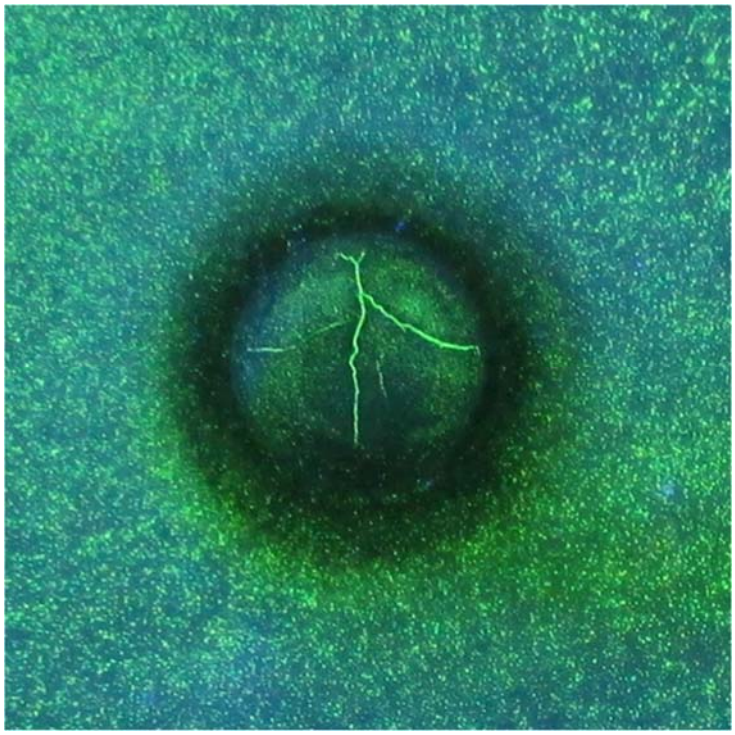

**Figure 32: Example of crack detection with MPI. Specimen n°VN253.**

Another particular aspect studied with MPI, is the case where LME crack is hidden by the presence of Zn layer above. This configuration is difficult to detect using Optical Microscope. To evaluate the MPI detection in this configuration, three specimens were controlled by MPI before and after Zn layer in the spot weld is removed using adequate chemical etching.

Figure 33 until Figure 35 show results obtained for spot welds with Zn and after Zn removed. It can be clearly observed that LME cracks are always detected for both cases and all indications even for small cracks still detected. For specimen n°9459, various small radial LME cracks with length less than 1mm are located inside the nugget near the indentation. It can be clearly shown in the Figure 35, that all these cracks are indicated by MPI.

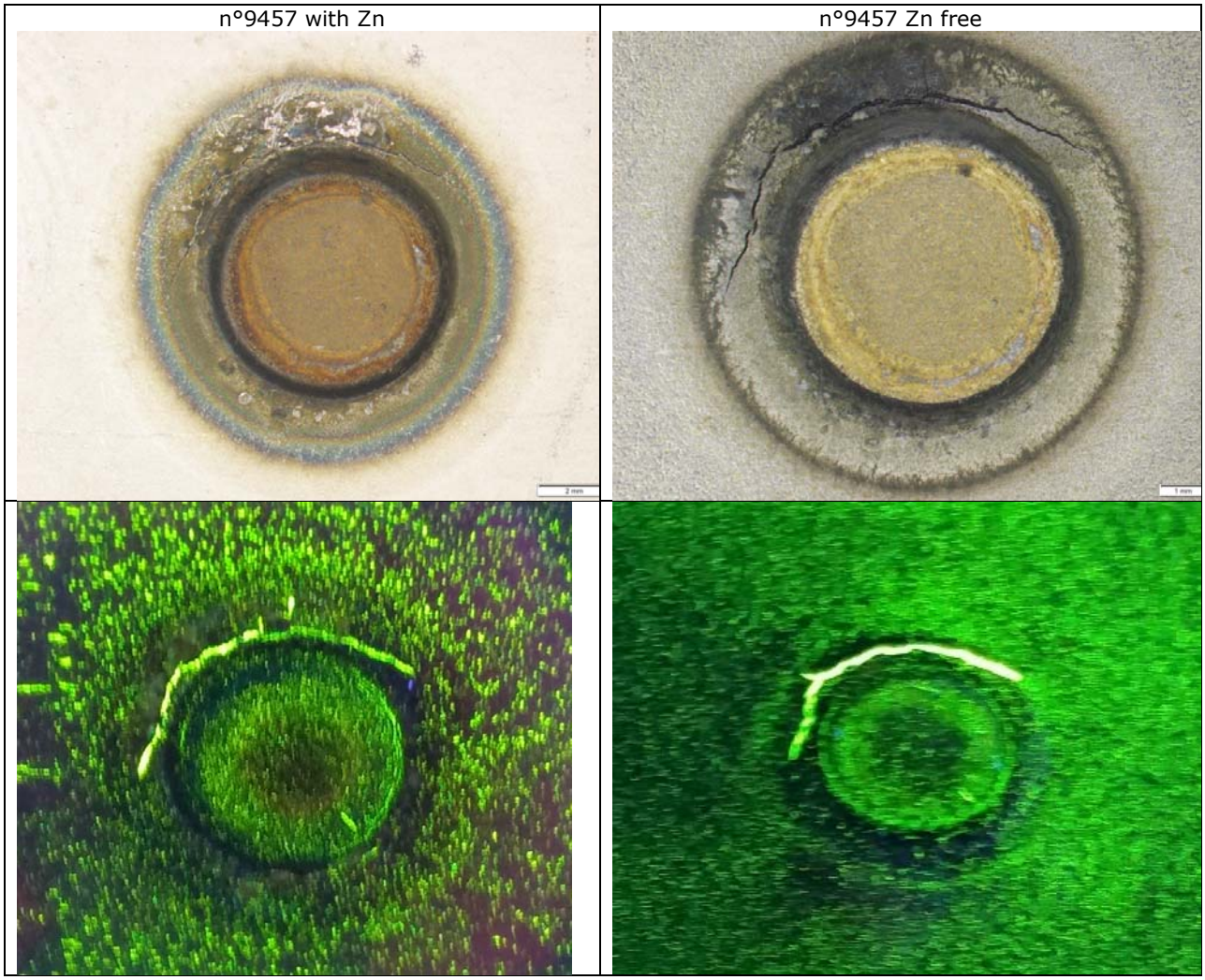


**Figure 33: Specimen n°9457. Magnetic inspection before Zn removing (left), after Zn removing (right).**

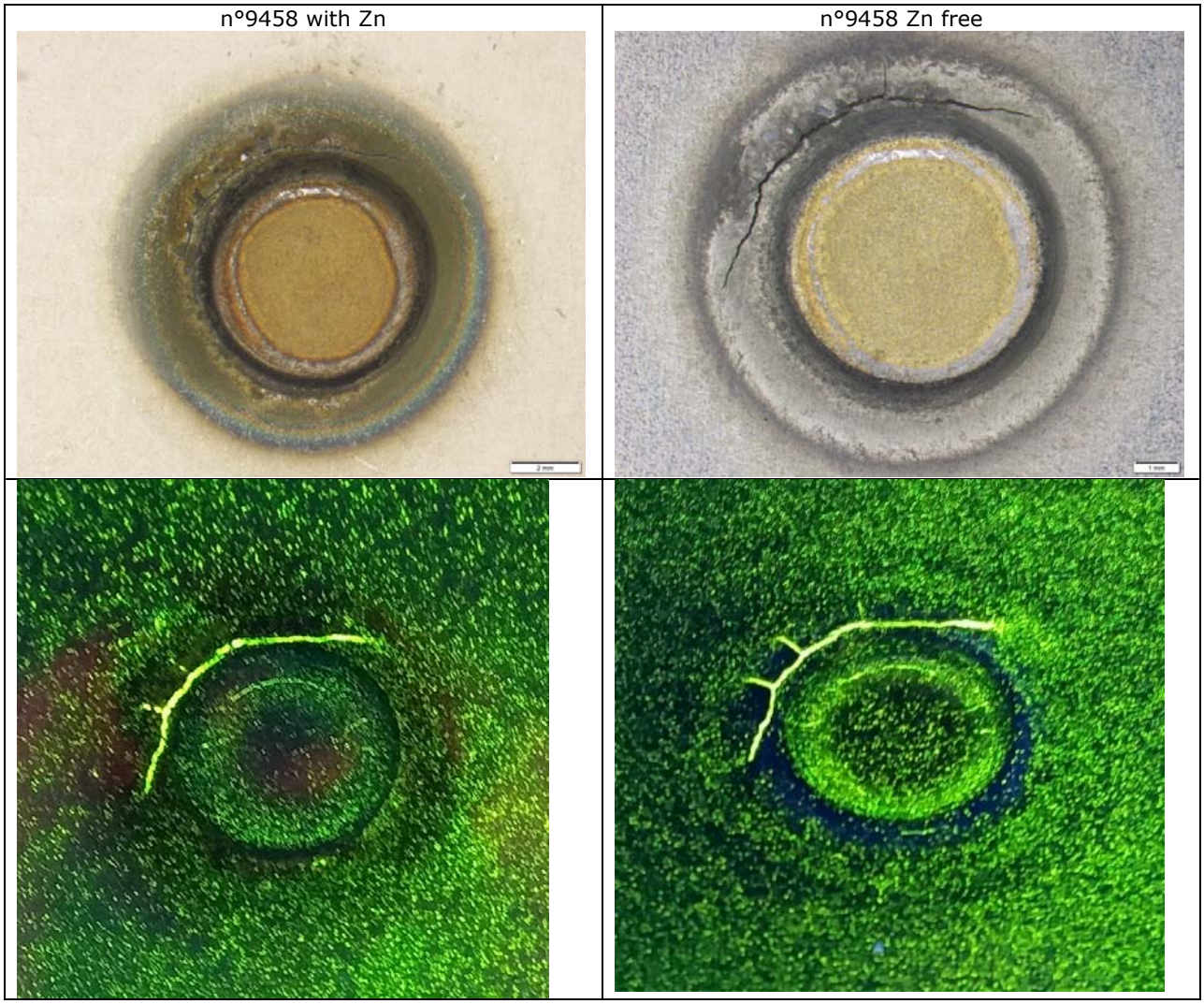


**Figure 34: Specimen n°9458. Magnetic inspection before Zn removing (left), after Zn removing (right).**

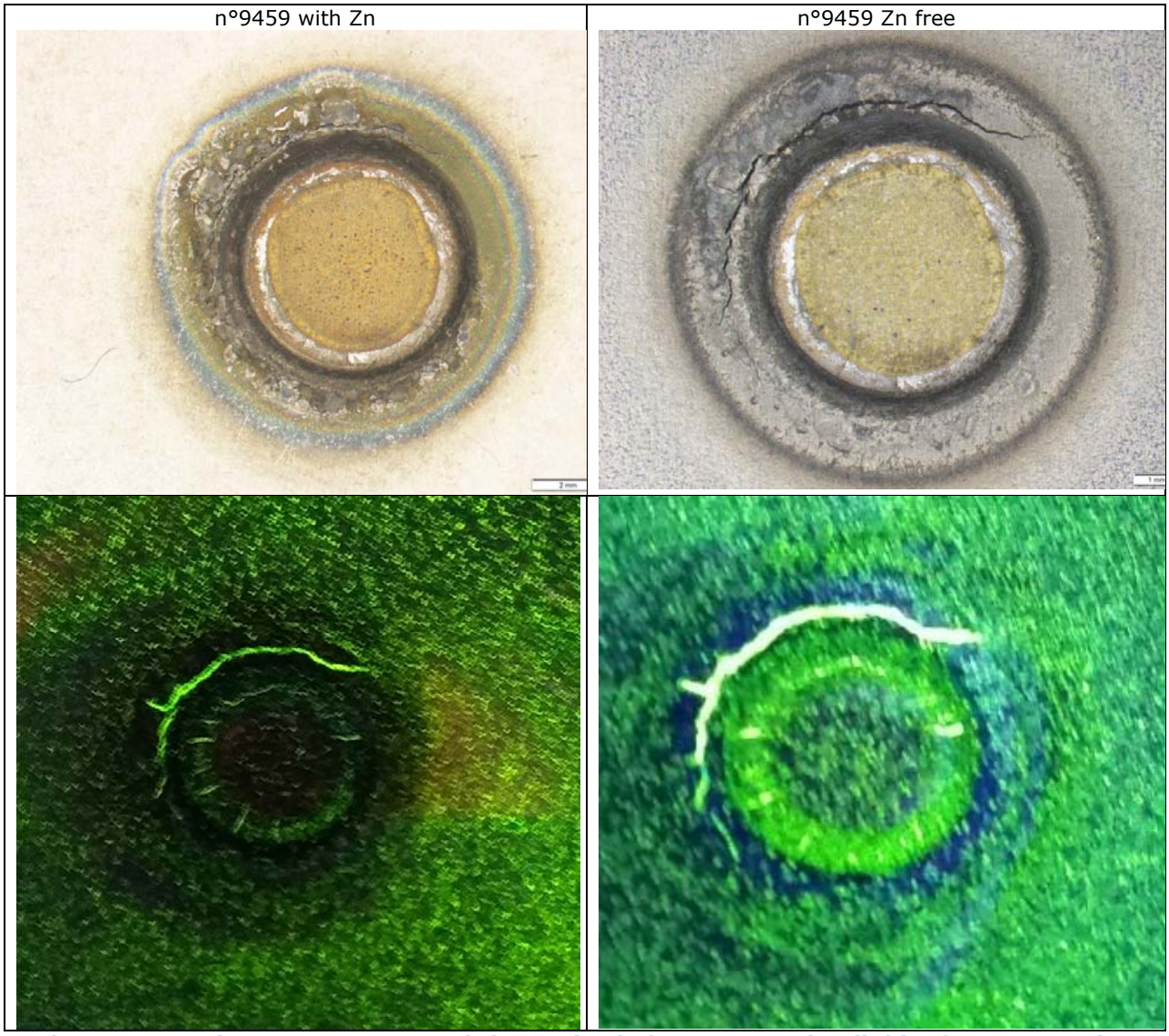


**Figure 35: Specimen n°9459. Magnetic inspection before Zn removing (left), after Zn removing (right).**

### 4.2.4. Practice recommendations

#### 4.2.4.1. Applicability

MPI is suitable for LME crack detection in laboratory and can compete with all other NDT investigated in this report. Some industrial uses Dye penetrant method in laboratory to detect cracks as an alternative to microscope observation. However, compared to MPI, dye penetrant has more limitation and is time consuming. The duration of control is more than 20 min per spot weld. The MPI, is simple to apply, doesn't require high qualified operator and is very fast. The control time is approximated to 5-10s per spot.

MPI has a strong potential for LME crack detection, in production condition. This requires some further development for the automation and industrialization of the method. This is possible since some fully automated workstation were already deployed in automotive for drive shafts and crankshafts control and the feasibility of automatic detection was proven in this work (see the following paragraph).

#### 4.2.4.2. Implementation

The advantage of MPI is that there is no need of calibration step for detection. Implementation in laboratory condition is very simple and easy.

Component required are:

- Dark chamber (for a higher sensitivity to small defects)
- Hand-held, electromagnetic yoke "TIEDE TWM42N"
- UV Led lamp
- Magnetic liquid "BABB CO B101C", grain size range from 1 to 10µm – Average size 4µm
- Visual inspection and camera for photo capturing
- A washbasin for piece cleaning
- Chemical product treatment to preserve the environment

In production condition, for an automatic classification of spot welds, two options are possible:

- Design an MPI workstation where real pieces or all the car body is magnetized and spread with magnetic liquid. Then, a robot equipped with a camera and UV light will capture the image of each spot weld and classify them automatically using an image processing algorithm or machine learning model.

- Embark all components on the head of the robot. First the robot needs to locate the spot weld position. Apply a magnetic field around the spot weld. Spray a magnetic liquid locally and then acquire an image via the camera. The result of detection can be displayed in real time or at the end of control.

#### 4.2.4.3. Reliability

Detection with MPI is relevant for crack detection. Various levels of LME cracks investigated in this program and promising results found. However, a particular attention should be paid to UV light orientation vs camera. It has been found that the image quality depends on camera orientation. The setup should be defined to avoid light reflection.

#### 4.2.4.4. Application Cost

##### *Production Environment*

In production condition, for an automatic classification of spot welds, two options are possible as indicated previously (paragraph 4.2.4.2):

For both cases the cost of such installation should be estimated to 200k€-300k€ (including the robot).

- Depreciation period= 5 years
- Robot working time per year= 3760 hours (16hours per day, 5 days per week and 47 weeks per year; 5 weeks for maintenance)
- Number of spots per minute= 1 spot weld; Spot weld time= 1min
- Productivity= 80% => Spot time= 1.25 min.
- Total number of spots weld per day= 768 spots. (= 16*60/(1.25))
- Number of RSW in 5 years: 768×5×47×5=902400 spot welds

Depreciation per spot weld calculated according to the formula (4), is estimated to 0.22 € for installation cost 200k€, and 0.33€ for installation cost 300k€.

*Laboratory Environment*

For laboratory application the cost of MPI is less than 1500 €.

Below more details:

- Hand-held, electromagnetic yoke "TIEDE TWM42N": 800€
- UV Led lamp : 50€
- Magnetic liquid "BABB CO B101C", grain size range from 1 to 10µm – Average size 4µm: 15€ per unit. It is a consumable; there should be one spray for 400 spot welds.
- Camera for photo capturing: 400€
- A washbasin for piece cleaning: 50€

The cleaning can be with water or with Oil spray: 20€ per unit.

Two analysis approaches can be considered:

- Conventional analysis: The operator applies MPI on spot welds, import photos in computer and classify spots based on visual analysis. In this case no additional cost.
- Automated analysis: The operator applies MPI on spot welds, import photos in computer and classify automatically spot welds using dedicated software. Additional costs must be considered for the software ≈ 5000€ (to be defined). The actual software developed enables spot welds classification in two states: healthy and damaged (with LME cracks). However further investigations can be conducted to classify LME crack into different categories (light, medium, intense).

For the following assumption (the same as for AE for comparison):

- Instrumentation cost: 1500 € (basic equipment)
- 1 operator /machine
- Working time of the machine = 4Hours per day for 30 weeks per year.
- Number of spots per day=200 spots; Number of spots per year =200*5*30= 30000 spots; 150000 spots in 5 years
- Consumable cost in 5 years= 150000/400×15€=5625€

Depreciation per spot weld calculated according to the formula (4), is estimated to 0.04€

$$\text{Depreciation per spot weld} = \frac{5625+1500}{150000} = 0.04€$$

#### 4.2.4.5. Automation

The feasibility of automatic LME detection was investigated in this work. To do that a specific setup was used to be closer as possible to image capturing in production environment:

- Distance camera-spot weld is constant.
- UV light and camera orientation are always the same for all weld spots
- The same image magnification

An image processing algorithm was then developed by IS for RSW, MPI image analysis. The algorithm is based on thresholding of pixel intensity and also on the size and distribution of intensity. As it can bee see from MPI images, the crack is characterized by a shiny light (high intensity) compared to background noise of neighbor area. A Hessian-based multiscale filtering is applied to differentiate the cracks from the noise (by enhancing elongated or tubular structures in intensity image), but some other elements of the points can also be enhanced with this filtering. Moreover, we apply a thresholding on the initial intensity image to remove the elements which were not revealed by UV light. Results are then combined to identify LME cracks. The model is then implemented in a dedicated software (using Matlab Software) for automatic MPI analysis of RSW. The software works as follows:

- The operator should upload the database (MPI images) and start classification.

- As in output, RSW were classified in two categories: Healthy spots and damaged spots.

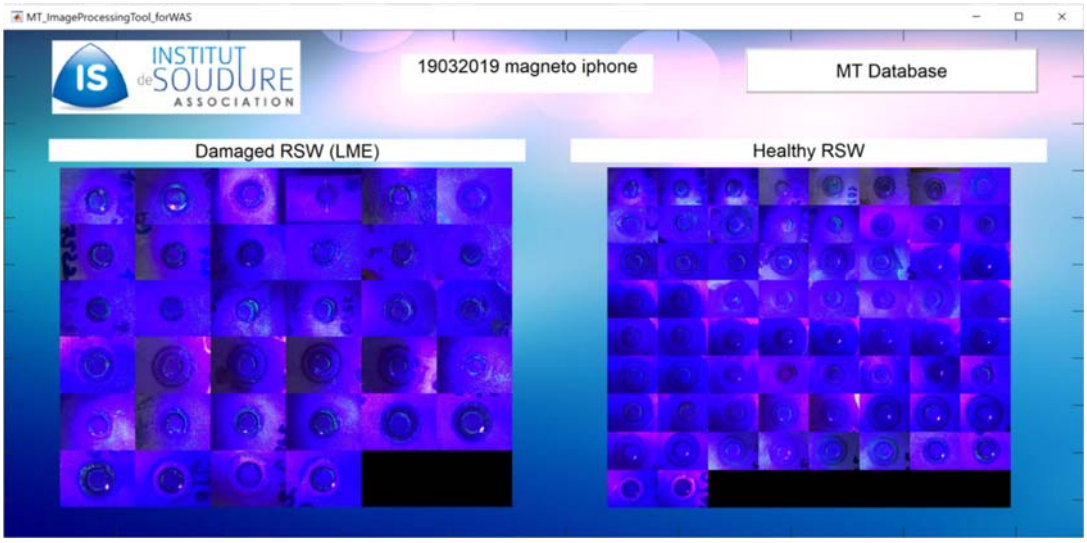


**Figure 36: Example of human-machine interface of the software developed by ISA for the automatic classification images of MPI.**

To verify the reliability of the model, a database of 100 spots (Figure 37) welds MPI images were captured using the setup described above.

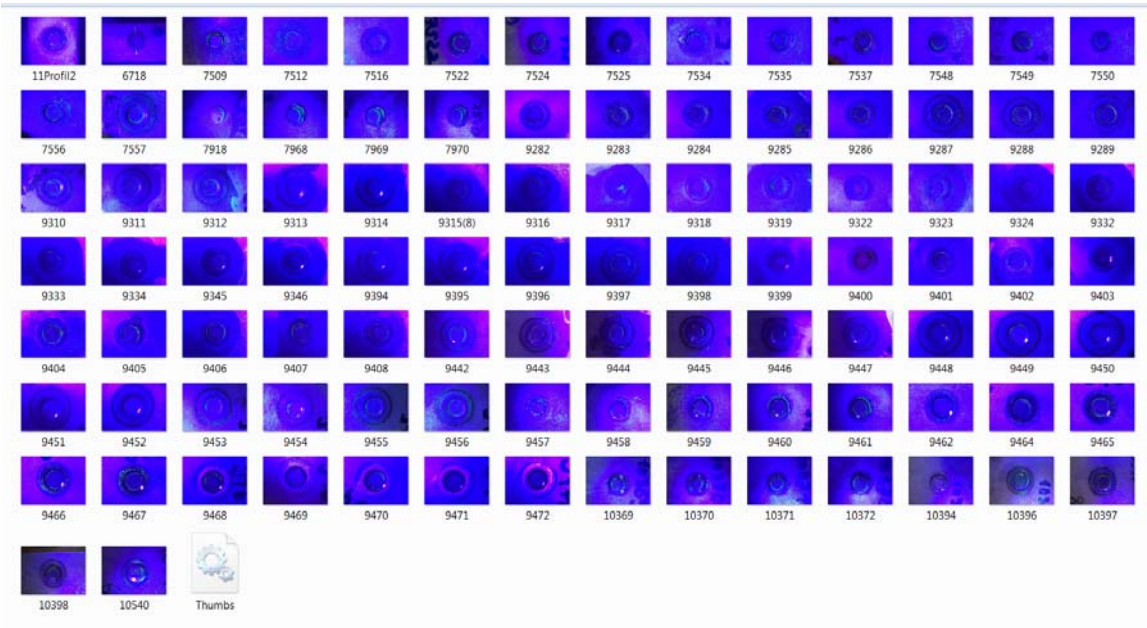


**Figure 37: Database of 100 Spot-welds MPI.**

The database is composed of 63 Healthy spots and 37 with cracks.

The application of the algorithm leads to two classifications:

- Healthy spots: 66 spot welds
- Damaged spots: 34 spot welds

After manual observation and analysis of categories, it was found only 10 misclassifications, composed as follows:

- Healthy spots: 5 misclassifications (which means that 5 spots with crack were not detected).
- Damaged spots: 2 misclassifications (which means that 2 healthy spots were considered with crack).
- The two misclassifications in the damaged category (Figure 38), concerns two healthy spots. When subjected to closer scrutiny, it was found that they were subjected to corrosion since Zn was removed before welding and these spots were produced several months ago. The corrosion disturbs the magnetic particle displacement which leads to a concentration of particle that algorithm is not able to distinguish with cracks.

For the five misclassifications, it is due to a low intensity of light above crack.

The result still very encouraging since a high success rate is found: 93%.

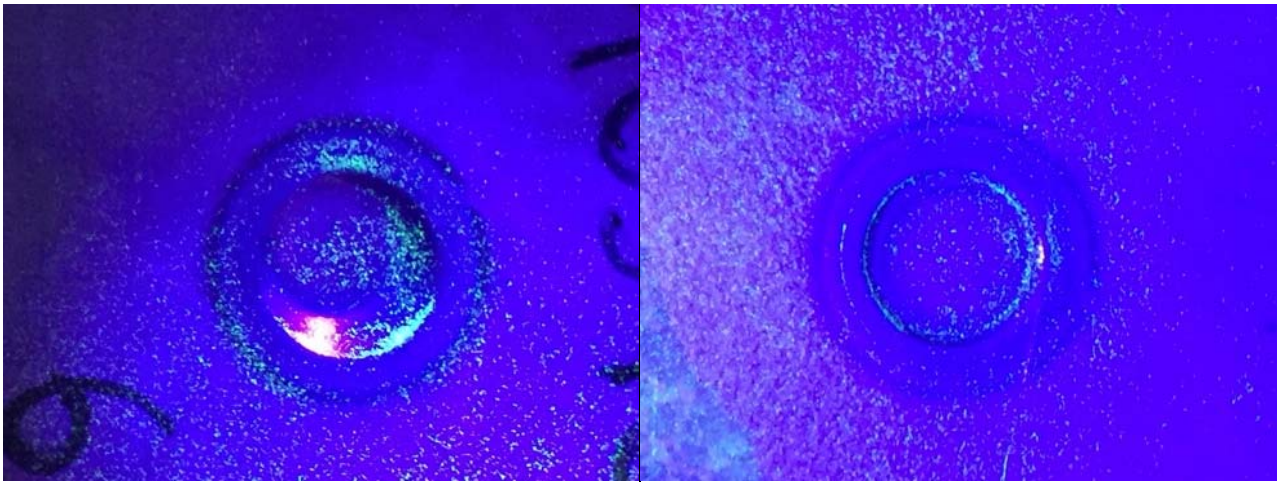

**Figure 38: Examples of misclassified spots due to corrosionConclusion**

### 4.2.5. Conclusions

Magnetic Particle inspection is a relevant NDT technique for LME cracks detection, with no need for specific skills. It permits also to know the shape and the length of a detected crack. The current software, developed in this project to detect cracks, can be upgraded to provide crack length. Currently, this technique doesn't permit to know the crack depth. However, if a relationship between the *length*, the *opening*, and the *depth* of a given crack can be established, the MPI can then called to assess the depth.

## 4.3. Eddy Current Array (ECA)

### 4.3.1. Background

Conventional eddy current technology (ECT) is based on the creation of electromagnetic field (primary field) around the wire when alternating electric current is passed through. When the coil is placed near an electrically conductive material, the electromagnetic field permeates the material and causes the flow of an electrical current (according to Ampere's Law) called eddy current. These currents are flowing circularly and parallel to the surface and generate a second electromagnetic field on the coil. Due to Lenz-Faraday's Law, these electromagnetic fields are detected and measured by a second coil providing a voltage output. Defect inspection is based on the fact that these measured voltages differ in cases of sound and defective material (Figure 39).

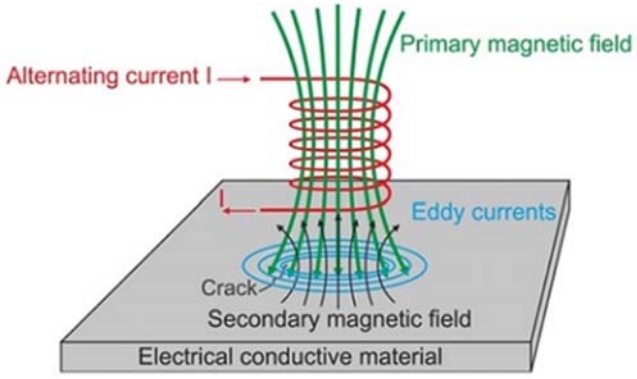


**Figure 39: ECA principle.**

Eddy current arrays (ECA) are the natural extension of ECT. ECAs are composed of arrays of coils that activate in sequences intended to eliminate interference between them. The array slides on top of surfaces, offering an overall wider coverage and better sensitivity to defects than conventional eddy current testing (Figure 40). ECA technology can detect surface-breaking defects and, to some extent, subsurface defects. ECA probes can also be shaped to match more "exotic" geometries, which enable single-pass scanning of geometries that traditionally pose serious challenges to other inspection technologies.

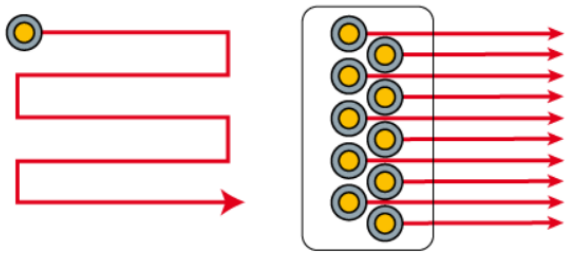

**Figure 40: Single coil= raster scan (left); multiple coils= one-line scan (right)**

ECA technology is used as an alternative to other surface inspection technologies in such industries as the oil, gas, and petrochemical industry; the power generation and nuclear industries; the aerospace industry; and the heavy equipment and mining industries. ECAs also very successfully supplement Ultrasonic Testing (UT) and Phased-array (PA) because these suffer from what is often referred to as a "dead zone" near the surface, making it difficult for them to detect near-surface defects.

Therefore, surface applications of ECA technology are numerous, ranging from weld inspection on pressure vessels and pipes, to corrosion mapping.

### 4.3.2. Methodology & Experiments

- **Specimens**

To evaluate the potential of ECA on crack detection and also depth estimation, the first step was to start with artificial defect obtained by Electrical Discharge Machining (EDM) with known features:

- Length: 3 mm
- Opening: 0.1 mm
- Location: near indentation: 3mm radius from spot weld center
- Depth: 0.1 to 1.4 mm
- Form: curved

EDM features are chosen as closer as possible to LME crack features.

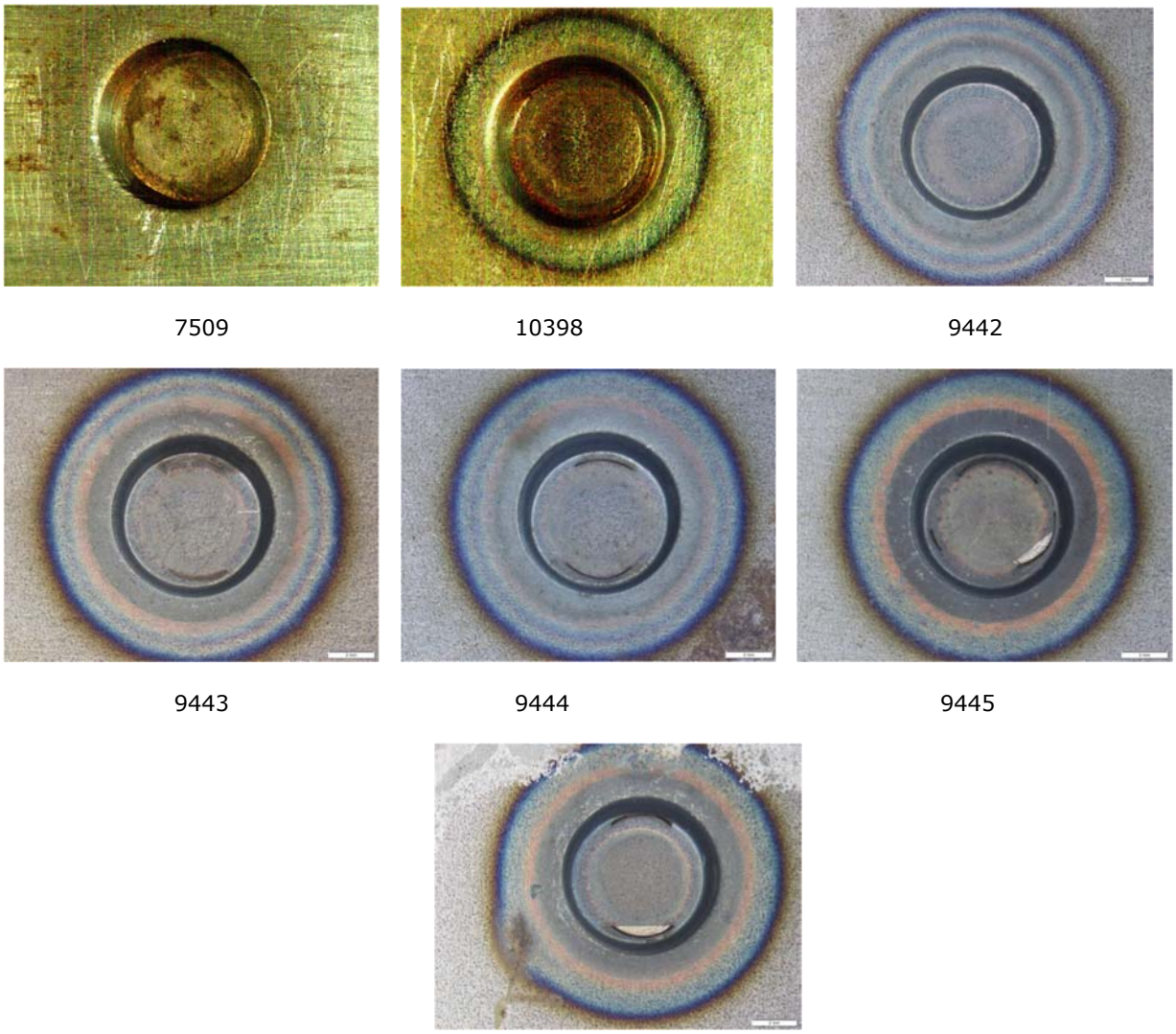


**Figure 41: Specimens used for ECA study: Healthy spot welds and spot welds with EDM.**

**Table 8: EDM features.**

| EDM n° | Length (mm) | Depth (mm) | Specimen n° |
|---|---|---|---|
| **1** | 3.0 | 0.1 | 9443 |
| **2** | 3.0 | 0.2 | 10398 |
| **3** | 3.0 | 0.3 | 9443 |
| **4** | 3.0 | 0.6 | 9444 |
| **5** | 3.0 | 0.7 | 7509 |
| **6** | 3.0 | 0.8 | 9444 |
| **7** | 3.0 | 1.0 | 9446 |
| **8** | 3.0 | 1.4 | 9446 |
| **9** | 1.0 | 0.7 | 9445 |
| **10** | 3.0 | 0.7 | 9445 |
| **11** | 5.0 | 0.7 | 9445 |

- **Topologies**

Topologies refer to how coils are organized inside a probe and their activation patterns used in combination to create at least one eddy current channel. Each topology has its own characteristics. The following table shows all topologies tested.

**Table 9: Topology of ECA probe.**

| Topologies | Distribution inside a probe | Characteristics |
|---|---|---|
| Impedance | 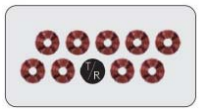 | + Non-directional<br>+ Sensitive to small and long defects in all directions<br>+ Works for all conductive materials<br>- Very sensitive to surface conditions and handling<br>- Sensitive to the air gap |
| Short Double Driver Axial /Transverse » (SDDA /SDDT) |  <br>Axial (SDDA)<br>  <br>Transverse (SDDT) | + Is less sensitive to variations in the gap than impedance<br>+ Optimal for detection of small / shallow defects (better resolution than SDL)<br>- Directional, creates axial and / or transverse channels<br>- Sensitive to transceiver fault<br>- Low performance on carbon steel |
| « Long Single Driver Transverse /Axial » (SDLA /SDLT) | 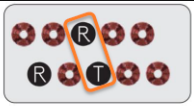 <br>Axial (SDLA)<br> 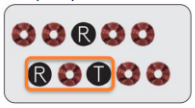 <br>Transverse (SDLT) | + Is less sensitive to gap variations than impedance and SDS<br>- Directional, creates axial and / or transverse channels<br>- Sensitive to transceiver fault<br>- Less sensitive to very small defects |
| « Sub-Long Driver Transverse /Axial » (SLA /SLT) |  <br>Axial (SLA)<br> 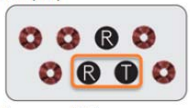 <br>Transverse (SLT) | + Has a resolution lower than the SDS, but higher than the SDL<br>+ Is more sensitive to variations in airgap than SDL, but less than SDS<br>- Directional, creates axial and / or transverse channels<br>☐ Rarely used |

- **Ectane 2**

The acquisition instrument used is an Ectane 2 128. This instrument is used for surface and tube inspections and offers up to 128 channels. Ectane 2 has been used with Magnifi 4.5R4.


**Figure 42: ECA system Ectane 2.**

- **Table XY**

To optimize the scan conditions, a motorized and programmable translation table is used to perform the manipulations of the CF elements on the samples studied. The XY table was used to make a Raster Scan on the samples. A scanning speed of 40 mm/s was used in scan and increment. The samples were arranged to allow a single acquisition to cover all defects. This type of scan consists of using an axis for the scan and an axis for incrementing. This technique covers a large area. The XY table is used to test different resolutions to help determine the requirements of the prototype probe to be produced.

Resolution is the distance between two measurements. The resolution in X is the spatial frequency at which acquisition is performed in mm/sample. The Y resolution is the distance between two scan "lines". The scan lines of a Raster Scan are the equivalent of the channels found on an ECA (Eddy Current Array) probe and the distance between each scan line is equivalent to the spatial offset between each channel. So the Y resolution is the increment (represented by ΔY in Figure 43) that the XY table does between each scan line. It is therefore possible to test different resolutions in Y to determine the number and the offset of rows that a probe must have.


**Figure 43: Representation of the path carried out by the XY table on the samples studied. A kapton tape placed above specimens to facilitate probe movement.**

The idea of a rotating scan centered on the welded point was considered, but after a preliminary analysis it was agreed that this technique had more disadvantages than advantages. The main disadvantage is that a rotating scan would have a large dead zone in the center of the welded spot. In addition, this type of scan would have required that the probe has a length of half the diameter of the welded point, which is much too small to place several coils.

- **Coils building**

Several topologies have been tested for pancake coils with a diameter of 2 mm and 1.5 mm. The coils are arranged in a T-shape. The spacing between the elements varies from 0.25 mm to 0.75 mm. Here is an example of a T-assembly.

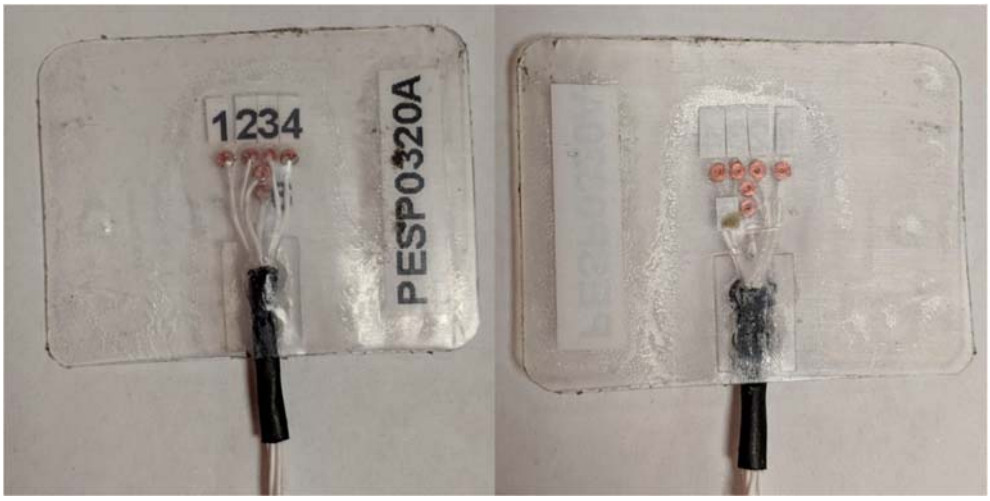


**Figure 44: Example of assembly of test coils. On the right we have the face of the top and on the left the face of the bottom which will be in contact with the spot weld.**

- **Workstation**

Due to the small size and imperfect profile of specimens, two small measuring stations were printed to facilitate manual scans. The stations consist of plastic plates with a hole for placing the samples. To level the face of the sample to be scanned with the plastic plate, adjustment screws were added to the bottom of the holes.

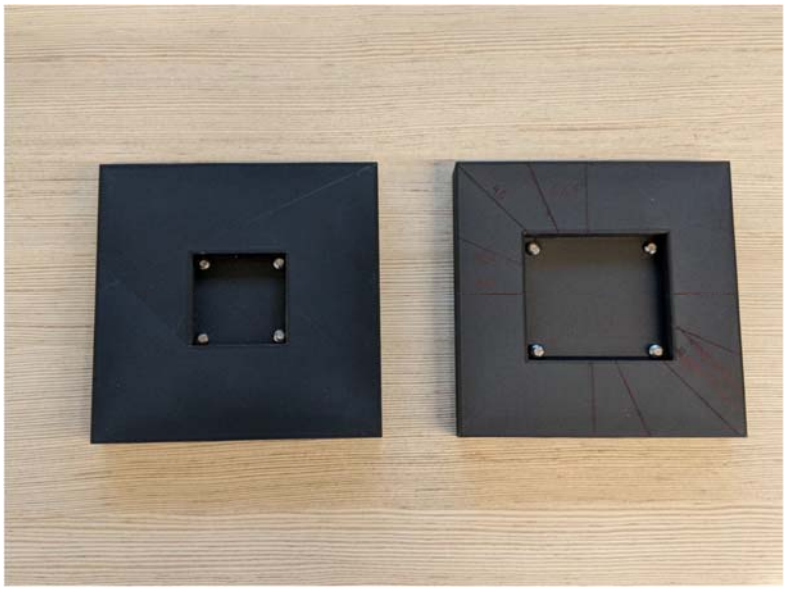

**Figure 45: Photo of the two measuring stations. The left station is used for 35mm×35mm specimens and right station for 45mm×45mm specimens.**

- **Preparation of samples**

Specimens were glued to a flat surface using double-sided tape. Care was taken to minimize the gap between the specimens to facilitate sliding of the test coils. To protect the test coil assemblies from sharp edges, specimens were covered with a Kapton tape. In addition, this protective layer enhances sliding of the test coils on specimens.

- **Programming the XY table**

To optimize the measurement time, all the samples are scanned in one shot (one acquisition). We enter the dimensions of the surface to scan in the user interface of the XY table. The resolution parameter is set to 0.25 mm/sample in both scan axes. These parameters must also be entered in the Magnifi Scan Parameters section.

- **Magnifi Settings**

To detect the defects of the samples, custom setups have been created for the different topologies to be tested. The scan settings must be adjusted to Encoder and Raster Scan. Several values of drive, gain and frequencies were tested to produce the results presented in the next section.

- **Acquisition**

The acquisition is done autonomously using the XY table.

### 4.3.3. Results & discussions

In order to determine the optimal topology to be used for weld point inspection, all topologies presented previously were tested and leads to the following conclusions:

• The Impedance topology is too sensitive to lift-off (spot weld surface due to indentation).

• The SDL topology can deal with lift-off but not enough sensitive to small crack and also it cannot distinguish between crack and the edge created by the indentation.

- Semi-Long topology is a good compromise between lift-off and crack detection.
- 1.5 mm diameter coils provide better accuracy for detecting small defects.
- The smallest crack detected using XY table, has a 0.2mm depth deep by using the XY table.

Below C-scans obtained by semi-long topology:

**Table 10: C-scans results obtained with the Topology Semi-Long.**

| Spot welds according to scan orientation | C-scan |
|---|---|
| 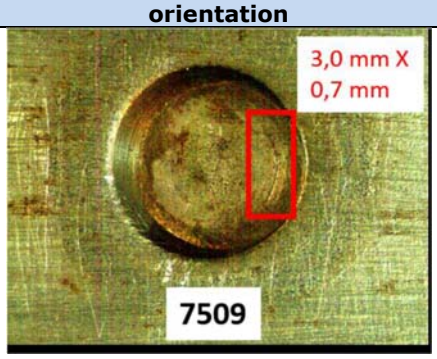 | 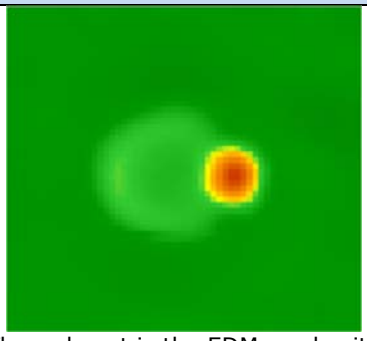 The red spot is the EDM crack with 0.7 mm depth |
| 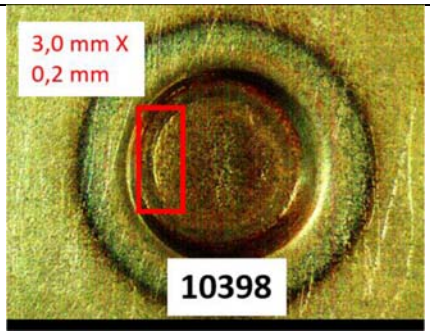 | 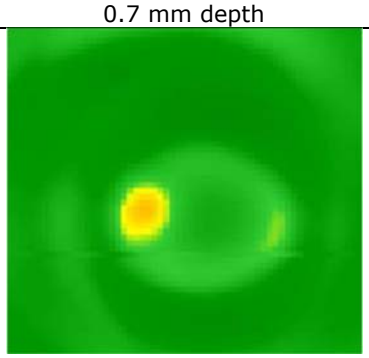 The yellow spot left is the EDM crack with 0.2 mm depth |
| 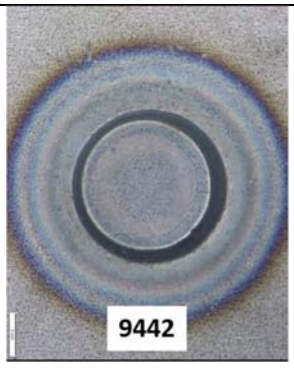 | 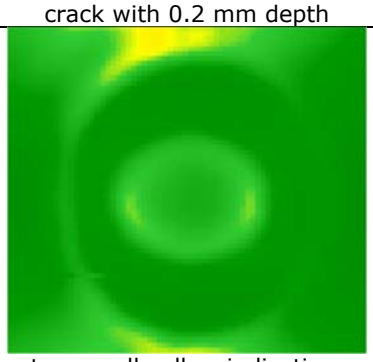 The two small yellow indications are the spot weld edge, indentation |

| | |
|---|---|
| 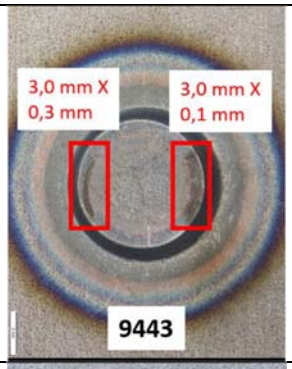 | 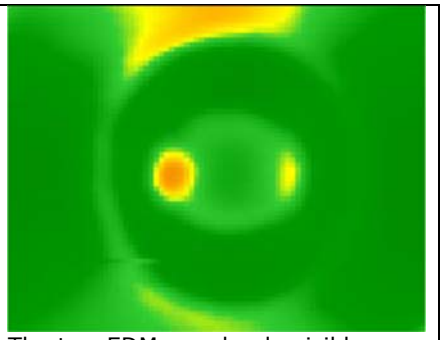 The two EDM are clearly visible |
| 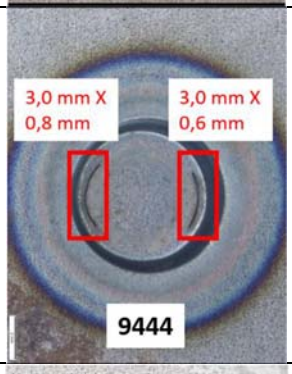 | 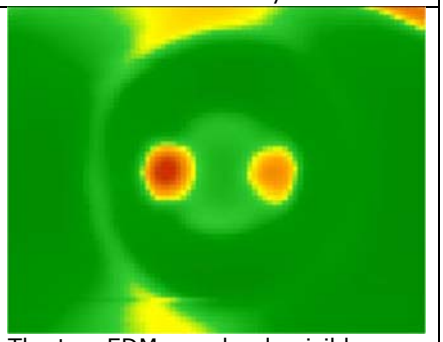 The two EDM are clearly visible |
| 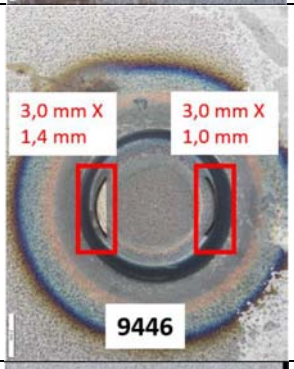 | 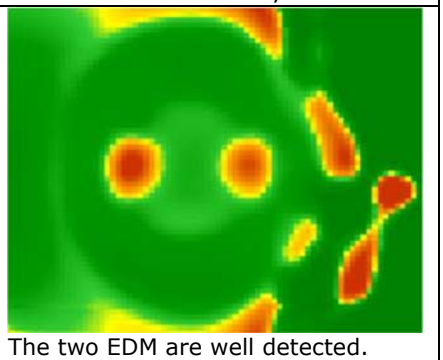 The two EDM are well detected. |
| 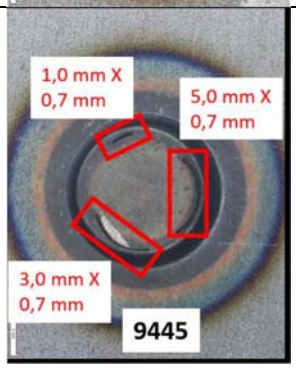 | 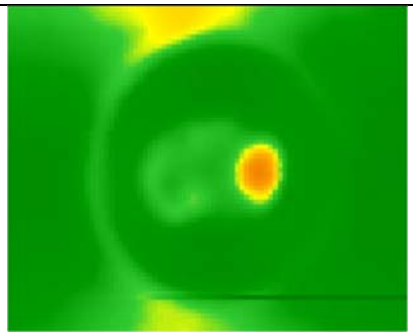 With Transverse scan, the EDM of 5mm×0.7mm is detected |

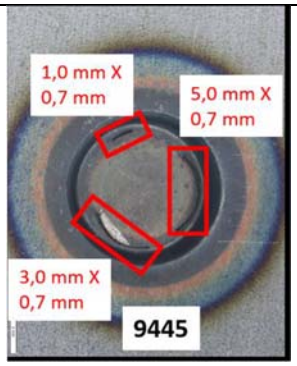


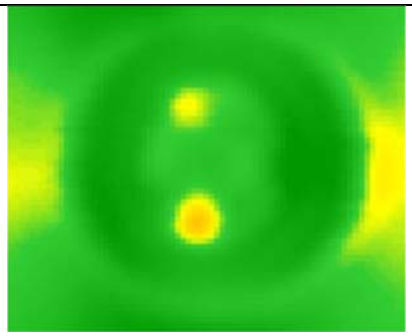

With axial scan, EDM of 1mm×0.7mm and EDM of 3mm×0.7mm are detected

Based on the above analysis, an ECA probe prototype was developed. The suitable topology for spot weld inspection is Semi-Long. The coils will have a diameter of 1.5 mm. The probe frequency is 750 kHz. To maximize the resolution of the Y scan, three rows of coils were built with 0.75 mm Y-shifted. This arrangement allows a resolution of 0.5 mm/sample. Since the transverse results are acceptable, only the semi-Long transverse topology is used and the user will have to make 4 passes to cover all crack orientations (transverse, axial and oblique) on a spot weld.

The mechanics of the probe is a padded type to allow the ECT elements to fit the spot weld geometry and overcome the lift-off problem induced by indentation. The coverage area of the probe is 20 mm.


**Figure 46: New Padded ECA probe developed in this project for RSW.**

To cover the transverse, axial and oblique orientations, four passes are required as indicated in Figure 47.

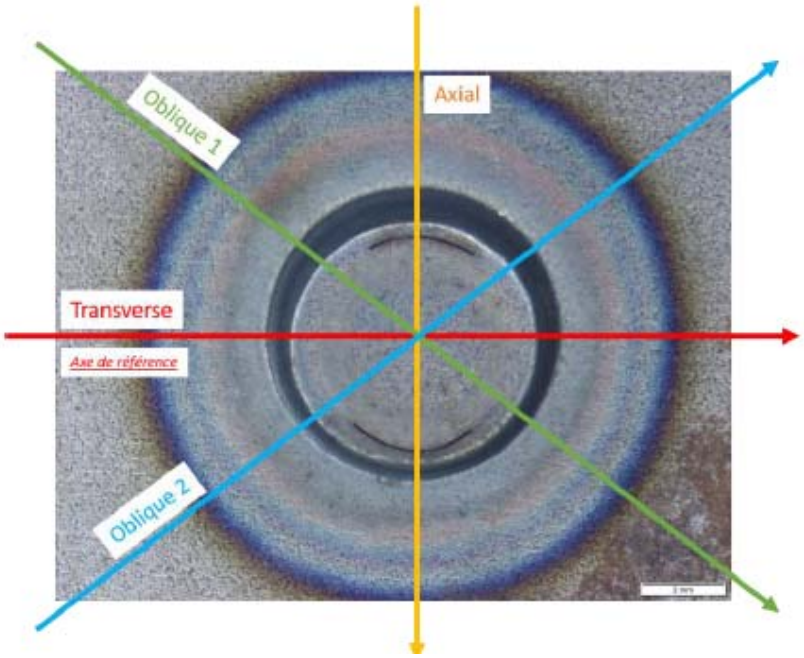


**Figure 47: Scan orientations.**

C-scans results are presented below. For each specimen, a photo with optical microscope is given to show crack feature and ECA C-scans with 4 scans for each spot weld: (Axial, Transverse, Oblique 1, and Oblique 2).

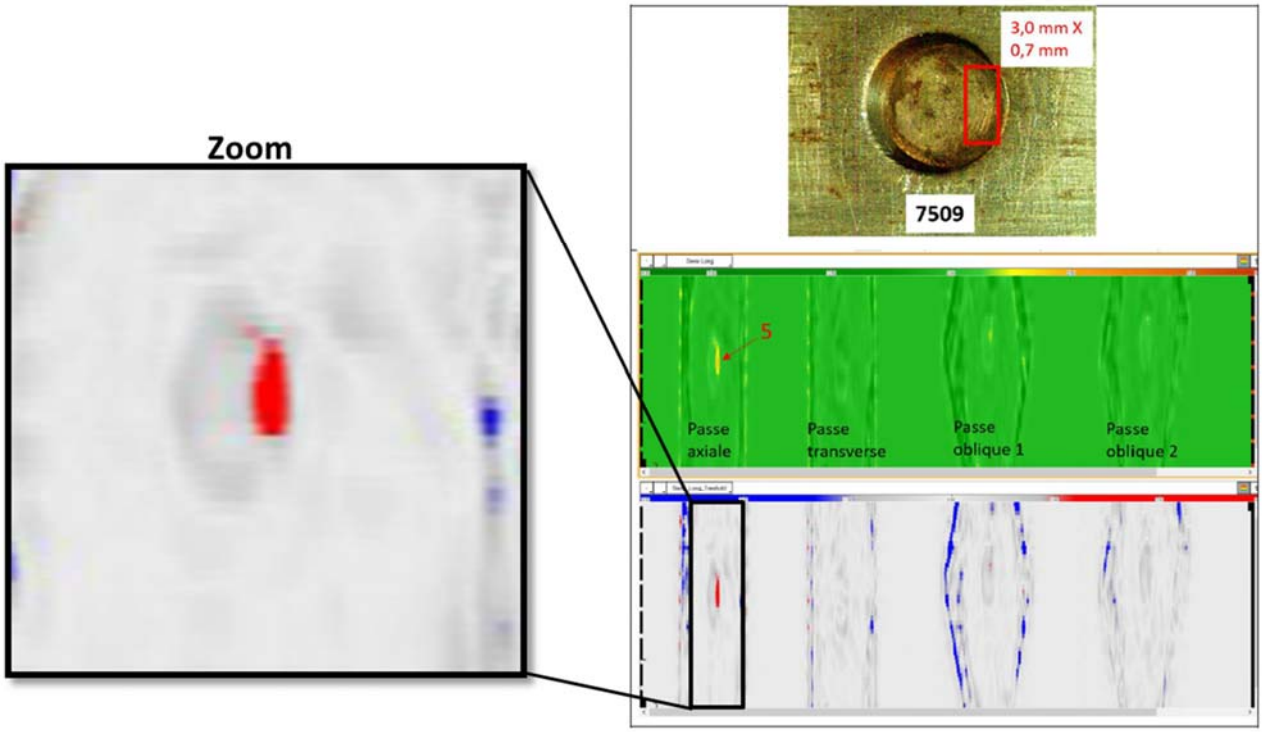


**Figure 48: C-scans of specimen n°7509.**

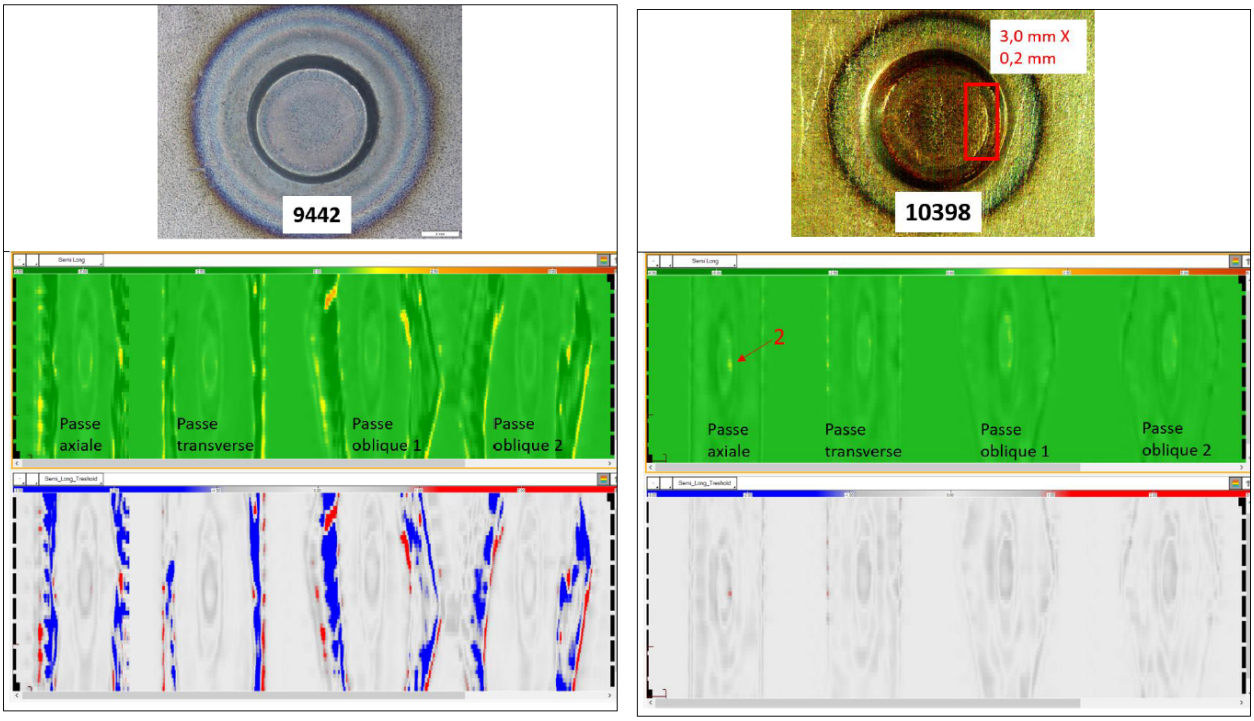


Figure 49: C-scans of specimens n°9442 and 10398.

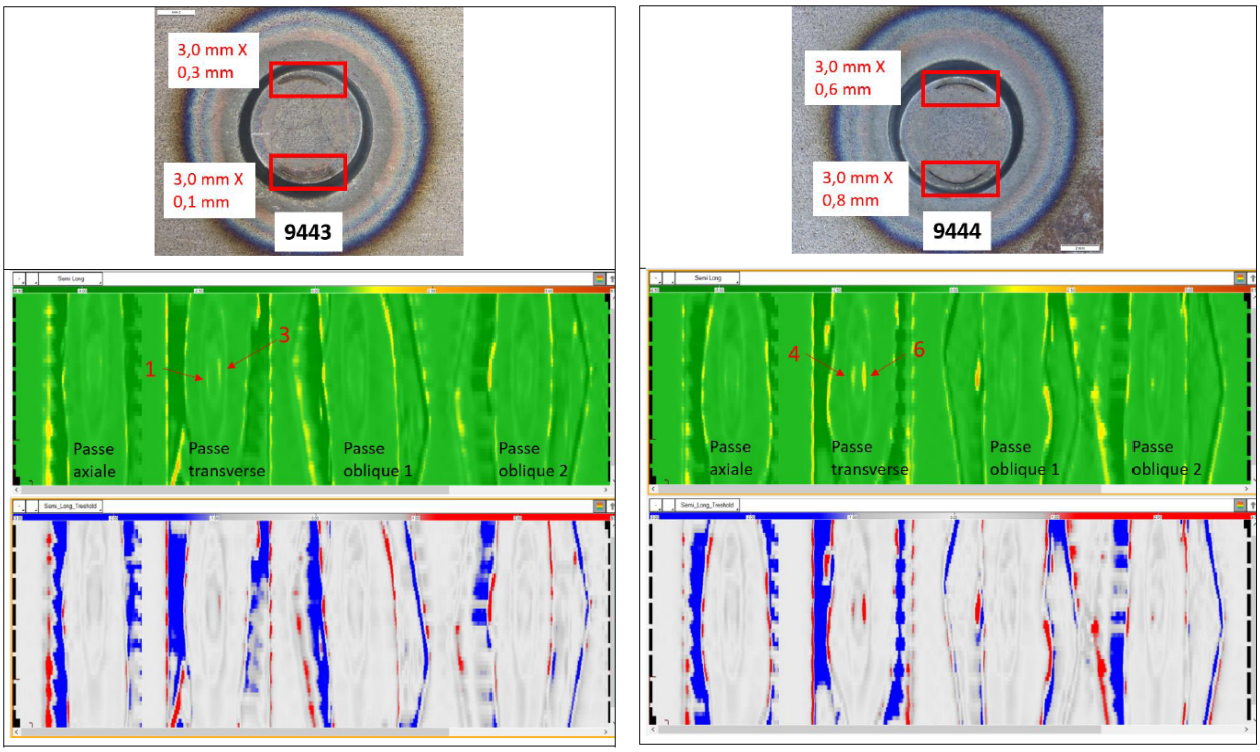


Figure 50: C-scans of specimens.

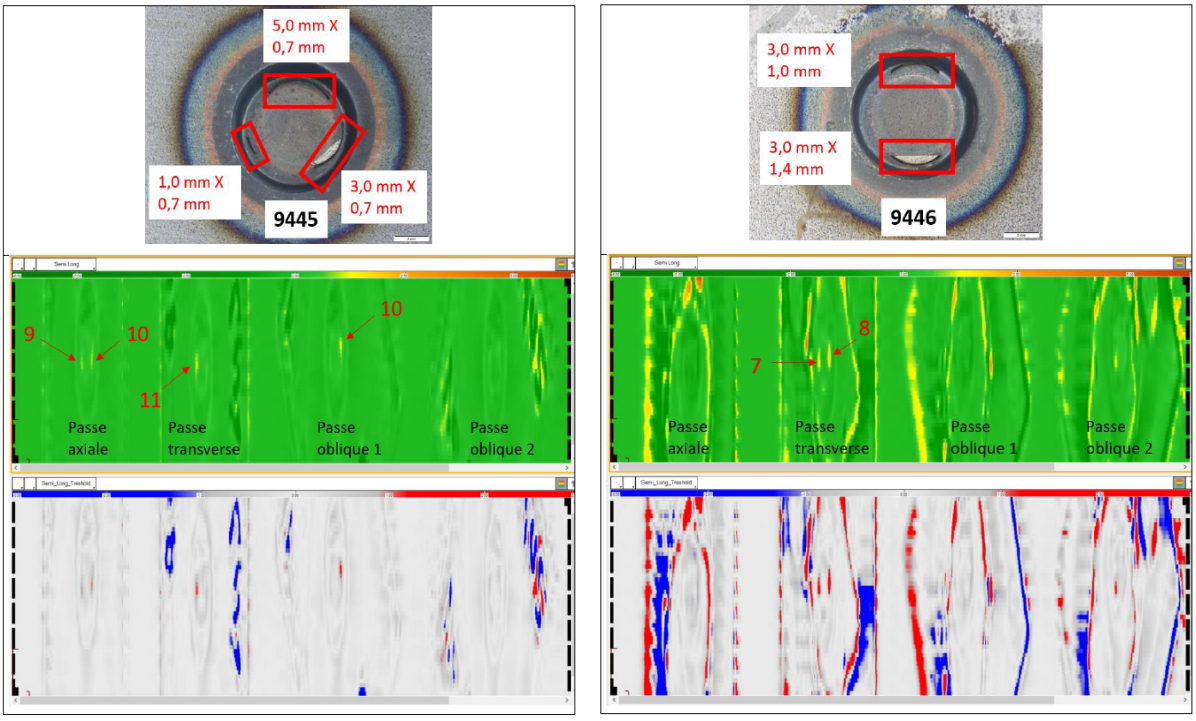


**Figure 51: C-scans of specimens.**

It has been found that all cracks have been detected with ECA, except the crack with 0.1mm depth. The detection is possible in our case but in blind inspection it will be difficult to distinguish between the signal coming from the indentation and the one from crack. The amplitude is similar. Therefore, the minimum depth detected by ECA is 0.2mm.

A correlation between signal amplitude and crack depth was established. It can be noted that amplitude of signal increases with crack depth. A sizing curve was then defined and the model for depth estimation based on amplitude measurement from transverse scan was established. This model was directly implemented in the software "Magnifi", which allows an automatic crack depth estimation in real time after the scan completed.

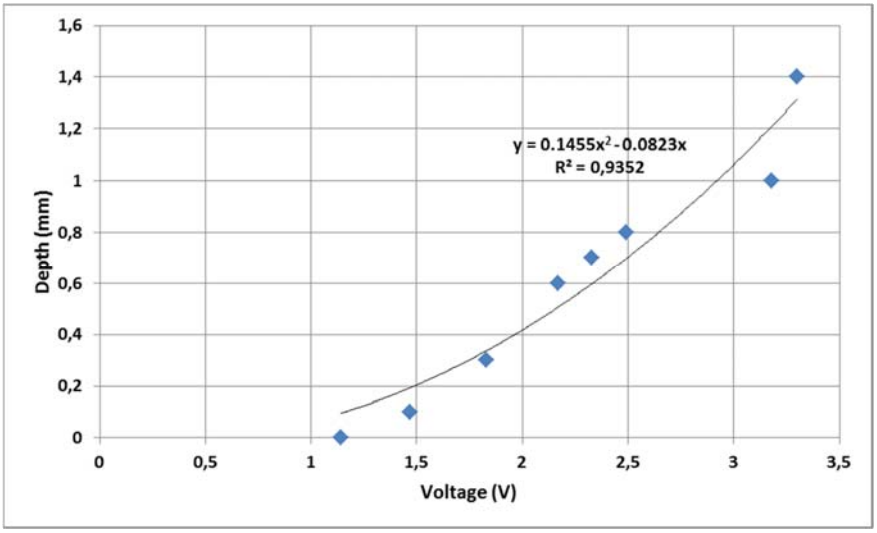


**Figure 52: Sizing curve.**

To verify depth estimation, a second inspection was carried on all specimens used previously. Crack depth estimation result was very encouraging and presented in the table below. The accuracy is around 0.1mm which is very satisfying.

**Table 11: Depth estimation: Second inspection.**

| Crack n° | Depth (mm) | Estimated depth with ECA (mm) | Deviation |
|---|---|---|---|
| 3 | 0.3 | 0.4 | 33.30% |
| 4 | 0.6 | 0.7 | 16.70% |
| 5 | 0.7 | 0.9 | 28.60% |
| 6 | 0.8 | 0.7 | 12.50% |
| 7 | 1 | 0.9 | 10% |
| 8 | 1.4 | 1.3 | 7.10% |

To summarize, at this stage of the program, all ECA probes available on the market are not suitable for RSW application. No solution based on ECA or ECT was found in the literature and also among suppliers. Trials done with a mono element Eddy Current at the beginning of this program was not conclusive. To provide an inspection method able to estimate LME crack depth, a new ECA padded probe was developed. Various topologies were investigated, and the Transverse Driver configuration was chosen. This configuration requires four passes to cover all crack orientations. The approach to be followed for the development of ECA solution for LME crack depth estimation, based on a sizing curve, is the following:

- Choice of the MTC of specimens. It is important to note that ECA response will depend on steel grade and also the Zn layer. The sizing curve is available only for one MTC. A setup is required for each new MTC.
- Use of specimens with EDM notches with different known depth. EDM notches features were chosen to be closer as possible to LME cracks in term of opening (0.1mm), form (circular), location (closer to indentation inside the nugget which is representative of LME location and is the most complicated case due to the lift-off generated to the ECA probe).
- Determination of the appropriate topology of the ECA probe.
- Build of the ECA probe
- Determination of the sizing curve: Find the correlation between ECA response vs EDM depth and establish the model. The model accuracy will depend on the number of inputs (EDM depth).
- Implementation of the model on ECA software for an automatic calculation of EDM depth.
- Evaluate the accuracy of the model by re-testing all specimens.
- Evaluate the reliability with a blind inspection with different operator (see paragraph 4.3.4.3).

All the steps cited above are investigated and already finished. To extend the use of ECA probe for real LME cracks located inside and outside indentation with the presence of Zn layer and for one MTC configuration, a relevant data base is required. It should cover a large range of LME depth and also length since ECA is sensitive to the volume of the crack i.e. opening, length and depth. This should be deeply investigated and therefore several sizing curves established, based on crack length. This length can be approximated with C-Scans followed by an automatic selection of the suitable sizing curve. Furthermore, all specimens must be characterized by Computed Tomography (CT). As this step requires a consequent budget for CT scans, it can be considered as future prospects for project extension.

### 4.3.4. Practice recommendations

#### 4.3.4.1. Applicability

ECA method has potential for LME crack depth estimation in laboratory and production conditions. Due to the complexity of LME features (i.e. location outside and inside nugget and also closer to indentation, form: linear or circular with some networks, very thin opening which decreases with depth and can be partially filled with Zn, also the presence of Zn on surface and residual copper can disturb measurements), a classification of three categories can be considered:

- Category 1: Depth < 0.2 mm
- Category 2: 0.2mm ≤ Depth< mid-thickness
- Category 3: Depth≥ mid-thickness

#### 4.3.4.2. Implementation

Implementation requires a learning step for LME characterization for each MTC configuration. This step is essential and involves the production of a large range of LME crack depth which must be characterized with CT scans followed by a sizing curve establishment.

For manual control, operators must be trained and qualified to be able to apply the control protocol.

For automation inspection in production, the probe can be embarked to a robot. An industrialization study is needed.

#### 4.3.4.3. Reliability

To verify the reliability of the model, a blind inspection has been carried out by new operator. Results are displayed in Table 12. It has been found that depth estimation is less accurate in blind inspection but is sufficient for crack classification in categories. One can note a success rate of 70% when cracks are classified according to their depth.

**Table 12: Blind depth estimation: Third inspection**

| Crack n° | Depth (mm) | Estimated depth with ECA (mm) | Deviation |
|---|---|---|---|
| 3 | 0.3 | 1.1 | 266.66% |
| 4 | 0.6 | 1 | 66.66% |
| 5 | 0.7 | 0.8 | 14.28% |
| 6 | 0.8 | 1.5 | 87.50% |
| 7 | 1 | 0.9 | 10% |
| 8 | 1.4 | 1.1 | 21.42% |

#### 4.3.4.4. Application Cost

*Production Environment*

The average price of basic ECA equipment (portable station + RSW probe) is about 87 k€. The industrialization of the solution for production application may reach 100 k€-150k€ (including the robot).

Considering the following assumptions:

- The ECA probe will be embarked on the head of the robot. First the robot needs to locate the spot weld position. Apply four passes (the actual solution developed but further investigation can be conducted to improve the probe and reduce the number of passes) and estimate the maximum crack depth.
- Final solution cost: 150k€
- Depreciation period= 5 years
- Robot working time per year= 3760 hours (16hours per day, 5 days per week and 47 weeks per year; 5 weeks for maintenance)
- Number of spots per minute= 1 spot weld; Spot weld time= 1min
- Productivity= 80% => Spot time= 1.25 minute.
- Total number of spots weld per day= 768 spots. (= 16*60/(1.25))
- Number of RSW in 5 years: 768×5×47×5=902400 spot welds

Depreciation per spot weld calculated according to the formula (4), is estimated to 0.16 € for installation cost 150k€.

*Laboratory Environment*

The cost of basic instrumentation is approximately 87 k€.

Instrumentation components are:
- ECA probe: 10k€ (available for the prototype developed with 4 passes required for each spot weld).
- Ectane®2: 55 k€
- MAGNIFI-4.X-FUL-HK: 14 k€
- EDDYFI-LAPTOP-MAGNIFI: 2.7 k€
- ECTANE2-E64RNM-ESP-N2: 4.8 k€

For the following assumption (the same as for AE, MPI and PECT for comparison):
- 1 operator /machine
- Working time of the machine = 4Hours per day for 30 weeks per year.
- Number of spots per day=200 spots; Number of spots per year =200*5*30= 30000 spots; 150000 spots in 5 years

Depreciation per spot weld calculated according to the formula (4), is estimated to 0.58€

$$\text{Depreciation per spot weld} = \frac{87000}{150000} = 0.58€$$

#### 4.3.4.5. Automation

Based on the feedback of other ECA systems used in Industry and also based on discussions with suppliers such as Eddyfi, the automation of the controls is possible. The mains steps for the achieving of an experiment are detailed in section 4.3.3. The idea is so to automatize these steps. A robot is consequently required; the one used for welding cannot be used for NDT by ECA because the two tasks (welding and NDT by ECA) cannot be executed simultaneously. Once the weld is carried out, a cooling time is needed before applying the ECA probe. This constraint should be taken into account. In addition, with regard to current development, the scan time of a given spot (4 scans in total) is larger than its achieving time. To reduce this time, another probe should be developed to permit scanning the spot-weld in one shoot.

### 4.3.5. Conclusion

ECA is an NDT technique able to detect LME cracks, based on a learning step. Its reliability is closely linked to the learning step. This technique is unfortunately sensitive to the presence of zinc, and this should be considered in the learning step. Concerning the in-field automation, the technique is not technically mature to be deployed. Besides, it could be used to assess the depth but many investigations to make it more robust are required. Characterization is also based on a learning step.

## 4.4. Phased Array Ultrasonic Testing (PAUT)

### 4.4.1. Background

Ultrasonic Testing (UT) uses high frequency sound energy to conduct examinations and make measurements. Ultrasonic inspection can be used for flaw detection/evaluation, dimensional measurements, material characterization, and more. A typical UT inspection system consists of several functional units, such as the pulser/receiver, transducer, and display devices. A pulser/receiver is an electronic device that can produce high voltage electrical pulses. Driven by the pulser, the transducer generates high frequency ultrasonic energy. The sound energy is introduced and propagates through the materials in the form of waves. When there is a discontinuity (such as a crack) in the wave path, part of the energy will be reflected back from the flaw surface. The reflected wave signal is transformed into an electrical signal by the transducer and is displayed on a screen. In the example below a typical pulse echo inspection configuration is illustrated. The reflected signal amplitude is displayed versus time. Signal travel time can be directly related to the travel distance. From the signal, information about the reflector location, size, orientation and other features can be determined.

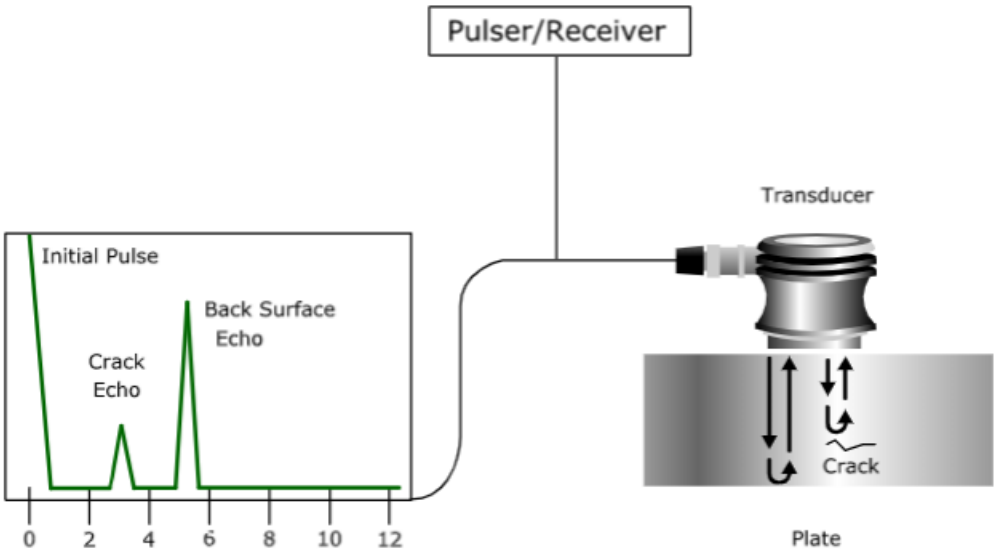


**Figure 53: Pulse-echo configuration.**

Manual Ultrasonic technique using A-scan equipment is widely used for NDT steel welds and in particular for resistance spot welds. In the case of RSW, a dedicated transducer has been developed by Krautkramer in 1986 enabling nugget diameter evaluation without gel couplant. A rubber bullet with dry contact between transducer and spot weld has been patented. This solution has been used later by various companies to develop industrial systems (GE). The main issue with conventional UT is that the technique is highly operator oriented and interpretation of signals requires a significant experience and good operator skills. In the work of M. Thornton & all [7], it has been stated that only 20% accuracy was achieved by experienced operators for nugget weld sizing using conventional A-scan method. On that way, and due to volume production in automotive industry, spot weld checking requires a robustness automated system. Conventional UT is not suitable for cracks detection and characterization due to low reproducibility and operator skills influence.

Phased array UT is a relatively new technique. It can be defined as an upgrade of the conventional UT. The probe is made up of numerous small piezo-electric elements, each of which is pulsed individually with computer-calculated timing. The order and the temporal sequence of elements activation are given by the "delay laws", or "focal laws" (the focal laws integrate the laws of delays, as well as other information).

Below an example of different delay laws:

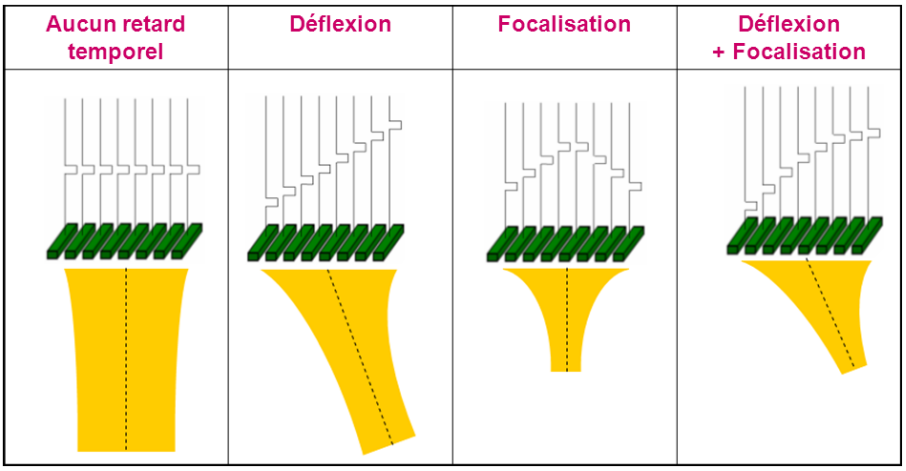


**Figure 54: Representation of delay laws according to the types of beams generated.**

This technique can be used to inspect more complex geometries that are difficult and much slower to inspect with single probes. PAUT can be used to inspect almost any material where traditional UT method have been utilized and is often used for weld inspections and crack detection. The main benefit of phased array is improving resolution trough focalization of the energy of the ultrasound in a desired point (or area). PAUT is also able to create detailed and accurate cross-sections of the inspected area and is particularly useful in situations where there is less area for mechanical scanning because it's able to sweep the beam without moving the probe.

Different presentation of result is possible. The most basic is A-scan presentation (Figure 53), in which echo amplitude and transit time are plotted on a simple grid with the vertical axis representing amplitude and the horizontal axis representing time. Another way of presenting this information is as a B-scan view (Figure 55). It is a means of ultrasonic data presentation which displays a cross section of the specimen indicating the approximate length (as detected per scan) of reflectors and their relative positions. C-scan is a 2D view of ultrasonic data displayed as a top or plan view of the test specimen). D-scan (nonparallel scan) shows the data collected when scanning the transducer pair perpendicular to the direction of the sound beam along a weld.

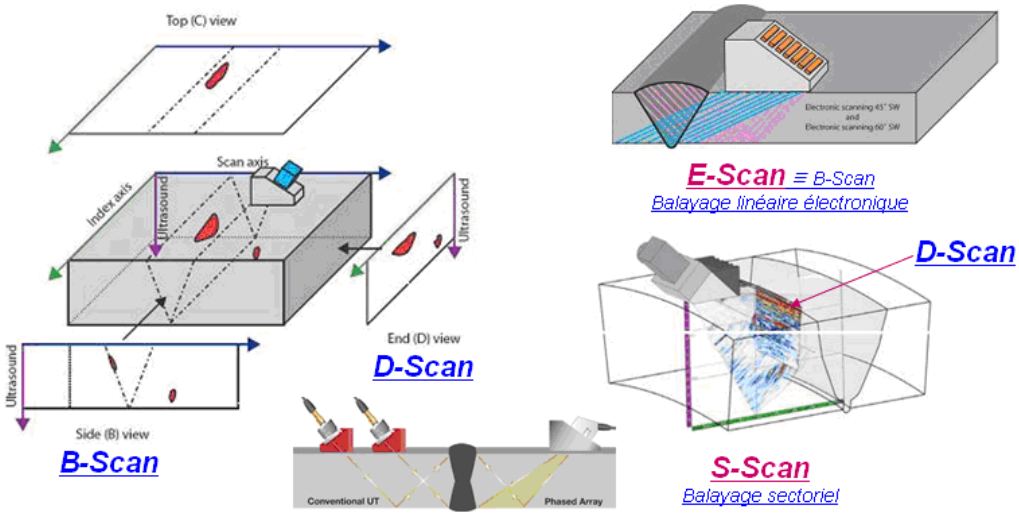


**Figure 55: Example of different scan view.**

### 4.4.2. Methodology & Experiments

#### 4.4.2.1. Manual PAUT

At the beginning of the project, detection of LME cracks was evaluated using manual PAUT probe (Figure 57).

Specimens investigated were first controlled with Magnetic Particle Inspection (MPI) and then classified into three categories (healthy, light LME, heavy or intense LME) and compared to PAUT results.

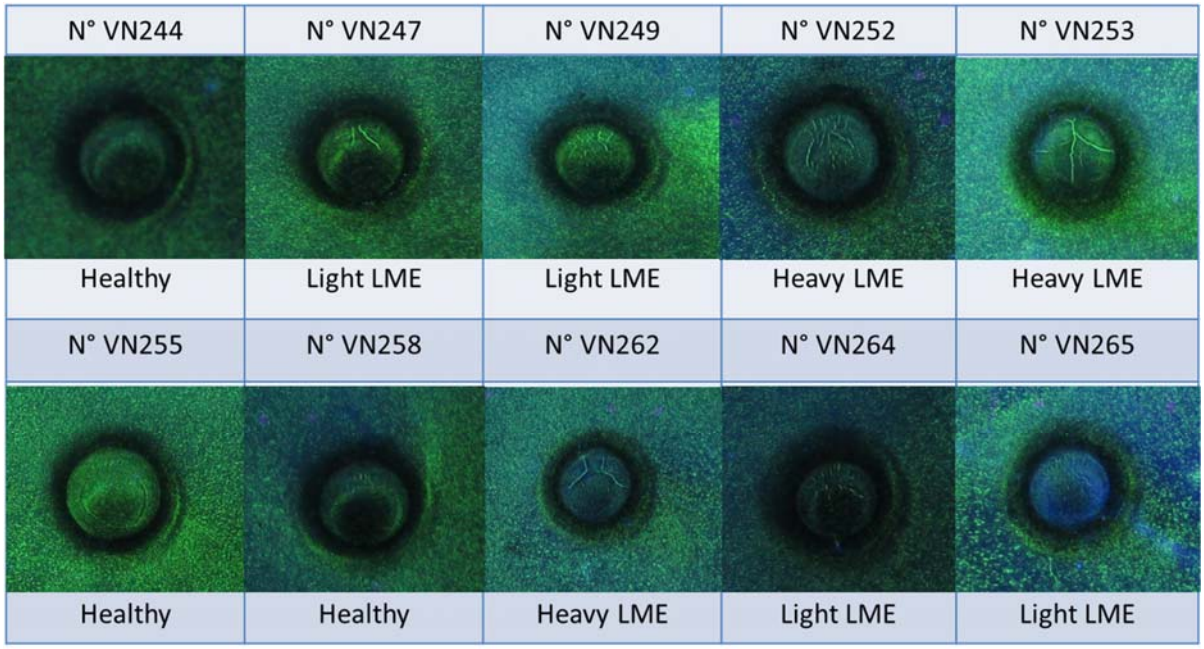


**Figure 56: Classification of spot weld according to the level of LME crack using MPI.**

The setup of the PA system is based on a calibration phase carried out on carbon steel block with a notch of 2mm height, located on the upper surface. Below the setup:

Ultrasonic system: M2M GEKKO n° BPINS000720

Probe mounted on a rexolite wedge

- Frequency: 15MHz
- Linear array of 64 elements
- Pitch = 0,31mm
- Elevation = 7mm
- Serial 13218-1001
- Wedge LW60° - serial 13220-1001 - $V_{rexolite}$ = 2350m/s

Acquisition cycle

- Sectorial scan with sweep range from 60° to 89°
- Aperture 64 = elements
- Focalization = 20mm sound path

Specimens were controlled using PA probe which is moved around the spot weld with 360°.

Figure 57 Phased array probe positioned laterally from the spot weld.

#### 4.4.2.2. Numerical Simulation

To improve LME detection and automate the inspection using immersion bench, simulation using CIVA software were carried out. The aim is to define the suitable probe configuration in terms of delay law calculation, frequency of the probe, orientation and distance from the spot weld. Simulation enables to test different configuration and allow understanding of echoes response from calibrated defects. The specimen used is a 2D cross section of spot weld extracted from CT scans. A calibrated defect with features closed to LME cracks is introduced inside the spot weld.

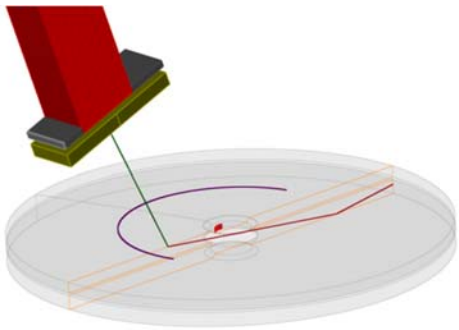

Figure 58: Simulation of PAUT inspection of a spot weld with calibrated defect.

#### 4.4.2.3. Automated PAUT

In order to automate the PAUT method and provide relevant cartography of spot welds, the rotation movement of the probe should be mechanized and encoded. The use of immersion tank is chosen to improve the coupling (limitation of the effects of the surface condition to ensure the propagation of ultrasound within the test piece). ISA immersion tank was then adapted for RSW inspection. A support for specimen and a support of PAUT probe were designed and manufactured. The probe can be positioned at certain distance from the spot weld and oriented to generate creeping waves on specimen surface. The probe turns around the spot weld with 360°. The acquisition step is 0.1°. The water between the probe and the spot weld ensure ultrasonic wave propagation. The immersion tank is located in Institute de Soudure, Yutz. The control of this equipment as well as the acquisition of ultrasound data are performed by the Analis V2.6.6 software.

The acquisition system is MultiX++ controlled by Multi2000 v6.12.3 software. The probe is a linear array with 64 elements and a frequency of 15MHz with a 0.31mm pitch and 0.05mm gap.

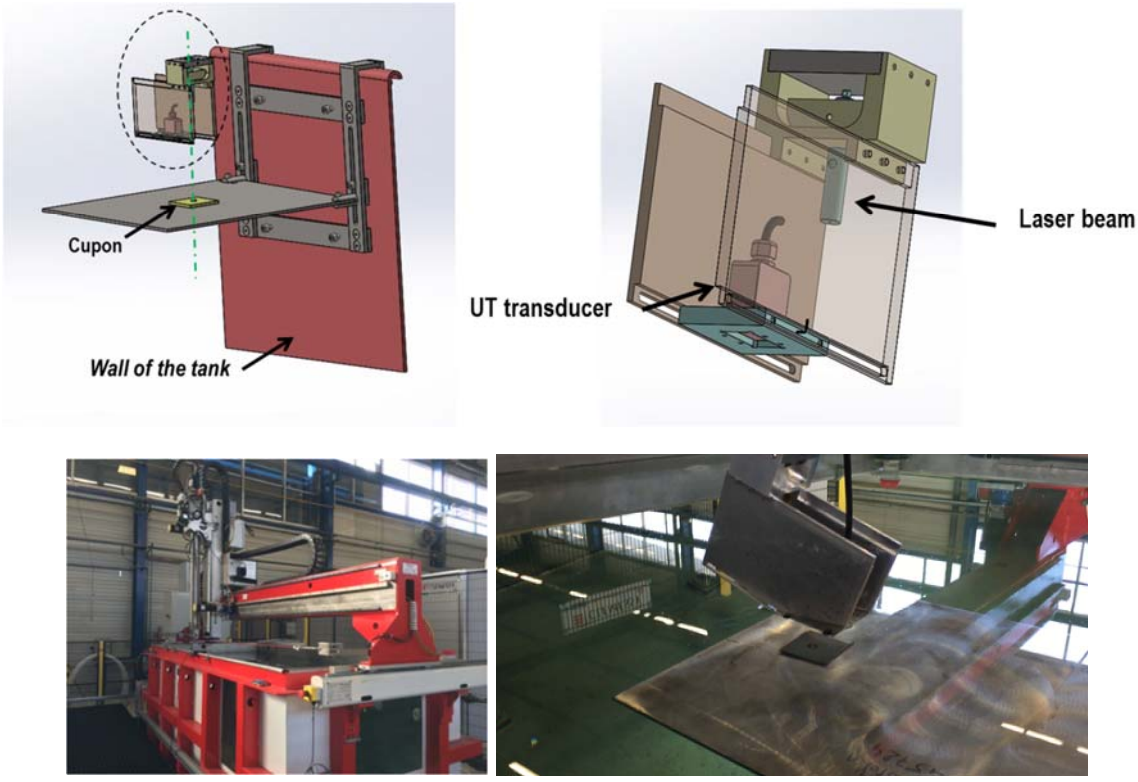


**Figure 59: Designed supports for specimen and probe (upper left). Zoom of the probe support upper right). Immersion tank (bottom left). Zoom of specimen and probe supports (bottom right).**

For all trials, the setup applied is shown in table below.

**Table 13: Setup**

| Nb elt / group | Step | First element | Wave type | Angular déviation | Nb step | Focalisation | Angle of incidence | Water column |
|---|---|---|---|---|---|---|---|---|
| 32 | 4 | 1 | T | 54 to 86° | 16 | 0.5 mm | 21.7° | 22.2mm |

The adjustment and the position of gate for each series of test are described below.

There are two trials steps:

- Trials 1 : were carried out on the following specimens :
  - Specimen with an LME cracks outside the indentation (slight tilt between the two sheets of specimens, more detail is given in paragraph 5.5.3.3: n°8457, n°8458 et 8459
  - Specimen without defect : n° 8289
  - Specimen with EDM crack inside the spot weld near indentation: n°10394, n°7509, n°10398.

For these trials, the gain was adjusted to the maximum due to the absence of reference part.

- Trials 2 : were carried out on the following specimens :
  - n°7523, n°7525
  - n°7536, n°7537
  - n°7516, n°7548, n°7549
  - n°7918, n°7969
  - n°10371, n°10372
  - n°10394, n°10398, n°7509

For these trials, the gain was set so that it does not saturate the defect signal. Two gates positions have been investigated (Figure 60):

- A gate "PIECE" was positioned in the volume of the sample (1/2 skip)
- A gate "ALL" was positioned before entry into the sample and after so as to record the signal on the skip

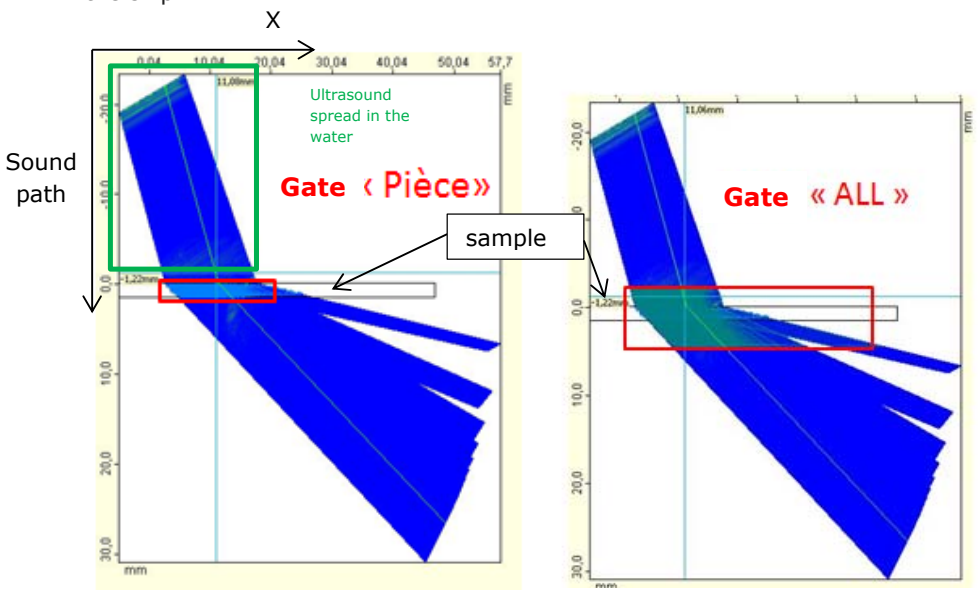


**Figure 60 : Illustration of the position of gates**

### 4.4.3. Results & Discussions

#### 4.4.3.1. Manual PAUT

The probe is positioned at about 5mm laterally away from the spot weld and inclined with an angle of 60° to try to generate sub-surface waves which travel parallel to the spot weld surface, called creeping waves. For each specimen (spot weld), experimental sector scan results obtained at the position of probe which is marked with an arrow, are shown in the following images (

Table 14). S-scans are produced when a phased array is used to electronically sweep an ultrasonic beam through a range of angles. In our case, the angle varies from 60° to 89°. The data collected is displayed as a B-scan image which shows the angular segment covered by the beam.

The large amplitude indication shown in the S-scan seems to come from the direct path reflection of the LME crack. Moving the probe radially away from the LME crack, results in the disappearance of the indication.

It's worth noting that detection is possible when LME crack is in front of the beam and also when the probe is positioned at the same side to LME crack. At this stage it is difficult to determine which waves mode has a good interaction with LME crack. The configuration of probe used, generate mainly creeping waves but other surface waves such as Rayleigh and also longitudinal and transversal waves can be generated.

**Table 14: Detection of LME cracks with manual PAUT.**

| VN249 |
|---|
| 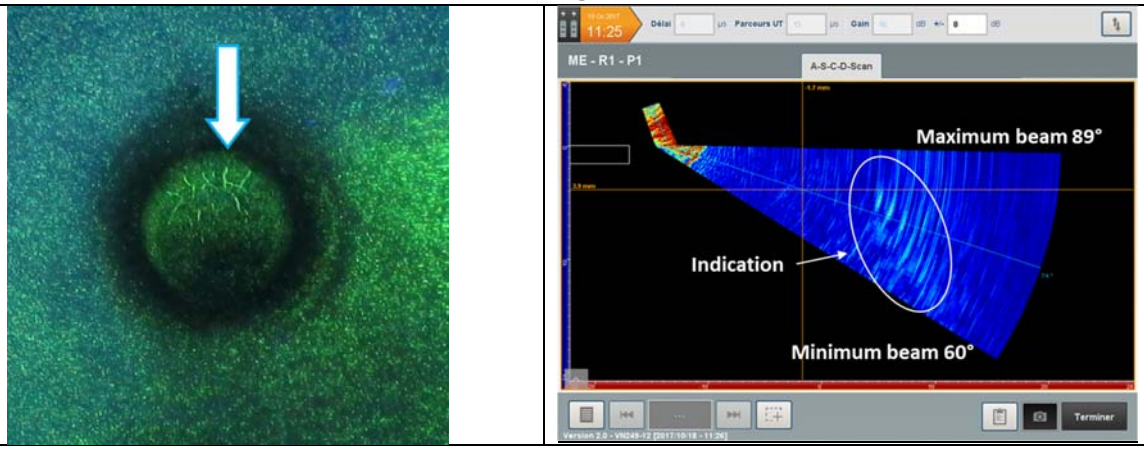  |
| S-scan recorded at the indicated position of the probe (arrow).<br>Indication amplitude < 50% |

| VN252 |
|---|
| 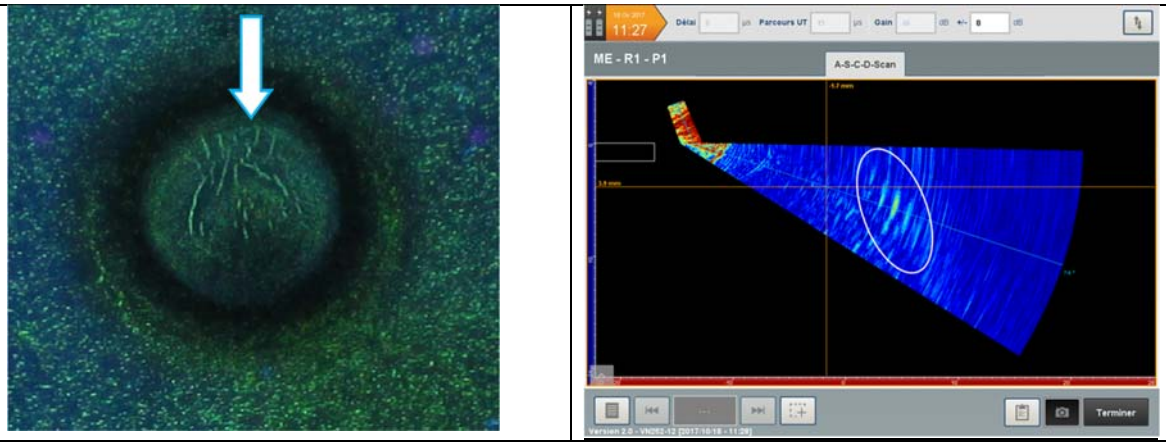  |
| Indication amplitude > 50% |

| VN253 1/3 |
|---|
| 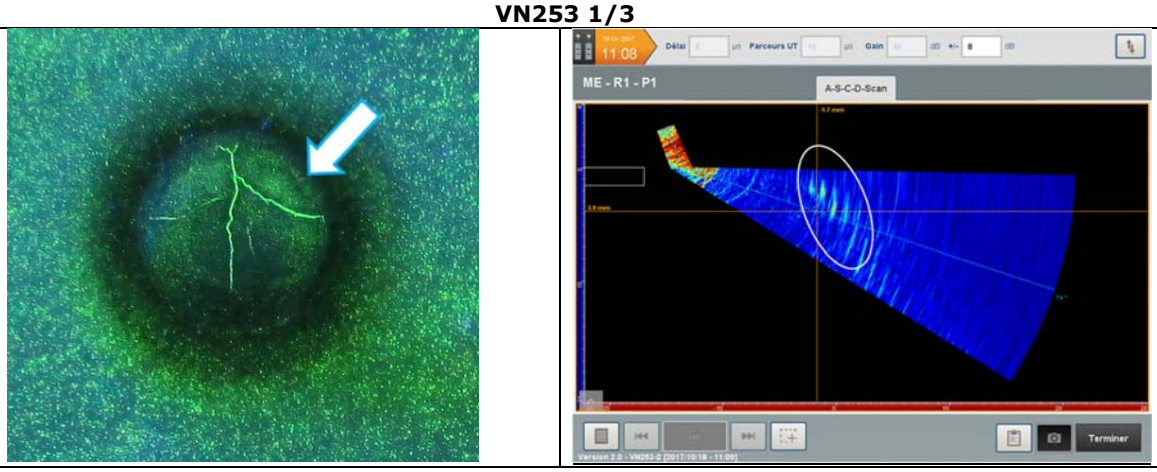  |
| Indication amplitude > 50% |

| VN253 2/3 | |
|---|---|
| 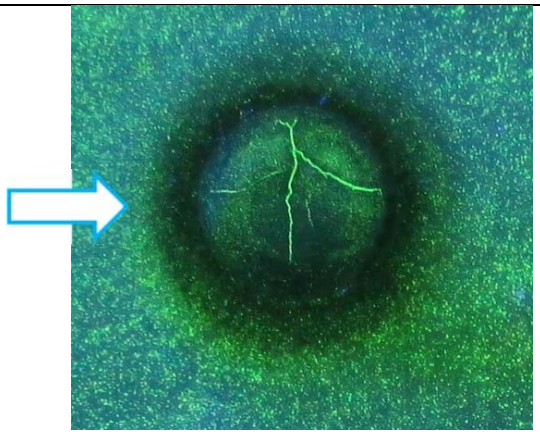 | 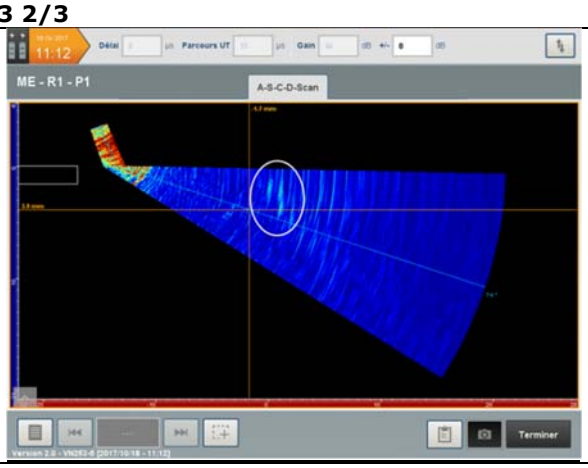 |
| Indication amplitude > 50% | |



| VN253 3/3 | |
|---|---|
| 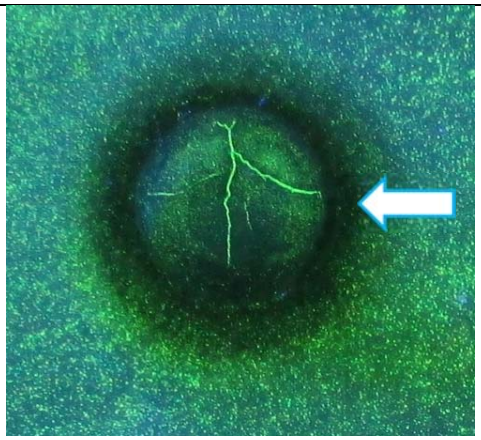 | 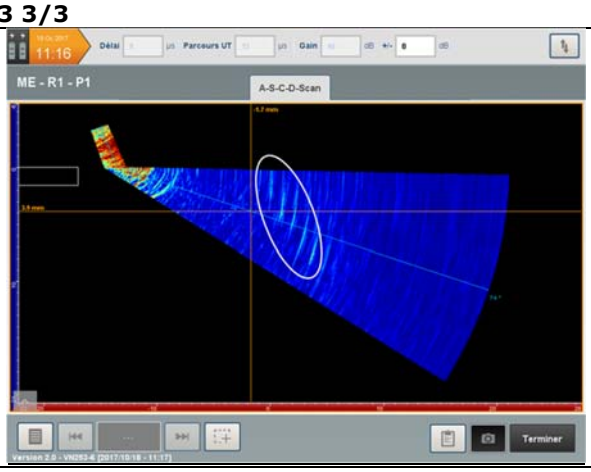 |
| Indication amplitude > 50% | |



| VN258 | |
|---|---|
| 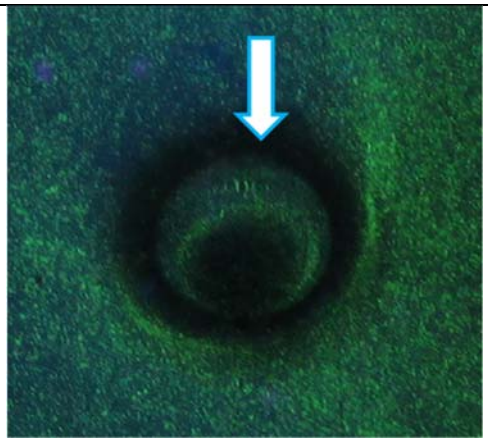 | 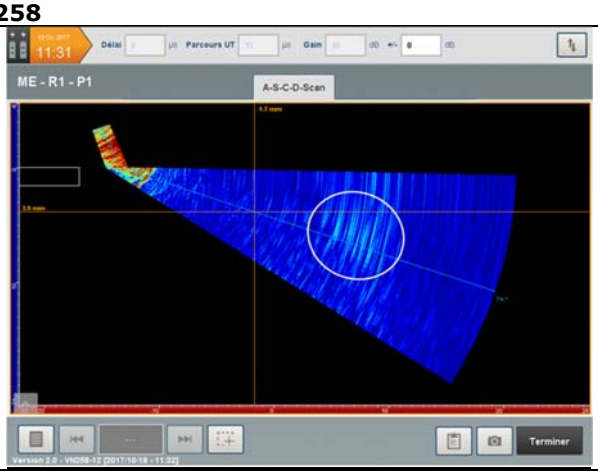 |
| Indication amplitude < 50% | |

| **VN262 1/2** |
|---|
| 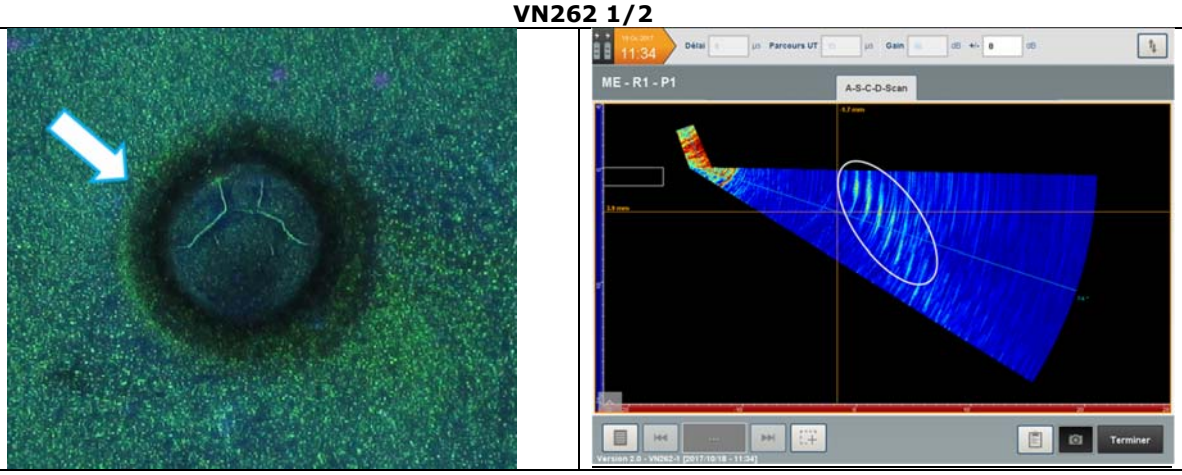 |
| Indication amplitude > 50% |

| **VN262 2/2** |
|---|
| 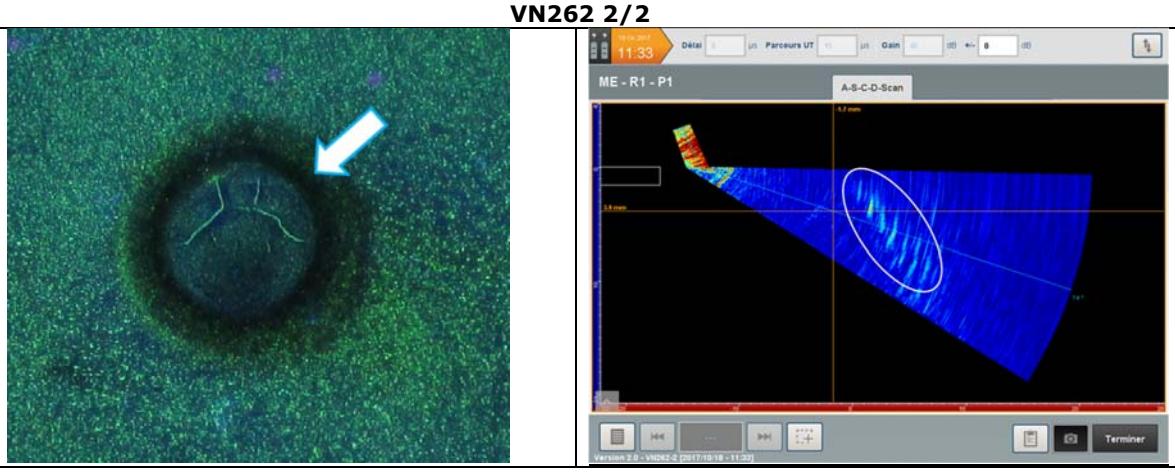 |
| Indication amplitude > 50% |

| **VN264** |
|---|
| 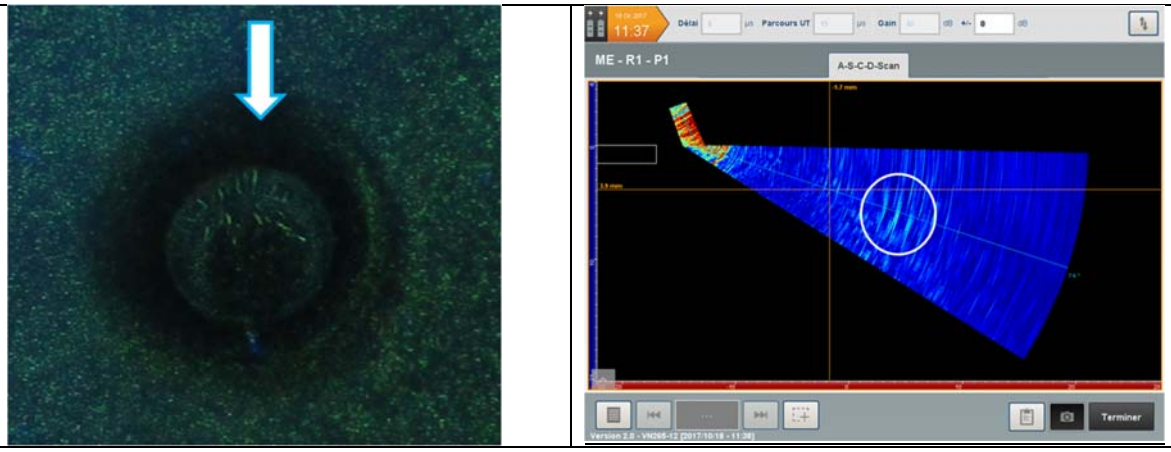 |
| Indication amplitude < 50% |

The comparison between MPI and manual PAUT classification is shown in Table 15. A color code was given to each category:

- Healthy: Green color which is equivalent to low amplitude indication by PAUT <20%
- Light LME: Orange color which is equivalent to medium amplitude indication by 20%≤PAUT <50%
- Heavy/Intense LME: Red color which is equivalent to high amplitude indication by PAUT ≥50%

A good correlation between MPI and PAUT classification is obtained when the same color is obtained for both classifications in Table 15. Among the 10 spot welds controlled, only two misclassifications are observed.

- Light LME of the specimen n°VN247 was not detected by PAUT. No significant indication recorded; the S-scan was similar to healthy spot.
- Healthy spot of the specimen n°VN258 was misclassified with PAUT. An intermediate indication was detected by PAUT.

**Table 15: Comparison between MPI and PAUT classification**

| Specimen N° | LME category (using MPI) | Amplitude level of PAUT | Observation |
|---|---|---|---|
| VN244 | Healthy | <20% | Good correlation between PAUT and MPI |
| VN247 | Light LME | <20% | Light LME not detected |
| VN249 | Light LME | <50% | Good correlation between PAUT and MPI |
| VN252 | Severe LME | ≥50% | Good correlation between PAUT and MPI |
| VN253 | Severe LME | ≥50% | Good correlation between PAUT and MPI |
| VN255 | Healthy | <20% | Good correlation between PAUT and MPI |
| VN258 | Healthy | <50% | An indication detected while no LME visible with MPI |
| VN262 | Severe LME | ≥50% | Good correlation between PAUT and MPI |
| VN264 | Light LME | <50% | Good correlation between PAUT and MPI |
| VN265 | Light LME | <50% | Good correlation between PAUT and MPI |

It has been highlighted in this section that detection of LME cracks is possible using manual PAUT. The probe is positioned on a rigid wedge with a fixed angle which is coupled to the specimen using grease. The probe turns around the spot weld and a series of scans with different angles are performed to generate a sectorial scan for each probe position. It has been shown that LME crack detection is possible. A reflection signal can be observed at the circumferential positions where cracks are located. A qualitative evaluation seems to be possible i.e. classification of LME cracks into three categories according to amplitude indications. However, establishing a link between indication amplitude and the LME cracks features such as length and depth is a challenging item due to the complexity of signals analysis. Furthermore, interaction modes between LME cracks and waves still to be determined and optimized. To do that, a simulation of wave propagation in RSW was investigated in the following section.

#### 4.4.3.2. CIVA Simulation

In this investigation, CIVA software (in particular CIVA UT with CIVA-ATHENA 2D module) developed by the French Atomic Energy Commission (CEA) is used to model the phased array ultrasonic inspection of RSW. This tool consists in a hybrid module, using both conventional semi-analytical methods of CIVA and the Finite Elements code ATHENA (from EDF). The connection with Finite Elements allows taking into account more complex phenomena that can occur in a UT inspection. To study bulk waves beam propagation on RSW, 4 steps are required:

1. DRAW 2D CAD model
2. Extrusion to build 3D model
3. Beam computation
4. Defect response

The first step is to draw in two-dimensional profile in the computer-aided-design (CAD) facility included in the CIVA software, the specimen and spot weld model. In our case, the model is created from the dimension extracted from 2D cross-section of CT scan (Figure 61-a). After that, the model was extruded to create the three-dimensional solid model (Figure 61-b). The 3D model is used for beam field prediction. In fact, the software gives the ability to overlay resulting beam profiles and beam/defect responses onto the 3D model.

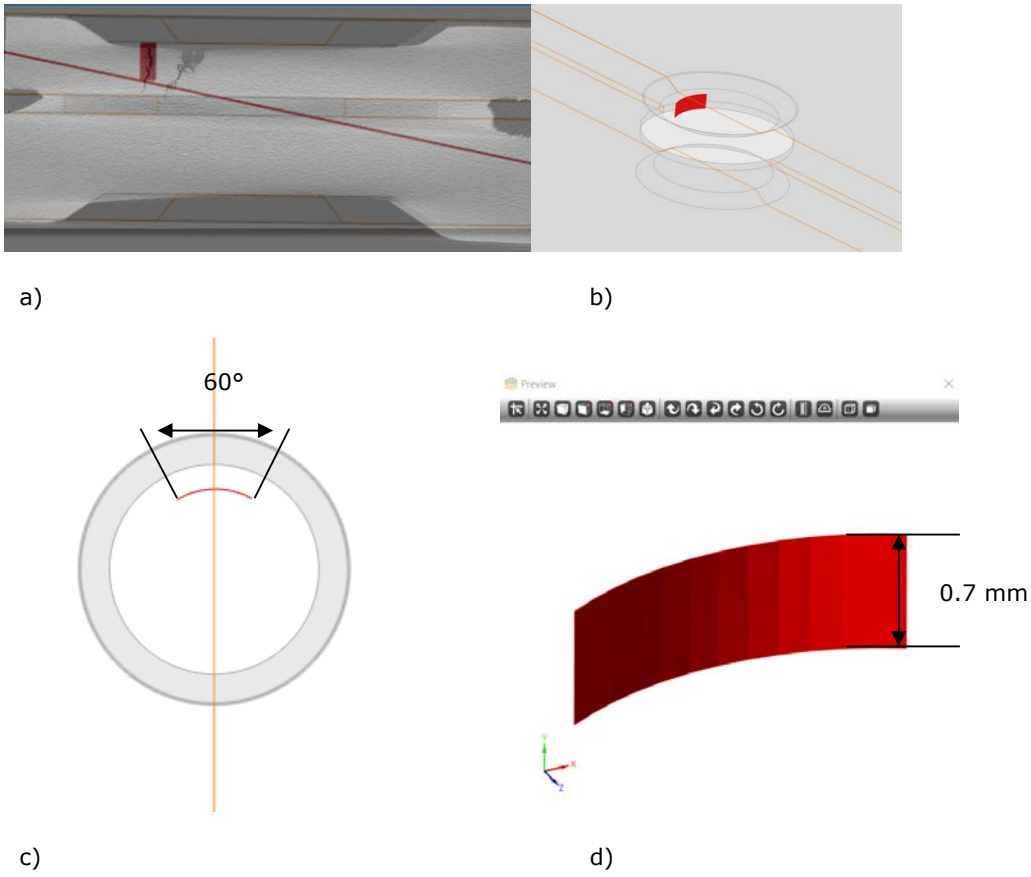


**Figure 61: a) 2D CT scan of cross-section of a spot weld and superimposition of the 2D model. b) CAD 3D model implemented in CIVA. C) Top view of the 2D model and position of crack. D) Geometry and depth of LME crack.**

For beam computation, various setups must be described:

- Material properties for each zone and weld
- Defect features and implementation. The LME crack was implemented using the multi-faceted defect creation tool. It is located inside the spot weld, closer to indentation based on the example of CT-scan cross section (Figure 61-c). The length introduced is constant, 60° with different depth studied: 0.7mm, 0.4mm, 0.2mm (Figure 61-d).
- Phased array settings: the transducer crystal element characteristics and geometry, phased array crystal assembly. This part describes how the focal laws are oriented and focused in the piece. The combination of linear and sectorial scanning improves intercepting the defect in the welded spot. The active elements and the position of the probe are selected to allow a significant focus ratio. In our case the probe defined is a 15MHz linear array probe which will be the same used for experiments. The probe is composed of a set of elements juxtaposed and aligned along a linear axis. They enable a beam to be rastered, focused, swept and steered along a single azimuthal plane (active axis) only. All parameters related to the crystal shape, focusing and signal should be defined such as crystal shape (Incident dimension, orthogonal dimension, number of elements, gap between elements, elements width) and focusing (Signal choice, center frequency, bandwidth, phase, sampling frequency, number of points).
- Inspection mode: wave type, impact parameters, water path…
- Computation zone: The zone between the impact beam and the spot weld.

The probe is placed in a position that allows propagation and focusing of the beams in the welded spot (Figure 62-a). The water path is chosen to permit in real conditions to reproduce the control in immersion tank.

Figure 62-b shows the beam profile ultrasonic modeling results for several angles in the sectorial scan obtained in the computation area.

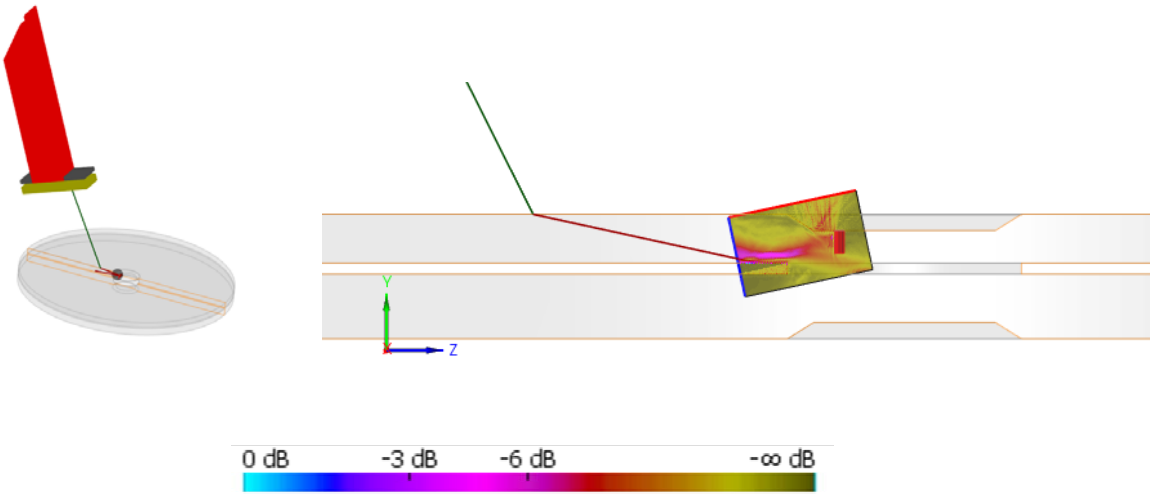


**Figure 62: Position of probe (left). Position of the computation zone in the CAD 2D model (right).**

If we take a closer look to cartography representing beam interaction with the specimen geometry either in 2D and 3D modeling (Figure 63), we can see clearly that the beam generated interacts with the crack and a the beam is reflected in the position of the crack. This interaction induces an increase of the signal amplitude which could be identified during experiments with adequate signal processing methods.

Figure 64 shows a zoom of the beam ultrasonic modeling results for three crack depths: 0.7mm, 0.4mm and 0.2mm. These profiles indicate the ray paths talking into account mode conversion and back wall reflection over the angular sector scan. Analysis of these profiles reveals greater detection of crack depth varying from 0.2 to 0.7mm. The simulated parameters are then validated and will be used for experiments using PAUT in immersion tank.

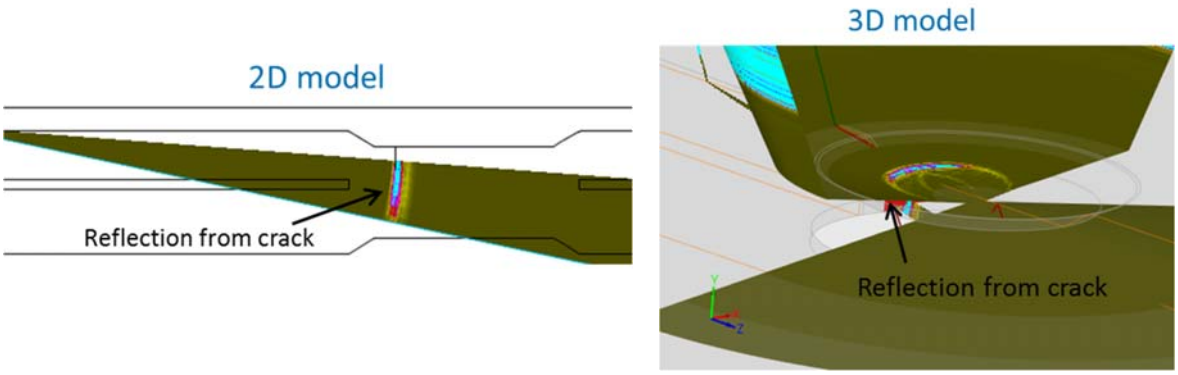


**Figure 63: Beam profile ultrasonic modeling results at several crack depth: up (crack depth=0.7mm), middle (crack depth= 0.4mm), bottom (crack depth=0.2mm).**

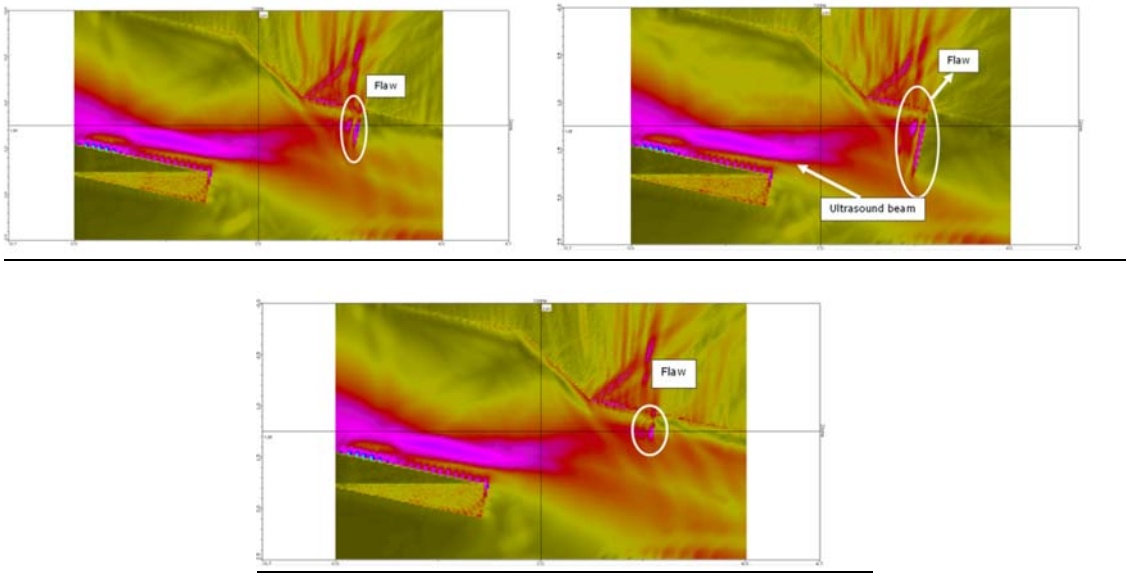


**Figure 64: Beam profile ultrasonic modeling results at several crack depth: up (crack depth=0.7mm), middle (crack depth= 0.4mm), bottom (crack depth=0.2mm).**

Below the optimized configuration defined:

- Probe: 15 MHz
- Probe angle : 21.7°
- Orthogonal probe distance from the spot weld: 22.2 mm
- Angular deviation: 54° to 86°

#### 4.4.3.3. Automated PAUT in Immersion Tank

To adapt the immersion tank for spot weld inspection, a probe and piece supports were designed and manufactured. The probe support contains a laser beam which is aligned with column axis (rotation axis) and the spot weld center. Then the probe should be positioned laterally away from the spot weld and turns around the spot weld by keeping the distance constant. Prior to the installation of the probe, an evaluation of probe position

and orientation is required using an additional calculation based on Geogebra software. The aim of this calculation is to evaluate the offset value of the probe during spot weld inspection i.e. the distance between the probe center and the column axis. Inputs are (Figure 65):

- B: is the rotation center of the column (bigle)
- BA is the length of the column
- The probe support is located in the A position. The probe support was designed to enable the lateral translation of the probe
- Angle: 19.69° is the angle between the column axis and the orthogonal axis of the spot weld
- C: the center of the spot weld
- EC: the distance of the beam impact to spot weld center

Using the free dynamic mathematics software Geogebra, the probe offset during the inspection was determined by calculating the distance from the probe center to the column axis (length of DA). The offset value is 96.55 mm.

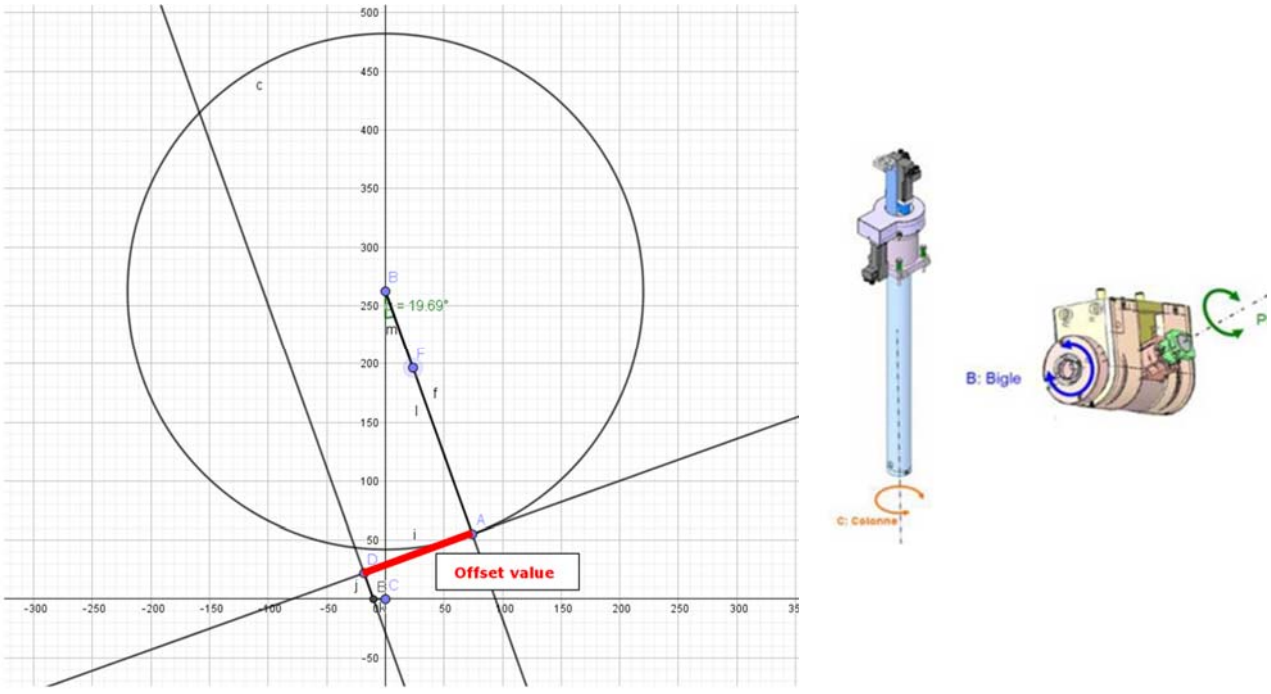


**Figure 65: Offset value calculation using Geogebra software (left). Column rotation angles (right)**

Once the setup is defined, the first step during PA inspection is to calibrate the probe orientation according to the spot position. This step was more difficult as expected due to the non coplanarity of the two sheets of the specimen. Indded, an angle was noticed between the two sheet an can vary from specimen to another. In the example shown in Figure 66, an angle of 5° was measured. This deviation complcates the calibration and induce an additional step to calibrate the angle between the probe and the specimen. This was carried out by determining using ultrasound longiitudinal waves, the probe orientation wich should be parallel to the top sheet. In example of calibration is shown in Figure 67, in which one can note the difference of time of flight (travel time betwwen the pprobe and top sheet) of the reflection coming from the top sheet. This indicates a non-coplanarity between the probe and the top sheet. Furthermore, the spot weld is biased compared to the probe center. After calibration, issues have been fixed(Figure 68). Then, the suitable orientation of the probe is performed according to the aformentionned setup.

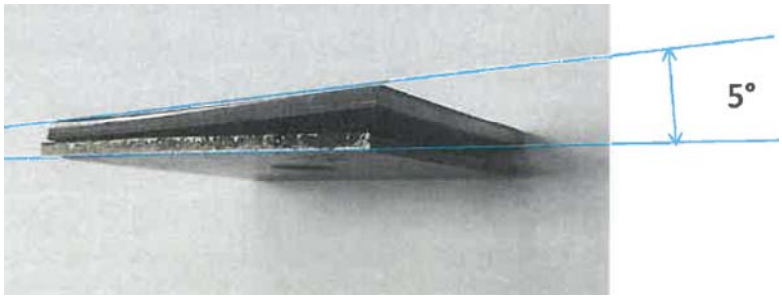


**Figure 66: Example of non-coplanarity of the two sheets of a specimen.**

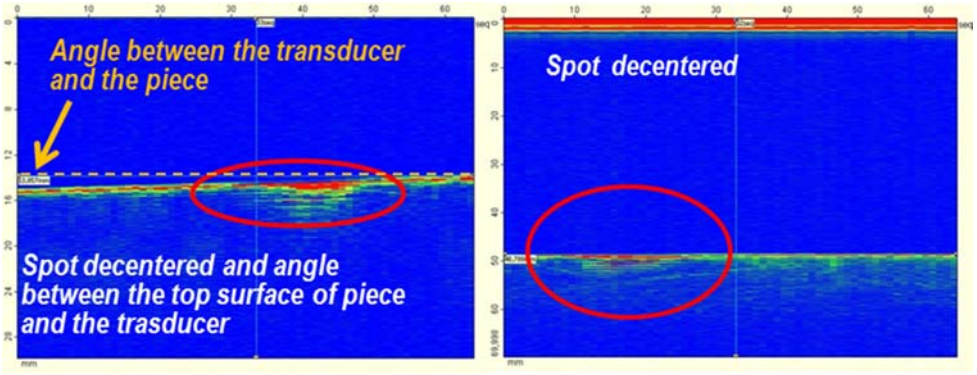


**Figure 67: Example of B-scan (Longitudinal waves) showing a non-coplanarity between the probe and the top sheet of the specimen. X axis is position and Y axis is time of flight. Left, spot decentered and angle between the probe and the top sheet. Right, spot decentered.**

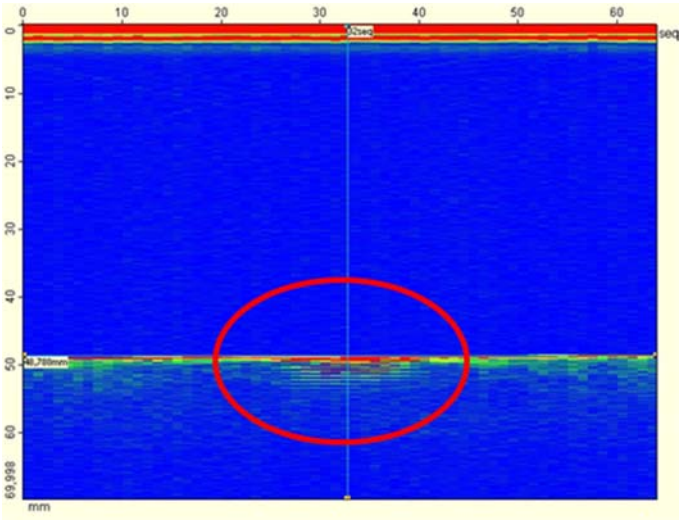

**Figure 68: Example of B-scan after calibration.**

For each spot weld, and each probe position, the inspection procedure is based on the generation of S-scan from 54° to 86°. For one spot, 3600 S-scans are generated. To facilitate the analysis and manipulation of data and also the understanding of results, a new representation called corrected C-Scans is proposed. These C-scans display on the X-axis the rotation angle and on the Y-axis the projection of the S-scans, i.e. top view of the S-scans. An example is explained in the Figure 69.

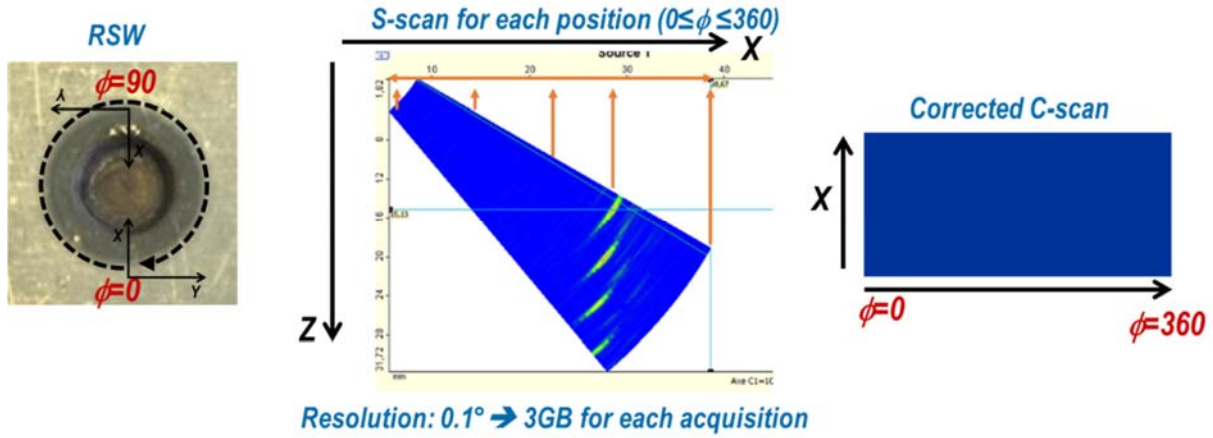


**Figure 69 : Illustration of C-Scan corrected.**

For non-specialist it still hard to understand the relationship between corrected C-scans and a spot weld geometry. A certain amount of brain gymnastics is required to correlate the C-scan visualization and spot weld image. The Y-axis is the propagation time of the beam inside the specimen. The zero of the Y-axis represents the beam impact. To further facilitate interpretation, the Cartesian coordinate images have been converted to polar coordinates by means of image processing algorithm as following:

- C-scans were converted to a grey level so that each pixel varies from 0 to 255 (8 bits) which corresponds to c-scan amplitude varying from 0 to 100%

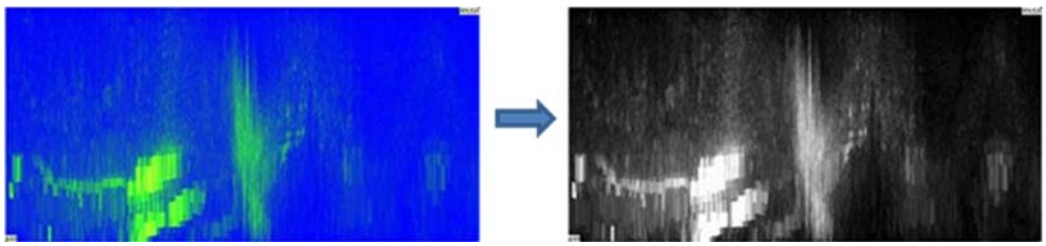

**Figure 70: Conversion of image on grey level.**

- The dimensions of the image / pixel resolution are measured: Number of rows and number of columns to find the resolution of the pixel in the c-scan:
  - Resolution of a pixel in height = (amplitude max – amplitude min) / number of rows.
  - Resolution of a pixel in width = 360° / number of columns.

- A color scale was applied: In order to enhance the visualization of the indications, a conventional ultrasonic color scale was applied to c-scans.

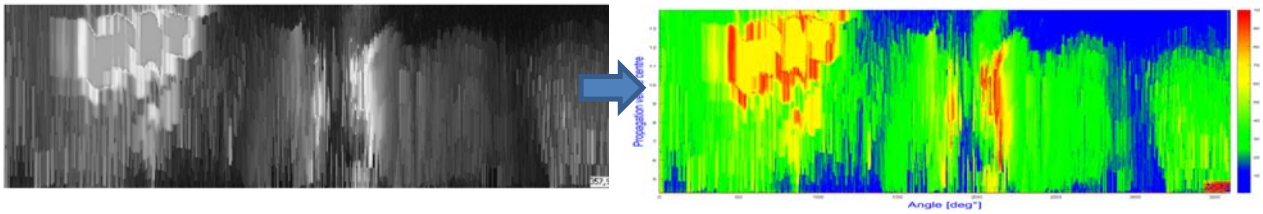


**Figure 71: Definition of color scale for amplitude from 0-100%.**

- Conversion of Cartesian coordinates into polar coordinates, Creating a circular grid:
  - The number of sectors is the same as the number of columns of pixels in the original image
  - The number of circles is the same as the length of the beam at a given mechanical position (and the same as the number of lines in the original maps). The filling of the amplitudes is done by correspondence between the pixel of the C-scan and the elementary surface which corresponds to it on the circular grid:

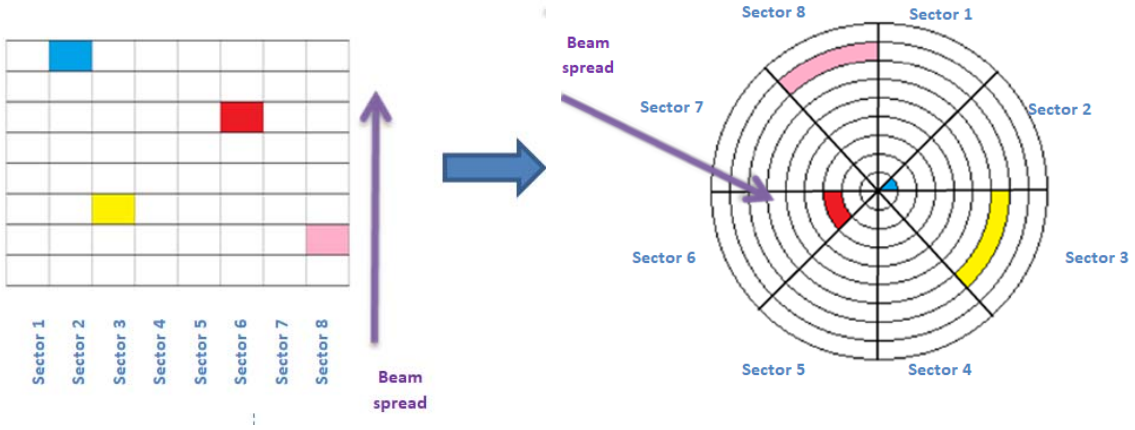


**Figure 72 - Conversion from Cartesian coordinates to polar coordinates.**

Two polar representations are possible, full disk or crown with an inner radius equal to 10% the outer radius.

The circumference of the crown (outer circle) represents the angular position of the probe around the spot weld which varies from 0° to 360°. For each position (each 0.1°), the radius is the beam spread (or propagation time). The beam impact on the specimen is located in the circumference. An example of two polar C-scans is shown in Figure 73.

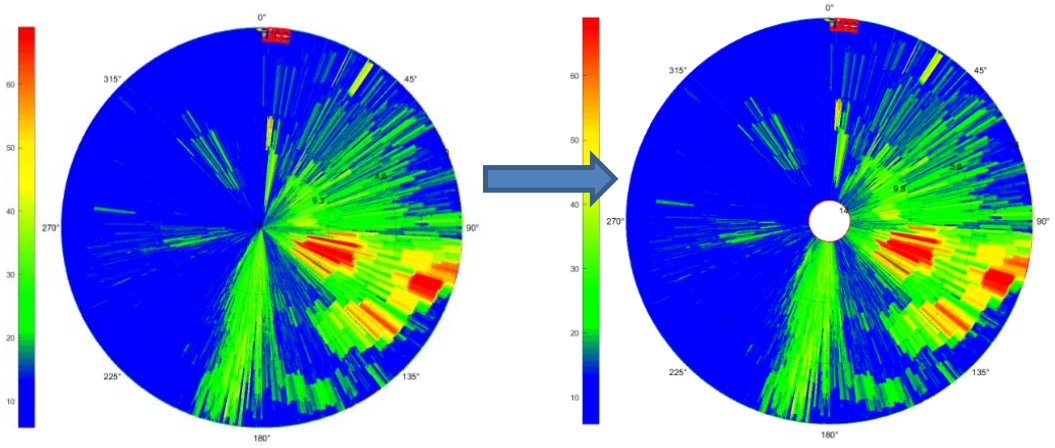

**Figure 73 : Polar C-scans, full disk (left) and crown (right).**

An example of result of specimen n°8457 is shown in Figure 74:

- The indication circled with dashed line corresponds to the position of the LME crack in the specimen.
- The indication marked with arrows comes from the reflection of the opposite interface between the two sheets. It is also noted that the signal is not constant along the specimen probably due to the disorientation of the beam / indentation.
- The signal circled with solid line comes from an indication close to the surface. The origin from this signal was not explained.

To confirm this, the specimen was rotated by 90° and a new acquisition was carried out. The result is shown in the lower part of the Figure 74. It can be noted that C-scan features have also shifted with 90°. It is worth noting that the position of the LME crack corresponds perfectly to the indication detected.

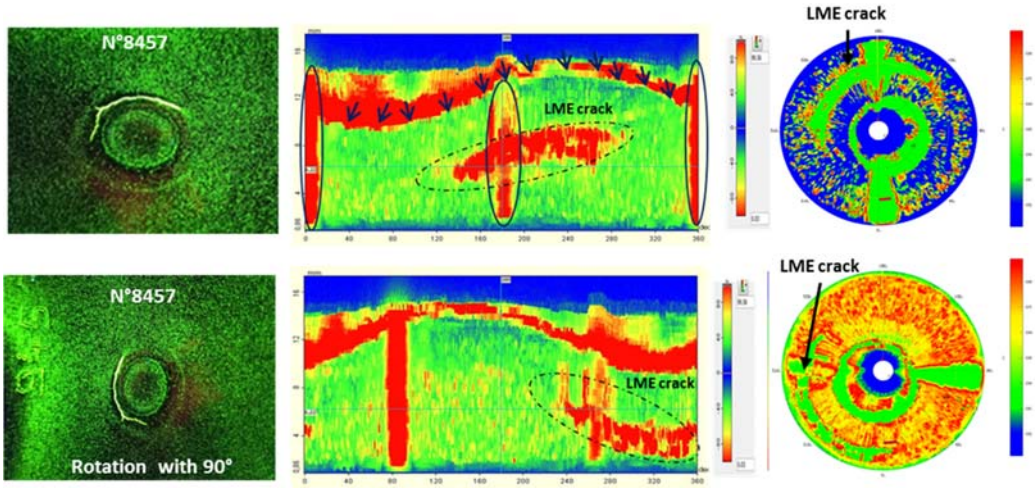


**Figure 74: C-scan result of specimen n°8457. MPI image indicating the position of LME crack left), Cartesian C-scan (middle) and polar C-scan (right). A rotation of 90° was applied to the specimen to verify LME crack detection.**

The same result is obtained for two other specimens with LME cracks located outside indentation. Despite the presence of some indications which could be linked to the geometry of specimens, LME crack for both specimens are detected by PAUT. The position indicated in the polar C-scan is with a good agreement with MPI inspection.

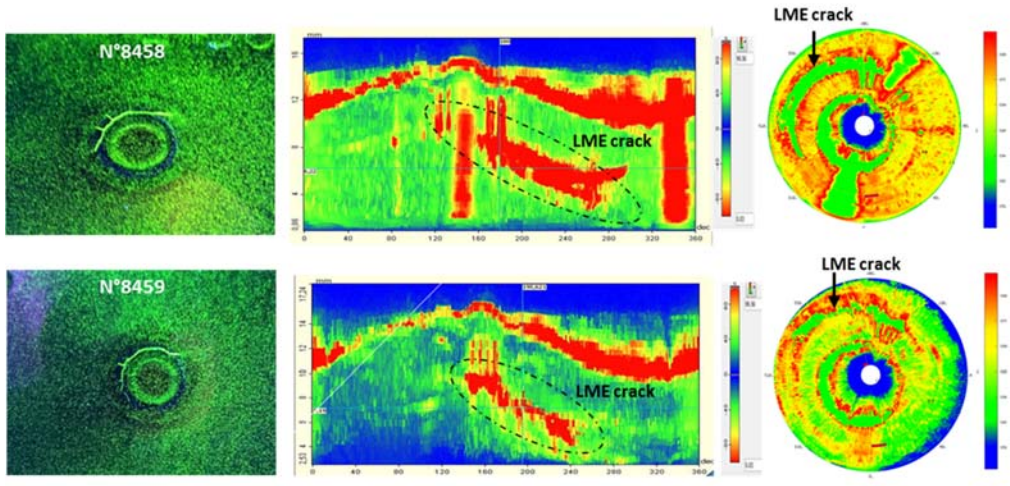


**Figure 75: C-scan result of specimens n°8458 & n°8459.**

To identify the origin of artefacts/indications suspected to be linked to the geometry, healthy spot weld has been controlled with PAUT with the same procedure as damaged spot welds (Figure 76). The ultrasonic signature of artefacts of healthy spots is found to be similar to damaged ones. Orthogonal indications are still there as well as the fluctuating signal. The origin of the orthogonal still unexplained, it is mainly linked to surface or sub-surface phenomenon. However, the signal coming from the interface between the two sheets in reinforced by findings in modeling. By going through beam propagation modeling inside the specimen, it can be observed that the beam is reflected on the opposite side of the spot weld, in particular in the interface between the two sheets (Figure 76-middle). Furthermore, if the rotation of the probe is tilted even with 1mm, this will induce a delay in the time of flight (propagation time) of the echoes coming from the interface which explains the fluctuation form (Figure 76).

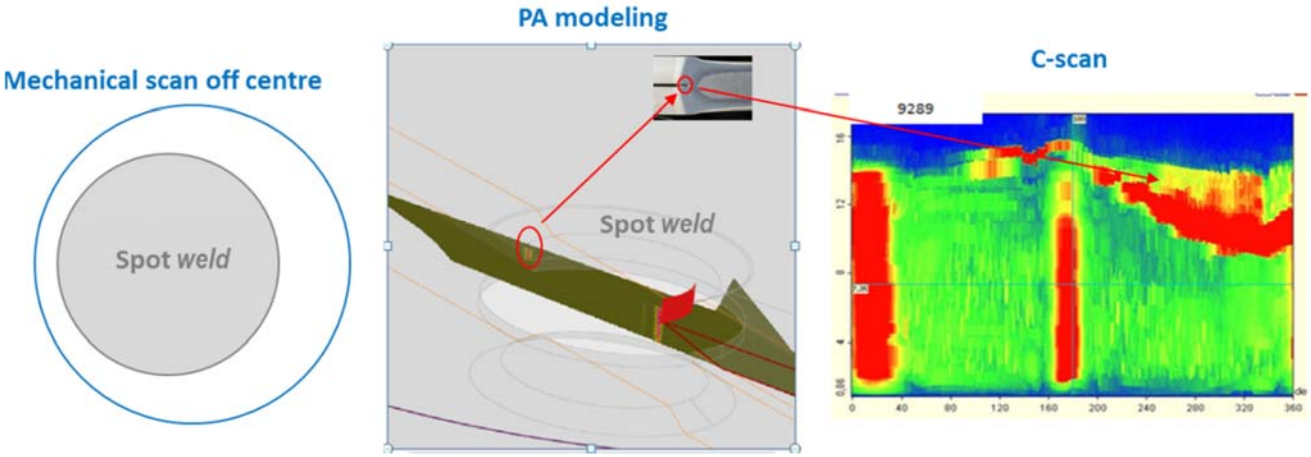


**Figure 76: C-Scan of specimen n°9289 (healthy).**

In order to avoid artefacts coming from the interface between the two sheets located on the opposite side of the spot weld, the analysis window (gate in UT terminology) was reduced. New tests were performed on spot welds with calibrated EDM cracks. Three specimens are then investigated: specimen n°10394, n°7509, and n° 10398. Each specimen contains one EDM crack located at the same position: 40°-120° which corresponds to a length of 3mm. The depth varies from 0.2mm (specimen n°10398) to 0.7mm (specimen n°10394, 7509). Result is shown in Figure 77. Despite the location of EDM cracks, inside the spot weld closer to the indentation, they have been detected for all specimens. Nevertheless, if a blind inspection is considered, it will be difficult to identify the position of the EDM for the specimen n°10398 due to the presence of four indications (60°, 170°, 260° and 320°).

From first trials, the conclusion that can be drawn is that implementation of PAUT using immersion tank is difficult due to various factors:

- The non–planarity of the two sheets which complicates the calibration phase, in particular the probe angle positioning.
- Geometry of specimens in particular the low inspection area which is about 10mm located in a very challenging zone, presence of indentation, very thin thickness up to 1.4mm, presence of a gap between the two sheets (interface)
- LME crack features, which is located on surface inside and outside indentation, with a random orientation with small opening (few µm) and depth (few hundred of µm)

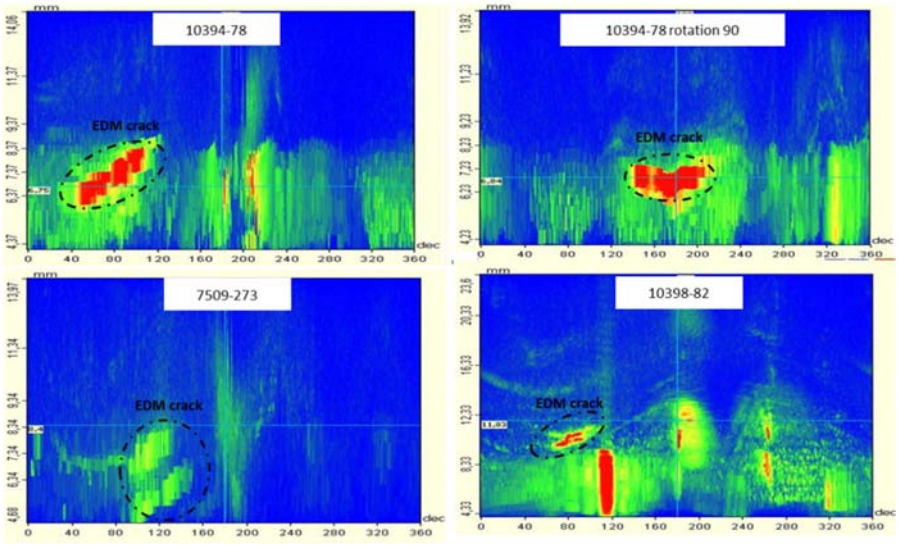


**Figure 77: Corrected C-scan for EDM specimens**

A working methodology has been developed which deals with aforementioned constraints and lead to encouraging results. Real LME cracks outside indentation and artificial cracks (EDM) inside indentation have been detected despite the fact that some artefacts still unexplained. At this stage, the wave modes allowing this detection have not been identified and seem to be difficult to identify because of the angles involved (mode conversion, small thickness ...).

To extend and verify LME crack detection for other specimens with different crack levels, a second trial has been performed. Moreover, an investigation of the capability of PAUT method on crack characterization is conducted in particular on crack length and depth.

Results are summarized in Table 16. A comparison in terms of detection and crack length identification was carried out between MPI and PAUT. The criterion "coherence" is based on different statements such as:

- Crack detection
- Crack length and position identification
- Facility of C-scans interpretation (Presence of unexplained artefacts/indications)

Based on these parameters, three levels have been defined:

- Low coherence "o"
- Average coherence "oo"
- Good coherence "ooo"

For all specimens investigated, it has been found that detection is possible. PAUT is able to distinguish between healthy spot welds and damaged ones with LME cracks. In the case of healthy spots, no indication/reflection detected in the C-scans while for spots with LME cracks indications appear at similar positions compared to MPI method. When a difference in crack length between PAUT and MPI is observed, it could be explained by the disorientation of the ultrasonic beam when it meets the crack. Sometimes, there are some unexplained signals which complicate the C-scans interpretation.

Concerning the samples with EDM cracks (n°10398, n°10394, and n ° 7509), an attempt at determining the relationship between signals and depth was not successful.

MPI images and C-scans are presented from Figure 78 to Figure 88.

**Table 16: Summary table of results**

| Specimen n° | Position and length of cracks | | Coherence | Comment |
|---|---|---|---|---|
| | MPI | PAUT | | |
| **7523** | 0 °-180° continuous<br>180°-270° discontinuous | 10°-250° | ooo | Signal not identified but the signature is different as a flaw |
| **7525** | 0°-190° continuous | 20°-220° * | o – oo | *Doubt as to the position and the length of the flaw detected |
| **7536** | 90°-270° continuous<br>270°-360° discontinuous | 30°-150° | oo | |
| **7537** | 90°-180° continuous<br>240°-360° discontinuous | 40°-180° | oo | Test 1 |
| **7537** | 90°-180° continuous<br>Punctually misdirected indications 240 à 360° | 115°-215° | oo | Test 2 |
| **7516** | No indication | No indication | ooo | |
| **7548** | 0°-170° | 45°-120° | oo | |
| **7549** | 0°-110° continuous | 75°- 224°<br>280°-320° ? | o | Difficult to identify crack indications |
| **7918** | No indication | No indication | ooo | |
| **7969** | 100°-300° | 70°- 300° | ooo | |
| **10371** | No indication | No indication | ooo | |
| **10372** | No indication | ** | oo - ooo | ** Presence of an unexplained indication (in volume) |
| | **Crack Depth** | | | |
| **10398** | Depth= 0.2mm<br>40°-120° | 60°-125° | ooo | Ok for length and position<br>But no relationship between depth and signals identified |
| **10394** | Depth= 0.7mm<br>40°-120° | 40°-110° | ooo | Ok for length and position<br>But no relationship between depth and signals identified |
| **7509** | Depth= 0.7mm<br>40°-120° | 50°-110° | o | Some signals still unexplained<br>And no relationship between depth and signals identified |

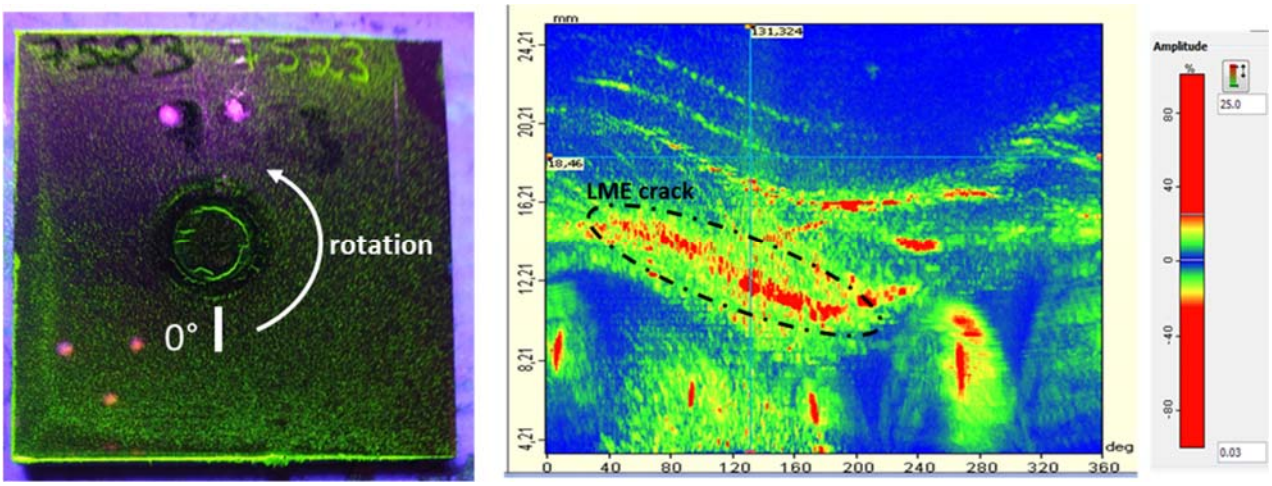


Figure 78: Specimen n°7523. Comparison of MPI (left) and PAUT (right) results.

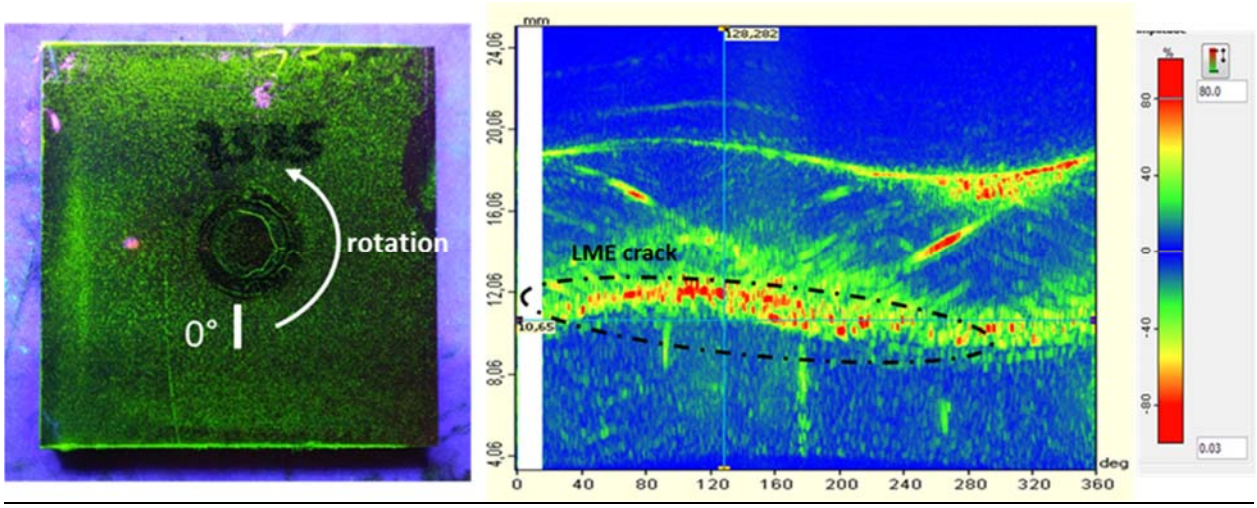


Figure 79: Specimen n°7525. Comparison of MPI (left) and PAUT (right) results.

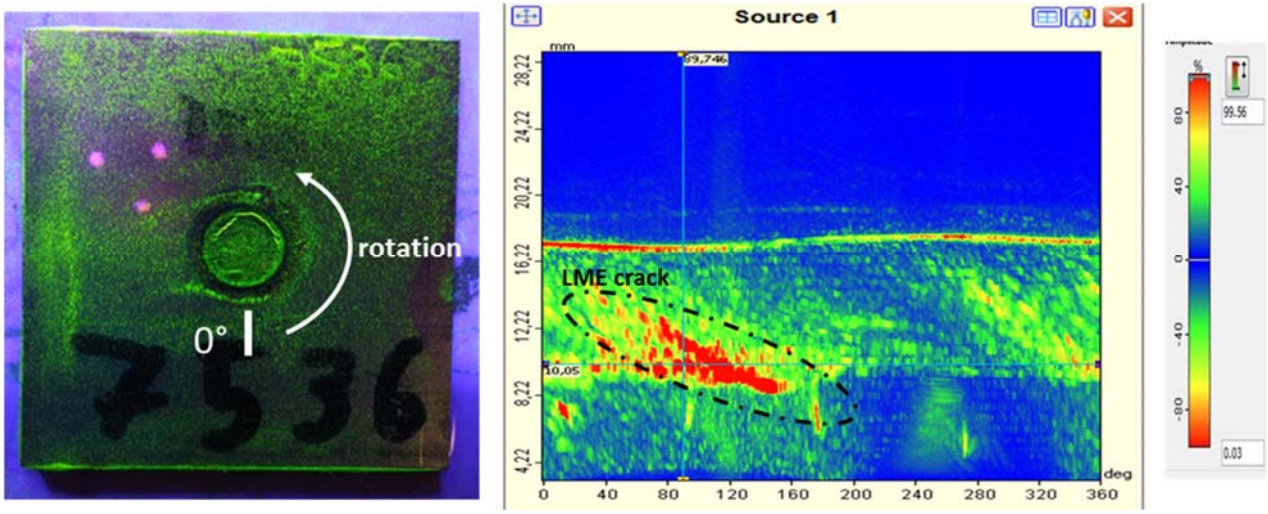


Figure 80: Specimen n°7536. Comparison of MPI (left) and PAUT (right) results.

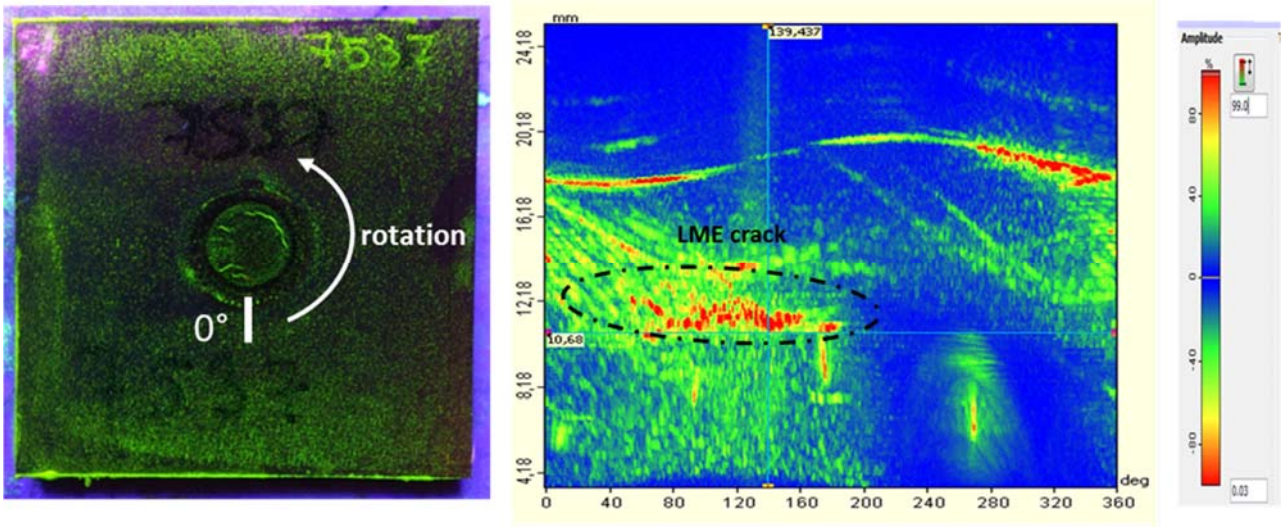


**Figure 81: Specimen n°7537. Comparison of MPI (left) and PAUT (right) results.**

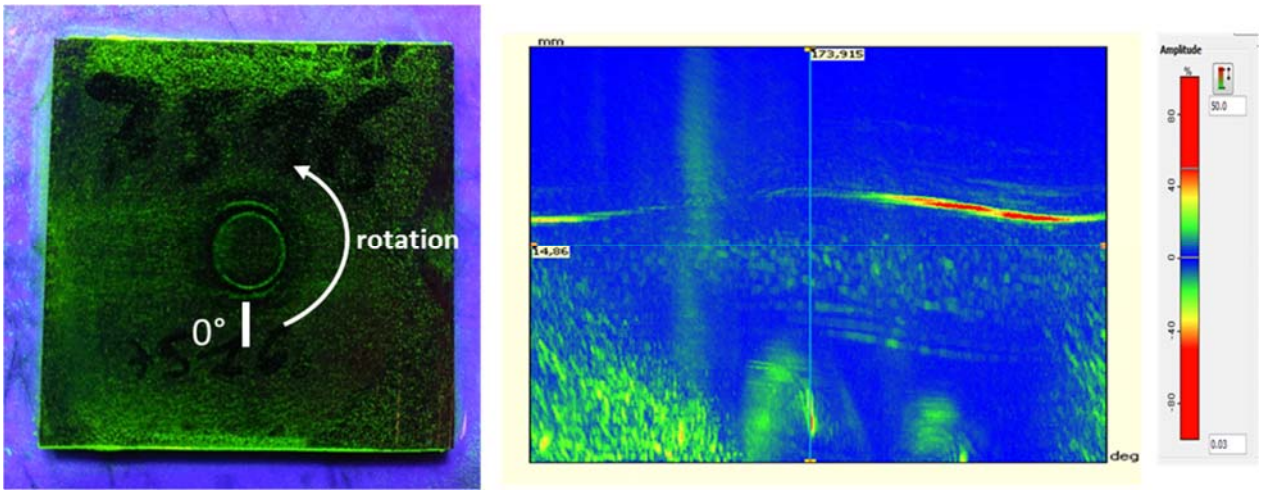


**Figure 82: Specimen n°7516. Comparison of MPI (left) and PAUT (right) results.**

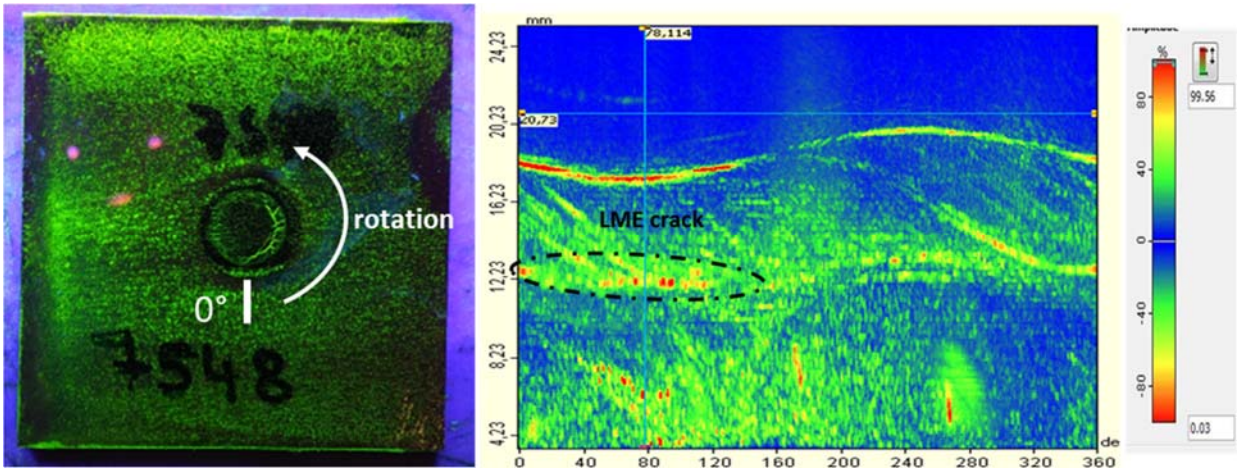


**Figure 83: Specimen n°7548. Comparison of MPI (left) and PAUT (right) results.**

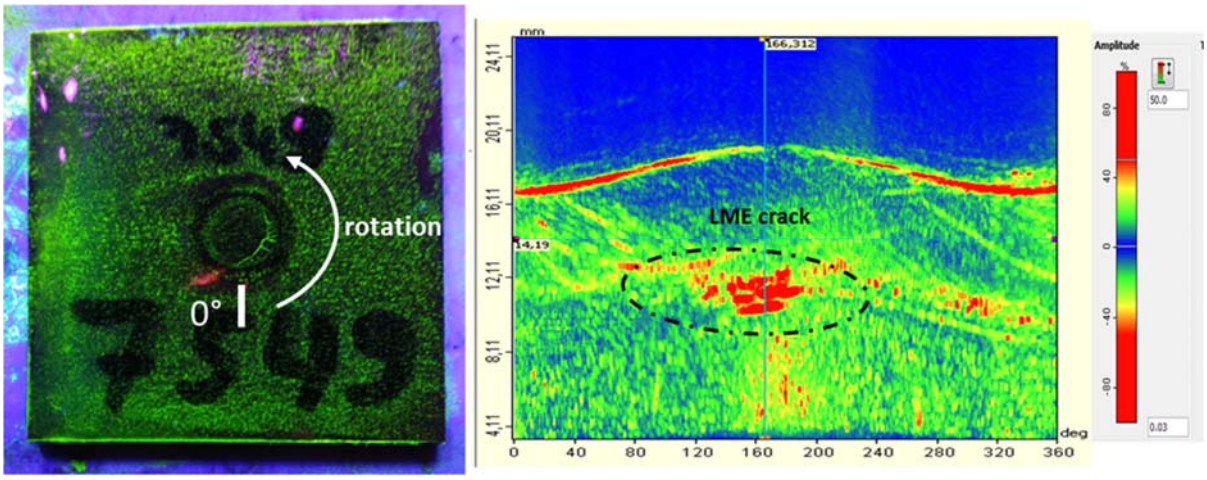


**Figure 84: Specimen n°7549. Comparison of MPI (left) and PAUT (right) results.**

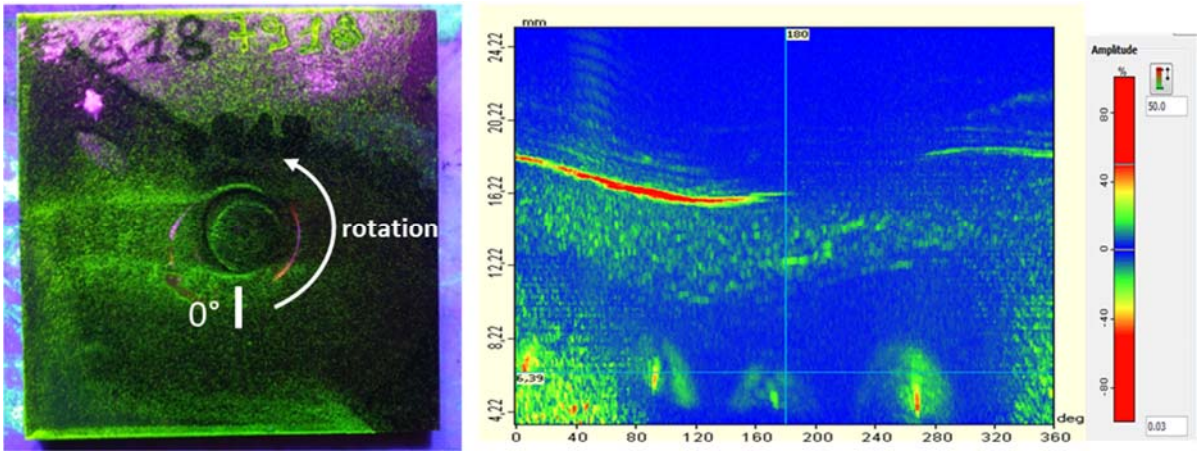


**Figure 85: Specimen n°7918. Comparison of MPI (left) and PAUT (right) results.**

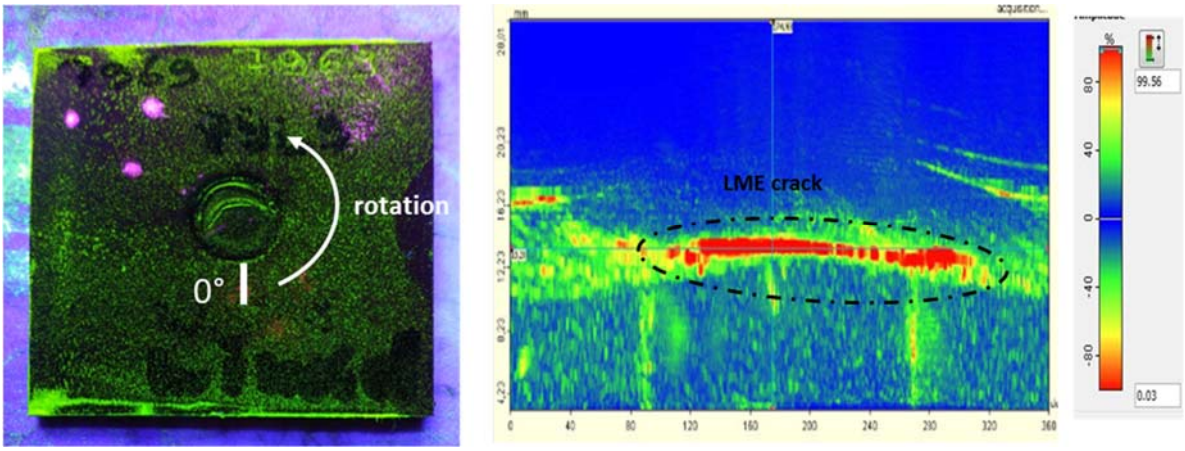


**Figure 86: Specimen n°7969. Comparison of MPI (left) and PAUT (right) results.**

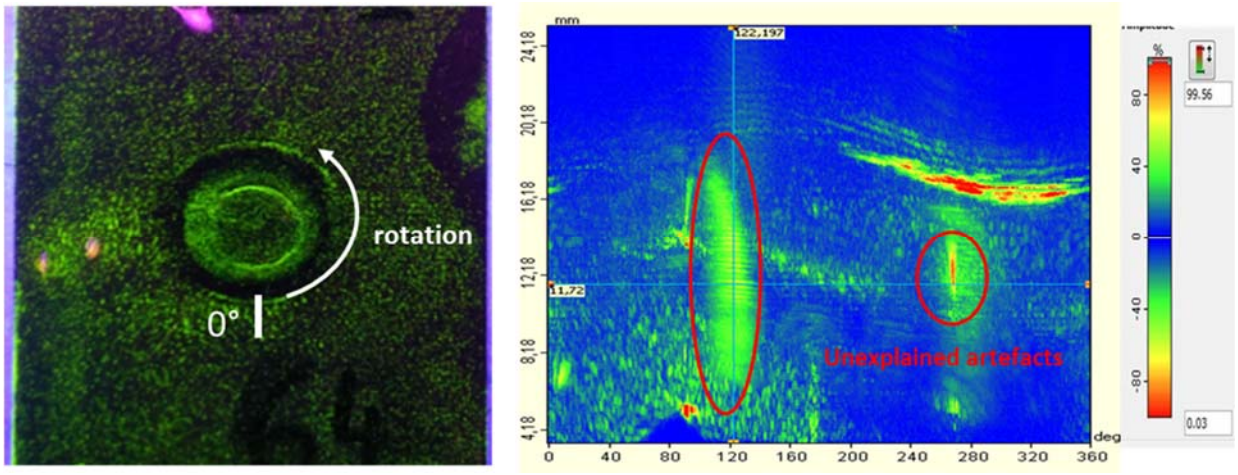


**Figure 87: Specimen n°10371. Comparison of MPI (left) and PAUT (right) results.**

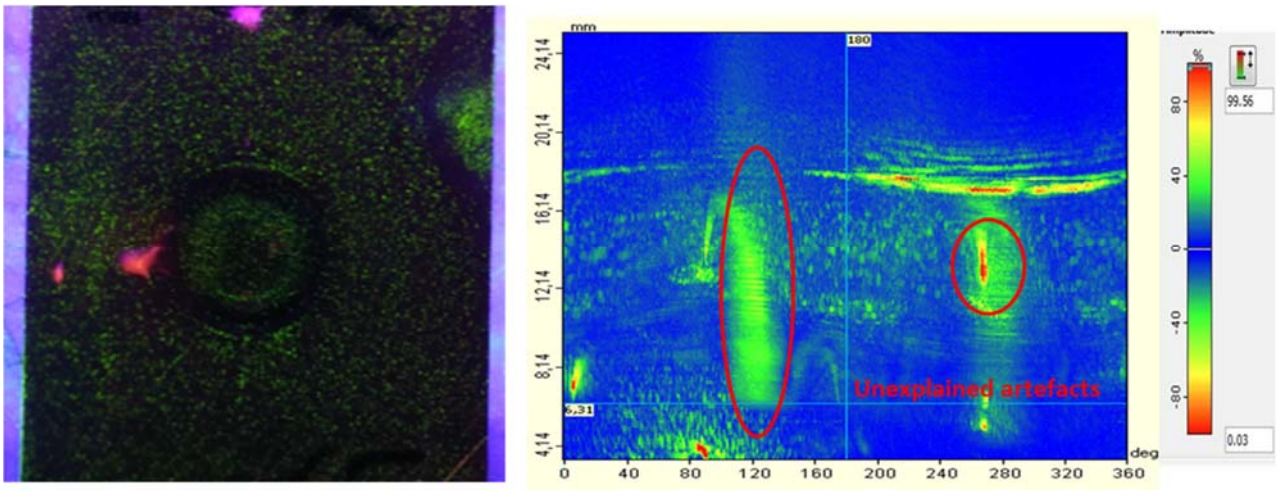


**Figure 88: Specimen n°10372. Comparison of MPI (left) and PAUT (right) results.**

### 4.4.4. Conclusion

Although a number of significant and encouraging results have been obtained using PAUT method, we must remember that there is no available PAUT system in the market suitable for RSW application, in particular for LME crack detection. RSWA system from Tessonics and the mini-scanner from Amsterdam Technology were evaluated and found to be not suitable for LME crack detection (see sections 4.7 and 4.8).

At the beginning of the program, manual PAUT was investigated and led to a good correlation compared to MPI, classification of cracks into three categories:

- Healthy: equivalent to low amplitude indication by PAUT < 20%
- Light LME: equivalent to medium amplitude indication by 20% ≤PAUT <50%
- Heavy/Intense LME: equivalent to high amplitude indication by PAUT ≥ 50%

To improve crack features quantification, such as length and position, mechanical PAUT was developed using immersion tank. Probe and specimen supports were developed and manufactured to adapt the immersion tank to RSW application. Prior to trials, the setup was optimized based on wave propagation modeling to understand and overcomes the complex RSW geometry and in particular crack features. Experimental results are promising in terms of crack detection, but further investigations are needed to understand artefacts and improve the method

and facilitate his use. Currently, the system requires considerable operator skills. For example, the technique is extremely sensitive to the probe angle and when the two sheets are not coplanar, this further complicates the implementation.

## 4.5. Eddy Current Pulsed Thermography (ECPT)

### 4.5.1. Background

Continuous improvement of computational resources and instruments contribute to the development and widening of the application scope of Infrared thermography. Last decade, this technique was used in diagnostics and monitoring in many fields: composite and metallic structures, art object...

Infrared Thermography is based on the application of a radiation heat transfer to the specimen surface using a short and high-power thermal pulse. This energy is then absorbed by the material surface and converted into heat. The interaction of heat diffusion between regions having different thermal properties such as LME crack will disturb the heat distribution, leading to the creation of thermal contrast.

A wide stimulation sources can be listed: Optical (flash and halogen lamps), mechanical and inductive. For our application, Zinc coated AHSS or Mild steel will have a low emissivity, and thus high reflectivity and low absorptivity. For thermography inspection on such surface, measurements will be disturbed due to reflection of the shiny surface of the plate. According to [8], different solutions are possible: explore different angles of flash, lamp and camera, by covering the measurement area with some high emissivity material (e.g., powder), or by using another type of excitation source such as induction heating.

For inductive thermography, a short inductive heating pulse is generated by a coil. The specimen can be inside the coil, case of Helmholtz pair coil [9,10] or close to it, case of Ferrite yoke.

The Helmholtz coil is known to generate a uniform magnetic field in a wide region around a center point of the coil pair axis [11]. This configuration requires an access on the two sides of the spot weld which could be a constraint for deployment for particular piece geometry.

Ferrite yoke combines both the advantages of magnetic flux leakage and ECPT. The magnetic flux between the two poles is relatively uniform and leads to a relatively uniform Eddy current field orthogonal to the magnetic flux. Heating is generated through hysteresis loss and eddy current loss. The interaction between the applied field and LME cracks also disturb heating response and create a thermal contrast. Therefore, this configuration is then chosen in this program.

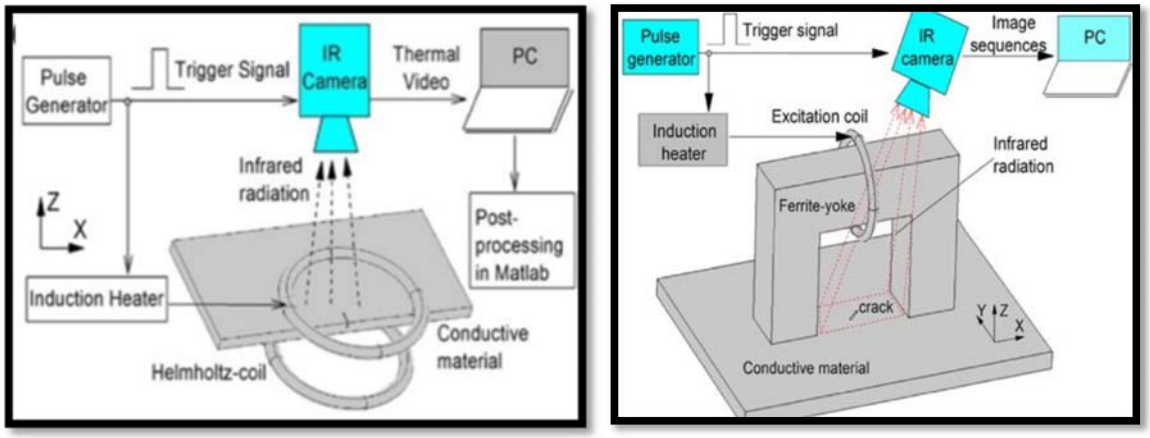


**Figure 89: Helmholtz pair coil left and ferrite yoke, right. [11]**

Concretely, due to conduction, the heat propagates from the external surface of the specimen to the interior and leads to a continuous decrease of the surface temperature. However, in the defect area, filled with air, the heat flux faces a higher thermal resistance that reduces the heat transfer rate. Most of these methods need a reference point from the sound area. Therefore the defect area has a higher temperature than the sound area. During cooling, the sound area cools down faster that the defect area.

In the literature, various techniques in pulsed thermography have been proposed for depth estimation and detailed by P. H. Vahid [12]. Most of them predict defect depth based on a time feature, such as :

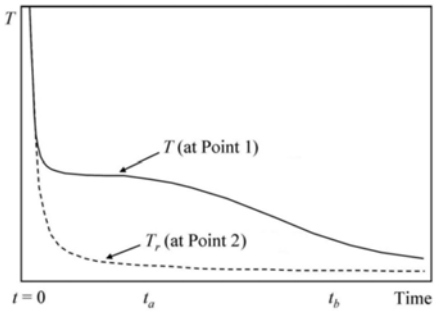


**Figure 90: Temperature profile in defect area (T) and sound area (Tr). [12]**

**Peak Temperature Contrast Method :** It was found that the peak contrast time is approximately proportional to the square of the defect depth, and the proportionality coefficient depends on the defect size ; the smaller the size of defect, the lower the maximum contrast and the shorter the peak contrast time [13].

$\Delta$T= T-Tr with T: temperature of defect area and Tr: temperature of sound area.

**Peak Temperature Contrast Slope Method:** is the first derivative of the thermal contrast. It was also find that the peak slop time ts is approximately proportional to the square of the defect depth and the proportionality coefficient does not depend on defect size the peak time of the first derivative of the temperature curve [13]. The authors in [] demonstrated the relationship between ts and the defect depth L as:

$$t_s = \frac{3.64L^2}{\pi^2\alpha}$$

**Pulsed Phase Thermography Method:** is proposed to calculate defect depth in the frequency domain, by applying the Discrete Fourier Transform (DFT) to temperature data.

$$F_n = \sum_{k=0}^{N} T(k)e^{\frac{2\pi jkn}{N}} = Re_n + Im_n$$

Where j is an imaginary number, n designates the frequency increment, and N is the frame number in the sequence.

The phase delay is calculated as:

$$\Delta\emptyset = \emptyset_d - \emptyset_s$$

Where $\phi_d$ is the phase of a defective pixel, and $\phi_s$ is the mean phase value of a selected sound area.

Phase contrast is used to determine **blind frequency** i.e. the phase frequency at which the defect becomes visible for the first time), which is directly linked to the depth of the defect [14].

**Logarithmic Peak Second Derivative Method:** It is mentioned that the peak of the second derivative of the surface temperature on a logarithmic scale can be used to determine defect depth [15]

**Least Squares Fitting Method:** proposed by Sun [16], this method uses a theoretical heat transfer model to fit the temporal thermography data at each surface point.

All these approaches have been investigated by [] and the conclusion is that peak temperature contrast are not able to detect the depth of defects. The peak temperature contrast slope and logarithmic peak second

derivative cannot be used to predict the depth of defects that are comparable to specimen thickness. Least squares fitting method is not appropriate for high thermal conductivity materials such as aluminum and steel. Pulsed phase thermography method is not suitable for shallow defects due to the high level of noise at higher frequencies.

In this study, an attempt was done on Time onset and first and second derivative without success. A focus was then carried out on pulsed phase thermography based on blind frequency.

### 4.5.2. Methodology & Experiments

To prove LME crack detection few specimens with different level of LME cracks were investigated by ECPT. Trials performed with the collaboration of ArcelorMittal.
For depth estimation study, two kinds of specimens were used:

- Spot welds with EDM: Depth is known
- Spot welds with LME cracks: depth measured by CT scans

Spots with EDM were used for calibration of the method while spots weld with LME crack, for result validation

**Table 17: Specimens and Maximum Depth of LME crack measured by CT scans (left) and EDM (right).**

| Sample reference | Max Depth (measured by CT) |
|---|---|
| 7538 | 0,22 |
| 7538 | 0.35 |
| 7538 | 0.36 |
| 7536 | 0.2 |
| 7536 | 0.16 |
| 7567 | 0.13 |
| 7546 | 0.7 |
| 7546 | 0.9 |

| Defect n° | Length (mm) | Depth (mm) | Specimen n° |
|---|---|---|---|
| 1 | 3 | 0.1 | 9443 |
| 2 | 3 | 0.2 | 10398 |
| 3 | 3 | 0.3 | 9443 |
| 4 | 3 | 0.6 | 9444 |
| 5 | 3 | 0.7 | 7509 |
| 6 | 3 | 0.8 | 9444 |
| 7 | 3 | 1 | 9446 |
| 8 | 3 | 1.4 | 9446 |
| 9 | 1 | 0.7 | 9445 |
| 10 | 3 | 0.7 | 9445 |
| 11 | 5 | 0.7 | 9445 |

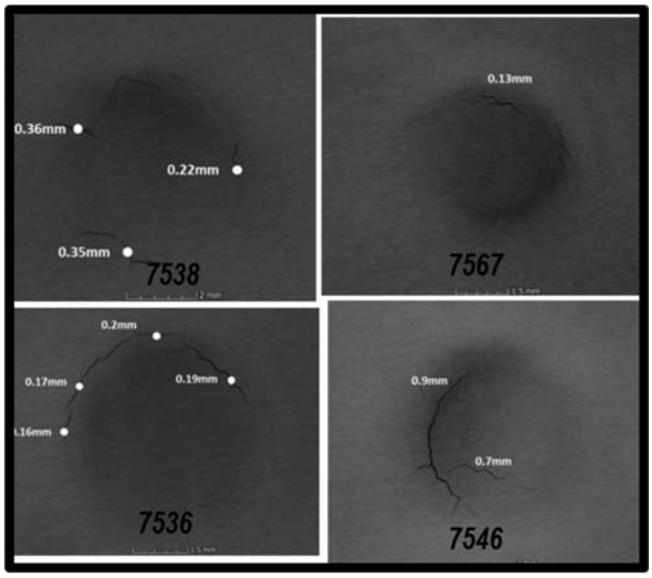


**Figure 91: CT scans of specimens and maximum depth location measured by CT scans.**

Experimental device used in this study is composed of:

- Ferrite yoke driven by an excitation generator. Ferrite orientation is chosen so that the magnetic flux is perpendicular to the LME crack.
- Generator deliver a short excitation during 50 ms at
- Camera positioned at approximately 10 cm from the specimen. The spatial resolution is 18µm per pixel. The frequency of acquisition is 350Hz (350 images per second)

The processing part was developed by ISA using a dedicated code implemented in MATLAB software. As trials performed at a WorldAutoSteel member company, only original data of thermograms (Digital level) are available for depth estimation.

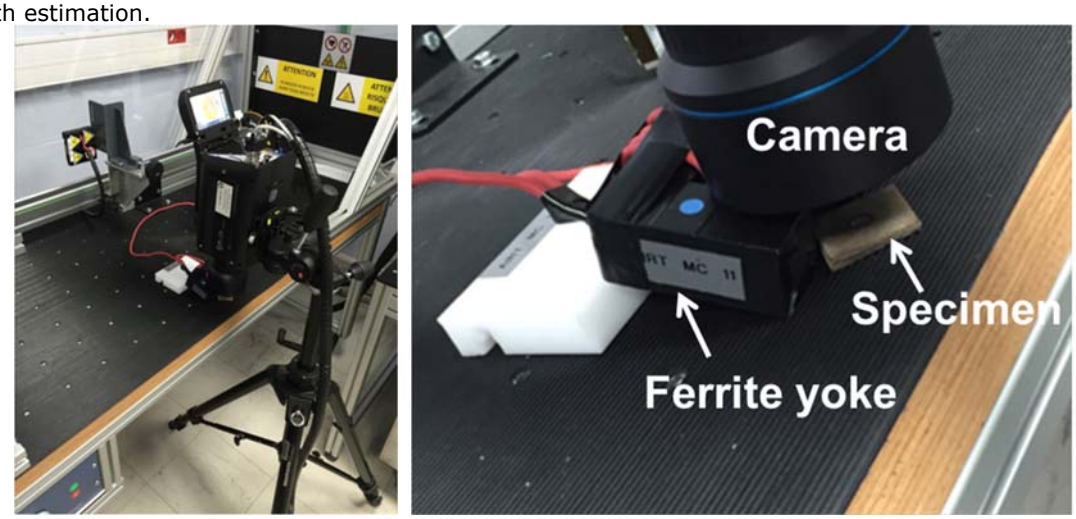


**Figure 92: Experimental setup.**

### 4.5.3. Results & discussions

Figure 93 shows the necessary steps that should be performed for the proper implementation of IT as a nondestructive testing for LME crack depth estimation. The first stage is conceived to assess Digital level sequence recorded by the camera due to short inductive heating pulse generated by the ferrite yoke.

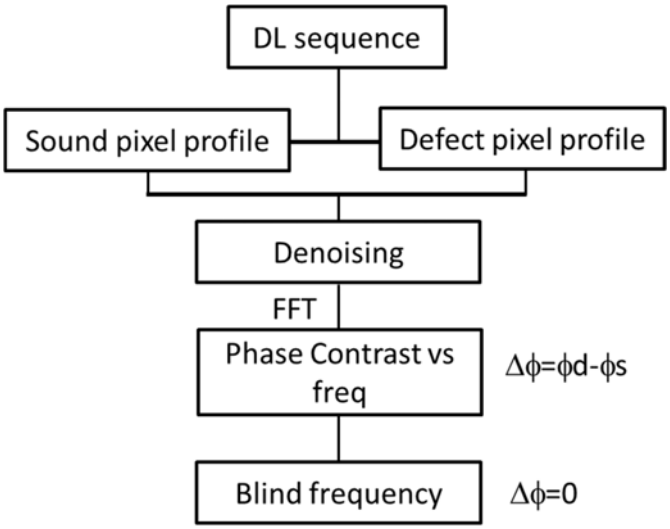


**Figure 93: Process chain for LME crack depth estimation.**

DL sequence was extracted which represents the Digital level of each pixel of the scanned surface over time. A manual sound and defect pixel location are then chosen, and the digital profile calculated.

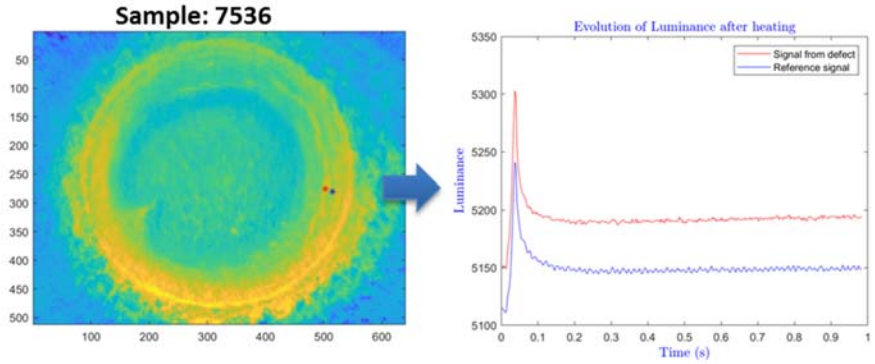


**Figure 94: DL image of the sample: 7536 (left). DL profile of sound and crack areas (right).**

In order to eliminate most of the background noise produced by external artifacts such as vibration, the 'de-noising' step of the temporal signals is important to improve depth estimation accuracy.

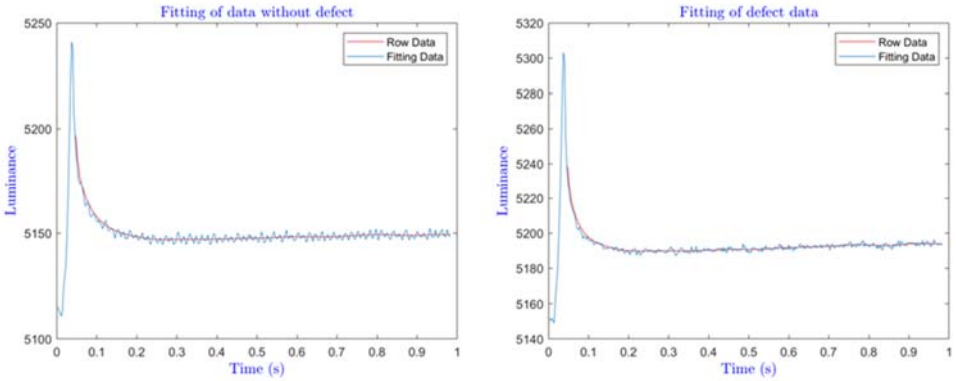


**Figure 95: Denoising phase.**

Once signal de-noised, a DFT is applied to both profiles and phase contrast calculated. The blind frequency corresponds to the intersection of the contrast phase with frequency axis: $\Delta\phi=0$
According to the literature [14], deeper defects are detected at low frequencies while only shallow defects are visible at high frequencies.

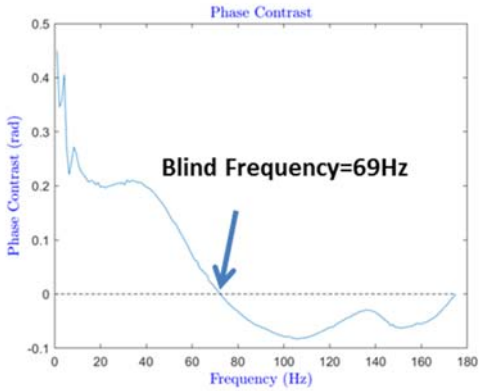


**Figure 96: Determination of blind frequency.**

The detection of LME crack by is feasible using PECT. As it can be shown in the following figures, there is a good agreement between phase images obtained by PECT and those obtained by Optical Microscope.

The interaction between eddy current, magnetic flux and crack, generates a heat disturbance detected by phase image. The application of Laplacien filter enhances the contrast between sound area and crack. The advantages of PECT compared to optical microscope, is the facility of detection when the crack is located near the indentation. Using Optical Microscope, different observations at different magnification is required to be able to observe the crack while for PECT, detection is ensured in one shot.

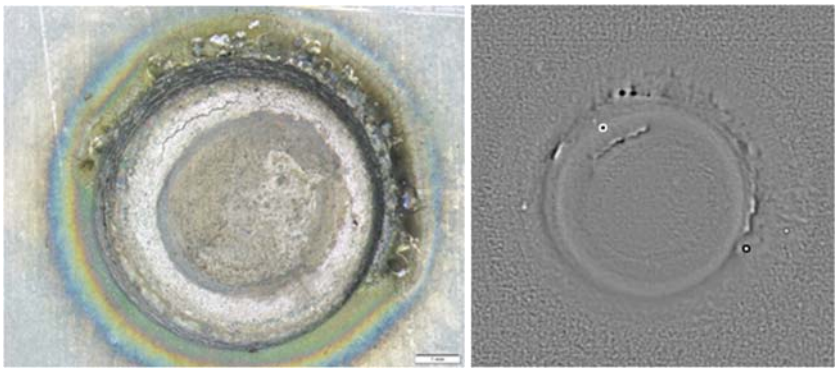

**Figure 97: Visible inspection using optical microscope (left). Laplacien filtered phase image (right).**

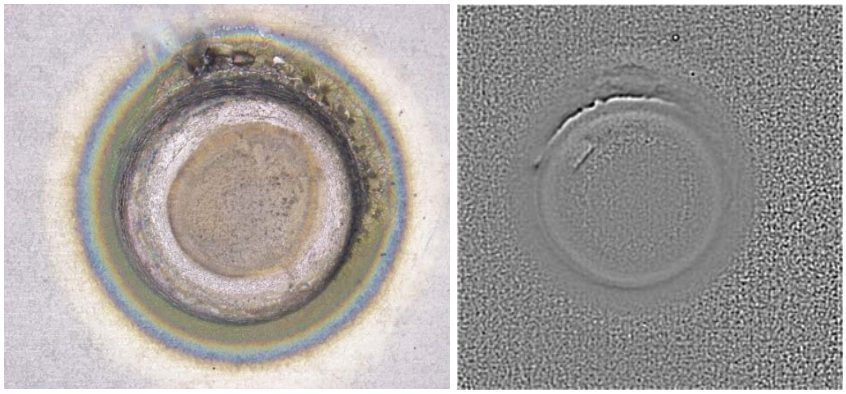

**Figure 98: Visible inspection using optical microscope (left). Laplacien filtered phase image (right).**

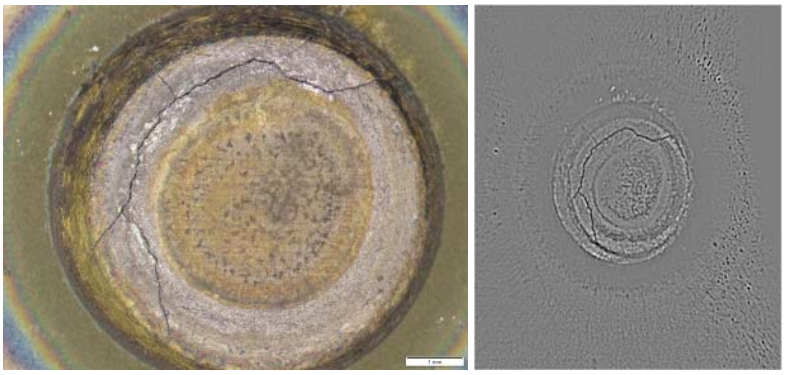

**Figure 99: Visible inspection using optical microscope (left). Laplacien filtered phase image (right).**

Phase contrast proofiles obtained from specimens with EDM show a strong relationship between EDM depth and blind frequency. Deeper EDM are detected at low frequencies while shallow EDM are visible at high frequencies.

To establish an empirical model for LME crack depth prediction, a linear fitting was carried out between EDM depth and the inverse square of blind frequency. Therefore, this model was used to predict LME crack depth based only on blind frequency as in input.

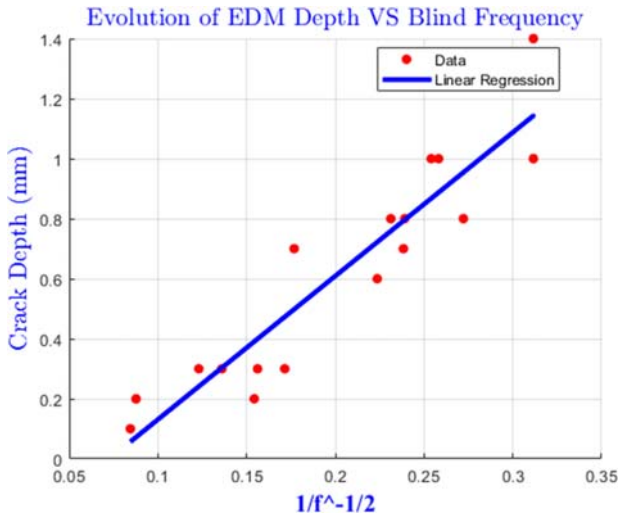


**Figure 100: EDM depth vs blind frequency linear fitting.**

The prediction of LME crack depth based on our model is encouraging since it overestimate the real crack depth with approximately 20%. This accuracy could be sufficent for LME crack classification in three category:

- Category 1: Depth≤0.2mm
- Category 2: 0.2mm<Depth < mid-thickness
- Category 3: Depth > mid-thicness

Based on depth estimation in Figure 101, below the classification proposed:

- Category 1: no specimen
- Category 2: 7536, 7538 and 7567
- Category 3: 7546

One can note only one misclassification which is the specimen n° 7567.

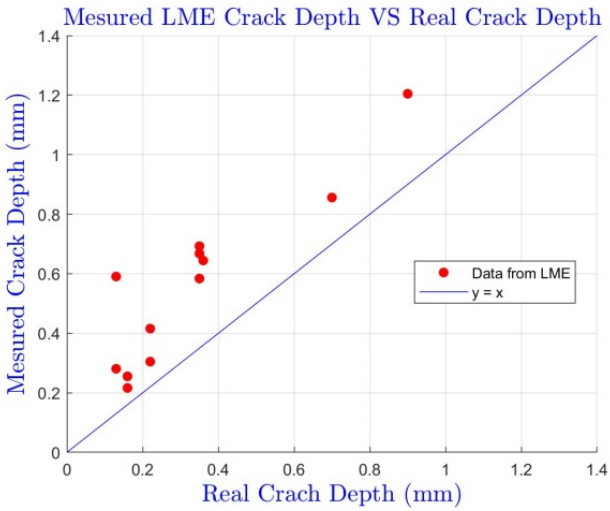


**Figure 101: Estimated crack depth vs real crack depth.**

### 4.5.4. Practice recommendations

#### 4.5.4.1. Applicability

PECT is well adapted for LME crack detection in laboratory and production application. It has also a potential for depth estimation in laboratory and production application. Prior to implementation, a calibration study should be performed in order to validate the performance of depth estimation. PECT provides qualitative information on crack length, opening and location using a simple visual observation of PECT pictures and quantitative information on crack depth using advanced analysis. For quantitative analysis and identification of the crack length and depth, further investigations are needed to develop the suitable image processing algorithm.

#### 4.5.4.2. Implementation

To be able to inspect a high number of spot welds according to production cadency, the method needs to be fast. The main solution is to mount the camera and heating system to a robot in order to achieve an automatic inspection.

#### 4.5.4.3. Reliability

In terms of detection of small and big LME cracks, this method is relevant as proven in laboratory condition. However, for production application, the environment is totally different, and reliability may depend on various factors:

- The heating homogeneity (high indentation can modify heat propagation and affect results)
- Shiny surfaces due to reflection from environment can disturb measurements
- Calibration phase for depth estimation

#### 4.5.4.4. Application Cost

##### *Production environment*

The cost of PECT instrumentation used is approximately 130k€. The industrialization of the solution for production application may reach 200 k€-250k€ (including the robot). The high cost is due to high resolution cooled camera. Further investigations are needed to evaluate the performance of low-cost cameras for LME crack detection and characterization.

Considering the following assumption:

- Depreciation period= 5 years
- Robot working time per year= 3760 hours (16hours per day, 5 days per week and 47 weeks per year; 5 weeks for maintenance)
- Number of spots per minute= 1 spot weld; Spot weld time= 1min
- Productivity= 80% => Spot time= 1.25 minute.
- Total number of spots weld per day= 768 spots. (= 16*60/(1.25))
- Number of RSW in 5 years: 768×5×47×5=902400 spot welds

Depreciation per spot weld calculated according to the formula (4), is estimated to 0.22 € for installation cost 200 k€,

##### *Laboratory environment*

The cost of PECT instrumentation is approximately 130k€.

Instrumentation components are:

- Induction generator: 20 k€
- Inductor: 6500€ Mini-cracky LT but other this cost can be significantly decreased using homemade inductors
- Camera: 75 k€
- Software: 25 k€

For the following assumption (the same cadency as for AE, MPI for comparison):

- Instrumentation cost: 60 k€ (basic equipment)
- 1 operator /machine
- Working time of the machine = 4Hours per day for 30 weeks per year.
- Number of spots per day=200 spots; Number of spots per year =200*5*30= 30000 spots; 150000 spots in 5 years

Depreciation per spot weld calculated according to the formula (4), is estimated to 0.86€

$$\text{Depreciation per spot weld} = \frac{130000}{150000} = 0.86€$$

#### 4.5.4.5. Automation

Development of an automated algorithm for features extraction from thermograms and depth estimation should be automated. Also automatic classification of cracks according to their depth is important to make the solution time and cost effective.

Concerning its possible use in production, the analysis provided for ECA is available for the ECPT technique.

### 4.5.5. Conclusion

The ECPT NDT technique permits the detection. It allows also the characterization, basing on a learning step. It reliability depends many parameters such as the learning step and the skills of the analyst. The main advantage of this technique is its no-need for a coupling material.

## 4.6. CT technique & RoboTom system

### 4.6.1. Background

X-ray Computed tomography (XCT) is a nondestructive technique which is the most common kind of technics used for medical application. The scan procedure is briefly described as follows: A conical beam from an X-ray source penetrates the investigated object. The attenuated radiation is measured by a large area detector. In order to irradiate the object from all sides, the object rotates in the X-ray cone. During rotation a set of projections is measured and stored. The set of projections is then used to reconstruct the 3D structure of the object. The advantage is that we can view and slice the object at any angle we want. A CT image is typically called a slice, as it corresponds to what the object being scanned would look like if it were sliced open along a plane. The gray levels in a CT slice image correspond to X-ray attenuation, which reflects the proportion of X-rays scattered or absorbed as they pass through each voxel. X-ray attenuation is primarily a function of X-ray energy and the density and composition of the material being imaged.

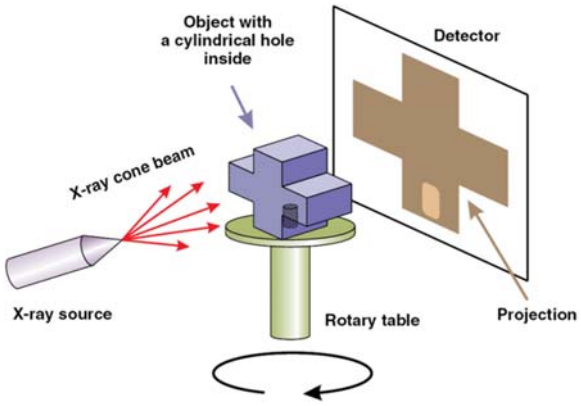


**Figure 102 : Illustration of 3D cone beam CT principle [17]**

When a large object has to be inspected with high resolution, conventional XCT has its limitation. If we take the example of resistance spot weld, for a real piece of several thousand of mm or either a specimen of 100mm length and 3-4 mm thickness, the area of interest is around 10 mm diameter and LME crack is few µm opening and few mm in depth. As the specimen/piece is large, a high absorption will be observed for longitudinal direction, so depth estimation and RSW reconstruction will be limited. For this reason, XCT is suitable for RSW inspection in a small specimen.

In the case of large assemblies, the company RayScan Technologies has developed in 2018 an XCT robot for inspection of the complete set of joining elements of a car body. This robot is called "RoboTom" provide a local tomography of regions of interest (ROI). This development was collaboration between AUDI Brussels, Rayscan and Fraunhofer EZRT.

In this robot, X-ray tube and X-ray detector are attached via an arm on a frame. The frame is being hold by the robot and brought into position. In contrast to conventional XCT, the X-ray tube is rotated with 360° around the region of interest such that the beam axis is always pointed to the detectors center. According to Rayscan [18],During a scan, the cone beam defined by the detector surface encloses a primary field of view in the form of a polyhedron, which converges to an equilateral pyramid in case of a detector with a square sensor. Every object detail within this primary field of view is visible on every projection image and can thus be reconstructed based on a maximum number of samples. The further out there is an object detail, the fewer samples are available. Nevertheless, this secondary field of view can also be 3D reconstructed. The following illustration shows the setup.

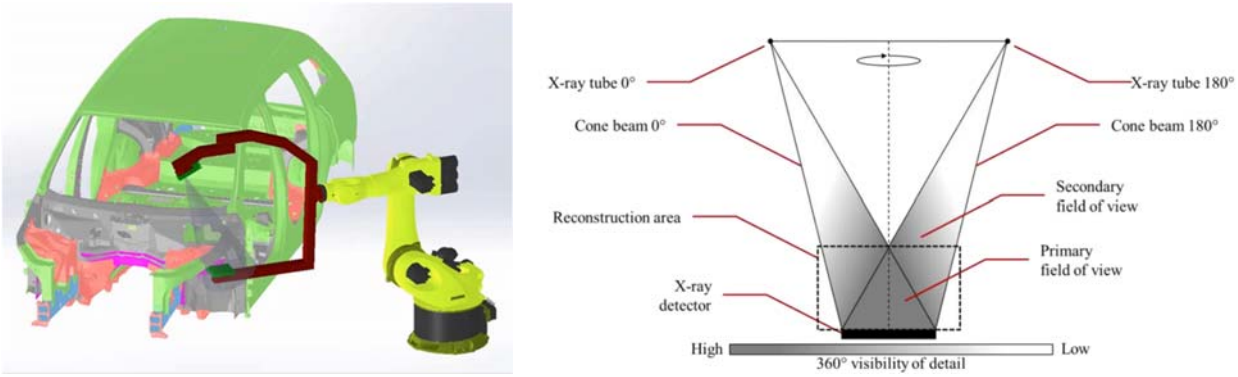


Figure 103: RoboTom scan geometry. [18]

### 4.6.2. Methodology & Experiments

XCT is used in this program as a nondestructive reference which provides relevant information on LME crack features in particular depth and form inside the weld spot. Various specimens with a small size (15mm*15mm) were controlled at the beginning of the program, and then dimensions increased to 35mm*35mm which is a good compromise between specimens size and scans resolutions.


Figure 104: 7 specimens 35mm*35mm chosen for XCT scans.

All XCT have been performed by our subcontractor North Star Imaging. The system used is the NSI X5000 with the following setup:

- X-Ray Source: 240KV
- X-Ray tube Type: Micro-focus
- X-Ray Detector type: Flat Panel (DDA)
- X-Ray Detector size: 40cm*40cm , 2048*2048 pixels, grade option Premium
- Resolution is 10µm (voxel size).

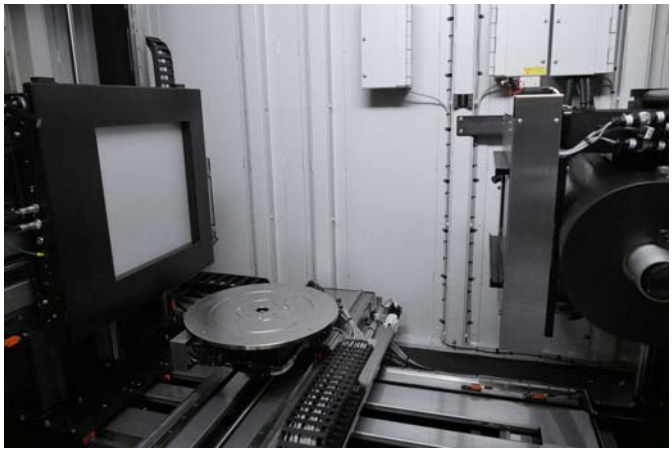

Figure 105: Interior of the NSI X5000. Flat panel left and source right.

For a standard CT scan, the acquisition time is around 1 hour while for our scans, time was reduced to 15 minutes with a reconstruction time between 5-10minutes.

For the evaluation of depth estimation/measurement by RoboTom, Three specimens were chosen which were already characterized by XCT.

Blind depth estimation is then performed by RoboTom and then results compared to XCT.

RoboTom Setup:

- X-Ray Source: 140KV
- Focal spot < 500µm
- Time of acquisition by specimen: 3 minutes
- Resolution= 100µm but 50µm after reconstruction.

### 4.6.3. Results & discussions

- **XCT of specimens 15mm*15mm**

The following table summarizes depth measured with XCT on 15*15 cm² specimens.

**Table 18: Depth measurement with XCT.**

| Specimen n° | Weld time (ms) | Depth (mm) |
|---|---|---|
| V9235 | 1280 | 1.114 |
| VN244 | 640 | 0.05 |
| VN247 | 960 | 0.26 |
| VN249 | 1280 | 0.31 |
| VN252 | 1600 | 0.31 |
| VN262 | 1600 | 0.84 |
| VN265 | 1600 | 0.2 |
| VN269 | 1600 | 0.32 |

The analysis of CT scans with suitable software such as VG studio enables the user to manipulate 3D data and extract depth measurement in different location and also visualize the crack from different view and slices: Top view, lateral view and 3D view. Figure 106 shown the example XCT result of the specimen n°V9235. The RSW was obtained with an extend weld time of 1280ms. It is clearly shown that the LME crack is located inside the nugget near the indentation with small networks located in the corner. The maximum depth is 1114 µm of the main crack. One of the most important results that can be extracted from 3D scans is the 3D form and dimensions of the LME crack. This was successfully determined in the figure x using image processing algorithms which identify the crack surface for each slice. The real 3D form of the crack in then extracted and exported to STL format that can be used for CAD and simulation. Implement the real crack feature in the CAD model will lead to improve simulation and mechanical behavior prediction. The crack bloc file was shared with IPK and implemented in simulations.

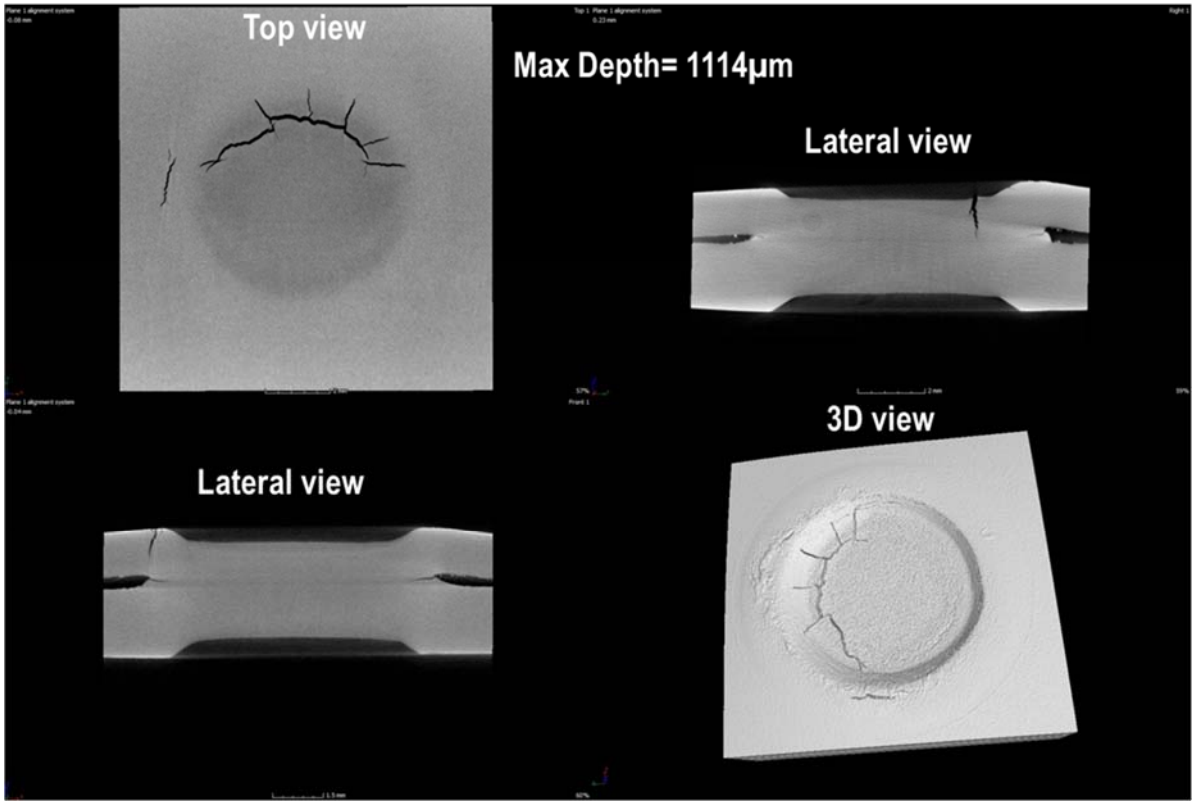


Figure 106: XCT scans of specimen n° V9235.

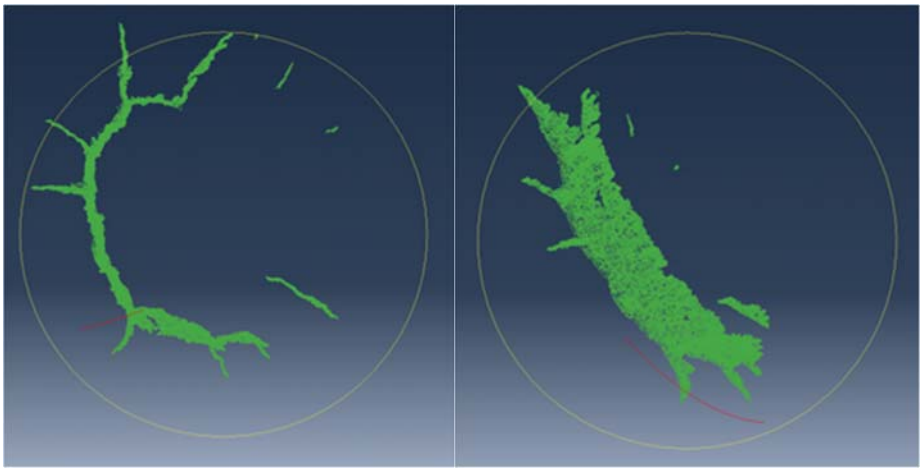

Figure 107: 3D extraction of crack features.

Below the XCT results of the 8 specimens controlled. In the case where crack is partially filled with Zinc, it is not obvious to be categorical, on the detection of the crack tip. Steel and Zinc density have relatively close densities and it will be reasonable to think that with XCT and on this scale, a crack filled with Zn would not be detectable.

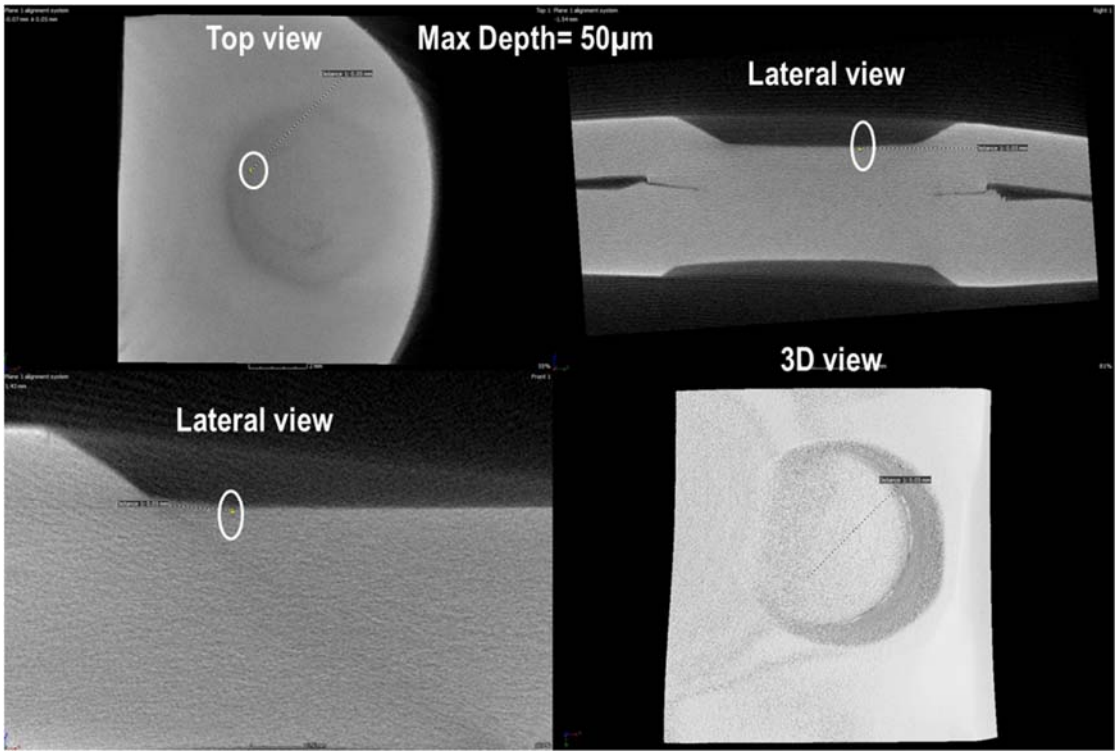


**Figure 108: XCT scans of specimen n° VN244**

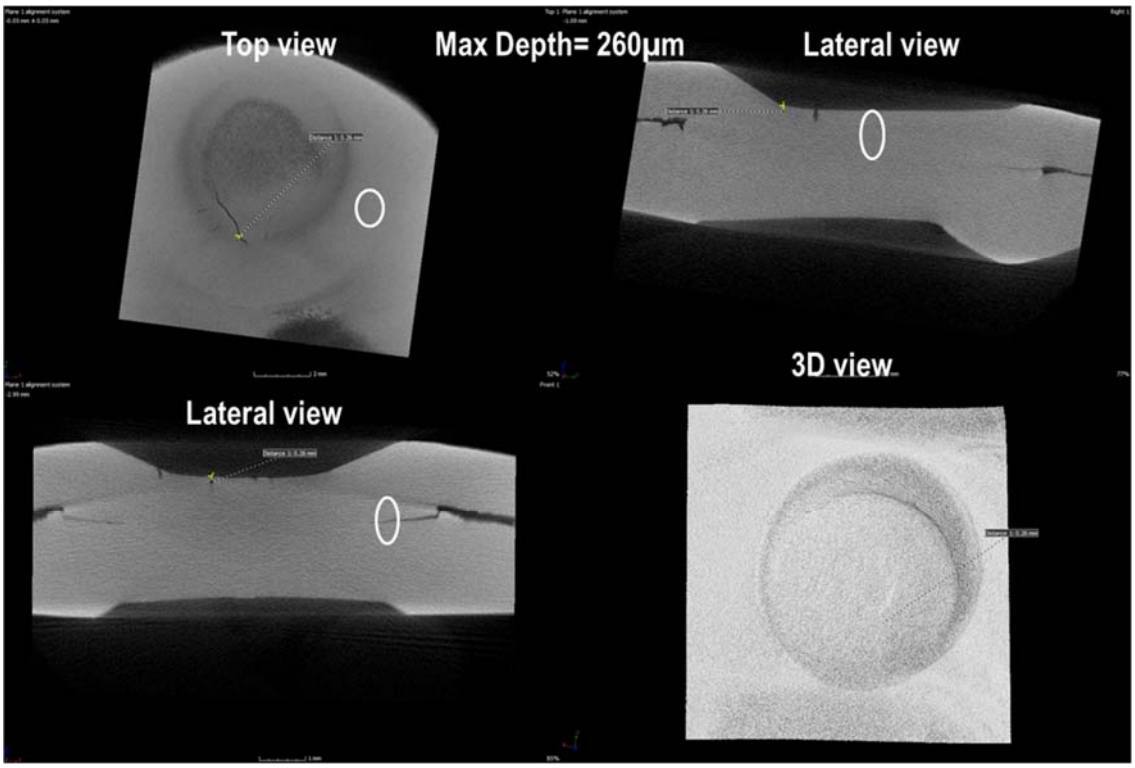


**Figure 109: XCT scans of specimen n° VN247**

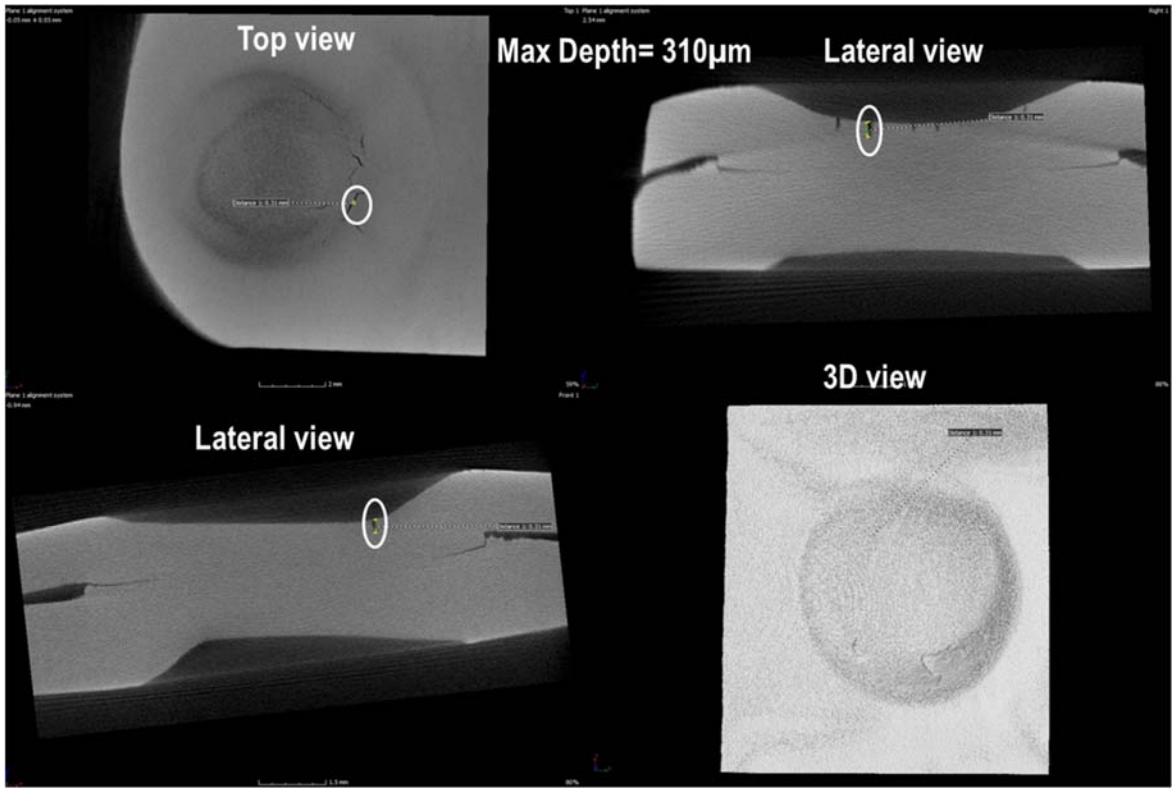


Figure 110: XCT scans of specimen n° VN249

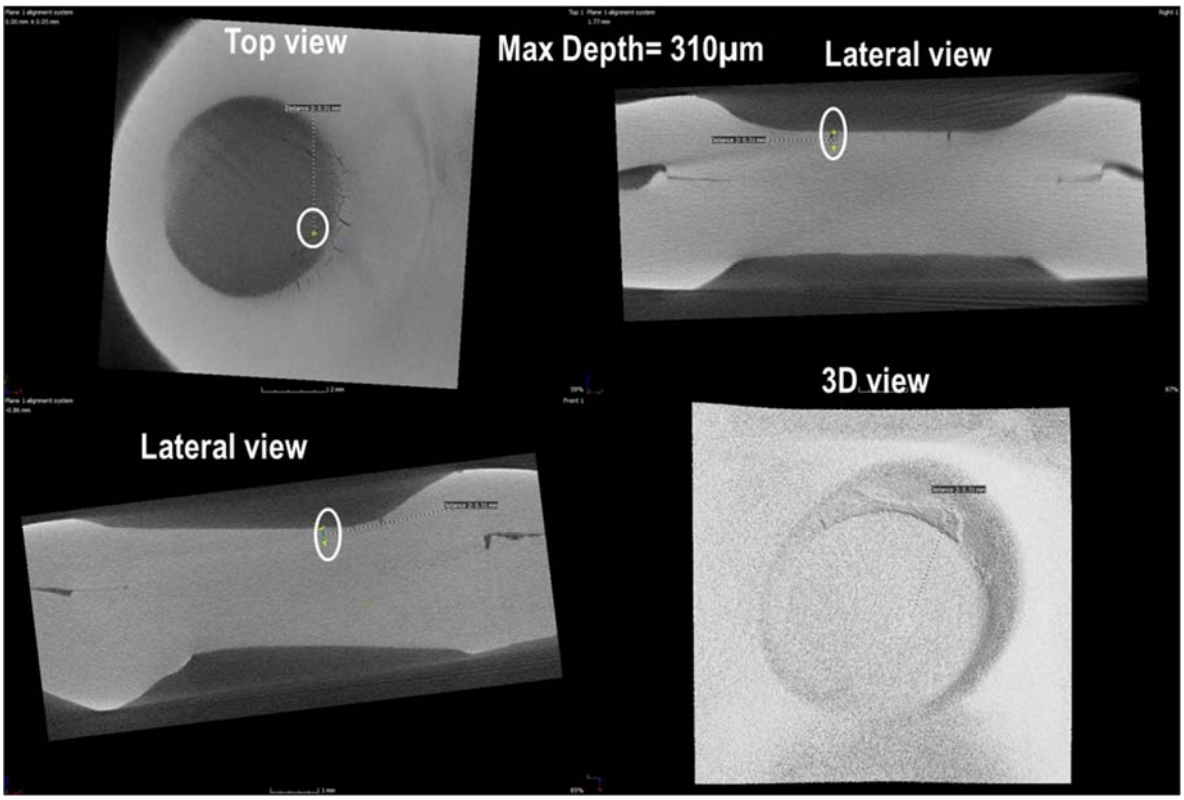


Figure 111: XCT scans of specimen n° VN252

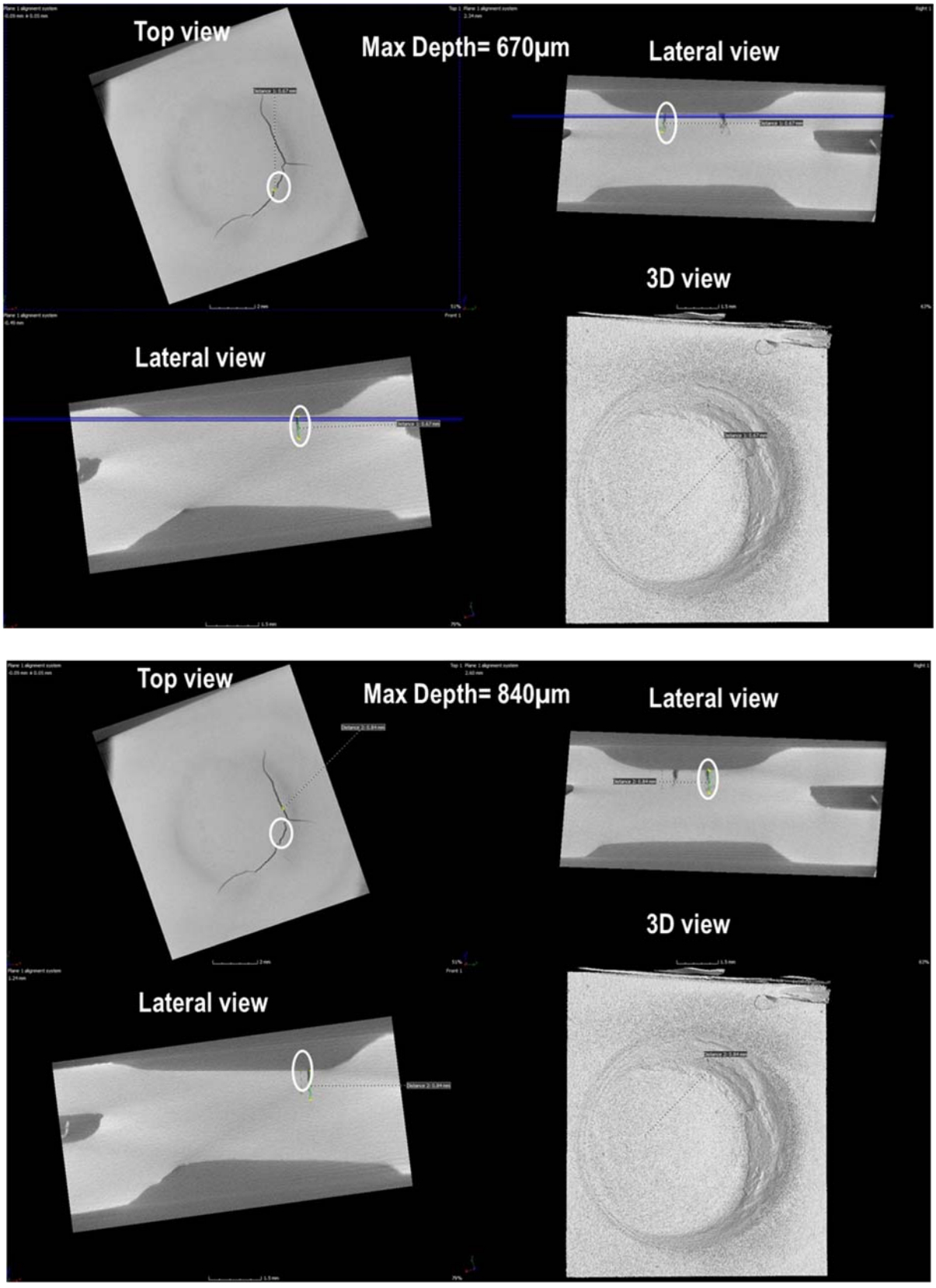


**Figure 112: XCT scans of specimen n° VN262**

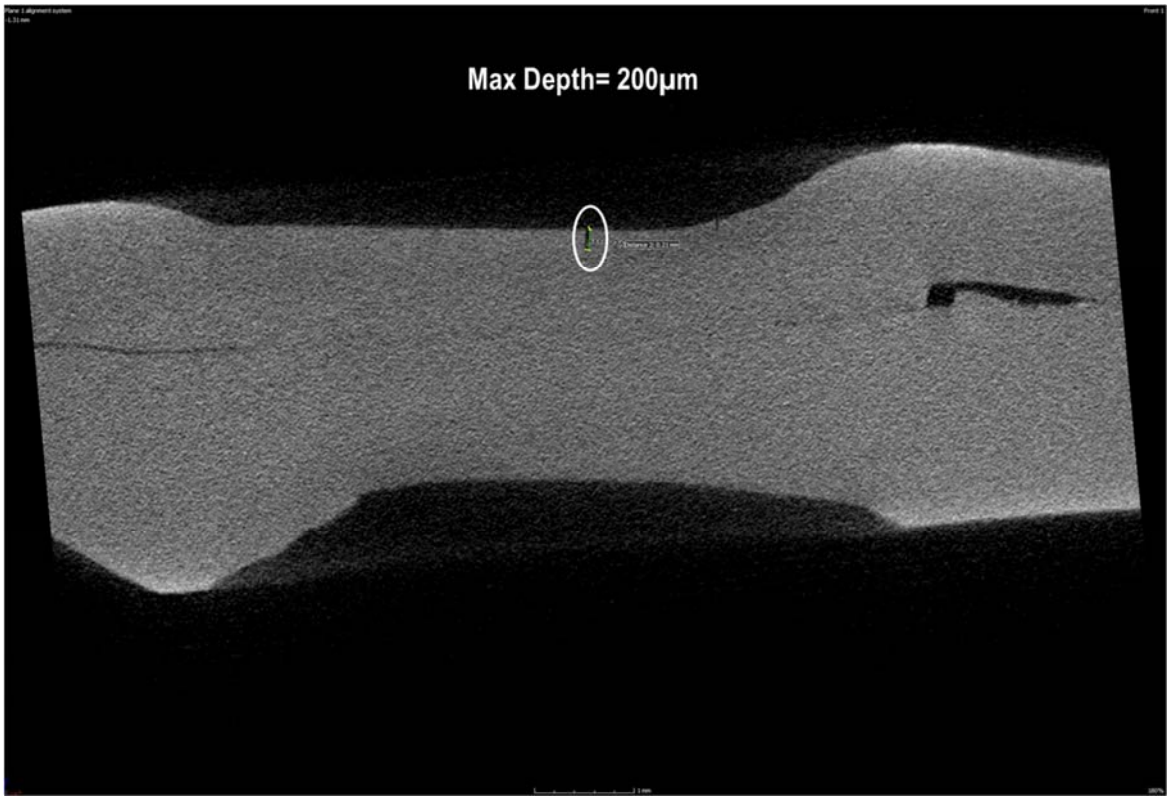


**Figure 113: XCT scans of specimen n° VN265**

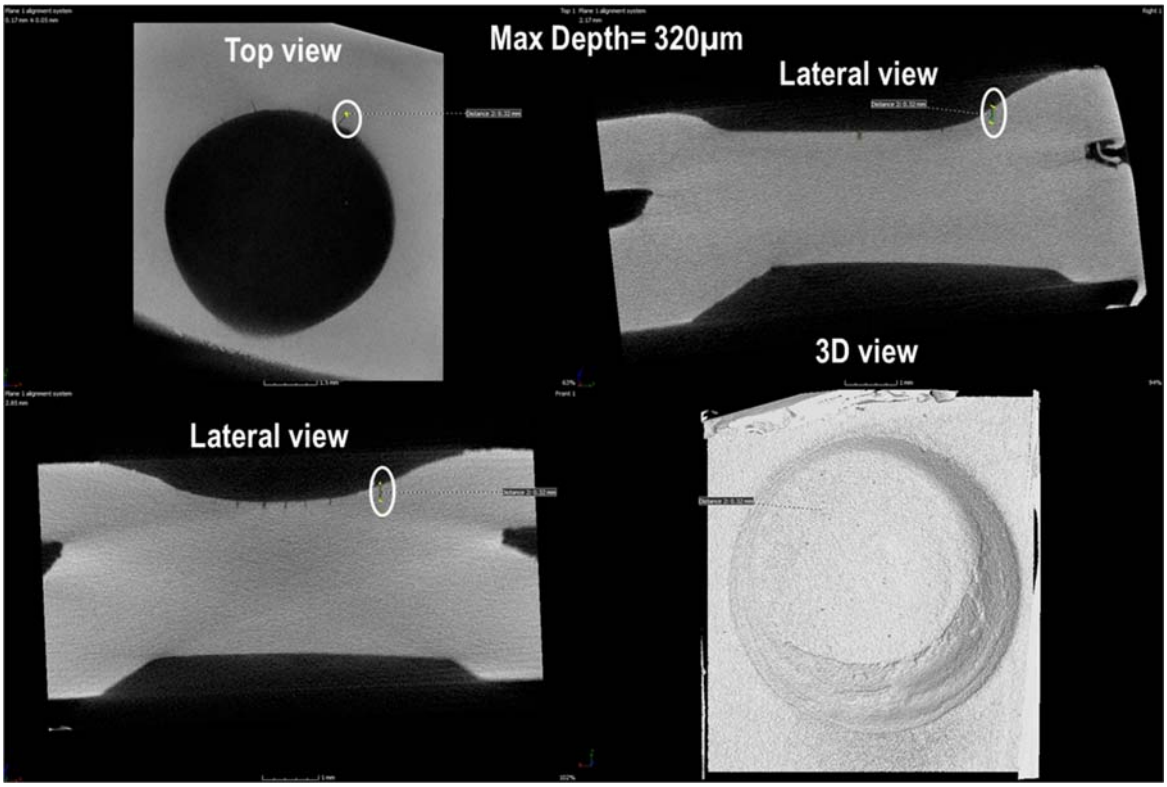


**Figure 114: XCT scans of specimen n° VN269**

- **XCT of specimens 35mm*35mm**

Figure 115 to Figure 118 are XCT results of the 7 specimens with dimensions 35mm*35mm. The resolution obtained is similar compared to small specimens. For each specimen, crack features, in particular depth at different location have been determined. These specimens were used as a reference for evaluation of other NDT such as Thermography and RoboTom. The conclusion that can be drawn from these XCT scans is that crack depth is not uniform. For the main crack of the specimen n°7525, the depth varies from 0.42mm to 1.18mm. And what it makes difficult the detection of LME crack by various NDT, is that the opening is very thin, about 10-20µm. Furthermore, the orientation can be slightly inclined to the top surface and the opening decreases with depth, which complicates depth estimation.

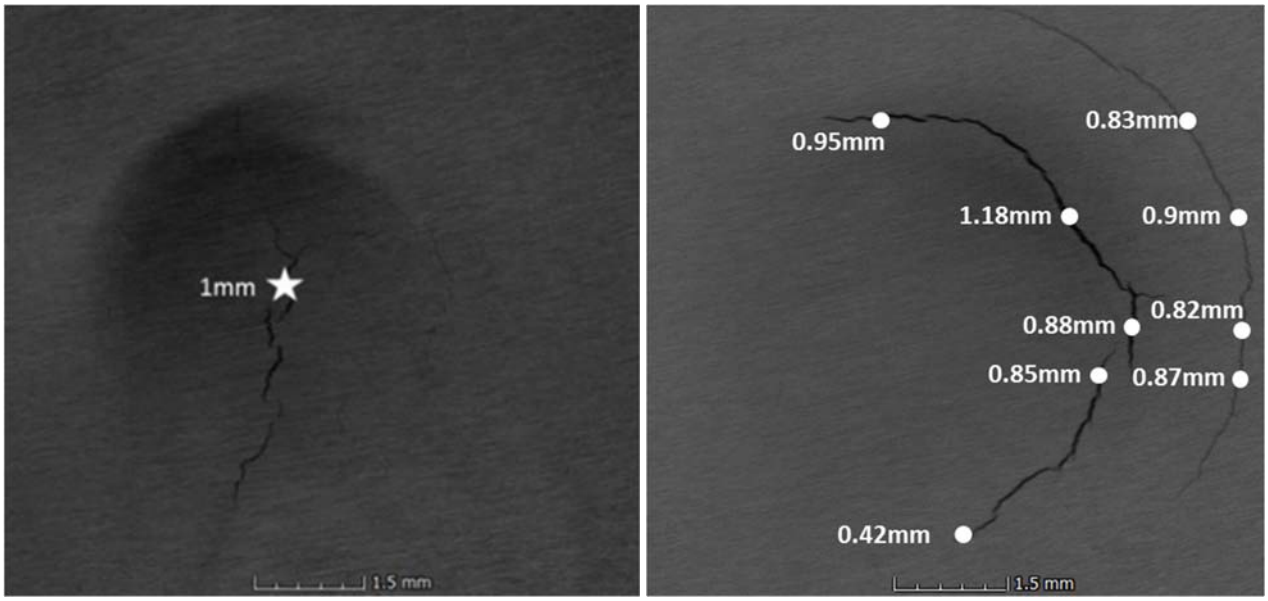


**Figure 115: XCT scans of specimen n°7555 left and n°7525 right.**

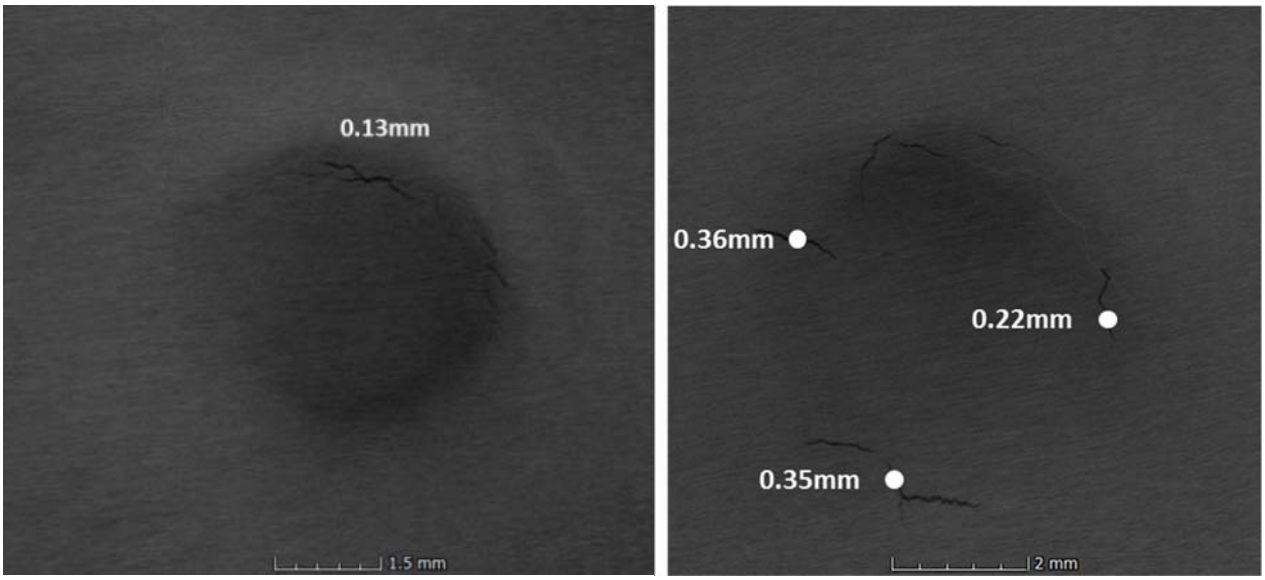


**Figure 116: XCT scans of specimen n°7567 left and n°7538 right.**

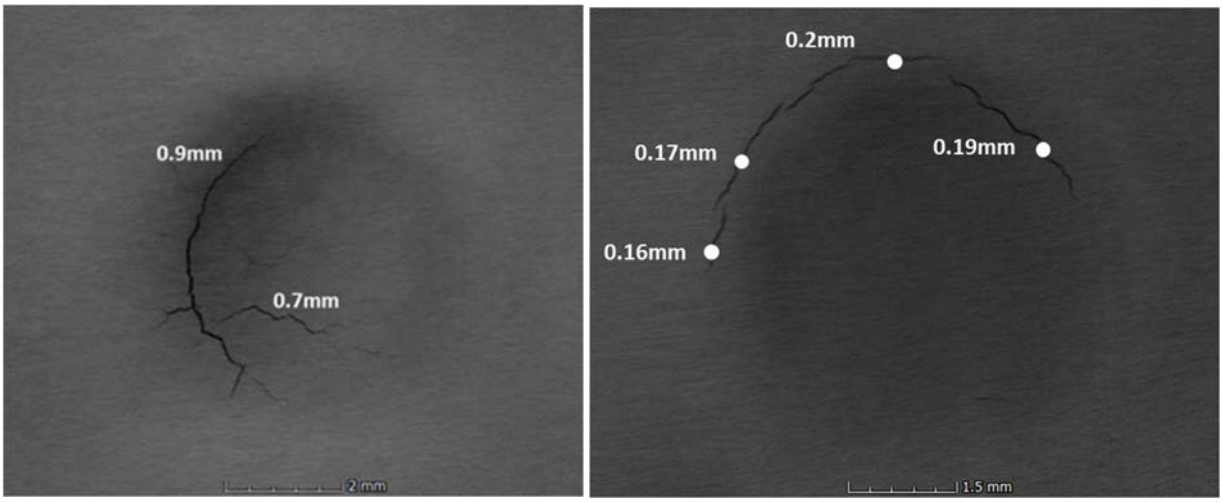


**Figure 117: XCT scans of specimen n°7546 left and n°7536 right.**

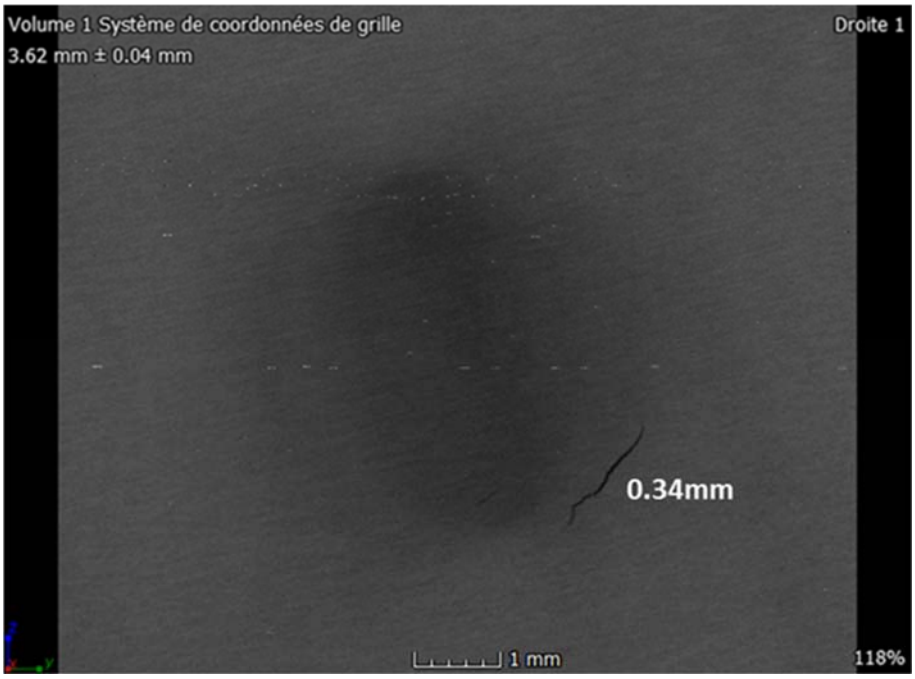


**Figure 118: XCT scans of specimen n°10369.**

- **Evaluation of RoboTom scans**

As indicated previously, three specimens were blind controlled with RoboTom. The normal resolution due to the setup and equipment configuration is 100µm was decreased to 50 µm using reconstruction to improve depth estimation.

The following figures show CT scans of the three specimens controlled. The comparison between depth measured with RoboTom and with conventional XCT are quite similar.

For the specimen n°755, the maximum crack depth estimated by RoboTom is 1.10 mm while the one measured by conventional XCT was 1mm. For specimen n°7456, maximum depth estimated is 1.05mm vs 0.9mm with

conventional XCT. Finally for specimen n°7567, maximum depth estimated is 0.11mm vs 0.13 with XCT. One can note that 3D scan of the spot is difficult to recognize which is due to the method of scan. As the beam is tilted at 360° from the top surface of the spot, the reconstruction of the 3D volume still difficult, however, depth estimation accuracy is acceptable.

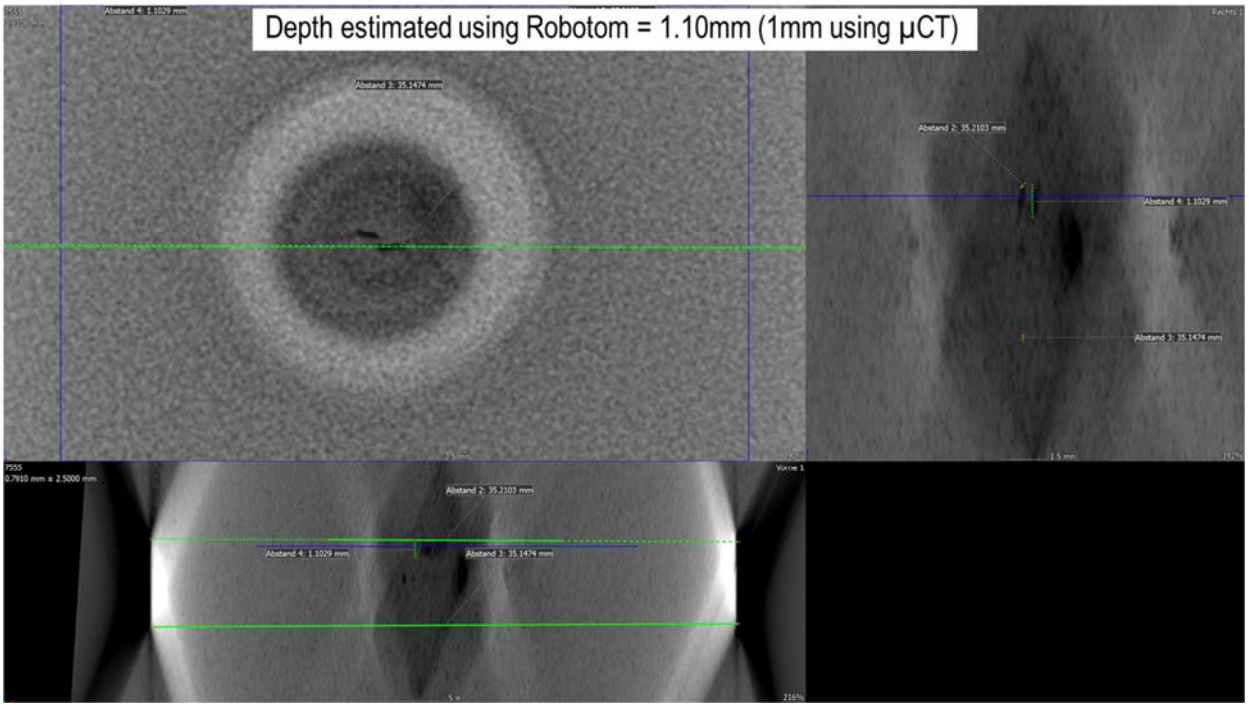


**Figure 119: RoboTom scan of the specimen n°7555.**

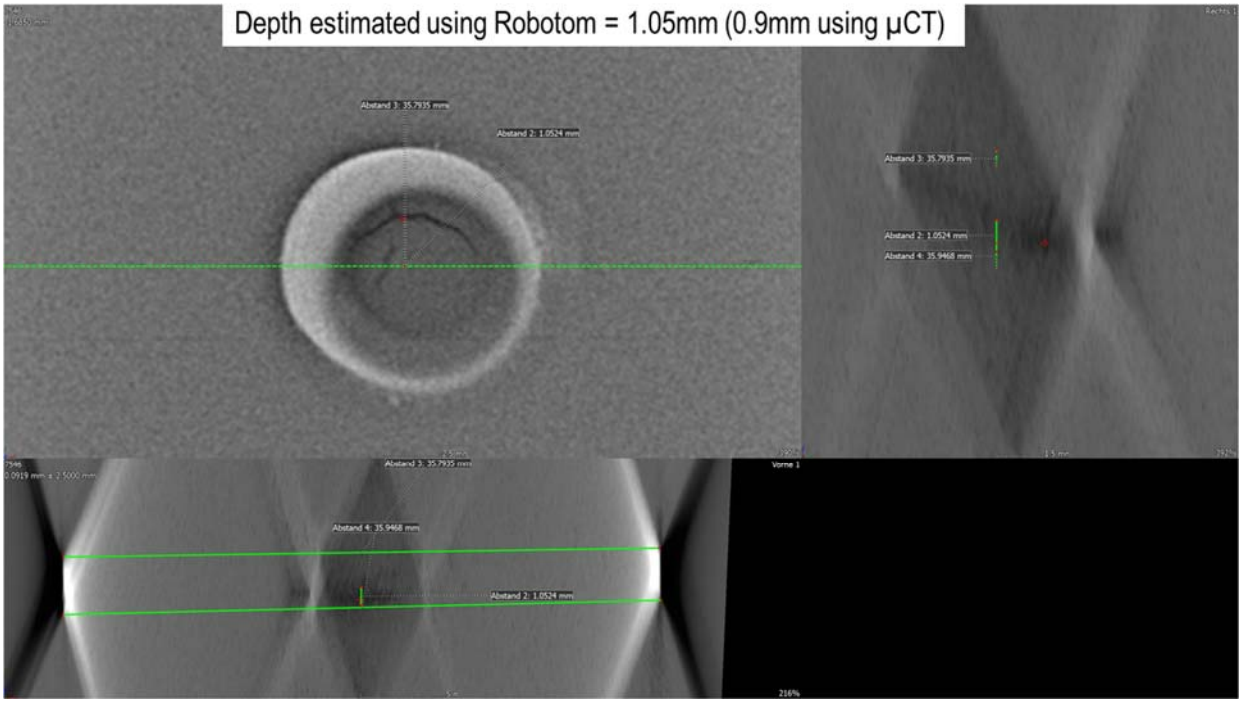


**Figure 120: RoboTom scan of the specimen n°7456.**

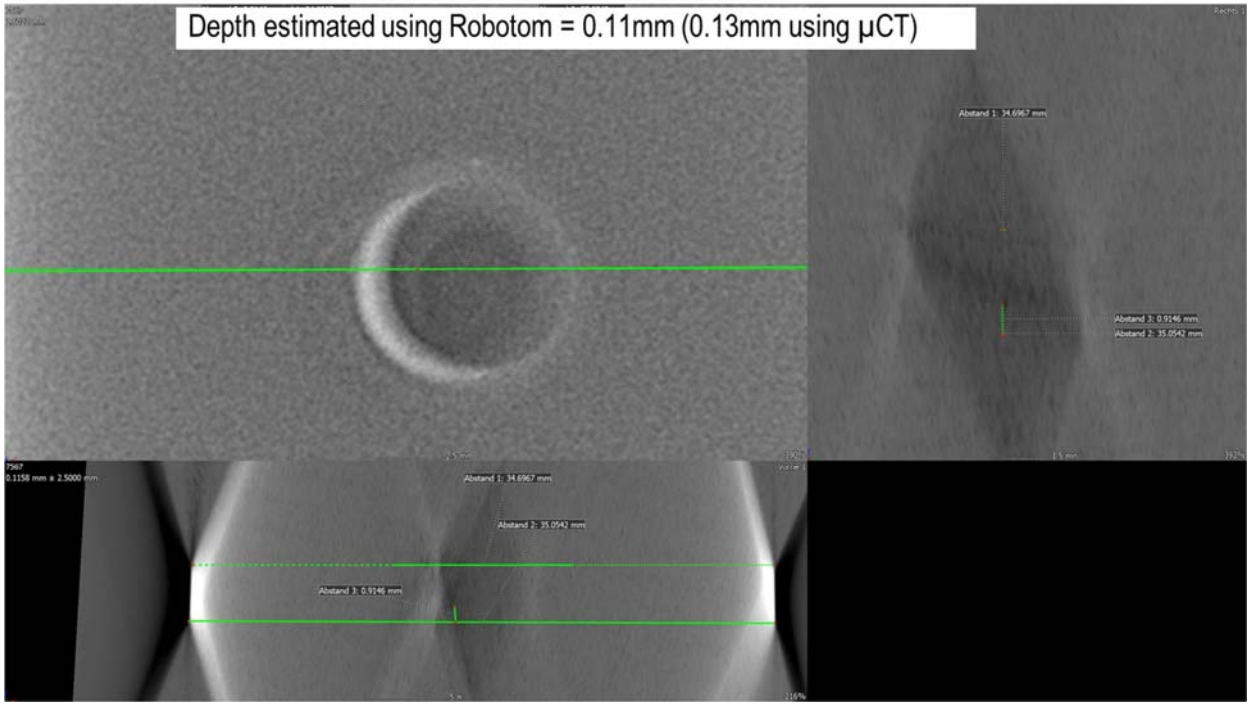


**Figure 121: RoboTom scan of the specimen n°7567.**

### 4.6.4. Practice recommendations

#### 4.6.4.1. Applicability

Conventional XCT technique is suitable for LME crack detection and characterization in laboratory condition. Due the high cost of the control (≈500€ by spot if test is done by subcontractor) it is rather used for characterization providing that specimen dimensions are acceptable (small size). Identification of LME crack features (length, opening, depth, location) is manually performed by a qualified operator.

The RoboTom system is a good solution for crack detection and characterization in production environment. When spot welds in real automotive components (large components) needs to be scanned, RoboTom will be the best CT solution. This system was designed to fully control all joining elements of a car body and one system has already deployed at AUDI. It can be very easily adapted for RSW application. . Further development will be needed to fully automate the analysis of CT scans.

#### 4.6.4.2. Implementation

No calibration step is needed for RoboTom to estimate LME crack depth. However, a validation phase should be performed prior to implementation in order to validate the setup and accuracy of measurements.

Many configurations are possible for implementation in production conditions:

- The robot can turn while the body car is fixed. An automation of the movement of robot for each joining element should be encoded.
- The car body can turn while the robot is fixed (or by limiting the movement of the robot).

For security reasons, a cabinet is required to avoid radiations of operators. Modular X—ray shielding cabinets is possible and can be customized according the need of automotive manufacturer/ car components providers. An example of cabinet dimensions that can be provided by Rayscan is given below.

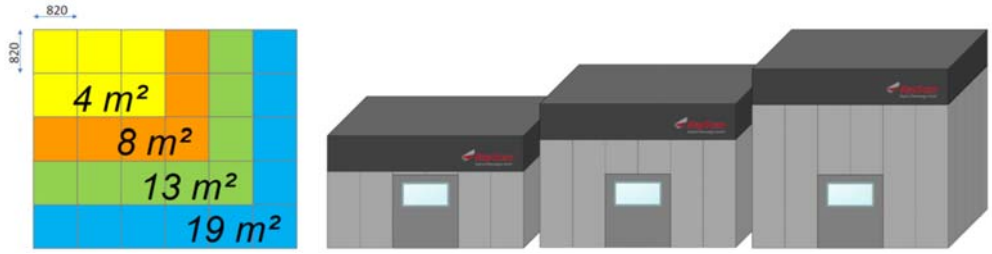


**Figure 122: Easy modular X—ray shielding cabinets.**

Only qualified operators can manipulate this kind of system.

According to Rayscan, the solution is fast: 2min/scan but various RSW can be scanned in one shot. Length of the area is estimated to 1m.

#### 4.6.4.3. Reliability

The reliability will depend on different factors such as accessibility of the RSW, geometry complexity and also the setup and the resolution of voxels used.

#### 4.6.4.4. Application Cost

##### *Production environment*

According to Rayscan, the cost of RoboTom is estimated to 300k€ without the cabinet. It is important to note that the X-ray source and Flat panel detectors can be mounted to any robot. A budget of 350-400k€ should be provided for deployment.

An estimation of spot control cost still difficult to evaluate at this stage but estimation is tried based on the following assumption:

- Cost of instrumentation = 300k€ (without the cabinet and industrialization).
- Depreciation period= 5 years
- Robot working time per year= 1880 hours (8 hours per day, 5 days per week and 47 weeks per year; 5 weeks for maintenance)
- Time for operators per years = 1880 hours (one operator by workstation)
- Number of operators: one per day
- Charged salary per operator per year= 50k€
- Overhead costs = 30%
- Number of spots per minute= 0.25 spots (1spot each 5 min)
- Productivity= 80% => Spot time= 6.25 minute.
- Total number of spots weld per day= 76 spots. (= 8*60/(6.25))

Considering this assumption, depreciation per spot weld is estimated to 3.35 €.

$$\text{Depreciation per spot weld} = \frac{300000}{89300} = 3.35€$$

The salary cost per spot weld unit is calculated as follows:

The salary cost per spot weld unit is estimated to 3.64 €.

*Laboratory environment*

For the following assumption:

- Instrumentation cost: 300 k€ (without the cabinet)
- 1 operator /machine
- Working time of the machine = 4 Hours per day for 30 weeks per year.
- Number of spots per day=30 spots; Number of spots per year =30*5*30= 4500 spots; 22500 spots in 5 years

Depreciation per spot weld calculated according to the formula (4), is estimated to 13.33 €

$$\text{Depreciation per spot weld} = \frac{300000}{22500} = 13.33\ €$$

The salary cost per spot weld unit is calculated as follows:

The salary cost per spot weld unit is estimated to 14.44 €.

#### 4.6.4.5. Automation

The system is already fully automated for car body joining elements testing. The automation of slices reconstruction and depth estimation will require some algorithmic development, but it is feasible based on Rayscan experience.

### 4.6.5. Conclusion

RoboTom system permits detection and characterization of LME cracks in large assembly. It should be noted that the system requires some algorithmic upgrade to be used automatically in production.

## 4.7. RSWA System

### 4.7.1. Background

RSWA is an ultrasonic device designed for quality control and NDE of resistance spot welds. RSWA is a portable and simple-in-operation device capable of producing images of spot weld's internal structures. In addition to weld image, this device performs estimation of the nugget diameter and compares it with predefined minimum nugget requirements. Using the unique technology of multi-channel ultrasonic matrix transducer, RSWA collects data from the surface and from the internal structures of the nugget. Special algorithms use this data to reconstruct the image of the spot weld and estimate the average diameter of the nugget area.


Figure 123: RSWA System (left) and zoom on probe (right).

### 4.7.2. Methodology and Experiments

The general operation mode of an RSWA instrument is that single elements of the matrix transducer are pulsed and the respective single-element A-scans are received digitized and evaluated. No beam-forming is performed nor are virtual apertures being built. The gates for evaluation are being set automatically based on a setup measurement on a bare plate (area w/o spot weld) and cover the region of the fusion zone. Whenever there's no echo coming back from the fusion zone that means that both plates have been welded well. On the other hand, whenever there is an echo being reflected from region of the fusion zone, this normally means that both plates are not welded properly, or some kind of porosity formed during welding. Depending on the chosen color palette, well welded areas are colored in green and areas without weld are colored orange.

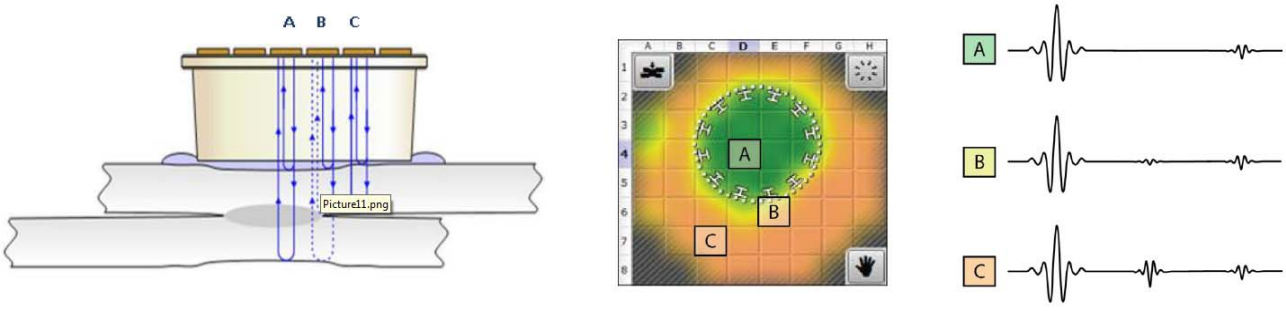


Figure 124: Measurement principle.

The probe was placed on all specimens on both sides with orientation shown in Figure 125.


**Figure 125: Orientation of probe on specimens.**

Four specimens have been tested which are already characterized by CT-scans (Figure 126). The crack features were not communicated to the operator, blind inspection is then performed.

All specimens have been tested from both sides with a 120-element matrix probe with 1.25 x 1.25 mm pitch a nominal frequency of 15 MHz. The RSWA F2 instrument was set to the following settings:

- Minimum size adjustment: off
- Secondary Echo Processing : Subtle
- Peack Detector: Aggressive
- Surface Follower: 25%
- Echo Shape Processing: Off


**Figure 126: spot welds used for RSWA evaluation. Lower pictures, with depth dimensions were not communicated to the operator during blind inspection.**

### 4.7.3. Results and discussions

To make C-scans more comparable, C-scans taken on the backside are mirrored.

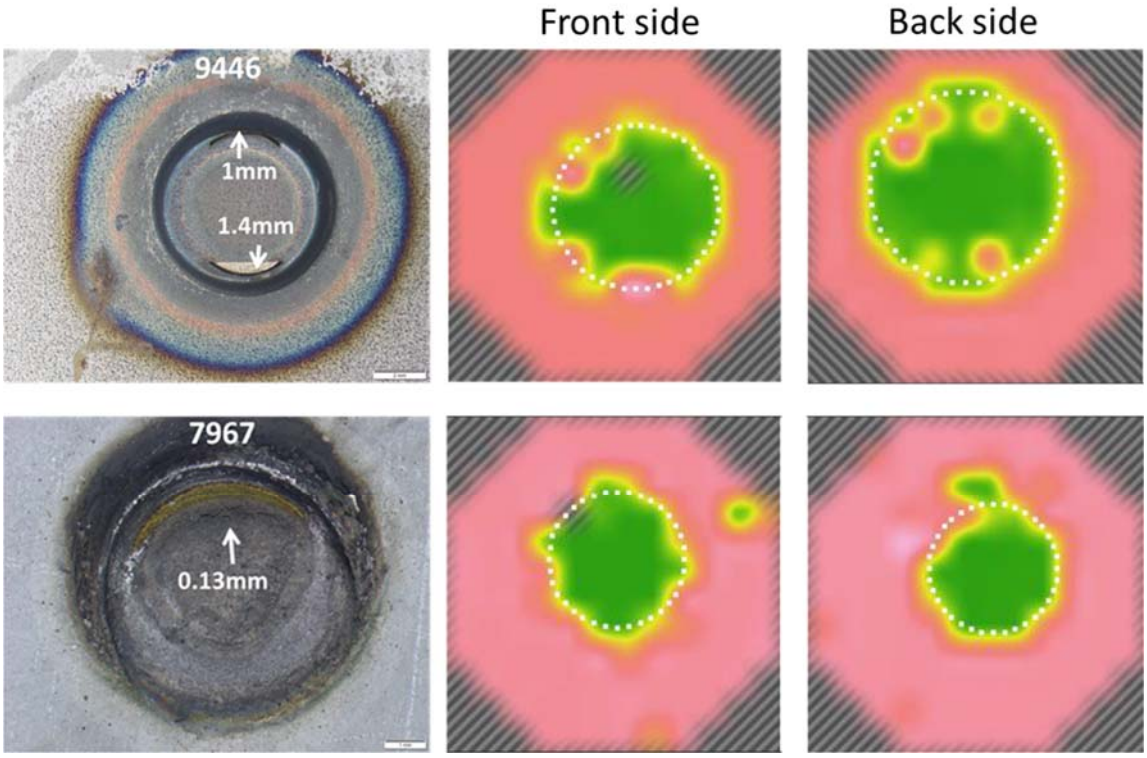


**Figure 127: Overview of all measured C-scans on specimens n°9446 and n°7967. C-scans from the backside are mirrored for comparison.**

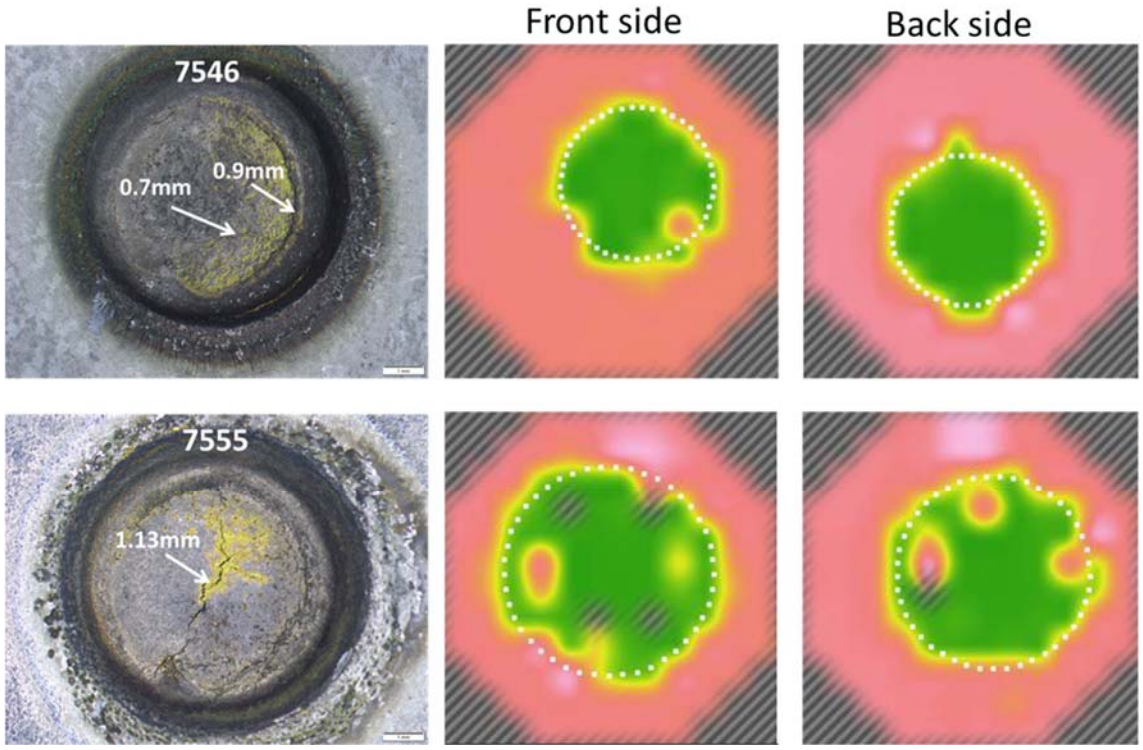


**Figure 128: Overview of all measured C-scans on specimens n°7546 and n°7555. C-scans from the backside are mirrored for comparison.**

What becomes obvious is that on all specimens - at least on one side – circular shaped features are visible, mostly around the circumference. On the instrument user interface, the operator sees a 11x11 matrix in the C-scan (without corner elements). These squares correspond to the elements of the matrix probe. If the operator choses one square on the C-scan, the respective A-scan is displayed (Figure 129).
When comparing now an area/element that shows the circular shaped feature, one sees that the A-scan belonging to the highlighted element (Figure 129) shows a peak that is appr. 180° phase shifted compared to a reflection from the backside of the 2nd plate (reflection at interface steel/air, Figure 130).

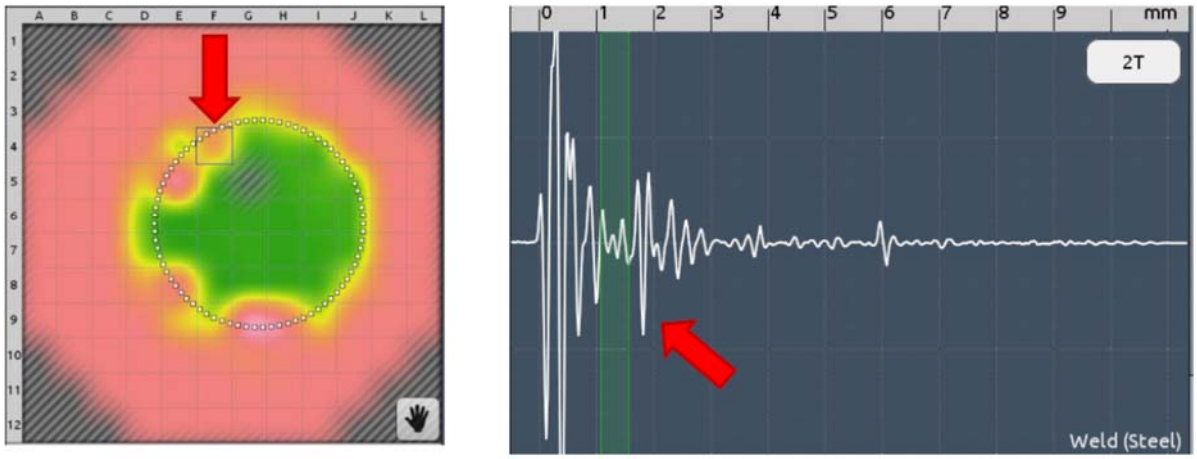


**Figure 129: When selecting a square (element, red arrow) in the C-scan (left), the corresponding A-scan is displayed on screen (right). In case of a circular feature, peak shows a 180° phase shift compared to reflection at the backside of the stack.**

When comparing this peak to a peak from the backside of the top plate one sees that position of this peak is in the same depth (Figure 130) as the peak from the circular feature. That means that the reflection causing this peak in the A-scan originated from somewhere close to the backwall of the top plate. However, since a reflection from the backwall of the top plate is coming from a steel/air interface (even if the air gap between top and bottom plate is infinitesimally small) the phase relation is the same as the reflection coming from the backside of the back plate and thus also 180° phase shifted compared to a peak from the circular features.

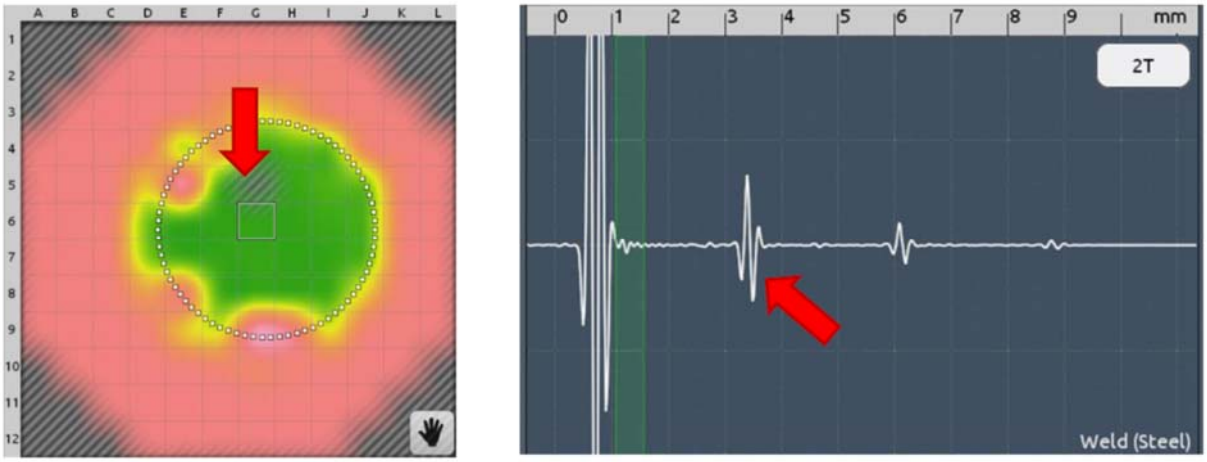


**Figure 130: Selecting an element from the welded area, the A-scans shows only reflection from the backside of the stack, thus from the interface steel/air.**

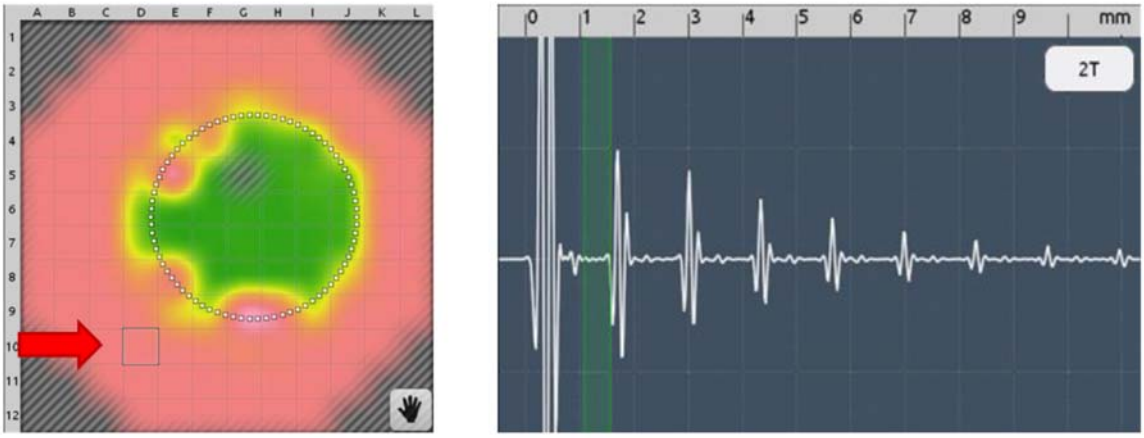


**Figure 131: A-scan from an element outside of the welded area.**

The appr. 180° phase shift now gives rise to the assumption that the peak originated from the lower end of a crack. From theory – especially on time-of-flight-diffraction (TOFD) techniques – this phenomenon is well known. The position of the peak gives rise to the assumption that the crack reaches almost all the way down through the top plate. Since only the tips of the crack diffract the sound, one cannot reliably decide on the start and the end of crack. However, the locations of the circular features give a strong indication about the extend (Figure 132). Furthermore, if this assumption should turn out to be true, based on the grid that is being displayed in the C-scan one can estimate the extension of the cracks since one square represents the size of one element of the ultrasound probe, namely 1.25 x 1.25 mm. This means, that the potential cracks in Figure 132 have a length between 2 -3 mm.

The C-scan of sample 9446 was chosen for this evaluation since the circular features are clearly visible and well defined. However, also the other samples show an irregular structure with circular features indicating the presence of cracks in the respective positions if the assumptions that have been made are proven to be true.

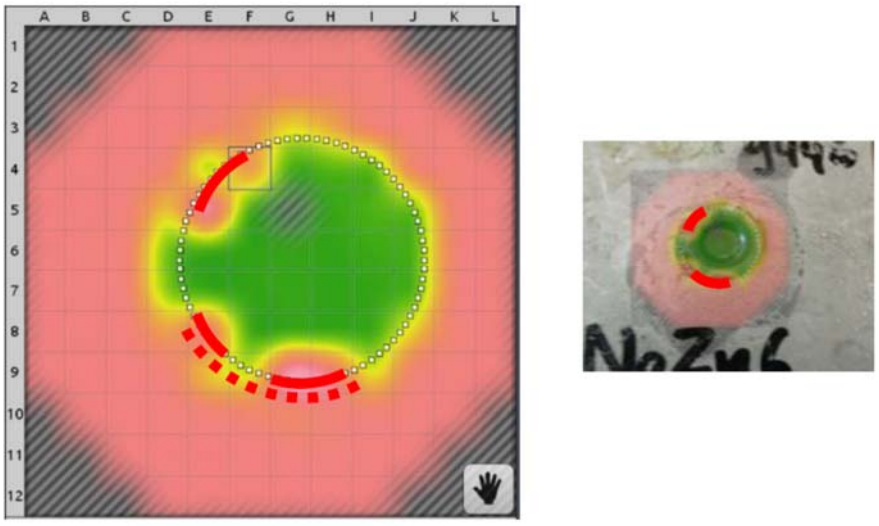


**Figure 132: Possible location and extend of cracks. Since start and end of cracks cannot be evaluated at this juncture, e.g. one cannot say if the lower circular features are 2 cracks (solid red line) or actually one bigger crack (dotted red line).**

After blind inspection of all specimens, microscope pictures were communicated to the operator to be compared to C-scans images. A superimposition of C-scans and microscope pictures is shown in Figure 133.

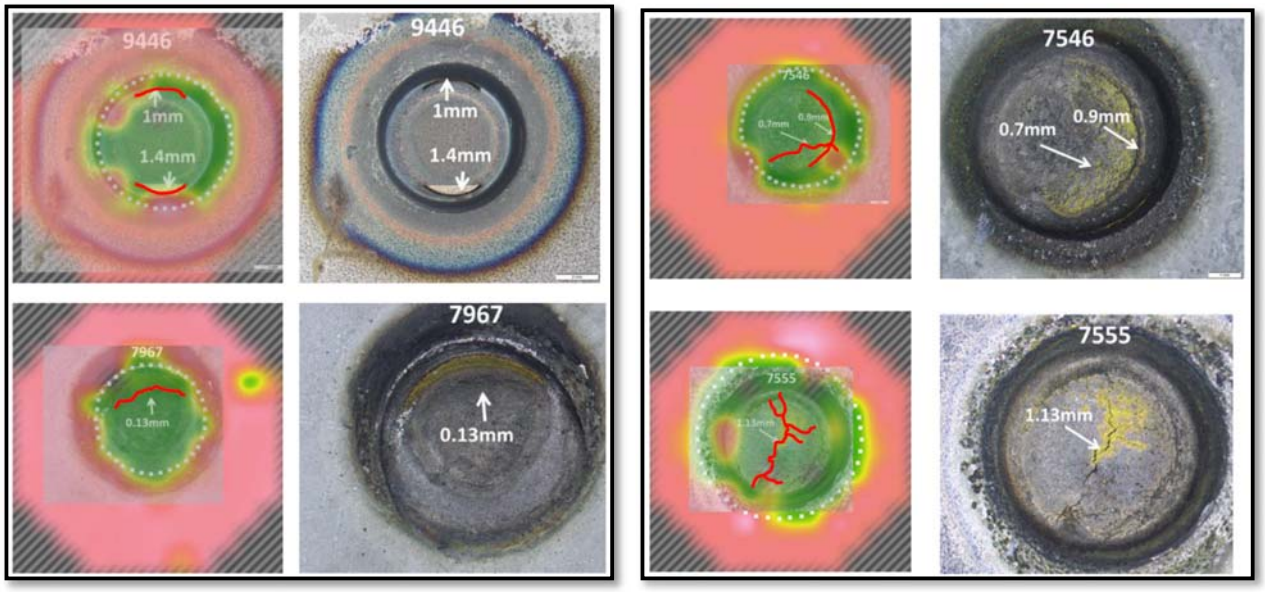


**Figure 133: Superimposition of c-scans data and microscope pictures with cracks trailed in red (left). Original microscope pictures (right).**

A low correspondence between features in ultrasound C-scan and cracks in the microscope pictures was shown. Not all circular features coincide perfectly with the end of cracks and not all ends of cracks coincide perfectly with circular features. The reason for this possibly relates to a combination of the divergence angle of the ultrasound field radiated by each element and the location of the end of the crack in relation to the position of the element (Figure 134): each ultrasound probe (in this case it's the single element) has a certain divergence angle beyond the nearfield-length which is a function of the probe's diameter, its frequency and the sound velocity (Equation 6).

$$\sin \emptyset \approx 1{,}2 \times \frac{velocity}{diameter \times frequency} = 1.2 \times \frac{2730\frac{m}{s}}{0.00125m \times 15 \times 10^6 Hz} = 10.02° \qquad (6)$$

$$sin^{-1} \propto = \frac{C_{steel}}{C_{plexiglas}} \times sin\emptyset = \frac{5920}{2730} \times sin10.02° = 22.25° \qquad (7)$$

When the sound reaches the interface between delay line and the top steel plate, the transition is described by Snell's law which gives us the propagation angle α in steel (Equation 7). With a delay line thickness of 4.4 mm, a top steel plate of exemplary 1.0 mm and the respective trigonometric calculation, the theoretically maximum distance d between the boundary of the element and a crack reach all the way through the top plate can be calculated to be appr. 2.2 mm.

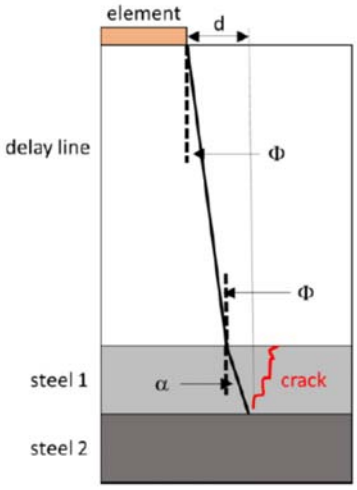


**Figure 134: Theoretical maximum distance between crack tip and elements edge.**

This result means that the spatial distance between a circular feature in the C-scan (resulting from a crack tip) and the real location of a crack tip can theoretically be up to 2.2 mm. However, it has to be noted that this is a simplified approximation. Furthermore, position of the tip as well as its orientation might alter the result.

### 4.7.4. Conclusion

The system is not able to detect and characterize cracks

## 4.8. RIWA System

### 4.8.1. Description and principle

The RIWA (Real Time Integrated Spot Weld Monitoring) system is a device capable of performing quality inspection of spot welds during the welding process. A high-frequency transducer is integrated into the welding gun electrode; this transducer generates ultrasonic waves that pass through the cooper electrode cap into the welded plates. These waves are reflected and received by the same transducer (Figure 135). The range of interest is the area between the two plates under the electrode cap. Several pulses are emitted during the welding process. The time interval between reflections arriving from front and back wall of the specimen are called time of flight (TOF). The TOF is inversely proportional to temperature. The more material is heated the bigger delay the back-wall reflection will experience, a characteristic curve forming the melting process of the plates is shown in Figure 136. Here the top line is the dynamics of the front wall and the bottom line in the middle of the image is representing dynamics of the back wall. During welding, the heat generated in the plates reduces the speed of sound in metal and causes back wall reflections to arrive later. The process reverses when current is shut off.

The union of all A-scans obtained during the process is treated by software and generates a B-scan that can be seen as a signature of the welding process. Each column in the B-scan represents an A-scan obtained at a certain time during welding. Figure 136 shows an example of a B-scan where the A-scans were taken every 2 milliseconds, in that the image is clear to see that the melting and solidification of the material between the plates.

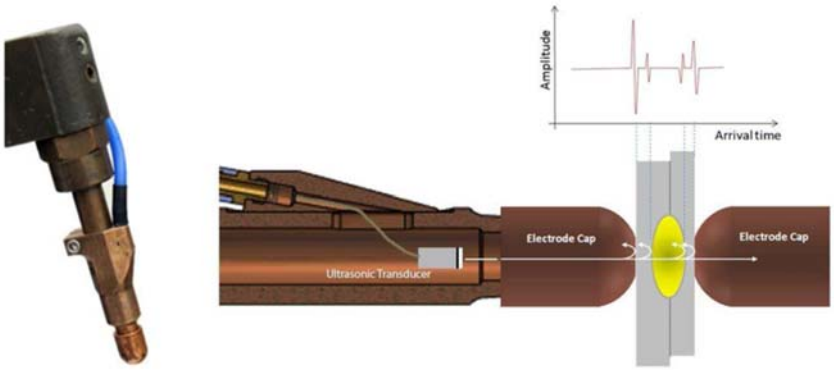


Figure 135: RIWA System. Real electrode (left). Principle (right). (Source: Tessonics)

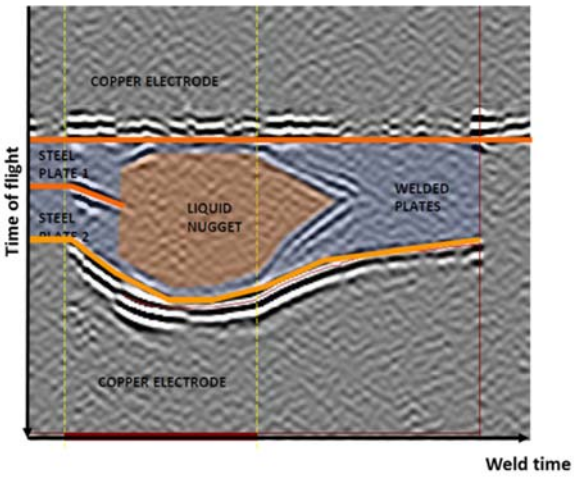


Figure 136: Ultrasonic B-scan. (Source: Tessonics)

### 4.8.2. Methodology and Experiments

Specimens have rectangular shape with dimension 50mm x 300mm. The plates were set in two different arrangements, as follows:

1. Crack generation: Welding of damaged Samples = Spots with cracks (Zn coated samples)

- MTC: DP1200 8317 (top sheet) – 1.60 mm / Mild steel 8976 (bottom sheet) – 2.00 mm


Figure 137: Damaged spot welds with LME cracks. 640ms

2. Calibration Step: Welding of reference Samples = Healthy spots without cracks (Zn free samples)

- MTC: DP1200 8317 Zn free (top sheet) – 1.60 mm / Mild steel 8976 Zn free (bottom sheet) – 2.00 mm


**Figure 138: Healthy spot welds. 640ms**

The goal was to check the response of RIWA system related to the eventual crack detection of the Zn-coated sheets generated on the specimen of Figure 137. The first attempt on building the cracks were performed using a tentative schedule of 1200 ms @8.4 kA. Although it was relatively easy generate the expected cracks (Figure 139), some side effects were experienced, including overheat in the tip of caps, with subsequent boiling of the water from the cooling system (Figure 140). The boiling of water appears near 700ms and disturbs ultrasonic waves propagation which makes the B-scan unusable.

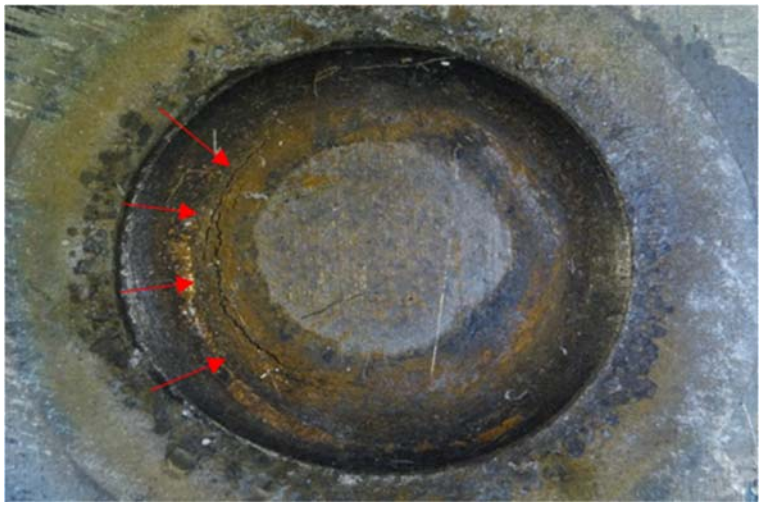

**Figure 139: LME crack obtained at 1200ms and 8.4kA.**

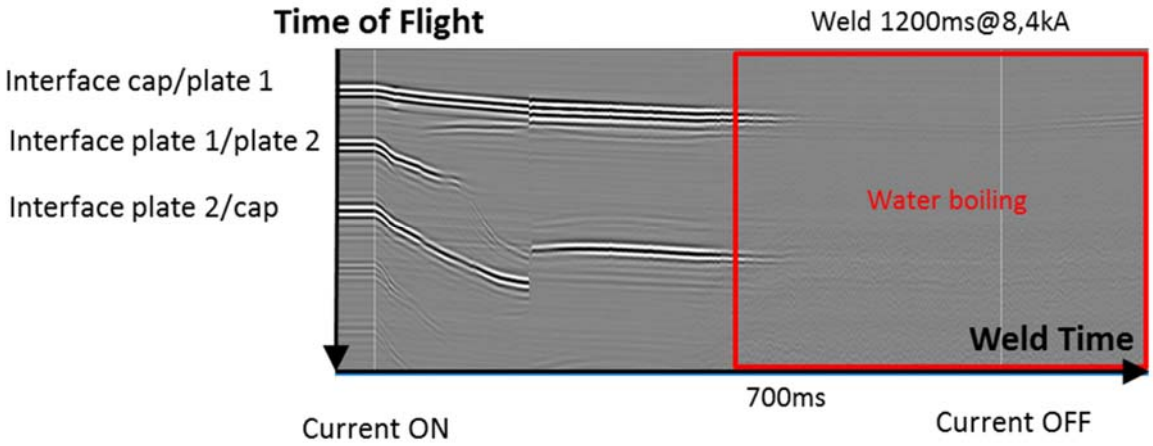


**Figure 140: B-scan of spot weld obtained at 1200ms and 8.4kA. Water Boiling.**

In this sense, a new welding schedule was designed to obtain similar effect, reducing the weld time to 640ms.

The new welding setup is as following:

| | |
|---|---|
| Current Type: | MFDC |
| Welding Time: | 640 ms |
| Welding Current: | 8.4 kA (spot n°1-5) and 8.1kA for spot n°6. |
| Forge Time: | 200 ms |
| Welding Force: | 4.0 kN |
| Electrodes diameter: | 6 mm |

Spot welds were checked to confirm the presence of superficial cracks in the contact surface of the electrodes, as it was expected on the Zn coated plates. In all welds observed, it was possible to identify the presence of cracks, as pictures below illustrate. However, the LME crack was barely visible (light LME crack). At the same time, Zn free specimens did not present any cracks in the spots, within the same welding parameters being applied to both samples.


**Figure 141: LME crack obtained at 640ms and 8.4kA.**

The RIWA tests were conducted utilizing a 15 MHz transducer integrated on the lower electrode (fixed arm), positioned in a 120 mm straight shank (Figure 142). One excitation per ms is generated.

Figure 142: Lower electrode where the transducer is imbedded.

### 4.8.3. Results and discussions

All 12 B-scans were successfully collected during the trials. Even with the schedule set to 640ms, it was possible to notice some initial effects on the water boiling, close to the open gun stage. However, this effect did not affect the general assessment of the collected scan. Below are listed the main remarks over this inspection:

- The collected scans shown a consistent pattern between the analyzed welds, as shown in the figures. As expected, melting started earlier inside the DP1200 plate, reaching the lower plate several milliseconds after. For all spot welds, material expulsion was present, and it was detected by the software, together with all the remaining parameters.

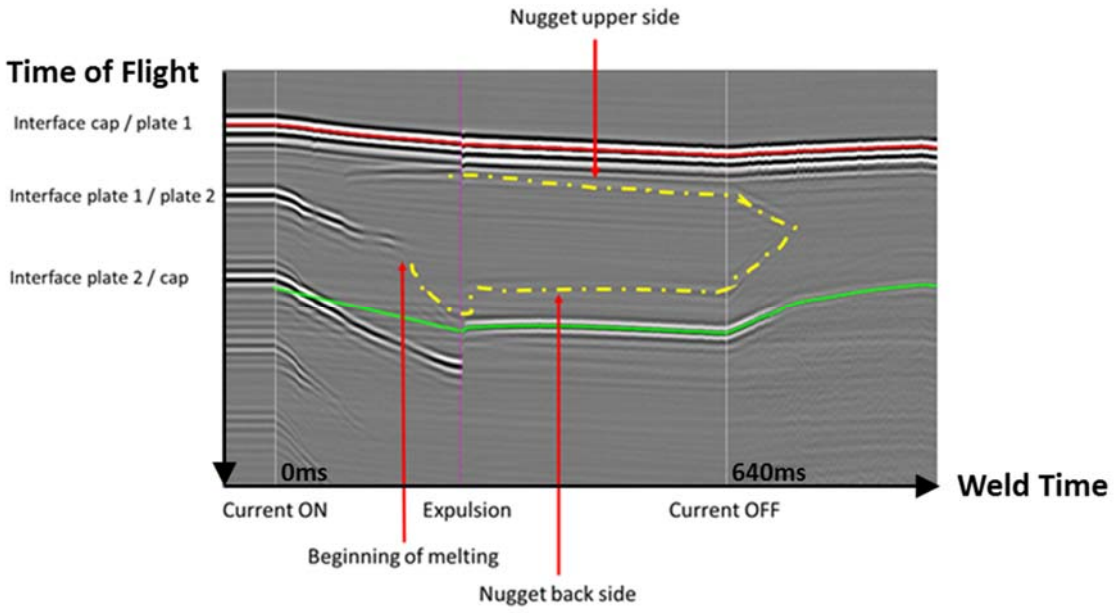


Figure 143: Zn coated specimen– Spot n°6

- The surface cracks detected through optical microscope does not seem to be detected by the existing ultrasonic beam coming from the single element transducer, as its direction matches the direction of the

ultrasonic beam. No other noticeable characteristic was detected when comparing all the B-scans between each other in terms of additional reflections/absorptions/amplitude decays.

- Water boiling was still noticeable in the later stages of the welding process (after current OFF and weld solidification). We do not believe that any main characteristic of the scan was affected due to this particular phenomenon.

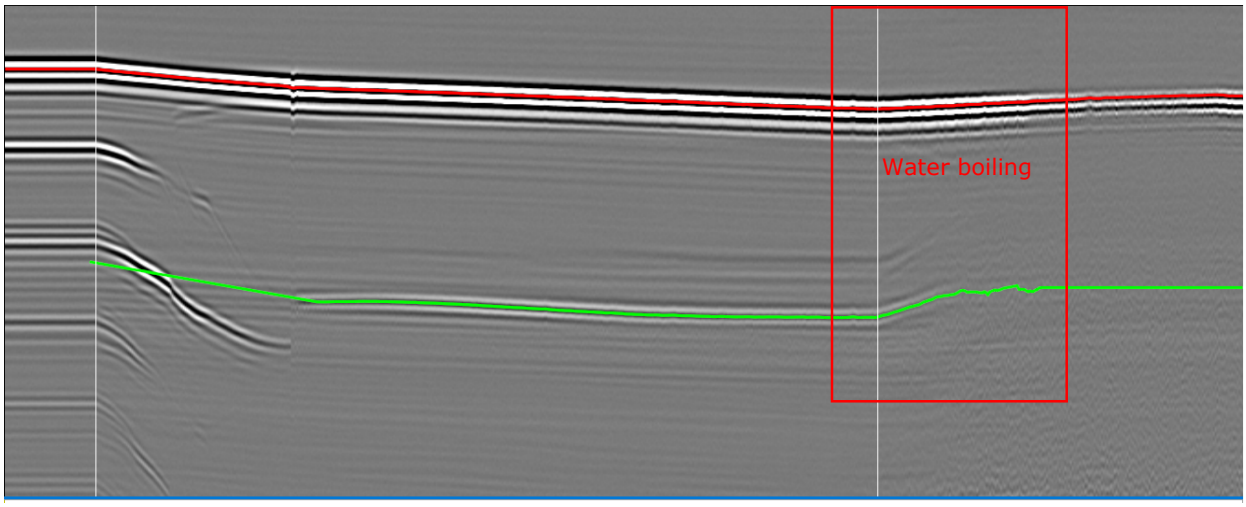


**Figure 144: Zn free specimen– Spot 6 – Boiling issues**

- As a qualitative perception, heating dissipation tends to be higher in the Zn free plates, since the observation in the samples demonstrated an increase in the boiling phase for these specimens.

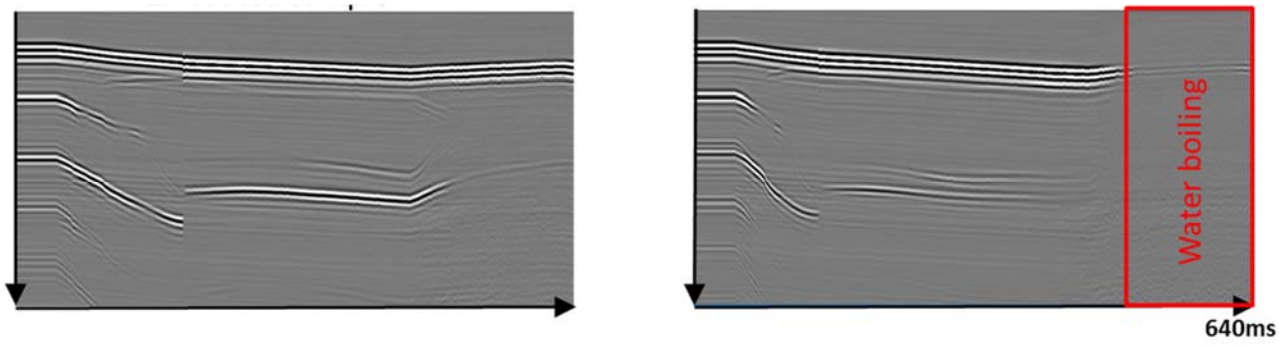


**Figure 145: Zn free specimen-spot 5@640ms (left). Zn coated specimen-spot n°5@640ms (right).**

### 4.8.4. Conclusion

No major changes were noticed in the B-scans collected between cracked and healthy spot. Further research is needed to overcome the water boiling issue and generate intense LME cracks. To be sensitive to surface cracks on spot welds, surface waves could be a path of research since it was proven in the PAUT session that this type of waves may be sensitive to LME cracks.

## 5. Final Conclusions

In total, 6 NDT methods and 4 systems are investigated:

11. Acoustic Emission
12. Magnetic Particle Inspection
13. Eddy Current Pulsed Thermography
14. Eddy Current Array
15. Phased Array
16. Computed Tomography
17. Mini Scanner System (Amstech)
18. RoboTom System (Rayscan)
19. RSWA System (Tessonics)
20. RIWA System(Tessonics)

Among them, the suitable ones for detection **AND/OR** characterization* are given below:

- Acoustic Emission – this is the only method suitable for process monitoring and would be able to provide information on LME occurrence time. It can also detect and locate in time other phenomena such as expulsion/splash.
  - A calibration phase is required for each MTC to determine signature of healthy spots
  - Provides binary answer on the presence of LME crack (Yes/No
  - Doesn't provide information on LME criticality
  - Can be used in laboratory and production environment. However, only noise and robot interference have been checked in production. Further investigations are needed for LME crack detection in production.

- Magnetic Particle Inspection – implementation is fast, and results are relevant.
  - Suitable for LME crack detection and provide relevant information on crack length, location.
  - No learning step required
  - It doesn't require high operator expertise. Provide qualitative information on crack length and location.
  - Software was developed for automatic classification of MPI pictures which classify spot welds into two categories: healthy and damaged (with LME cracks). However, for quantitative analysis and identification of the crack length, further improvements are required.
  - Can be used for laboratory and production.

- Eddy Current Pulsed Thermography–
  - Learning step required to define the setup (coil position, heating setup, analysis approach)
  - Provide information on crack length and location.
  - Learning step is required to define the model used for LME depth prediction.
  - Accuracy depends on various factors (setup, heating homogeneity, mechanical vibration, roughness, indentation…)
  - Detection and characterization have been proven in laboratory.
  - In production, this method can be used for LME crack detection and characterization

- RoboTom– mainly used for large assembly in production and can be used if already deployed (2D scans are sufficient for LME detection)
  - Can provide a local tomography of region of interest.
  - Feasibility of LME depth estimation was proven for small specimen

* The word characterization in ISA presentations and deliverable means that the NDT method is able to provide all LME crack features including **the depth** (length, opening, location). When the LME crack depth is not estimated by the NDT, the method was classified in the category of detection.

- Computed Tomography– mainly used for small specimens.
  - Extraction of the real 3D LME form and features is possible
  - Can be used for LME crack characterization in laboratory.

- Eddy Current Array–
  - Feasibility proven for EDM cracks depth estimation.
  - A large database with known crack depth is required for learning step to define the setup and sizing curve for each MTC.
  - Sensitive to various factors (steel grade, residual Zn/Cu on surface, corrosion…)
  - Further investigation is needed for LME crack depth estimation in both environments laboratory and production

The cost of investment for each suitable technique is given below and the cost of the testing of each spot weld is assessed based on **some assumptions** that are provided earlier in this report. Note that the application of a given technique requires an adaptation in the production line (space, cost, etc.)

**Table 19: NDT cost**

| | Laboratory | | Production | |
|---|---|---|---|---|
| **NDT technique** | **Instrumentation cost** | **Additional cost per Spot weld** | **Instrumentation cost** | **Additional cost per Spot weld** |
| Acoustic Emission | 30k€ | 0.2€ | 50k€ | 0.013€ |
| Magnetic Particle Inspection | 1.5k€ | 0.04€ | 200k€ | 0.22€ |
| Pulsed Eddy Current Thermography | 130k€ | 0.86€ | 200k€ | 0.22€ |
| Eddy Current Array | 87 k€ | 0.58€ | 150k€ | 0.16€ |
| RoboTom | 300k€ | 13.33€ | 300k€ | 3.35€ |

According to the cost of NDT methods and their performance, below the recommended NDT:

**Table 20: Recommendations**

| | Laboratory | Production | |
|---|---|---|---|
| | | **On-line** | **Off-line** |
| **Detection** | AE (binary answer during the welding process)<br>MPI | AE | MPI<br>PECT<br>RoboTom (if already deployed) |
| **Characterization** | XCT<br>RoboTom | | RoboTom (already available)<br>PECT (further investigations) |

Only Acoustic Emission provides a simple detection with a binary answer related to the presence of LME crack (Yes/No).

But all other NDT mentioned provide more than a simple detection:

- Magnetic Particle Testing
  - Qualitative information of LME crack length, location, opening using visual observation of MPI pictures.
- Eddy Current Array

- Qualitative information of LME crack length, location, opening using visual observation of C-scans.
- Only estimation of EDM crack was proven. Further investigations are needed for LME crack depth estimation.

- Pulsed Eddy Current Thermography
  - Qualitative information of LME crack length, location, opening using visual observation of pictures.
  - Estimation of LME crack depth
- RoboTom
  - Quantitative information of LME crack length, location, opening using with manual analysis of CT-scans
  - Measurement of LME crack depth

## 6. Perspectives

NDT Findings in this program are a considerable advance in the field of detection and characterization of cracks, compared to the state of the art. However, further investigations and efforts are needed to rule on their application either in laboratory or production. If we take the example of Acoustic emission, it has been proven that detection is possible in laboratory and industrial environment but in production, only interference and noise have been assessed. It will important to continue working on real components and rule on the applicability of AE in production environment. This will require a large database conducted on real components, in production environment. The first step will be to work with one gun and afterwards increase the difficulty by testing two or more guns welding simultaneously.

Another important point is the gun type. During trials performed in BAOMARC, it has been found that the AE signature of electric and pneumatic gun is totally different. Therefore the analysis method may be different. It is worth noting that the most complicated case is studied in this program which is electric gun. The signal is affected by the current flow which hided the LME crack signature, but this big challenge was successfully solved.

For Eddy Current Array technique, feasibility has been proven for the case of EDM crack. It is important to remind that no probe available on the market and that a new promising procedure developed and applied for RSW in particular on EDM cracks. An important step was taken but still further developments to extend the use of ECA probe for real LME cracks located inside and outside indentation with the presence of Zn layer. To do that a relevant database is required. It should cover a large range of LME depth and also length since ECA is sensitive to the volume of the crack (i.e. opening, length and depth). This should be deeply investigated and therefore several sizing curves established, based on crack length. This length can be approximated with C-Scans followed by an automatic selection of the suitable sizing curve. Furthermore, all specimens must be characterized by Computed Tomography (CT).

## 7. Bibliographic references

[1] W. D. JOLLY, "The use of acoustic emission as a weld quality monitor" Master Research supported

[2] US 3824377 A: "Acoustic emission spot welding controller", 1974.

[3] Y. LUO, L. JINGLONG, W. WEI, "Characterization of nugget nucleation quality based on the structure-borne acoustic emission signals detected during resistance spot welding process", Measurement 46 (2013) 1053-1060.

[4] ASTM E751 / E751M – 17: Standard Practice for Acoustic Emission Monitoring During Resistance Spot-Welding

[5] P. Vijayaraghavan, " Magnetic Particle & Penetrant Inspection of Aerospace Components During Manufacture & Service", National Seminar & Exhibition on Non-Destructive Evaluation, NDE 2014, Pune, December 4-6, 2014 (NDE-India 2014) Vol.20 No.6 (June 2015) - The e-Journal of Nondestructive Testing - ISSN 1435-4934 www.ndt.net/?id=17848.

[6] Thomas VETTERLEIN and all, "Application of Magnetic Particle Inspection in the Field of the Automotive Industry", ECNDT 2006-Th.1.3.3

[7] M. THORNTON , L.HAN ,N, M.SHERGOLD , "Progress in NDT of resistance spot welding of aluminum using ultrasonic C-scan", NDT&E International 48, 2012 (30-38)

[8] Anna Runnemalm, Jörgen Ahlberg, Anders Appelgren and Stefan Sjokvist, Automatic Inspection of Spot Welds by Thermography, 2014, Journal of nondestructive evaluation, (33), 3, 398-406.

[9] Abdoulaye Taram annd all, « Nondestructive testing of resistance spot welds using eddy current thermography », Vol.57, Noo 18/20 June 2018/ Applied Optics.

[10] Beate Oswald-Tranta, "Investigations for determining surface crack depth with inductive thermography", 19th World Conference on Non-Destructive Testing 2016.

[11] Guin Yun Tian, « Eddy current pulsed thermography with different excitation configurations for metallic material and defect characterization », Sensors 2016, 16, 843; doi: 10.3390/s16060843

[12] Peyman Hedayati Vahid, « Automatic defect detection and depth estimation using pulsed thermography », Mémoire, Université LAVAL, Québec, Canada, 2014.

[13] JG Sun : Analysis of pulsed thermography methods for defect depth prediction. Journal of Heat Transfer, 128(4):329–338, 2006.

[14] C. Ibarra-Castanedo and X. Maldague, « Defect Depth Retrieval from Pulsed Phase Thermographic Data on Plexiglas and Aluminum Samples », Thermosense XXVI, edited by Douglas D. Burleigh, K. Elliott Cramer,

G. Raymond Peacock, Proc. of SPIE Vol. 5405 (SPIE, Bellingham, WA, 2004) · 0277-786X/04/$15 · doi: 10.1117/12.540855

[15] Steven M Shepard and all, « Reconstruction and enhancement of active thermographic image sequences. Optical Engineering, 42 (5):1337-1342, 2003

[16] JG Sun, « Analysis of pulsed thermography methods for defect depth prediction. Journal of heat transfer, 128(4):329-338, 2006.

[17] Jason M Warnett and all, « Towards in-process x-ray CT for dimensional metrology », Meas.Sci. Technol. 27 (2016)035401 (14pp). doi:10.1088/0957-0233/27/3/035401

[18] Michal Krumm and all, « Rapid Robotic X-ray Computed Tomography of Large Assemblies in Automotive Production », 8th Conference on Industrial Computed Tomography, Wels, Austria (iCT 2018)

**WorldAutoSteel**

Avenue de Tervueren 270
1150 Brussels – Belgium
T: +32 (0) 702 89 33
F: +32 (0) 702 88 99
steel@worldautosteel.org

**World Steel Association**
**worldsteel.org**